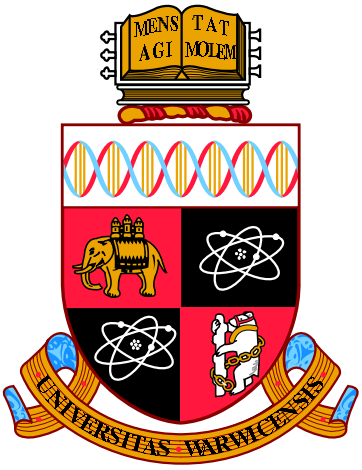

Active Liquid Crystals in Confined Geometries

by

Diana Khoromskaia

Thesis

Submitted to the University of Warwick

for the degree of

Doctor of Philosophy

Centre for Complexity Science

April 2017

THE UNIVERSITY OF WARWICK

Contents

Acknowledgments

First and foremost I would like to thank my supervisor Gareth Alexander for providing me the fascinating topic of this thesis. I am grateful for the guidance, the stimulating discussions, and the invaluable help and advice. Learning from him was a most inspiring experience.

I would like to thank Carl Whitfield for his help with various topics related to this work. I further thank Stefan Grosskinsky, Matthew Turner, Marco Polin and many other members of the Soft Matter group for scientific advice throughout my PhD. For the pleasant working atmosphere, especially on Friday afternoons, I thank Joel Nicholls, Tom Machon, Davide Michieletto, and Dario Papavassiliou.

I was lucky to share my time at Warwick with friends and colleagues who made it truly enjoyable and memorable, in particular Merve Alanyali, Elena Camacho-Aguilar, Tom Rafferty, Jonathan Skipp, Federico Botta, Liz Buckingham-Jeffery, Neil Jenkins, Bernd Taschler, Quentin Caudron, and Sergio Morales. I thank Andrea Thamm, Julia Neugebauer, and Theresa Strauch for their support and friendship from afar.

I am greatly indebted to my parents, Venera Khoromskaia and Boris Khoromskij, for all the support I have received throughout the years. You are my guiding examples in life and research. Finally, I thank Martin Fritzsche for continual encouragement and motivation, which were vital for the completion of this thesis.

Declarations

This thesis is submitted to the University of Warwick in support of my application for the degree of Doctor of Philosophy. It has been composed by myself and has not been submitted in any previous application for any degree. Parts of the material in this thesis have been published as follows:

- Parts of the material in Chapters 3 and 4 have been published in:
  D. Khoromskaia and G. P. Alexander, *Motility of active fluid drops on surfaces*, Phys. Rev. E 92, 062311 (2015).

- Material from Chapters 3, 5, and 6 is currently being prepared for publication.

Abstract

Active liquid crystals, in which the rod-like constituents endow the fluid they are immersed in with active stresses, have proven successful as a paradigm for biologically inspired complex fluids with orientational alignment. These include suspensions of swimming bacteria or cell extracts comprising cytoskeletal filaments and molecular motors, whose natural environment is characterised by spatial confinement.

In this thesis we study active liquid crystals in three confined geometries – a planar thin film, a droplet on a flat surface, and a spherical shell. For alignment fields with topological defects, which are known to be energy minima for passive liquid crystals in these geometries, we investigate with analytical and numerical methods the effect of activity. Novel results include defect-driven motility of active drops and shells as well as the formation of stable flow vortices in spherical confinement.

In the first part we calculate analytically the active flows in a thin film, which are driven by a generic defective alignment field, and identify the type of flow singularity that a defect with arbitrary topological strength generates. The sliding velocity of an active drop, which moves due to an asymmetrically placed defect within, is calculated analytically. In general, asymmetry in the alignment generates motion of the drop due to directed flows in the bulk, although slip at the substrate and active flows resulting from gradients in the drop shape counteract this motion. Steady state shapes of a drop with a central defect reveal the formation of a hole or a cusp in its free surface.

The thin film model is adapted to a spherical shell in the second part, where locally the defect-driven flows are analogous to a flat film. Globally, the active flow is restrained by the Poincaré-Hopf theorem, which prescribes a total winding of $+2$. We find that the flow typically forms two counterrotating vortices, which is shown to have crucial implications for the defect motion and for the swimming behaviour of the shell. The dynamics of different defect configurations are simulated numerically with a particle-based model, where the defects move due to elastic forces and active advection, which is extracted from an exact expression for the active flow in the shell. We recover the oscillatory motion of four half-integer defects known from experiments and interpret it in view of the two counterrotating vortices, which advect the defects. The onset of oscillations is captured analytically in a linear stability analysis. Further, new predictions are provided for the scaling of measurable quantities, like oscillation frequency and defect speed, for the dynamics of additional defect-pairs and for polar shells, in which unit strength defects are found to attract or repel due to active flows. Finally, the swimming speeds of active nematic shells through a passive medium are calculated analytically, or numerically if half-integer defects are present. Remarkably, shells with triangular defect arrangements are found to be swimming and rotating.

In summary, this work furthers the understanding of geometrically confined active liquid crystals, highlighting the role of topological defects and the active flows they produce. The results presented here could also find application in microfluidics, for instance aiding in the design of artificial crawlers and swimmers.

Abbreviations and Symbols

ALC	active liquid crystal
LC	liquid crystal
SPP	self-propelled particle
MT	microtubule
ATP	adenosin triphosphate
PEG	polyethylene glycol
μ	dynamic viscosity of active suspension or fluid
γ	surface tension
σ_0	activity parameter
K, K_i	Frank elastic constants
m, m_i	topological strength of a defect
γ_1	liquid crystal rotational viscosity
ν_1	liquid crystal flow-alignment parameter
l_a	intrinsic active length scale
ξ	effective sliding friction coefficient, equivalent to slip length
α_0	constant director phase
r_c	defect core radius
h_0	average film thickness
R	drop or shell radius
ε	aspect ratio in a thin film
U_0	typical active flow scale
T	typical active time scale

τ	elastic relaxation time
ρ	dimensionless cut-off length
v_0	speed of $+1/2$ defects
ν	ratio of active to elastic stresses for $+1/2$ defects
$\nu^{(1)}$	ratio of active to elastic stresses for $+1$ defects
β_{ij}	angular distance between defects i and j on the sphere

CHAPTER 1

Introduction

1.1. Active matter

"[...] Living matter, while not eluding the "laws of physics" as established up to date, is likely to involve "other laws of physics" hitherto unknown." Phrased by Erwin Schrödinger in "What is life?" [Schrödinger, 1944] as early as 1944, this statement foretells the decades-long endeavour of physicists to contribute to the understanding of the mechanisms governing the living world. Notwithstanding the vast complexity of even a single cell [Phillips et al., 2009], a physical framework overarching a surprisingly diverse range of biological phenomena has emerged in the last twenty years. Mechanical processes inside eukaryotic cells, collections of crawling cells or swimming bacteria, schools of fish, and flocks of birds — all are encompassed by the framework of active matter [Marchetti et al., 2013; Ramaswamy, 2010; Prost et al., 2015]. From a condensed matter physics perspective these systems may be regarded as collections of active particles, which have the defining ability to transform chemical or other types of energy into directed motion. Being typically elongated entities, their geometry guides the direction of their self-propulsion and enables large numbers of such particles to align in parallel and move collectively. Such swarming behaviour was first reproduced in a model of "flying" magnets [Vicsek et al., 1995]. This launched a successful and still ongoing effort to classify active systems and identify universal behaviours like order-disorder phase transitions, fluctuations, and instabilities, based on symmetries and conservation laws at play in a particular system. The out-of-equilibrium nature of active matter, which stems from the local energy intake at the level of each individual active particle, leads to "other laws of physics" and a whole range of novel phenomena, which are nonexistent in equilibrium materials. Crucially, active materials spontaneously generate flows [Simha and Ramaswamy, 2002a], and the interplay of such flows with geometrical confinement and defective alignment of particles leads to a rich phenomenology, including motion on large scales [Sanchez et al., 2013; Keber et al., 2014], that is currently a vibrant area of research.

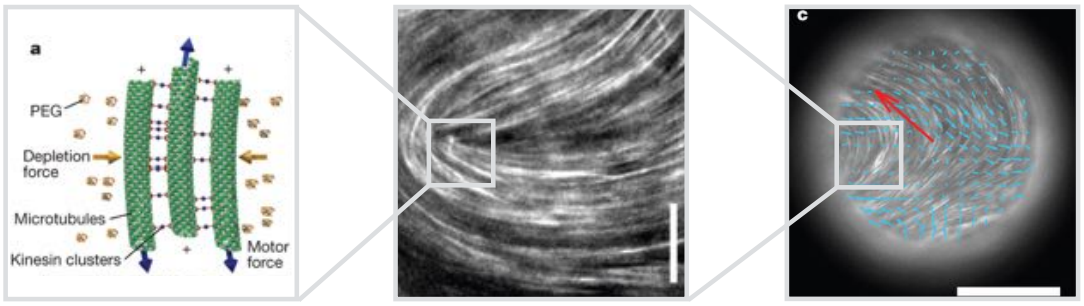

Figure 1.1: Illustration of the different levels of collective effects in an active liquid crystal on the example of an active nematic droplet, adapted from Reference [Sanchez et al., 2013]. The energy intake and initial motion is on the level of a single kinesin motor, which is then transformed to larger scales by a hierarchy of processes: 1) several kinesin-motors are bound into a cluster; 2) a number of clusters link two microtubule-bundles and make them slide past each other; 3) in a dense suspension the sliding microtubules align locally into a nematic phase; 4) the active nematic develops moving topological defects, which collectively create large-scale flows; 5) confined to the surface of an emulsion droplet these flows (blue arrows) lead to self-propulsion of the droplet (red arrow) when in contact with a surface. The relationship between active defects (middle box) and macroscopic motility (right box) is one of the topics of this thesis.

This thesis focuses on active liquid crystals (ALCs), which are orientationally ordered phases of active particles suspended in water. This class is most relevant for the description of the cytoskeleton of cells and of *in vitro* suspensions of intracellular filaments with their associated molecular motors, such as microtubules (MTs) and kinesin motors, but also for collections of swimming microorganisms like cells and bacteria. The behaviour of an active liquid crystal is strongly affected by the presence of boundaries. Employing confinement to induce specific behaviours of an active system is a topical field of research, aimed at microfluidic and biomimetic applications. Moreover, spatial confinement is a precondition for the functioning of most biological realisations of active matter at cellular and subcellular scales. It is thus a necessary part of any attempt to model such systems, for instance when modelling the swarming of bacteria in biofilms or the cytoplasmic flows in a cell.

Recent years have seen fascinating experimental breakthroughs on the side of ALCs in confinement. Dogic and coworkers have designed a well-controlled model system of an extensile active nematic material [Sanchez et al., 2013], which has already confirmed many theoretical predictions like the emergence of spontaneous flows and dynamic defect patterns. Moreover, it has opened the possibility to realise and manipulate active liquid crystals in new, more complex geometries [Keber et al., 2014; Wu et al., 2017]. Here, we model and offer theoretical predictions for two such geometries, a flat drop on a surface and a spherical shell.

Droplets coated with a layer of ALC were shown to self-propel over large distances when put in contact with a surface [Sanchez et al., 2013]. The ALC in this case consists

of bundles of MTs, connected with each other by clusters of kinesin motors that consume the chemical fuel adenosin triphosphate (ATP). Each of these motors converts the energy stored in one molecule of ATP into a step of 8 nm along a MT, but collectively they are able to propel the whole droplet, which can be as large as $\sim$ 100 μm in size. To date, there is no theoretical understanding of how such active droplets move. This astonishing transfer of tiny movements into large-scale motion and focusing of the energy taken in at the smallest scale requires self-organised coordination on several levels of processes, that work together in the droplet not unlike the cog wheels of a mechanical clockwork, as illustrated in Figure 1.1. One such "cog wheel" is the local alignment of the MT bundles and the fundamental relationship between gradients in the alignment field and active fluid flows generated by it. The flows on the surface of the drop can then push against the surrounding medium and propel the drop. Intertwined with this process are topological defects – singularities in the local alignment field, which cannot be removed by continuous deformations and which naturally are sources of strong gradients and active flows. The topology of a droplet enforces such defects, which should make them the main drivers of the flow and, therefore, of the macroscopic motion. We will investigate this connection for a droplet sliding on a flat surface and for a spherical shell immersed in a passive fluid.

Topological defects are fundamental features of ordered phases of matter and a topic of great current interest across disciplines[1]. They have universal properties tied to the symmetry – nematic or vectorial symmetry for instance – and the topology of the system. In combination with specific boundary geometries defects can generate new macroscopic properties of a piece of material, as evident from the variety of states known for drops and shells of passive liquid crystals [Lopez-Leon and Fernandez-Nieves, 2011]. The role of topological defects in active and living systems is far from being understood. Some intriguing new properties of defects resulting from activity have already been established, for instance self-propulsion and rotation [Kruse et al., 2004; Giomi et al., 2013, 2014] as well as their spontaneous generation in the bulk [Sanchez et al., 2013; Thampi et al., 2013]. However, many questions remain unresolved: What are the collective dynamics of defects under their self-generated active flows? What new interactions arise among active defects? How do defects in active systems affect the shape of surfaces, the large-scale flows, and the macroscopic motion? Understanding these relationships might open up possibilities for better control of active materials through the manipulation of defect structures and lead to a more complete classification of the states of active matter. This thesis addresses some of these questions for specific geometries.

[1]The Nobel Prize 2016 in Physics has been awarded to J. M. Kosterlitz, D. Haldane and D. J. Thouless for their work on topological phase transitions where topological defects play a crucial role.

1.2. Summary of this thesis

In this thesis we study the implications of topological defects in active liquid crystals in the context of various confined geometries. Our focus lies on the relationship between defects, the active flows they produce locally, and the resulting coherent large-scale flows and macroscopic motion, of the type found in the experiments pioneered by the Dogic and Bausch groups. We work in the framework of a thin film of active liquid crystal and choose two geometries for our analysis – a flat droplet on a surface and a spherical shell – which have received only little attention thus far [Joanny and Ramaswamy, 2012; Keber et al., 2014]. Both geometries are of considerable relevance for the design of biomimetic, self-propelling objects and provide the means to explore the physical basis of certain functions of biological cells, like cytoplasmic streaming, swimming and crawling.

The content of this thesis is presented as follows. In Chapter 2 the theoretical background on active liquid crystals is provided, including generalised hydrodynamics, liquid crystal elasticity, and the description of topological defects in two dimensions. Thereafter, existing theoretical and experimental work on ALCs in confinement is reviewed. The Chapters 3-6 cover the original contributions of this thesis and their discussions.

In Chapter 3 the hydrodynamic model for a thin film of ALC is presented. The active flow is obtained analytically for an imposed alignment field with an arbitrary collection of defects, that lies tangential at the film boundaries and represents an energetic minimum of a passive liquid crystal. The flow is driven by an active force which is decomposed into three contributions – splay and bend of the two-dimensional alignment field and coupling to shape gradients. We then calculate a generic relationship between the type of defect and the flow singularity it produces in the film, by expanding the active flow in the vicinity of a defect. This generalises previously known results to defects of any topological strength and yields a new scaling of the speed of the self-propelling half-integer defects. Further, for a half-integer defect the active flow in the defect core region is solved for analytically and matched with the thin film solution, to regularise the latter at the defect location.

A flat drop on a surface, which is modelled as a laterally bounded thin film, is studied in Chapter 4. For the geometry of a spherical cap and for defects of different type and position the structure of the analytically calculated active flow is analysed regarding its three contributions. Asymmetrically positioned +1 defects, or generally asymmetric splay or bend distortions of the alignment, generate directed bulk flows, but flows due to shape gradients are found to counteract those close to the contact line. The centre-of-mass velocity of a droplet with one defect or with a smoothly splayed

or bent alignment is calculated analytically. An optimal defect position maximises this velocity. Finite slip at the substrate reduces the velocity and an estimate is given for the amount of slip required to stall the motion. Further, the stationary shape is obtained analytically for an axisymmetric drop with one defect – a vortex defect or a spiral defect with different angles. This reveals that defects can strongly deform the drop, leading to a dip or hole in the former case and to a cusp in the latter. For asymmetric drops the initial deformations away from a spherical cap are estimated.

In Chapter 5 the thin film model is adapted to a spherical shell and solved for the instantaneous active flow in this geometry. Here, the Poincaré-Hopf theorem imposes a total winding of +2 in both the alignment field and the flow field and the implications of this are investigated in that chapter. A derivation of the equilibrium alignment field with defects on a sphere is provided. At this point the stereographic projection from the sphere to the complex plane is introduced, which is also used in subsequent calculations involving the active flow. The local active flow singularities at defects on the sphere are derived, showing the same structure as in a planar film. The interplay of these local flow singularities with the global topological constraint is shown for several exemplary defect configurations. It is shown that, in general, additional, not defect-based flow singularities are required to satisfy the constraint.

In the second part of Chapter 5 the motion of defects in active shells is studied with numerical simulations. The defects are modelled as particles that move due to advection in the active flow and due to elastic interactions with each other in an overdamped regime. To this end the liquid crystal elastic interactions of defects are formulated for a sphere. The active advection is extracted from the exact solution for the active flow, whereby the flow is locally averaged at a short-length cut-off distance from the defect to avoid divergence. An exact expression is given for the direction and speed of +1/2 defects on the sphere. A second order expansion of the flow at a defect reveals a different scaling for the active advection of +1 defects on a sphere as compared to +1/2 defects. Thereafter, the overdamped dynamical equations for different collections of defects on the sphere are solved numerically using a standard Runge-Kutta method. First, the dynamics of four +1/2 defects are simulated. We find an elasticity-dominated regime, where the defects settle into a deformed tetrahedron. In the activity-dominated regime the defects form pairs and undergo steady oscillations, moving through tetrahedral and planar arrangements at lower activity and on ever smaller, circular trajectories as activity is increased. The oscillatory motion is caused by two stable counterrotating active flow vortices, which advect the defects and lead to their effective attraction in pairs. The transition between these two regimes is quantified in a linear stability analysis. The dynamics of two +1 defects are similar and we find active attraction of vortex-like and repulsion

of aster-like defects for an extensile material. Finally, the effect of half-integer defect pairs added to the four-defect configuration at random or specific locations is studied.

Chapter 6 contains a theoretical analysis of the swimming properties of an active nematic shell through a passive medium using the squirmer model. We calculate the translational and rotational velocities of a shell from the active flow on its surface analytically, or numerically if half-integer defects are involved. We find that the defect configurations considered in Chapter 5 do not lead to macroscopic motion, neither translational nor rotational, as the corresponding flows are variants of the two counterrotating flow vortices and therefore too symmetrical. However, a shell with a triangular defect arrangement, known from passive nematics, is found to be swimming and rotating.

In Chapter 7 we summarise and discuss the main results of this thesis and outline interesting directions for further research and potential applications.

CHAPTER 2

Active Liquid Crystals

2.1. Classification of active matter

Here we concern ourselves with systems that are commonly described as wet active matter with liquid crystalline order, or active liquid crystals. Such systems may be aqueous suspensions of biological filaments [Nedelec et al., 1997; Sanchez et al., 2013], with molecular motors providing the source of motion on the smallest scale, as well as collections of swimming cells or bacteria [Wioland et al., 2013]. A continuum description of the long-wavelength behaviour of these suspensions is based on the identification of slow variables, associated with conserved quantities and broken symmetries. In wet active matter the total momentum is conserved and its density is one of the fields entering the continuum model [Simha and Ramaswamy, 2002a; Kruse et al., 2004]. The resulting equations are those of liquid crystal (LC) hydrodynamics [de Gennes and Prost, 1995; Chaikin and Lubensky, 2000], modified by terms arising from activity, which will be introduced in Section 2.2.2.

The other class is dry active matter, in which any hydrodynamic interactions between the constituents are damped, for instance by strong friction with a substrate, and overall momentum is not conserved [Toner et al., 2005]. The number density of active particles becomes the relevant conserved field. On the microscopic scale this represents cell monolayers [Duclos et al., 2014] and motility assays of intracellular filaments [Schaller et al., 2010], but is also applicable to active objects on large scales, such as groups of animals in motion [Toner and Tu, 1998; Toner et al., 2005].

To describe dry active matter a different approach in the form of discrete, stochastic models may be taken, known under the name of self-propelled particle (SPP) models [Vicsek and Zafeiris, 2012; Cates and Tailleur, 2015]. In the simplest case the eponymous particles have an orientation and a prescribed velocity and align with their neighbours according to some rules and subject to noise [Vicsek et al., 1995]. Agent-based computer simulations of SPPs have been successful in describing for instance collective motion of birds [Pearce et al., 2014] and provide a framework to incorporate

new, system-specific behavioural rules [Pearce and Turner, 2014]. In the context of active liquid crystals topological defects allow for an effective description as SPPs interacting via an elastic potential [Giomi et al., 2014; Keber et al., 2014]. We will employ this approach in Chapter 5 to study the motion of defects in an active nematic shell in simulations.

Orientationally ordered active systems are also differentiated according to the symmetry of their orientation field and the type of stresses they exert on their surrounding. Polar particles, which have a well-defined direction of self-propulsion, flock into phases with vectorial order. Locally, particles move in parallel, leading to directed motion of the whole flock. Motile cells, swimming bacteria, and moving animals intrinsically have this head-tail asymmetry. On the microscale, there are also instances of active particles which are head-tail symmetric, such as melanocytes, fibroblasts, and other spindle-like cells [Kemkemer et al., 2000; Duclos et al., 2014, 2016]. They order into nematic phases, which are invariant under locally reversing the orientation of the constituents. Nematic symmetry is well-known from liquid crystals, which consist of aligning rod-like molecules. Nematic "flocks" do not move, on average, and allow for different types of topological defects than polar flocks. This type of order occurs not only if the active particles are apolar, but also if the interactions between particles are insensitive to their polarity or if the collection is well-mixed, with equal amounts of oppositely polarised particles [Sanchez et al., 2013]. In this sense, an active particle does not have to be self-propelling, but is only required to exert anisotropic forces on its environment. One distinguishes between extensile and contractile forces in the direction of local orientation.

There are also examples of active matter, which are not biological in origin: vibrated granular rods [Narayan et al., 2007]; collections of colloidal particles, for instance activated by light [Palacci et al., 2013, 2014], by magnetic fields [Bricard et al., 2013], or by chemical gradients; suspensions of artificial swimmers and swimming droplets; and swarms of moving robots, like bristlebots [Giomi et al., 2012] or kilobots [Rubenstein et al., 2014]. Most of these systems however do not fall under the realm of active liquid crystals, because they are either dry or lack liquid crystalline alignment, like spherical colloidal particles and droplets.

We stress, that we do not aim to describe "living liquid crystals". Although previously having been used as a synonym for active liquid crystals [Simha and Ramaswamy, 2002b], this term has recently been reintroduced for a new type of active matter, which consists of bacteria immersed in a bath of passive nematic liquid crystal [Zhou et al., 2014] and hence requires a different theoretical description than the systems considered here.

2.2. Continuum description of active liquid crystals

As the continuum description of ALCs is an extension of liquid crystal hydrodynamics, this section first introduces the basics of nematic liquid crystals and the generalised elasticity that is associated with distortions in the nematic alignment field. We then present the derivation of active hydrodynamic equations after Simha and Ramaswamy [2002a], focusing on the active stress term, but also mention various generalisations. The new features that these systems acquire due to activity are reviewed, in particular flow instabilities, rheology, and fluctuations.

2.2.1. Elasticity of nematic liquid crystals

The term liquid crystal denotes a whole range of mesomorphic phases of matter, which have properties in between simple fluids and crystals. The simplest such phase is the nematic liquid crystal, for instance consisting of rod-like molecules in suspension. A nematic has no positional order whatsoever and can be well described as a fluid with an additional director field $\boldsymbol{n}(\boldsymbol{x})$, which represents the mean local alignment of the rod-like units [de Gennes and Prost, 1995]. As the units are head-tail symmetric, all physical properties of a nematic material are invariant under inversion of the director $\boldsymbol{n} \to -\boldsymbol{n}$, so it can be visualised as a headless vector field or line field, like in Figure 2.1 (a).

The emergence of orientational order can be rationalised as a phase transition, in which the rotational symmetry of the isotropic liquid state is broken, for instance in the framework of a Landau-De Gennes theory [de Gennes and Prost, 1995]. The isotropic-to-nematic transition can be induced by an increase in concentration or a decrease in temperature, the material then being lyotropic or thermotropic, respectively. In the ordered phase the director is typically assumed to have unit magnitude

$$\boldsymbol{n}^2 = 1, \tag{2.1}$$

except at the locations of topological defects, see Section 2.4.

Like in any ordered medium with a spontaneously broken continuous symmetry, there are long-wavelength distortions of the nematic order which give rise to the Frank free energy [de Gennes and Prost, 1995]

$$E = \frac{1}{2}\int \mathrm{d}^3x \Big\{ K_1(\boldsymbol{\nabla}\cdot\boldsymbol{n})^2 + K_2[\boldsymbol{n}\cdot(\boldsymbol{\nabla}\times\boldsymbol{n})]^2 + K_3[(\boldsymbol{n}\cdot\boldsymbol{\nabla})\boldsymbol{n}]^2 \Big\} \tag{2.2}$$

where the three terms represent splay, twist and bend deformations and the K_i are the corresponding Frank elastic constants. Equilibrium directors for given boundary

conditions are found by minimising the free energy (2.2) with respect to $\boldsymbol{n}$, $\frac{\delta E}{\delta \boldsymbol{n}} = 0$. Away from equilibrium, changes of the director are driven by the molecular field

$$\boldsymbol{h} = -\frac{\delta E}{\delta \boldsymbol{n}} \cdot (\mathbf{I} - \boldsymbol{n}\boldsymbol{n}) \,, \tag{2.3}$$

where $\mathbf{I}$ is the unit tensor. Only the component perpendicular to $\boldsymbol{n}$ is included, to satisfy the constraint (2.1).

Although in most real liquid crystals the values of the three constants can be quite disparate, it is insightful to work in the one-elastic-constant approximation, $K_i = K$. In particular, it offers a simplified description in which far greater analytic progress can often be made. The principal effect of anisotropy in the elastic constants is to break the symmetry between different geometric distortions (splay and bend), however, in active materials this geometric coupling (distinction between splay and bend) is already provided by the active forces so that all qualitative phenomena should be captured even in the one constant approximation. In this approximation the energy functional (2.2) reduces to

$$E = \frac{K}{2} \int \mathrm{d}^3x \Big\{ |\boldsymbol{\nabla} \boldsymbol{n}|^2 \Big\} \,. \tag{2.4}$$

In two dimensions, a unit magnitude director is determined by its local angle of orientation $\alpha(\boldsymbol{x})$,

$$\boldsymbol{n}(\boldsymbol{x}) = \cos(\alpha(\boldsymbol{x}))\hat{\boldsymbol{e}}_x + \sin(\alpha(\boldsymbol{x}))\hat{\boldsymbol{e}}_y \,. \tag{2.5}$$

In terms of $\alpha(\boldsymbol{x})$ the elastic energy (2.4) is written as

$$E = \frac{K}{2} \int \mathrm{d}^2x \, (\boldsymbol{\nabla} \alpha)^2 \tag{2.6}$$

and its variation is $\delta E = -K \int \mathrm{d}^2x (\nabla^2 \alpha) \delta\alpha$. So, in the one-elastic constant approximation, a director satisfies the equilibrium condition if its local angle is a harmonic function,

$$\nabla^2 \alpha(\boldsymbol{x}) = 0 \,. \tag{2.7}$$

An obvious solution is a uniform director, but in general the real and imaginary part of any holomorphic function is harmonic [Needham, 1998]. In this thesis we are concerned with singular solutions to equation (2.7), which incorporate topological defects and are discussed in Section 2.4 and, more generally, in Section 3.3.

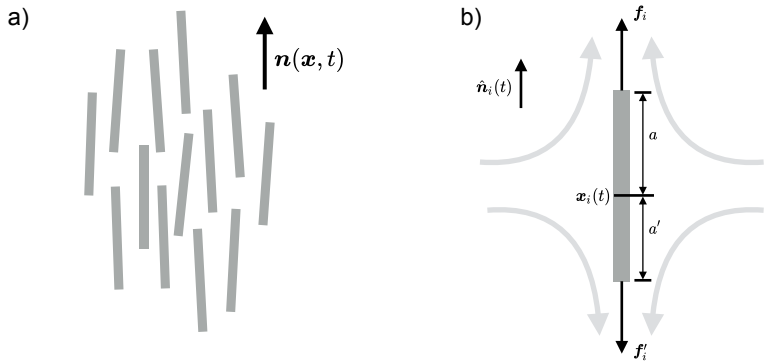

Figure 2.1: (a) In a nematic liquid crystal the rod-like particles are locally aligned on average along a direction given by the director field $\boldsymbol{n}(\boldsymbol{x},t)$, whereby $\boldsymbol{n}$ and $-\boldsymbol{n}$ are equivalent. (b) Cartoon of an active rod-like particle producing an extensile ($\sigma_0 > 0$) dipolar flow (light grey arrows). For a contractile flow ($\sigma_0 < 0$) the arrows would be reversed. The notation used to coarse-grain a collection of such force dipoles is shown.

2.2.2. Active liquid crystal hydrodynamics

We follow the derivation of the equations of motion for an active liquid crystal given by Simha and Ramaswamy [Simha and Ramaswamy, 2002a,b; Toner et al., 2005], where the form of the active stress was first established. Consider an orientationally ordered, three-dimensional suspension of active particles with nematic alignment. The long-wavelength, long-time behaviour of this material can be described in a generalised hydrodynamic approach [Martin et al., 1972], where one identifies the slow, or hydrodynamic, variables and writes down their time-evolution expanded to leading orders in gradients. Hydrodynamic variables are those for which the frequency of their fluctuations vanishes as their wavelength diverges, that is fluctuations of conserved quantities and Goldstone modes of spontaneously broken continuous symmetries. In an ALC variables of the first type are the mass density $\rho(\boldsymbol{x},t)$ and the momentum density $\boldsymbol{g}(\boldsymbol{x},t) = \rho(\boldsymbol{x},t)\boldsymbol{u}(\boldsymbol{x},t)$, where $\boldsymbol{u}(\boldsymbol{x},t)$ is the fluid velocity field. Here, density and velocity refer to the suspension as a one-component fluid, not distinguishing between the solvent and the active particles suspended in it. The concentration of active particles can be another hydrodynamic variable, but we consider it as constant for simplicity, $c(\boldsymbol{x},t) = c_0$.

Nematic order entails a slow variable of the second type, which we take to be the unit length nematic director $\boldsymbol{n}(\boldsymbol{x},t)$. Its time evolution can be directly adopted from standard liquid crystal theory [de Gennes and Prost, 1995; Chaikin and Lubensky, 2000],

$$\partial_t \boldsymbol{n} + (\boldsymbol{u}\cdot\boldsymbol{\nabla})\boldsymbol{n} + \boldsymbol{\omega}\cdot\boldsymbol{n} = \frac{1}{\gamma_1}\boldsymbol{h} - \nu_1 \boldsymbol{v}\cdot\boldsymbol{n}\,, \tag{2.8}$$

with the vorticity tensor $\omega_{ij} = (\partial_i u_j - \partial_j u_i)/2$, the strain rate tensor $v_{ij} = (\partial_i u_j +$

$\partial_j u_i)/2$, and the molecular field $\boldsymbol{h}$ given by (2.3). The phenomenological parameters are the rotational viscosity γ_1 and the flow-alignment parameter ν_1, distinguishing between rod-like ($\nu_1 > 0$) and disk-like ($\nu_1 < 0$) particles which align ($|\nu_1| > 1$) or rotate ($|\nu_1| < 1$) in shear-flow. Here, we consider rod-like, flow-aligning active particles ($\nu_1 > 1$), which are thought to reflect active biofilament suspensions. This choice is not consistent throughout the literature, perhaps because no experimental measurements are yet available regarding the collective response of such suspensions to shear flow. There is evidence for perfect flow-alignment of microtubules with shear flow in dilute motility assays [Kim et al., 2006]. Single, stiff or semi-flexible actin filaments, however, were found to tumble and even coil in shear-flow [Harasim et al., 2013; Lindner and Shelley, 2015].

For a constant density the continuity equation, $\partial_t \rho + \boldsymbol{\nabla} \cdot (\rho \boldsymbol{u}) = 0$ turns into the incompressibility condition for the fluid velocity

$$\boldsymbol{\nabla} \cdot \boldsymbol{u} = 0. \tag{2.9}$$

The time evolution of the velocity is in general given by the Navier-Stokes equation [Batchelor, 1967]

$$\rho(\partial_t \boldsymbol{u} + (\boldsymbol{u} \cdot \boldsymbol{\nabla})\boldsymbol{u}) = \boldsymbol{\nabla} \cdot \boldsymbol{\sigma}, \tag{2.10}$$

where $(\boldsymbol{\nabla} \cdot \boldsymbol{\sigma})_i = \partial_j \sigma_{ij}$.

The relative importance of inertial to viscous effects is captured by the Reynolds number $Re = \rho U L/\mu$ [Batchelor, 1967], which is small on the microscopic length scales relevant for experimental active liquid crystals. The kinematic viscosity of water at room temperature is $\mu/\rho \sim 10^{-6}$ m^2/s [Batchelor, 1967]. For instance, the bacterium *Bacillus subtilis* has a rod-shaped body of length $L \sim 5$ μm and swims at a speed $U \sim 15 - 20$ μm/s [Sokolov et al., 2007], resulting in $Re \sim 10^{-5}$. In microtubule-based active suspensions bundles of ~ 1.5 μm in length slide past each other at a speed ~ 3 μm/s in the dilute regime [Sanchez et al., 2013], leading to $Re \sim 10^{-6}$. Thus, in such systems all inertial terms in the fluid dynamics are negligible compared to the viscous terms. This approximation results in Stokes-type, linear equations, replacing equation (2.10) with a force balance

$$\boldsymbol{\nabla} \cdot \boldsymbol{\sigma} = \boldsymbol{0}\,. \tag{2.11}$$

The total stress tensor $\boldsymbol{\sigma}(\boldsymbol{x}, t)$ is composed of the pressure $p(\boldsymbol{x}, t)$, the viscous stress with dynamic viscosity μ, the elastic distortion stress $\boldsymbol{\sigma}^e(\boldsymbol{x}, t)$, and the active stress $\boldsymbol{\sigma}^a(\boldsymbol{x}, t)$,

$$\sigma_{ij} = -p\delta_{ij} + 2\mu v_{ij} + \sigma^e_{ij} + \sigma^a_{ij}. \tag{2.12}$$

The stress due to distortions in the director [Marchetti et al., 2013],

$$\sigma^e_{ij} = \frac{\nu_1}{2}\left(n_i h_j + h_i n_j - \frac{2}{3} h_k n_k \delta_{ij}\right), \tag{2.13}$$

arises from standard nematic elasticity, because the rods generate a shear-flow when they rotate [de Gennes and Prost, 1995]. In active systems this so-called "back-flow" is usually a small contribution compared to active effects [Yeomans, 2016].

The contribution from activity enters in the form of the active stress tensor

$$\sigma^a_{ij} = -\sigma_0\left(n_i n_j - \frac{1}{3}\delta_{ij}\right). \tag{2.14}$$

This term arises because it cannot be ruled out by symmetries[1] or conservation laws of the system [Simha and Ramaswamy, 2002a; Ramaswamy et al., 2003]. In equilibrium it does not occur, because forces entering the equations of motion have to be derived from a free energy functional. For a nematic such forces depend on derivatives of $\boldsymbol{n}$, not $\boldsymbol{n}$ itself, see equation (2.2). Further, in this derivation [Simha and Ramaswamy, 2002a] no relations are imposed among the phenomenological parameters, other than those arising from geometrical symmetries. An active system lacks the time-reversal symmetry on the microscopic level, which is present in linear non-equilibrium theories, where it yields Onsager reciprocal relations for the phenomenological parameters [De Groot and Mazur, 1984]. Here, in particular, the activity parameter σ_0 is not related to any other process. It characterises whether the active liquid crystal produces extensile ($\sigma_0 > 0$) or contractile ($\sigma_0 < 0$) stresses.

Derivation of the active stress from a suspension of force dipoles

The active stress (2.14) can be derived by coarse-graining the hydrodynamic effect of a collection of active particles suspended in a fluid [Simha and Ramaswamy, 2002a]. A self-propelled particle does not exert any net force or torque on the surrounding fluid as a consequence of Newton's Third Law, since the combined system of particle and fluid is force-free. It follows that the leading contribution to the fluid flow that an active particle generates[2] in the far field is a stresslet, the flow field associated with a force dipole [Yeomans, 2016]. This flow field, as illustrated in Figure 2.1 (b), has nematic symmetry and exists in two variants: the particle is a pusher and produces an extensile flow if it expels fluid along its body axis and pulls fluid in on the sides, and a puller, producing contractile flow, conversely. For instance, the MT-based

[1] In this setup the equations have to be invariant under rotations in space and under reversion of the director, $\boldsymbol{n} \to -\boldsymbol{n}$.

[2] For a swimmer, this is the time-averaged flow generated during one swimming stroke.

active nematic [Sanchez et al., 2013] generates local extensile stresses when the MTs slide past each other, as can be verified from Figure 1.1. Actin and myosin mixtures are usually contractile. Certain microorganisms also fit well into this classification, for instance the bacterium *Escherichia coli* is a pusher [Drescher et al., 2011]. For others it is insufficient, the single-cell alga *Chlamydomonas reinhardtii* behaves like a puller only on very large scales and *Volvox carteri* produces a unidirectional flow [Drescher et al., 2010].

Consider a small volume element of fluid that contains N active force-dipoles at the centre-of-mass positions $\boldsymbol{x}_i(t), i = 1, \ldots, N$. Each rod points along the direction given by the unit vector $\hat{\boldsymbol{n}}_i(t)$ and has the total length $a + a'$, allowing for a polar activity. The two forces $\boldsymbol{f}_i = f\hat{\boldsymbol{n}}_i$ and $\boldsymbol{f}'_i = -f\hat{\boldsymbol{n}}_i$ act on its ends, as shown in Figure 2.1 (b). The force density $\boldsymbol{f}^a$ generated by the presence of active particles in this volume element can be written as

$$\begin{aligned} f^a_k(\boldsymbol{x}, t) &= \sum_{i=1}^{N} \left\{ f_{i,k}\delta(\boldsymbol{x} - (\boldsymbol{x}_i + a\hat{\boldsymbol{n}}_i)) + f'_{i,k}\delta(\boldsymbol{x} - \left(\boldsymbol{x}_i - a'\hat{\boldsymbol{n}}_i\right)) \right\} \\ &= f \sum_{i=1}^{N} \hat{n}_{i,k} \left\{ \delta(\boldsymbol{x} - \boldsymbol{x}_i - a\hat{\boldsymbol{n}}_i) - \delta(\boldsymbol{x} - \boldsymbol{x}_i + a'\hat{\boldsymbol{n}}_i) \right\} \\ &\approx -f(a + a') \sum_{i=1}^{N} \hat{n}_{i,k}\hat{n}_{i,j}\partial_j \delta(\boldsymbol{x} - \boldsymbol{x}_i)\,, \end{aligned} \tag{2.15}$$

where the last line was obtained by expanding the expression for $a, a' \ll 1$. Because the directions $\hat{\boldsymbol{n}}_i$ are constant the spatial derivative extends over the whole expression. Taking the continuum limit, we have $\sum_i \hat{\boldsymbol{n}}_i(t)\hat{\boldsymbol{n}}_i(t)\delta(\boldsymbol{x} - \boldsymbol{x}_i) = c_0\boldsymbol{n}(\boldsymbol{x}, t)\boldsymbol{n}(\boldsymbol{x}, t)$, so that

$$f^a_k(\boldsymbol{x}, t) = -f(a + a')c_0\partial_j n_k n_j. \tag{2.16}$$

Identifying this expression with the divergence of a stress leads to the active stress (2.14). This calculation shows that the activity parameter σ_0 is proportional to the concentration c_0, the strength of the force-dipoles f, and the separation of the two forces in each of them. Notably, this first order contribution to the active stress does not distinguish between polar ($a \neq a'$) and apolar ($a = a'$) particles.

Alternative derivations and generalisations

Alternative derivations of active hydrodynamics can be grouped into two approaches [Marchetti et al., 2013]. One can start with a microscopic model, for instance with the stochastic dynamics of molecular motors on a network of filaments [Liverpool and Marchetti, 2006] or the microscopic description of swimmers and their hydrodynamic

interactions [Baskaran and Marchetti, 2009], and coarse-grain it in the style of the kinetic theory of rarefied gases [Pottier, 2010]. This approach relies on seemingly constrictive assumptions of low density and weak interactions, but it provides a valuable link between the parameters of a continuum description and the microscopic mechanisms. Further, it is also possible to use the framework of linear non-equilibrium thermodynamics [De Groot and Mazur, 1984], where the system is assumed to be driven away from a well-defined state of thermal equilibrium by a small force. This approach was used to describe the actin-myosin cell cytoskeleton as an active gel [Kruse et al., 2004] and will be summarised below, in Section 2.3. In essence, all approaches lead to similar systems of equations, in particular featuring the stress given in (2.14) as the main effect of activity, and thus to similar properties of active liquid crystals. Generalisations of the minimal system of equations (2.8)-(2.14) presented above may include a polar orientation field [Kruse et al., 2004], resolving the multiple components of the suspension and viscoelasticity [Joanny et al., 2007; Callan-Jones and Jülicher, 2011].

2.2.3. Properties of active liquid crystals

One of the fundamental properties of active liquid crystals is the instability of a uniformly oriented, nonflowing phase towards spontaneous splay or bend distortions of the director and fluid flow, which was first shown by Simha and Ramaswamy [Simha and Ramaswamy, 2002a,b]. In the bulk, active nematic suspensions and polar suspensions at low Reynolds numbers are unstable at long-wavelengths for any nonzero value of activity [Simha and Ramaswamy, 2002a]. In a confined geometry this instability can be suppressed for a nematic, since there is a threshold that relates the smallest dimension with the activity and elasticity of the material. For an active suspension in a slab-geometry it can be found that, if the thickness of the slab is smaller than a threshold

$$l_a \sim \sqrt{\frac{K}{|\sigma_0|}}, \tag{2.17}$$

the uniformly oriented, nonflowing nematic state is linearly stable [Voituriez et al., 2005; Ramaswamy and Rao, 2007]. The instability, leading to a tilt in the orientation in the contractile case [Voituriez et al., 2005], and the onset of spontaneous flows are recovered for films thicker than the threshold. Equivalently, this can be recast into a minimal activity, $|\sigma_0| \sim K/l_a^2$, which is required to destabilise the ordered nematic state in a given geometry. In the confined geometry this instability is reminiscent of the Frederiks transition in passive nematics between two plates, where in a sufficiently strong electric or magnetic field a uniform director spontaneously changes to a tilted configuration [de Gennes and Prost, 1995]. The active counterpart has two crucial differences, which

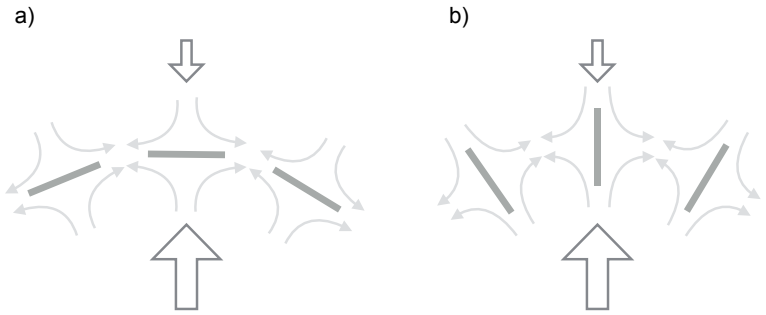

Figure 2.2: Illustration of the two fundamental instabilities in active liquid crystals: a) bend in the director is enhanced in extensile ALCs, b) splay in the director is enhanced in contractile ALCs. The size of outlined arrows represents the strength of the active fluid flow, which in both cases is such that it increases the distortion. Reproduced after Reference [Ramaswamy and Rao, 2007].

are that it occurs in the absence of external fields and that the tilt in the director is accompanied by steady flows. Figure 2.2 gives a pictorial explanation of the nature of these instabilities. Microscopically, the fundamental instability can be derived from the long-range hydrodynamic flows that the active particles exert on each other, which decay as $\sim 1/r^2$ with particle separation [Baskaran and Marchetti, 2009]. Suppression of the instability is therefore possible by mechanisms that screen this particular hydrodynamic interaction, for example elasticity of the surrounding medium, damping by substrate friction, or if the individual swimmer's symmetry is such that the dipolar $\sim 1/r^2$ term vanishes [Baskaran and Marchetti, 2009; Pooley et al., 2007]. Further, orientational order can also be stabilised by translational order [Ramaswamy and Rao, 2007] and, in the contractile case, by sufficiently strong shear flow [Muhuri et al., 2007].

In two dimensions, a whole range of phases and patterns are predicted in different variants of active hydrodynamic models [Marchetti et al., 2013; Prost et al., 2015], including striped flowing phases, travelling waves and swirls, bursts of active flows and consequent relaxation oscillations, and flow vortex and polar defect lattices [Voituriez et al., 2006; Marenduzzo et al., 2007; Giomi et al., 2008, 2011; Giomi and Marchetti, 2012; Tjhung et al., 2011]. The high activity regime in such systems, also called active turbulence, is characterised by chaotic flows and director distortions and has been studied extensively for the nematic case [Thampi et al., 2014b,a, 2013], where half-integer defects[3] are spontaneously generated, advected and annihilated. Due to the various quantitative observations of this regime in experiments [Dunkel et al., 2013; Sanchez et al., 2013] it is an area of ongoing research. For instance, recently the distribution of vortex sizes in the turbulence-like flow patterns has been linked to the intrinsic active length scale l_a

[3]See Figure 2.3 for an illustration of the different defect types, which will be explained in Section 2.4.1.

[Giomi, 2015].

Active liquid crystals have unusual rheological properties, generally associated with shear-thinning or -thickening. Isotropic suspensions of extensile nematic particles lower the effective viscosity, but contractile suspensions are shear-thickening [Hatwalne et al., 2004]. This was also generalised to polar filament-and-motor solutions with contractile activity [Liverpool and Marchetti, 2006]. At the isotropic-to-nematic transition the viscosity is predicted to diverge for contractile active nematics [Hatwalne et al., 2004; Liverpool and Marchetti, 2006; Cates et al., 2008]. Shear-thinning was confirmed experimentally for bacteria suspensions of *Bacillus subtilis* [Sokolov and Aranson, 2009] and of *Escherichia coli* [López et al., 2015], the latter even revealing a superfluid-like regime at high activity and volume fraction in which the effective viscosity vanishes, as predicted in the literature [Cates et al., 2008].

In polar active suspensions the fluctuations of the number N of active particles in a given volume are anomalously large compared to equilibrium fluctuations, $\sqrt{(\delta N)^2} \sim N^{\frac{1}{2}+\frac{1}{d}}$ with d the dimension [Simha and Ramaswamy, 2002a]. These large number fluctuations have been predicted first for dry systems, like active nematics on a substrate [Ramaswamy et al., 2003], and were confirmed experimentally with vibrated rods [Narayan et al., 2007].

2.3. Cellular cytoskeleton as an active gel

2.3.1. Active components of the cell

The cytoskeleton of eukaryotic cells [Lodish et al., 2007; Alberts et al., 2014] is a scaffold of biopolymers that provides a cell with structure and is the principal cellular component to carry out mechanical tasks like moving, changing shape, dividing, responding to and generating forces, and producing cytoplasmic flows [Serbus, 2005]. It is built of three types of protein filaments – actin filaments, microtubules, and intermediate filaments – of which only the former two are relevant for active processes [Prost et al., 2015]. MTs, schematically shown in Figure 1.1, are hollow tubes having a diameter of 25 nm and lengths of up to 20 μm *in vivo*. The tube is assembled from thirteen thread-like protofilaments, each being a string of polar tubulin subunits bound in head-to-tail fashion. Due to this assembly the MT as a whole acquires polarity, having a plus and a minus end. The plus end is favoured for polymerisation of further subunits, a process which requires binding of guanosin triphosphate. Because of their tubular structure MTs are the most rigid filament type and provide long-range organisation and structure in a cell. Combined into bundles, they are an integral part of the mitotic spindle, which is responsible for the separation of the chromosome pairs during cell

division.

Actin filaments are thinner and more flexible than MTs, with a diameter of 8 nm and lengths between 36 nm and several μm, depending on the structure. Polar G-actin monomers are activated by binding one ATP and assemble into a helical strand consisting of two linear chains. Twenty-eight monomers form one F-actin unit, which has one pointed and one barbed end due to the polarity-preserving assembly mechanism. The pointed end is strongly favoured for polymerisation. Actin is found in many different structures in the cell. The cell cortex is an isotropic mesh of short actin filaments underneath the cell membrane. The thin lamellipodium at the leading edge of crawling cells is a highly polarised and branched actin network. Bundled actin is found in stress fibres, which are important for cell shape, in thin membrane protrusions called filopodia, and in the contractile ring which separates the two daughter cells during cell division.

Although somewhat different structurally, both actin filaments and microtubules are polar and their ends are sites of active polymerisation and depolymerisation processes, resulting in treadmilling if the rates are equal, which can generate forces in the cell [Dogterom and Yurke, 1997]. Actin treadmilling is a crucial part of cell crawling, providing the force to push the cell membrane at the leading edge [Murrell et al., 2015].

The second source of activity in the cytoskeleton are the molecular motors, which are able to perform conformational changes when they consume chemical fuel and to "walk" along the appropriate type of filament. Cytoskeletal molecular motors also exist in three varieties: myosin, which walks and pulls on actin filaments, and kinesin and dynein, which use microtubules as tracks. Myosin motors consist of a neck domain and one or two head domains, depending on the type, and processive myosins turn one ATP molecule into a step of 5 - 10 nm along an actin filament. The ATP is hydrolysed into adenosin diphosphate and inorganic phosphate, whereby the motor performs a conformational change that produces a force on the object it is bound to, for example another actin filament. Together with the actin network architecture and the deformability of actin filaments [Lenz, 2014], the pulling force they provide is responsible for the contractile nature of the actin-myosin cytoskeletal structures like lamellipodium, cell cortex, and muscles, and of reconstituted actin-myosin gels [Mizuno et al., 2007; Köhler et al., 2011].

The kinesin family contains two-headed motors which walk on MTs, making a step of 8 nm, to the next tubulin subunit, upon binding of one ATP. Kinesins walk towards the plus end of MTs, whereas dyneins walk towards the minus end. This allows for instance kinesin-1 clusters to attach to and pull on antiparallel MTs, which is the mechanism providing microtubule sliding in the MT-based active nematic [Sanchez et al., 2013] described in Section 2.4.4. The main function of kinesins is intracellular

transport of vesicles on the long MT tracks which span a cell. This process is a prototype of a one-dimensional active system, which have been modelled extensively, for instance using stochastic exclusion processes [Kolomeisky and Fisher, 2007; Khoromskaia et al., 2014].

To study the active mechanical properties of the cytoskeleton *in vitro*, reconstituted actin-myosin [Pinot et al., 2012; Shah and Keren, 2014] or microtubule-kinesin [Nedelec et al., 1997; Sanchez et al., 2013] systems, or cell extracts with few components [Verkhovsky et al., 1999], are often used.

2.3.2. Active gel model

From a material perspective the actin-myosin cytoskeleton allows for a description as a viscoelastic gel of cross-linked actin filaments, which is driven out of equilibrium by the active processes described above. In addition, since the individual filaments are polar, the gel can have macroscopic polar alignment, described by the polarisation field $\boldsymbol{p}(\boldsymbol{x}, t)$. The active polar gel model was derived by Jülicher, Kruse *et al.* [Kruse et al., 2004, 2005]. It is very similar to the hydrodynamic model described in Section 2.2.2, therefore we only highlight the main differences here. In order to explicitly include actin treadmilling and motor activity, the setup is that of a multi-component gel, keeping track of the number densities of actin and myosin bound to the network and in solution, respectively. One assumes that the active state is a small perturbation away from thermal equilibrium, which allows to use linear non-equilibrium thermodynamics [De Groot and Mazur, 1984]. Pairs of fluxes and conjugate forces are identified from the entropy production rate. The active force is characterised by the chemical potential difference $\Delta\mu$ between ATP and its hydrolysis products, and the ATP consumption rate is the conjugate flux.

The main contribution from activity is again a stress of the form $\sigma_{ij}^{ag} = -\zeta\Delta\mu(p_i p_j - \delta_{ij}/3) - \bar{\zeta}\Delta\mu\delta_{ij}$, with new transport coefficients ζ and $\bar{\zeta}$, which are associated with contraction if they are negative and with extension otherwise. The first part is similar to expression (2.14), but gives a concrete connection to the two microscopic origins of activity in the gel. From the second part it follows that a compressible gel can contract or expand also in the absence of local alignment. Several effects follow from polar as opposed to nematic order. Self-advection in the direction of polarisation, $(\boldsymbol{u}+\lambda\boldsymbol{p})\cdot\boldsymbol{\nabla}\boldsymbol{p}$, represents treadmilling of actin filaments with another new parameter λ associated to activity. This term is for instance the origin of concentration bands in multi-component active gels [Giomi et al., 2008]. The free energy density (2.2) is augmented by a spontaneous splay contribution $\sim \boldsymbol{\nabla}\cdot\boldsymbol{p}$. Finally, to account for elastic properties of the cytoskeleton the active gel model can be combined with the Maxwell-model for a viscoelastic material, which behaves like a solid with elastic modulus $E = \mu/\tau$

on time scales smaller than the elastic relaxation time τ, and like a viscous fluid on longer times [Kruse et al., 2004].

2.3.3. Cell motility and other active processes

Variants of the active gel model, either in a simplified form or with additional phenomenological terms included from biology, have provided new insights into cell motility and other cellular processes [Jülicher et al., 2007; Prost et al., 2015].

Cell motility on a substrate

The two main processes leading to cell motility on substrates are actin treadmilling and actin-myosin contraction [Lodish et al., 2007]. A typical cell, crawling on a flat substrate, exhibits a strongly asymmetric shape, such as the crescent-like keratocyte [Mogilner and Keren, 2009]. The front part of the cell, the thin lamellipodium, is filled with a polarised and branched actin-myosin network which is anchored to the substrate and is continuously polymerising at the leading edge and depolymerising closer to the rear. The anchoring points, called focal adhesions, are highly force-sensitive and dynamic protein complexes in the membrane. Focal adhesions transmit the polymerisation forces to the substrate [Gardel et al., 2008], thus providing sliding friction to the motion of the cell [Schwarz and Safran, 2013]. Because of the anchoring, the treadmilling of actin generates a force at the leading edge that pushes the membrane forward. Treadmilling and myosin contractility give rise to retrograde flow of actin with respect to the substrate in the lamellipodium and to anterograde flow of actin at the back of the cell [Vallotton et al., 2005; Yam et al., 2007]. Simultaneously, myosin contracts the cell rear, which is retracted as the rearward focal adhesions dissociate from the substrate.

A stationary cell is not polarised, often assuming a round shape with the cell nucleus in the centre and with actin being polymerised along the edge and moving radially inwards. Motility is initiated by spontaneous or induced breaking of this symmetry, which is thought to be realised by myosin-mediated contraction of the prospective rear of the cell [Yam et al., 2007]. The symmetry breaking can be induced externally by chemical cues [Yam et al., 2007] or by mechanical force [Verkhovsky et al., 1999].

Active gel models have been able to reproduce certain aspects of the crawling motility of cells on substrates and have highlighted the role of myosin-induced contractile stresses and flows. For instance, a simple model for the lamellipodium is a thin film of polarised contractile fluid [Kruse et al., 2006; Jülicher et al., 2007]. On long time scales the average effect of focal adhesions can be modelled as a viscous friction force

[Gerbal et al., 2000]

$$\boldsymbol{F}^{v} = \xi \boldsymbol{v} \tag{2.18}$$

opposing the flow $\boldsymbol{v}$ of active fluid at the substrate with an effective friction coefficient ξ that is related to the average number of attached focal adhesions. When only the cross section of the film is considered, a contractile flow profile and a height profile consistent with observations of cells can be derived from the assumption that actin polymerisation is localised at the front [Kruse et al., 2006]. In this model the cell velocity was imposed and wetting phenomena at the cell front were not considered.

Early models of crawling cell motility focused on the spontaneous symmetry breaking [Callan-Jones et al., 2008] and the shape of the two-dimensional cell contour [Keren et al., 2008; Shao et al., 2010; Blanch-Mercader and Casademunt, 2013], with actin polymerisation and adhesion to the substrate being sufficient ingredients. Recently, the framework of active gels has allowed to also study the polarisation field of actin filaments [Ziebert et al., 2012] and the flow field [Tjhung et al., 2012; Marth et al., 2015] in these motile states. Such models suggest the symmetry breaking in the polarisation field as a motility-initiating mechanism [Tjhung et al., 2012]. In simple models of cells as contractile polar droplets the motile state is characterised by a splayed polarisation, a crescent-like shape, and a flow vortex pair in the interior, propelling the drop in the direction of splay [Tjhung et al., 2012; Whitfield et al., 2014; Marth et al., 2015]. Most models imply that a physical machinery underlies cell motility, which can self-organise and maintain motion even in the absence of signalling or external cues. The persistent motility of lamellipodial fragments of keratocytes, which contain not much more than the actin-myosin system [Verkhovsky et al., 1999], would support this view. However, there is no consensus on whether this physical machinery is dominated by treadmilling or by contractility.

In the models described above the cell is treated as a flat object, which misses some three-dimensional aspects of crawling cell motility, such as the structure of cytoplasmic flows during migration [Keren et al., 2009; Lewis et al., 2015], the role of membrane tension [Lieber et al., 2015], and the determination of the cell shape [Keren et al., 2008]. Few investigations so far have considered the full three-dimensional shape of crawling cells [Gabella et al., 2014; Herant and Dembo, 2010; Tjhung et al., 2015]. In one study, motile keratocytes, as well as their lamellar fragments, have shown parallels with droplets on a substrate, for instance pinning of the cell front on substrate ridges. The cell speed correlated with cell roundness, which could be understood by relating the contact angle at the leading edge with the force acting on the polymerising actin [Gabella et al., 2014]. A minimal model of a cell extract as a droplet of active fluid was able to reproduce in simulations various cell shapes observed with real, motile and stationary cells [Tjhung et al., 2015]. The shapes were a result of the interplay between active

contractile stresses from a polarised actin gel, strength of polarisation anchoring at the interface, and actin treadmilling. The typical lamellipodium shape emerged from the simulation for intermediate values of all three parameters and was accompanied by a splayed polarisation and fluid flow directed towards the leading edge and following the splay in the orientation. Measurements of cytosol flow in moving keratocytes also show this directionality [Keren et al., 2009]. Tjhung et al. [2015] also included variable friction of the type (2.18) to represent the adhesion strength of a cell to the substrate. The velocity of the model cell decreased substantially with slip, up to a reversion of the direction of motion, but a theoretical argument for this was not given. In another computational study realistic three-dimensional shapes of motile cells were generated using a hydrodynamic model [Herant and Dembo, 2010], although without including the polarisation field of active filaments.

Cell motility in three dimensions

In vivo cells usually migrate through three-dimensional tissue, which requires different mechanisms than crawling in the plane [Even-Ram and Yamada, 2005; Mogilner and Keren, 2009]. For example, one possible mode of migration is based predominantly on actin-myosin-contractility and cytoplasmic streaming in roughly spherical cells [Poincloux et al., 2011], with a reduced role for attachment and no actin treadmilling. A related mechanism involves strong shape deformations, where the cell forms spherical membrane protrusions called blebs [Charras and Paluch, 2008].

The former type of migration was reproduced in a model of a spherical actin cortex [Hawkins et al., 2011], where the myosin-mediated contractility drives spontaneous symmetry breaking in the thickness of the cortex and causes meridial cortical flows consistent with experimental measurements of displacements of Matrigel[4] around moving cells [Poincloux et al., 2011]. Measurements of flow fields of cytosol inside such cells are not yet available. This swimming-like migration was also obtained for three-dimensional active polar droplets immersed in passive fluid [Tjhung et al., 2012; Whitfield et al., 2014]. There, contractile active stresses spontaneously break symmetry and produce a splayed polarisation and flow in the form of a toroidal vortex ring, in the absence of treadmilling and friction at the droplet boundary.

Other cellular processes

Because the actin cortex of cells plays a major role in shape deformations, active gel theory was employed to describe processes like shape oscillations [Salbreux et al., 2007] and asymmetric steady state shapes [Berthoumieux et al., 2014; Callan-Jones et al., 2016] of

[4] A type of artificial extra-cellular matrix.

nonadherent cells, as well as strong deformations during the division of a cell, where the final stage is the constriction of a contractile actin ring [Salbreux et al., 2009; Turlier et al., 2014]. The mitotic spindle, also part of the cell division machinery, was shown to behave like a self-organising active nematic droplet with microtubule turnover [Brugués and Needleman, 2014]. Finally, cytosolic streaming can also occur in stationary cells, for instance, as a circulatory flow resulting from a spiral-like arrangement of the actin cytoskeleton that rotates the nucleus [Kumar et al., 2014].

2.4. Topological defects

2.4.1. Defects in liquid crystals

Apart from the Goldstone modes described in Section 2.2.1 a nematic director can also be distorted by topological defects [Mermin, 1979; de Gennes and Prost, 1995; Chaikin and Lubensky, 2000]. These are topologically stable singular points in the director, where the orientation is not defined. Figure 2.3 shows different types of such defects in a two dimensional nematic. In two dimensions defects are grouped into topological equivalence classes according to the winding number of the director around them. This means that defects in the same class can be transformed into one another by continuous changes of the director, while defects in distinct classes cannot – in the same way as they cannot be removed completely without making discontinuous transformations of the director.

Winding numbers

Consider the two dimensional vector field $\boldsymbol{n}(\boldsymbol{x}) = (\cos(\alpha(\boldsymbol{x})), \sin(\alpha(\boldsymbol{x})))$. Formally, the winding number [Chaikin and Lubensky, 2000], or index $\mathcal{I}$ [Needham, 1998], of the vector field around a point is the total change in the orientation $\alpha(\boldsymbol{x})$ along a loop Γ enclosing the point,

$$\mathcal{I} = \frac{1}{2\pi} \oint_\Gamma \boldsymbol{\nabla}\alpha(\boldsymbol{R}(s)) \cdot \mathrm{d}\boldsymbol{R}(s) = \frac{1}{2\pi} \oint_\Gamma \frac{\mathrm{d}\alpha}{\mathrm{d}s}\,\mathrm{d}s\,. \tag{2.19}$$

Γ is any closed loop parametrised by its arc length s, but it will be convenient to use a small circle centred at the defect. In two dimensions, a nematic director with

$$\alpha(\phi) = m\phi + \alpha_0\,, \tag{2.20}$$

where (r, ϕ) denote polar coordinates, solves the equilibrium condition (2.7) and has a single defect at the origin. Here, m is the winding number or topological strength of the defect, since $\int_0^{2\pi} \frac{\mathrm{d}\alpha}{\mathrm{d}\phi}\mathrm{d}\phi = 2\pi m$. For a nematic material $m \in \frac{1}{2}\mathbb{Z}$, since $\boldsymbol{n} \sim -\boldsymbol{n}$, so the director can change by multiples of π as a circle around the defect is traversed.

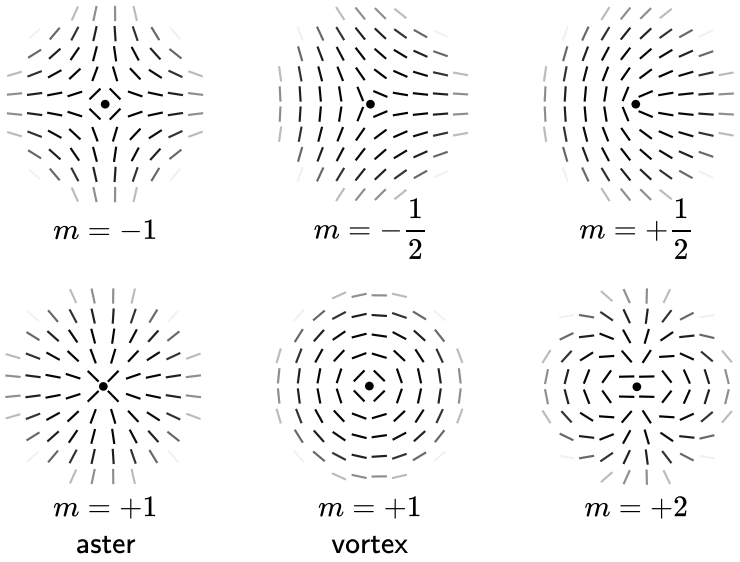

Figure 2.3: Topological defects in a two-dimensional nematic liquid crystal, classified by their topological strength $m \in \frac{1}{2}\mathbb{Z}$, which indicates how much the local director winds around the defect in multiples of 2π. The director field is represented by line segments and the point marks the singularity. For $m = +1$ two possible director geometries are shown: an aster, with pure splay distortions, and a vortex, with pure bend distortions. They can be obtained by adding a different phase α_0 to the local angle of orientation (2.20): $\alpha_0 = 0$ and $\alpha_0 = \pi/2$, respectively.

For a material with polar symmetry the orientation can change by multiples of 2π, so $m \in \mathbb{Z}$. In this way, characterising the defects that occur in a material allows to draw conclusions about its symmetry properties.

In the one-elastic-constant approximation a constant phase α_0 can be added to the local orientation, since bend and splay distortions are energetically equivalent. The phase alters the local geometry of the director around the defect, as illustrated in Figure 2.3 for $m = +1$. The local director has pure splay distortions for $\alpha_0 = 0$ and pure bend distortions for $\alpha_0 = \pi/2$. In the former case the defect is usually called an aster and in the latter case a vortex. Any intermediate choice of α_0 leads to a spiral-like director. This differentiation of defects according to their phase is important in active nematics due to the contrasting roles of splay and bend, as discussed in Section 2.2.2. Working with one elastic constant allows to study the entire family of directors parametrised by this phase and identify the differences that arise from activity.

If a curve encloses a region with more than one defect then their winding numbers are added to give the total winding number. This can be seen by deforming the curve into circular parts, each of them enclosing only one defect and contributing this defect's winding number, and linear parts, which connect the circles and do not contribute to the integral. Therefore, a texture with a pair of defects with opposite strengths, m and $-m$, is topologically equivalent to a texture with no defects at all. This is the

reason why defect pairs can be created from a smooth director field, if enough energy is supplied by a thermal fluctuation or – as we shall see in the next Section – by continuous energy input due to activity. Conversely, two defects of opposite strengths can annihilate and leave behind a smooth texture.

In three dimensional nematics there are point defects in the bulk called hedgehogs and point defects at boundaries called boojums[5] [Volovik and Lavrentovich, 1983], both existing in different topological strengths. Characteristic for bulk nematics are line defects, or disclinations[6], which only exist with half-integer winding, since integer strength defect lines can be removed by an escape of the director into the third dimension and are therefore topologically unstable [Alexander et al., 2012]. These half-integer defect lines can close upon themselves in three dimensions, creating complex topological structures, like knots and links. The classification of such structures is an active area of research [Machon and Alexander, 2013, 2014]. In thin nematic films the thickness determines which type of defect lines are energetically favoured. For instance, there is a critical thickness beyond which a defect line connecting two half-integer defects at the film boundaries becomes unstable in favour of two +1 boojums [Vitelli and Nelson, 2006].

Defects in passive liquid crystals can occur naturally during quenched isotropic-to-nematic transitions or can be induced by applied fields. A different path, which is also promising to control defects in active systems [Keber et al., 2014; Duclos et al., 2016], is to frustrate the order by well-chosen geometric constraints with specific anchoring conditions, for instance by complex sample boundaries or included colloidal particles [Senyuk et al., 2013]. In passive nematics this is a well-established way to control the appearance and locations of defects. The resulting defect structures, like loops, knots and links [Tasinkevych et al., 2014], can in turn be used to manipulate nanoparticles, guide self-assembly of molecular structures [Wang et al., 2015], or serve as a playground to explore the topological richness of nematic liquid crystals [Machon and Alexander, 2013, 2014].

Energy of defects

A nematic director with a defect as in (2.20) is a local free energy minimum, but by construction has a higher energy than the undistorted state. The total energy is composed of the core energy E_c and the elastic distortion energy E_{def}. Real defects have a defect core of size r_c at the location of the mathematical singularity, where

[5] Coined by N. David Mermin as a term for a surface defect, the word "boojum" originally describes a fictitious creature in Lewis Carroll's poem "The Hunting of the Snark" [Mermin, 1981].

[6] These give the nematics its name, which derives from the Greek word "nema" for thread [de Gennes and Prost, 1995].

the nematic melts and becomes isotropic or which is devoid of nematogens altogether, and E_c is associated with the creation of this region from a nematic state. Since $\boldsymbol{\nabla}\alpha = \frac{m}{r}\hat{\boldsymbol{e}}_\phi$, the elastic energy (2.6) for a nematic texture with one defect is

$$E_{def} = K\pi m^2 \int_{r_c}^{R} \frac{1}{r}\mathrm{d}r = K\pi m^2 \ln\left(\frac{R}{r_c}\right). \tag{2.21}$$

The integral is cut off at the defect core radius r_c, below which the continuum elastic theory breaks down, and at a length scale R, that represents the sample size. From equation (2.21) it is evident that the energetic cost of a single defect grows with its topological strength.

It can be shown that the elastic energy of a nematic director with a collection of defects, for which the expression is given in Chapter 3, with strengths m_j and inter-defect distances r_{jk}, is

$$E = K\pi \ln\left(\frac{R}{r_c}\right)\sum_j m_j^2 + 2K\pi \sum_{j<k} m_j m_k \ln\left(\frac{R}{r_{jk}}\right). \tag{2.22}$$

The first part are the self-energies E_{def} of all defects, as in (2.21), and the second are the pairwise interaction energies. According to (2.22), replacing a defect of strength m by two defects of strengths $\frac{m}{2}$, which are further apart than r_c, reduces the total elastic energy of the system. Thus, in two-dimensional nematics integer strength defects are generally unstable and decay into $\pm 1/2$ defects. The interaction between two defects is repulsive, if m_j and m_k have the same sign, and attractive otherwise. The strength of the interaction grows with decreasing distance r_{jk}.

The i-th defect, with position $\boldsymbol{r}_i = (x_i, y_i)$, experiences an elastic force $\boldsymbol{F}^{(i)}$ due to all other defects,

$$\boldsymbol{F}^{(i)} = -\boldsymbol{\nabla}_i E, \tag{2.23}$$

where $\boldsymbol{\nabla}_i = (\partial/\partial x_i, \partial/\partial y_i)$. The motion of defects in two dimensions or defect lines in three dimensions can be described by overdamped dynamics [Ryskin and Kremenetsky, 1991; Denniston, 1996; Giomi et al., 2014]

$$\xi\left(\frac{\mathrm{d}\boldsymbol{r}_i}{\mathrm{d}t} - \boldsymbol{u}(\boldsymbol{r}_i)\right) = \boldsymbol{F}^{(i)}, \tag{2.24}$$

in which the elastic force is counterbalanced by a friction force with an effective friction coefficient ξ and proportional to the defect velocity with respect to some background flow $\boldsymbol{u}$. This particle-like model will be employed in Chapter 5 to describe the motion of defects in the case when $\boldsymbol{u}$ is the self-generated active flow.

The friction coefficient may depend on various other parameters like the rotational

viscosity γ_1 in equation (2.8), the winding number of the defect, and the defect velocity [Giomi et al., 2014]. The dependence on the first two can be estimated from the energy dissipation rate $\mathcal{E}$ [Imura and Okano, 1973; Ryskin and Kremenetsky, 1991]. Consider one defect moving with constant velocity $\boldsymbol{v} = v\hat{\boldsymbol{e}}_x$ with no background flow. Then we have [de Gennes and Prost, 1995]

$$\mathcal{E} = \int \boldsymbol{h} \cdot \left(v \frac{\partial \boldsymbol{n}}{\partial x} \right) \mathrm{d}x \, \mathrm{d}y = \gamma_1 v^2 \int \left(\frac{\partial \alpha}{\partial x} \right)^2 \mathrm{d}x \, \mathrm{d}y \,, \tag{2.25}$$

where we have used the simplified form of equation (2.8) that holds in this case, $v\partial \boldsymbol{n}/\partial x = \boldsymbol{h}/\gamma_1$, to replace the molecular field. Assuming a director of the form (2.20) and a bounded domain of size R one finds

$$\mathcal{E} = \pi \gamma_1 m^2 \ln \left(\frac{R}{r_c} \right) v^2. \tag{2.26}$$

On the other hand, $\mathcal{E} = F^v v = \xi v^2$ with the viscous drag force F^v, so $\xi \propto \gamma_1 m^2$ follows from (2.26). By considering small variations of the director away from its equilibrium form (2.8) it is possible to remove from equation (2.26) the divergence with system size [Denniston, 1996].

The attraction between defects of opposite strength results in annihilation of such pairs. Consider two defects on the x-axis with $m_{1/2} = \pm m$ and $x_1 < x_2$. In the absence of flow, $\boldsymbol{u} = 0$, it can be shown that their separation $r_{12} = x_2 - x_1$ evolves according to

$$\frac{\mathrm{d}r_{12}}{\mathrm{d}t} = -\frac{4K\pi m^2}{\xi} \frac{1}{r_{12}}. \tag{2.27}$$

Therefore, shortly before two defects annihilate their distance scales as

$$r_{12}(t) \sim \sqrt{t_a - t}, \tag{2.28}$$

where t_a is the time of annihilation [Denniston, 1996; Tóth et al., 2002; Dierking et al., 2012; Giomi et al., 2013]. Recent work has also highlighted the importance of the relative orientation of defects and of the resulting hydrodynamic torques on the relaxational dynamics, for instance $+1/2$ defects tend to align anti-parallel as they repel [Keber et al., 2014; Vromans and Giomi, 2016]. An unconstrained nematic in equilibrium is defect-free, as all defects will have annihilated. On the other hand, if a nonzero total topological charge is enforced by boundary conditions, the excess defects will have strengths of the same sign and therefore will settle in configurations that maximise their spacing.

2.4.2. Defects on curved surfaces

On closed curved surfaces the presence and type of defects in a vector field is deeply connected to the topology of the surface and we follow Kamien [2002] to illustrate this connection. First, we introduce some basic differential geometry to describe surfaces and vector fields on them. Let M be a closed surface embedded in $\mathbb{R}^3$ and parametrised by $\boldsymbol{X}(s_1, s_2)$, with local coordinates s_1 and s_2. Two orthonormal basis vectors in the tangent plane are $\hat{\boldsymbol{e}}_i = \partial_{s_i}\boldsymbol{X}/|\partial_{s_i}\boldsymbol{X}|$, $i = 1, 2$, from which the unit normal is constructed as $\hat{\boldsymbol{N}} = \hat{\boldsymbol{e}}_1 \times \hat{\boldsymbol{e}}_2$. The vectorial surface element is $\mathrm{d}\mathbf{S} = \mathrm{d}S\hat{\boldsymbol{N}} = \mathrm{d}s_1\mathrm{d}s_2\hat{\boldsymbol{N}}$. The Gaussian curvature $K = \kappa_1\kappa_2$ is the product of the two principal curvatures κ_1 and κ_2 at each point on the surface, which are the minimal and maximal rate of change of tangent vectors. The Gauss-Bonnet theorem,

$$\oiint_M K\mathrm{d}S = 2\pi\chi\,, \tag{2.29}$$

relates the integrated Gaussian curvature to a topological invariant of the surface – its Euler characteristic $\chi = 2(1-g)$, where g is the number of handles, or the genus. A sphere has $\chi = 2$, a torus $\chi = 0$, a double-torus $\chi = -2$, *etc.*

Consider a tangent vector field on M given by $\boldsymbol{n}(s_1, s_2) = \cos(\alpha)\hat{\boldsymbol{e}}_1 + \sin(\alpha)\hat{\boldsymbol{e}}_2$. To find the winding number of this field inside an area Ω surrounded by the closed curve $\partial\Omega$, instead of $\boldsymbol{\nabla}\alpha$ as in equation (2.19), one has to integrate the covariant derivative $\mathbf{D}\alpha = \boldsymbol{\nabla}\alpha - \hat{\boldsymbol{e}}_1 \cdot \boldsymbol{\nabla}\hat{\boldsymbol{e}}_2$. This takes into account the spatially varying basis through the spin connection $\boldsymbol{A} = \hat{\boldsymbol{e}}_1 \cdot \boldsymbol{\nabla}\hat{\boldsymbol{e}}_2$. Suppose $\boldsymbol{n}$ is smooth with respect to the basis, then $\oint_{\partial\Omega} \mathbf{D}\alpha \cdot \mathrm{d}\boldsymbol{R} = 0$. On the other hand, using Stokes theorem, we have

$$\oint_{\partial\Omega} \mathbf{D}\alpha \cdot \mathrm{d}\boldsymbol{R} = \oint_{\partial\Omega} \boldsymbol{\nabla}\alpha \cdot \mathrm{d}\boldsymbol{R} - \iint_{\Omega} (\boldsymbol{\nabla} \times \boldsymbol{A}) \cdot \mathrm{d}\boldsymbol{S}. \tag{2.30}$$

The Gaussian curvature can be expressed as $K = \hat{\boldsymbol{N}} \cdot \big(\boldsymbol{\nabla} \times \boldsymbol{A}\big)$ [Kamien, 2002] and so, if we choose $\Omega = M$ and use (2.29),

$$\oiint_M (\boldsymbol{\nabla} \times \boldsymbol{\nabla}\alpha) \cdot \mathrm{d}\boldsymbol{S} = \oiint_M K\mathrm{d}S = 2\pi\chi\,. \tag{2.31}$$

As the integral on the left side of equation (2.31), in analogy to equation (2.19), counts the winding numbers m_j of all defects on the surface, multiplied by 2π, we have

$$\sum_j m_j = \chi\,, \tag{2.32}$$

which is known as the Poincaré-Hopf theorem [Hopf, 1989]. In particular, this implies that a vector field on a sphere necessarily has defects and that their topological

strengths will add up to $\chi = 2$. On a torus, on the other hand, defect-free vector fields are possible.

Topology only determines the minimal number of defects that a nematic has to have on a surface. The topography, that is the distribution of the curvature, affects the positions of defects and can also stabilise states with higher number of defects than the minimally required [Serra, 2016; Jesenek et al., 2015; Selinger et al., 2011; Hirst et al., 2013]. On toroidal nematic shells, for instance, defect pairs are created and prevented from annihilating if the torus is fat, that is if its aspect ratio is almost one [Jesenek et al., 2015]. The positive half-integer defects then accumulate on the outside, where the Gaussian curvature is positive, and the negative ones on the inside, where the curvature is negative, forming a metastable multiple-defect state. Generally, defects of positive (negative) topological strength are attracted to regions of positive (negative) Gaussian curvature [Selinger et al., 2011; Kralj et al., 2011; Pairam et al., 2013]. Conversely, defects can be employed to generate local curvature in soft vesicles with in-plane orientational order [Hirst et al., 2013; Nguyen et al., 2013].

2.4.3. Active defects

Defects in biological systems

The role of defects in living organisms is largely unexplored, although they do occur *in vivo* in many different settings. Some early observations about the topology of ridge patterns in fingerprints date back to Roger Penrose, who identified half-integer defects in these patterns and conjectured that the origin of these must be "something of a tensor character, such as a stress or strain" [Penrose, 1979]. While Penrose's intuition has not been confirmed with real fingerprint patterns yet, it is known that *in vitro* monolayers of various types of spindle-like epithelial cells display active nematic behaviour with typical half-integer defects [Kemkemer et al., 2000; Duclos et al., 2014], which can be stabilised by circular confinement [Duclos et al., 2016]. Such cells include melanocytes, which are responsible for pigmentation of the skin in human epithelia. Other active biological systems also display defect formation. Corneal epithelial cells of mice and rats are found to develop a spiral defect [Mort et al., 2009; Mohammad Nejad et al., 2014], probably as a result of the half-spherical space they grow and migrate on. In the interior of cells self-organised defective structures can also be found, for instance the mitotic spindle forms two aster defects at the poles [Brugués and Needleman, 2014] and the cytoskeleton can assume a spiral-defect-like organisation to rotate the nucleus [Kumar et al., 2014]. In *Vibrio cholerae* biofilms – droplets of bacteria attached to a surface – hedgehog-defect-like alignment is found at large cell numbers and densities [Drescher et al., 2016].

Phenomenology of active defects

There is, however, a number of new, non-equilibrium properties that defects acquire in an active material. Most importantly, the local polarity of splay and bend deformations can lead to translational and rotational motion of defects and to the generation of strong active fluid flows. Another characteristic of active defects is their spontaneous generation in the bulk, which was first observed in an active suspension of microtubules and kinesin motors [Nedelec et al., 1997; Surrey et al., 2001]. In very thin circular micro-chambers microtubules first formed asters, which became spiral defects with circulatory flow around the centre as the microtubules grew in length. In a laterally unconfined chamber irregular lattices of spirals or asters formed as steady states, depending on kinesin concentration.

Positive half-defects in active systems are special, because they self-propel due their locally polar director structure. This was first mentioned as an observation in monolayers of vibrated granular rods in the nematic phase [Narayan et al., 2007], anticipated from the prediction of director-curvature induced motion of dry active nematics [Ramaswamy et al., 2003].

The nature of a real active defect core will depend on the system and the defect type. For instance, spiral and vortex defects formed by biofilaments [Nedelec et al., 1997] have an empty core, the size of which is roughly the same for different confinements, but asters have an accumulation of molecular motors and microtubule ends at their centre. The core of a $-1/2$ defect formed by melanocytes can be empty, filled with one triangular cell, or with several cells with mixed orientations [Kemkemer et al., 2000]. In the microtubule-based active nematic [Sanchez et al., 2013] $-1/2$ defects have a bigger void at their core than $+1/2$ defects, see Figure 2.4. The reason might be that the very thin and long MT-bundles can fit well into the geometric structure of the director around the latter, with MT-bundles arranging locally in the shape of a "T". This can be altered by increasing the viscosity of the adjoining oil layer, in which case the void at the positive defect grows in size [Guillamat et al., 2016c].

The strength of an active defect is not governed by energetics only, as opposed to its passive counterpart, but seems to be sensitive to elasticity, activity, and system size [Marchetti et al., 2013]. In the MT-based active nematic only half-integer defects occur, which reveals its nematic symmetry [Sanchez et al., 2013]. But the same material confined to a small enough spherical surface develops a ring-like structure, equivalent to two vortex defects [Keber et al., 2014]. In simulations, an active nematic in a circle also forms as rotating spiral at low activity, which separates into two half-defects only at higher activity [Woodhouse and Goldstein, 2012]. In a different computational approach, where microtubules are modelled as active semi-flexible filaments, they are found to coil into

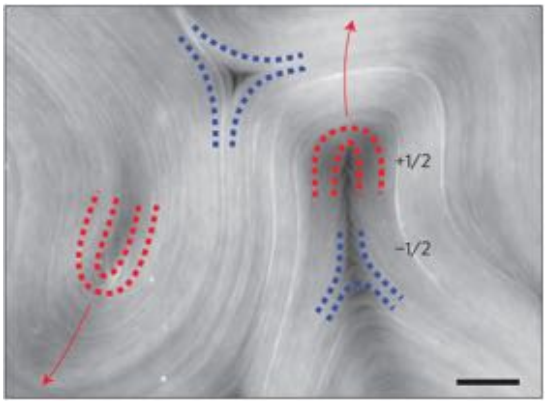

Figure 2.4: Positive (red) and negative (blue) half-integer defects in a quasi-two dimensional active nematic, from Reference [DeCamp et al., 2015]. Characteristic for the regime of high activity is the spontaneous unbinding of $\pm 1/2$ defect pairs, as seen in the right half of the figure, after which the self-propelling $+1/2$ defect moves away (in direction of red arrow).

an irregular array of spirals apart from displaying the usual half-integer dynamics [Prathyusha et al., 2016].

Theoretical description of active defects

Active liquid crystal theory provides a convenient framework to study defects in active systems, since parallels to passive defects can be drawn. Flows produced by single active defects of strength $+1$, $+1/2$ and $-1/2$ have been calculated analytically and several results regarding stability and interactions of defects are available.

The linear stability of $+1$ defects in active gels has been studied by Kruse et al. [2004, 2005]. In a passive LC there is a family of defects characterised by the phase α_0, see equation (2.20) with $m = 1$ for the polarisation angle, all of which are stable in the one-constant approximation. For unequal elastic constants the degeneracy is lifted and only asters are stable for $\delta K = K_3 - K_1 > 0$, whereas only vortices are stable for $\delta K < 0$. An active polar gel without self-advection, described by simplified equations equivalent to those in Section 2.2.2, is considered in a disk of radius R. In this description the polar nature of the material is reflected only in the topological strength of the defect, but not in the hydrodynamics, as explained in Section 2.2.2. For $\delta K = 0$, the active defect is only stable if $|\nu_1| > 1$ and if the phase α_0 satisfies the relation

$$\cos(2\alpha_0) = -\frac{1}{\nu_1}. \tag{2.33}$$

This is the same angle that a nematic liquid crystal would assume in shear flow. The spiral produces a rotating flow of the form $u_\phi(r) \propto r \ln(r/R)$, as a result of incompressibility and no slip at the boundary. For $\delta K \neq 0$ linear stability analysis

shows that for extensile activity the dependence on δK is like in the passive case, but both asters and vortices are turned into spirals by a sufficiently contractile activity [Kruse et al., 2005]. Simulations confirm this phase diagram [Elgeti et al., 2011].

Note, that the above results are obtained for disk-like particles, that is $\nu_1 < 0$ in equation (2.8). For rod-like particles a numerically produced phase diagram shows that contractile activity favours asters and extensile activity mainly favours spirals, with vortices occurring in a very small parameter region [Elgeti et al., 2011]. In the same work interactions between two +1 defects inside a circular patch were simulated. Two contractile active asters relaxed into a steady state separation, rather than leaving the droplet as passive defects would due to elastic repulsion. In the extensile case, two rotating spirals circled around each other, either steadily or with periodically changing sense of rotation [Elgeti et al., 2011].

In compressible active polar films phases with defect arrays were found numerically [Voituriez et al., 2006]. Two types of possible lattices were suggested, a triangular and a cubic, both constructed from elementary cells with one spiral defect and a flow vortex. We note, that although such lattices satisfy continuity in the flow, they require domain walls in the orientation and are therefore not energy-minimising director configurations.

Analytical results for the active flow generated by half-integer defects in active nematics were obtained by Giomi et al. [2014]. For this purpose a half-integer defect in a two-dimensional circular domain of radius R with no-slip boundaries was considered. The flow was calculated by integrating the active force generated by the defect against the Oseen tensor, which is the Green's function of the Stokes equation [Batchelor, 1967]. The $+1/2$ defect produces at its location a directed flow with the magnitude

$$v_0 = \frac{|\sigma_0|R}{4\mu} \tag{2.34}$$

in the direction of its comet-head in an extensile material, and in the opposite direction in a contractile material. To satisfy the no-slip condition, the flow field in the circular region is a vortex pair. On the other hand, the $-1/2$ defect generates at its location a stagnation point with three-fold symmetry. Therefore, positive active half-defects self-propel, whereas negative half-defects are stationary in the absence of external flows or forces. Introducing finite slip at the boundary does not change the main features of these flows [Giomi et al., 2014].

The self-propulsion of active defects can dramatically change the interaction between defects, for instance by competing with and even overcoming elastic attraction of a $\pm 1/2$ pair [Giomi et al., 2013]. In an extensile active nematic, if a $+1/2$ defect points with its comet-head in the direction of the $-1/2$ defect the annihilation happens faster.

The trajectories are increasingly asymmetric due to activity and $r_{12} \propto -\sigma_0 t$. Only at very short distances does the elasticity dominate and the scaling (2.28) is recovered. When the $+1/2$ defect points in the opposite direction its active propulsion slows the annihilation down. If v_0 is larger than a critical value the $+1/2$ defect will always overcome the elastic attraction and escape the pair. This is observed in the MT-based active nematic [Sanchez et al., 2013], where defect pairs are created and immediately separated, so that a constant defect density is maintained.

The interaction of two $+1/2$ defects was investigated in the context of a two-dimensional active nematic droplet, whose behaviour is controlled by an active capillary number [Giomi and DeSimone, 2014]. For contractile activity and normal anchoring at the boundary, the active flows generated by the two $+1/2$ defects act to increase their repulsion, which leads to elongation and even rupture of the droplet. In between these two cases, at intermediate capillary number, the elongated droplet is prone to a splay instability and starts moving [Giomi and DeSimone, 2014].

2.4.4. Experimental realisation of microtubule-based active nematic

Arguably, the most beautiful experimental realisation of an active nematic liquid crystal are the suspensions of cellular filaments and motors developed in the group of Zvonimir Dogic [Sanchez et al., 2013], see Figure 1.1. This seminal paper describes most of the distinctive features of active half-integer defects – spontaneous unbinding of defect pairs, self-propulsion of $+1/2$ defects – in addition to active turbulence and large-scale motion of active nematic droplets driven by the defect dynamics. The active suspension consists of microtubules, bipolar clusters of kinesin-1 motors, which can bind to two microtubules and pull on them, and ATP to drive the motors. An ATP regeneration system was incorporated to maintain its concentration. Polyethylene glycol (PEG) was added to facilitate the formation of MT-bundles through depletion interaction. When bundles are well-mixed regarding the MT polarity they are continuously extending. At higher concentrations, when MT-bundles formed a viscoelastic network in bulk, extension led to a cycle of buckling, breaking and reforming. When adsorbed to a flat water-oil interface, the MT-bundles form a dense two-dimensional active nematic phase. It is characterised by strong streaming flows and continual buckling and fracture of nematic domains. Fracture events produce pairs of $\pm 1/2$ defects, after which the positive defects move actively and the negative are advected in the flow, as shown in Figure 2.4 from a follow-up experimental work [DeCamp et al., 2015]. When the MT-bundle suspension is enclosed in an emulsion drop with diameters of ~ 100 μm, the active nematic adheres to the drop's surface. Such drops, when confined between two glass plates, move autonomously with average velocities up to $\sim 1 \mu\text{m s}^{-1}$. The trajectories are erratic, but show signs of periodicity. This motion was

caused by the active flow of a defective director on the surface, although quantitative data relating defect motion to drop velocity were not presented. Lastly, two active droplets next to each other seemed to interact, moving closer and further apart in a quasi-periodic fashion.

Further investigations of this material have focused on the tunable properties of the three-dimensional active network [Henkin et al., 2014], on the depletion interaction [Hilitski et al., 2015] and the sliding friction [Ward et al., 2015] between individual MTs, and on the effective viscosity of the two-dimensional nematic phase [Guillamat et al., 2016c]. Variations in the viscosity of the oil, which the active nematic shares one interface with, have a strong effect on the dynamics and orientational order. Notably, positive defects move slower and have a larger core with increased oil viscosity, while their number density increases [Guillamat et al., 2016c]. Another new direction which has been explored using this material is nematic ordering of the active $+1/2$ defects themselves, which occurs in very thin films [DeCamp et al., 2015].

Furthermore, the chaotic active flows in the MT-based active nematic can be suppressed in favour of more regular flow patterns by confinement to the surface of vesicles [Keber et al., 2014], which will be described in detail in Section 2.5.3, or by putting it in contact with a passive liquid crystal with controllable patterns [Guillamat et al., 2016a,b].

2.5. Active fluids in confinement: thin films, droplets, and shells

The drive to study geometrically confined active matter is rooted in two different, but related, motivations. Firstly, real living systems are often adapted to small spaces and complex boundaries, as illustrated by the cytoskeleton dynamics in the confinement of a cell, by suspensions of swimming bacteria living in porous media [Rusconi et al., 2014], and by the other examples in Sections 2.3.3 and 2.4.3. In order to understand and, perhaps, reproduce their active behaviours these constraints have to be taken into account. Secondly, there is growing interest in producing more regular and controllable active flows and dynamic patterns, as well as active motile objects, not least because flows and patterns found in living systems are often well-orchestrated in space and time and stable against noise. This can be achieved by confining an active fluid, since it is a way to suppress active turbulence and to stabilise topological defects. For instance, circular confinement creates stable, self-driven circulatory flows. Here, we discuss the main features that active fluids acquire in different types of confined geometries and outline open questions.

2.5.1. Thin films and drops on surfaces

The simplest confined geometry to consider is a thin, flat film of active fluid, where different types of boundary conditions are possible. A Hele-Shaw cell has two rigid, no-slip boundaries, whereas a freely suspended film has two shear-free, deformable boundaries. Intermediate situations can allow for partial slip at a boundary, which creates shear stress at this boundary through viscous friction as given in (2.18). Typically, the polar or nematic orientation field is anchored tangentially at both bounding surfaces. Key to the theoretical description of flows in this geometry is the thin film approximation, or lubrication approximation, in which gradients in the confined direction dominate [Oron et al., 1997].

Very thin films possess a quiescent, uniformly oriented steady state [Voituriez et al., 2005; Ramaswamy and Rao, 2007]. Above the threshold film thickness, as given by (2.17), different steady flow patterns are found in thin active polar films depending on the type of boundary [Voituriez et al., 2005]. In a freely suspended film the spontaneous flow is antisymmetric about the mid-plane of the film, such that the net flux vanishes. For two no-slip surfaces the flow is also antisymmetric, but it vanishes at the boundary. A unidirectional flow is obtained only for one no-slip and one shear-free surface, which corresponds to a thin film of active fluid coating a solid substrate. In this model [Voituriez et al., 2005] the flow component perpendicular to the bounding surfaces was set to zero, but interesting, new effects arise if the free boundary is allowed to deform and if the film extends in two directions [Voituriez et al., 2006; Sankararaman and Ramaswamy, 2009]. In a height-averaged description of a freely suspended active gel of varying thickness, which results in a compressible two-dimensional fluid, stripes of splay with anti-parallel flows and arrays of polar defects with vortices are predicted in simulations. Compressibility is described to be crucial for the occurrence of these instabilities [Voituriez et al., 2006]. In a similar setup, wave-like instabilities result from a coupling of polarisation, surface deformations, and concentration of active filaments [Sankararaman and Ramaswamy, 2009]. Thereby, filaments splay in the plane of the film, which generates fluid flow and film thickness gradients. A strong enough self-propulsion of the filaments weakens the growth of this instability [Sankararaman and Ramaswamy, 2009]. Thin films covered with self-propelled surfactants can be stabilised or destabilised depending on the propulsion velocity of the particles [Pototsky et al., 2014] and various oscillating, dynamic patterns are found for such films numerically [Pototsky et al., 2016].

Although the thin film approximation provides a suitable framework to study fluids coating curved surfaces, like cylinders and spheres [Takagi and Huppert, 2010], we know of no work where active liquid crystals have been considered in these thin geometries. The thin film approximation was, however, employed to describe the actin cortex in

a cylindrical and a spherical geometry, but only in the limit of weak or vanishing orientational order [Salbreux et al., 2007, 2009].

A much less understood situation is an active fluid film that is bounded in the lateral directions. Joanny and Ramaswamy [2012] have considered a drop of active fluid on a surface, focusing on the wetting properties and steady state shapes of symmetric drops with small equilibrium contact angles. The polarisation was assumed to be tangential to both bounding surfaces and to instantaneously follow the deformation of the free surface. In this way, the spreading dynamics and steady states can be in principle obtained from a single equation for the time evolution of the shape. First, the cross section of such a drop is considered, in which case the spreading is driven by the tilt in the orientation due to the confined shape, much like the instabilities considered by Sankararaman and Ramaswamy [2009]. Numerically, a flat, pancake-like steady state shape was obtained for extensile drops. Scaling arguments revealed that the height is controlled by the interplay of activity and surface tension, whereas at the edge the shape is a consequence of nematic elasticity and surface tension and grows as $\sim x^2$ with the distance x from the edge. A similar, but rounder shape was obtained numerically for the contractile case. The active droplet cross sections, with lateral size $R(t)$, deform into these final shapes according to the spreading law $R(t) \sim t^{1/4}$. Furthermore, an axisymmetric three-dimensional drop with an aster or a vortex defect was considered. Such directors minimise the elastic energy in the plane of the substrate, provided that the anchoring along the edge is chosen accordingly. For the drop with an aster defect, the defect was ignored and the final shape was taken to be the pancake shape obtained for the cross section, rotated around the symmetry axis. Due to the additional dimension, the spreading law changed to $R(t) \sim t^{1/6}$. For the vortex state, the defect was included which lead to a divergent radial contribution to the flow, $\sim 1/r$, which was likened to a centrifugal force. We note, that in this case the polarisation is strictly azimuthal and therefore not coupled to axisymmetric changes in the shape, so ignoring the defect would lead to trivial, passive spreading. It is important to allow for three-dimensional incompressibility in order to obtain this contribution to the flow, because in a two-dimensional consideration of an active +1 defect all radial components vanish [Kruse et al., 2004]. The steady state shape resulting from a vortex defect is calculated analytically and is non-monotonic, with a well at the defect location in the extensile case [Joanny and Ramaswamy, 2012]. Finally, the cross section can also represent an elongated drop with two half-defects at either side in the limit of large anisotropy.

In summary, the interplay of shape and orientation field in the confined geometry of an active droplet on a substrate was first analysed by Joanny and Ramaswamy [2012], but several interesting directions have been referred to future work. First,

the presence of the defect in the droplet was only considered properly for the vortex and only for that case was an analytical expression for the shape given. However, a deformation of the drop above the defect should also be expected in the case of an aster. Moreover, spiral defects and the rotating flows they generate [Kruse et al., 2004] have not been considered in this context, but should lead to rotation of the drop. Another natural extension of this work is to ask whether such drops can become motile due to asymmetry in the director. Chapter 4 addresses this question and provides an analysis of various aspects of motility that derives from the presence of defects in the droplet.

There are no experiments with active droplets on a surface available to date. The closest may be the active nematic droplets moving between two plates [Sanchez et al., 2013]. The propulsion of the droplet is due to frictional contact with a surface, although there are two rigid plates in this case, which prohibits any shape changes. The other important difference is that the active material only coats the surface of the droplets, whereas the interior is passive fluid.

2.5.2. Flow vortices and defects in circular confinement

A liquid crystal in circular, or thin cylindrical, confinement with appropriate anchoring is required to have defects with overall topological strength of $+1$ [Alexander et al., 2012]. When ALCs are confined to a circular geometry, in addition to the defects in the orientation, stable flow vortices emerge as a prominent feature.

In dense suspensions of *Bacillus subtilis* bacteria, which in bulk show active turbulent flows [Dunkel et al., 2013], confinement gives rise to a stable vortex state [Wioland et al., 2013, 2016b]. When confined to quasi-two-dimensional droplets, bounded by two glass plates $\sim 15 - 25$ μm apart, the bacteria self-organise into a vortex if the droplet diameter is in the range $20 - 70$ μm. The combined flow due to advection and swimming is purely azimuthal, but has a thin counterrotating boundary layer. Detailed measurements have revealed that the bacteria are oriented in an outward pointing spiral everywhere in the drop, but in the bulk they are advected by the vortex against their swimming direction [Lushi et al., 2014]. The emergence of the vortex and the boundary layer was rationalised in particle-based simulations [Lushi et al., 2014] and in continuum simulations and linear stability analysis of a polar extensile active fluid in a disk [Theillard et al., 2016], both emphasising the role of hydrodynamic interactions and geometry. The self-organisation of the vortex starts at the boundary, where the pusher cells align at an angle and produce a flow against their orientation, which is amplified to become the bulk vortex.

In simulations, a nematic ALC was found to circulate spontaneously in a disk [Woodhouse and Goldstein, 2012]. Different phases were found for increasing activity

above the circulation threshold, which was derived in a linear stability analysis of a homogeneous disordered state. The first phase was a rotating spiral defect, as predicted by Kruse et al. [2004]. At higher activity, the +1 defect separated into two +1/2 defects, which continued to circulate around the disk centre. At even higher activity, the defect pair shifts off-centre and the flow circulation centre itself starts to oscillate.

Recently, the MT-based active nematic was indirectly confined to circular domains by an underlying liquid crystal [Guillamat et al., 2016b]. The liquid crystal formed a lamellar phase with circular domains of different sizes, in which the viscosity in the radial direction is much higher than in the polar due to the structure of the LC. Large enough domains were able to capture the flowing active nematic, which then circulated inside the domain. Usually one pair of rotating +1/2 defects was captured, but they were periodically remodelled due to the active bending instabilities and other defect combinations with a total strength of +1 were also observed. Passive tracer particles were advected by the active flow on outwards spiralling trajectories [Guillamat et al., 2015]. We note, that this is only possible if the active flow inside the circular domain has a radial component, which means that it cannot be purely two-dimensional but has to pump fluid into its vortex centre, for instance from the passive fluid above the active nematic.

Circulatory flows are also found in active polar fluids confined to the cross section of a Taylor-Couette geometry [Fürthauer et al., 2012; Neef and Kruse, 2014]. A spontaneously formed single vortex can move the two coaxial cylinders with respect to each other and, at higher activity, states with multiple counterrotating vortices occur, which can be either stationary or travelling around the inner cylinder [Neef and Kruse, 2014]. Interestingly, in this model no defects in the orientation were created. In a cylinder, where full three-dimensional flows are allowed, an active nematic produces complex vortex structures in the cross section depending on the anchoring conditions, which either lead to half-defect lines or to a director escaped into the axial direction [Ravnik and Yeomans, 2013]. For tangential anchoring along the cylinder axis the spontaneous flow is unidirectional at intermediate activity, but bidirectional at higher activity. In both cases the cross-sectional flow component consists of symmetric arrangements of counterrotating vortices, but is much smaller than the axial component. Homeotropic or circular anchoring stabilises two +1/2 defect lines, which drive purely cross-sectional flow consisting of two counter-rotating vortex pairs. At higher activity the defects escape into the third dimension and the flow is again predominantly axial. In this numerical study, the +1/2 defects drive a flow for any nonzero value of activity [Ravnik and Yeomans, 2013].

In biological systems self-organised circulatory flows are characteristic of cyto-

plasmic streaming in plant cells [Goldstein and Tuval, 2008; Verchot-Lubicz and Goldstein, 2009; Woodhouse and Goldstein, 2012, 2013], with spherical or cylindrical confinement, and of cytosolic streaming in animal cells [Keren et al., 2009; Yi et al., 2011; Ganguly et al., 2012; Kumar et al., 2014]. Flows in motile cells have motivated a number of active polar [Tjhung et al., 2012; Whitfield et al., 2014; Marth et al., 2015; Whitfield and Hawkins, 2016] or nematic [Giomi and DeSimone, 2014] droplet models. The main findings of these models are summarised for the case of contractile activity. Typically, an active droplet is initialised with a uniform or a defective orientation field, depending on the anchoring along the boundary. At low activity the droplet deforms – it is elongated perpendicular to the axis of orientation due to contractile stresses and, in the nematic case [Giomi and DeSimone, 2014], by the repulsion of two half-defects – but remains immotile. Even for this uniformly aligned state the confinement to a droplet generates flow in its interior, which is symmetric and quadrupolar, provided there is finite slip at the boundary [Whitfield et al., 2014]. At a critical activity the director splays spontaneously and the droplet starts moving in the direction of the splay, propelled by a pair of counterrotating vortices. This symmetry breaking is also reflected in a crescent-like shape [Tjhung et al., 2012; Giomi and DeSimone, 2014; Marth et al., 2015]. However, also for a fixed, circular shape and an imposed splay similar flow fields and motility are found analytically [Whitfield et al., 2014]. A three-dimensional motile drop is equivalent to the flat drop rotated around its axis of propulsion [Tjhung et al., 2012]. The three-dimensional, splayed orientation develops a hedgehog defect at high activity. As activity is increased further, the defect approaches the centre, which brings the drop to a halt and restores the spherical shape [Tjhung et al., 2012]. If the droplet is instead initialised with a central hedgehog defect, or with an aster defect in two dimensions, the defect's position is linearly stable for contractile activity, but the defect moves away from the centre for extensile activity which leads to directed motion of the drop [Whitfield and Hawkins, 2016]. In an extensile drop initialised with uniform polarisation, spontaneous bend occurs at critical activity and, if self-advection along the polarisation is added, the droplet moves on spiralling trajectories [Tjhung et al., 2012].

The mechanism responsible for the generation of a bulk vortex in a drop of bacteria [Wioland et al., 2013] was recently harnessed to stabilise bacteria into a steady unidirectional circulation inside a thin "racetrack" channel [Wioland et al., 2016a]. This geometry has also revealed a different type of vortex formation, in which arrays of flow vortices emerge at a critical channel width, before the flow becomes chaotic. The vortex size matches the width of channel and the rotation sense is chosen randomly [Wioland et al., 2016a; Theillard et al., 2016]. Flow vortex lattices were also found in numerical studies of active nematics in a channel, where they were accompanied

by a regular arrangement of $\pm 1/2$ defects [Doostmohammadi et al., 2016b]. Similarly, a passive rotor, or even arrays of such rotors, can be set in rotation by a flowing active nematic [Thampi et al., 2016]. These examples suggest that active turbulent flows may be regularised into vortex lattices if the length scale of the geometric confinement matches the intrinsic active length scale l_a [Giomi, 2015].

We comment on the minimal and maximal domain sizes for which circulatory flows occur in experiments. For the *Bacillus subtilis* suspensions the length scale of ~ 70 μm characterises the domain size at which the flow vortex in a circle becomes unstable [Wioland et al., 2013], as well as the channel width for which laminar flow is replaced by a chain of channel-spanning vortices [Wioland et al., 2016a], and the size of characteristic swirls in bulk active turbulence [Dunkel et al., 2013]. In the MT-based active nematic vortices were found up to the largest measured domain sizes, ~ 200 μm [Guillamat et al., 2016b]. This is larger than the typical length scale of folds in an unconstrained active nematic, ~ 100 μm [Sanchez et al., 2013], possibly because vortices are not self-organised, but forced by the underlying LC structure. Naturally, there is also a minimal domain size for the emergence of a stable vortex, which is ~ 20 μm for *Bacillus subtilis* suspensions [Wioland et al., 2013] and ~ 30 μm for MT-based active nematics at standard conditions [Guillamat et al., 2016b]. In the active nematic this length scale increases with bending rigidity of MTs and decreases with ATP concentration, which means that at stronger activity $+1/2$ defects are able to circulate with a smaller separation. Thus, in this experiment the minimal domain size is thought to be connected to the intrinsic active length scale l_a [Guillamat et al., 2016b; Giomi, 2015].

In active systems with high frictional dissipation stable vortices can also arise in the absence of spatial confinement, for instance in active nematics on a substrate at the transition from the wet to the dry regime [Doostmohammadi et al., 2016a] or, experimentally, in motility assays [Schaller et al., 2010; Sumino et al., 2012]. Cellular monolayers on substrates, which belong to the class of dry active matter, also display stable defects [Duclos et al., 2016] and collective rotation [Segerer et al., 2015; Li and Sun, 2014; Mohammad Nejad et al., 2014] in circular confinement, for instance in self-organised droplets [Rappel et al., 1999].

2.5.3. Shells and spheres

Active liquid crystal shells are realisations of a different type of confined geometry and constitute a new area of research, initiated by the seminal experiments conducted by the groups of Dogic and Bausch [Keber et al., 2014]. As activity now interferes with elasticity, active nematic shells display new, dynamical versions of features known from their passive counterparts. Therefore, we first review the latter and thereafter describe vesicles coated with an active nematic [Keber et al., 2014] and related active

systems.

Passive nematic shells

It is a topological requirement that nematic order on a sphere has to have defects with a total strength of +2, as shown in Section 2.4, but one can imagine many possible arrangements of defects that satisfy this and differ in their elastic energy. An elegant argument for finding the energetic ground state for the more general problem of n-atic[7] order on a sphere was given by Lubensky and Prost [1992]: take the smallest number of minimum strength disclinations and put them as far apart as possible, to minimise their mutual repulsion. For a nematic this translates to four +1/2 defects arranged at the vertices of a tetrahedron. This result laid the ground for a large amount of theoretical and experimental work on nematic shells [Lopez-Leon and Fernandez-Nieves, 2011], nudged also by Nelson's idea to functionalise such objects in order to make micron-scale "atoms" with a "valence" that is controlled by the defect configuration [Nelson, 2002]. Although the tetrahedral ground state was predicted in the one-elastic-constant approximation in a strictly two-dimensional setup [Lubensky and Prost, 1992; Nelson, 2002], it is found in experiments [Fernandez-Nieves et al., 2007; Lopez-Leon et al., 2011] and simulations of nematic layers with finite thickness [Huber and Stark, 2004; Skačej and Zannoni, 2008; Bates et al., 2010; Kralj et al., 2011; Nguyen et al., 2013; Wand and Bates, 2015]. Other defect configurations can, however, be induced by varying the shell thickness, by elastic anisotropy, applied fields, and deviations from the spherical shape.

Vitelli and Nelson [Vitelli and Nelson, 2006] have studied theoretically the crossover from a two-dimensional spherical nematic to a three-dimensional nematic shell using a similar director formalism to [Lubensky and Prost, 1992] with one elastic constant. They derived a threshold for the shell thickness beyond which the tetrahedral configuration becomes unstable and is replaced by two antipodal +1 boojums on the outer surface. This configuration is similar to the ground state of polar order on a sphere, but there are two more +1 boojums on the inner surface of the shell and the director is escaped into the radial direction in between the surfaces, that is it acquires a component perpendicular to the shell. It is also shown that the tetrahedral state, for thin enough shells, should be stable against thermal fluctuations [Nelson, 2002; Vitelli and Nelson, 2006].

Experimentally, nematic shells can be realised by inserting an aqueous droplet into a nematic droplet, which itself is immersed in water [Fernandez-Nieves et al., 2007; Lopez-Leon et al., 2011; Koning et al., 2016]. If these shells are thin and homogeneous in thickness three defect configurations are observed with similar frequency of occurrence: the tetrahedron of four +1/2 defects, two antipodal +1 defects, and one +1 and two

[7] A rotation of the local direction by $2\pi/n$ results in a physically equivalent state. Polar ($n = 2$) and nematic ($n = 1$) order are special cases.

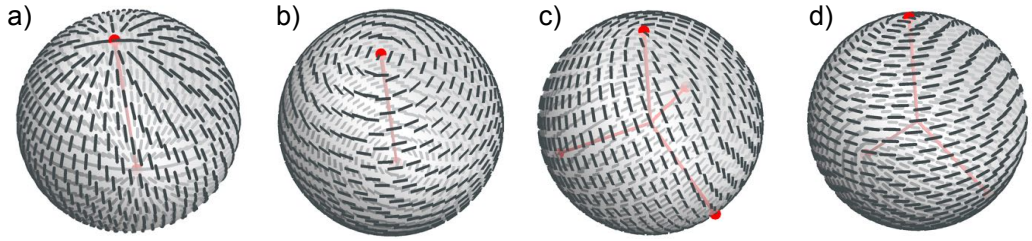

Figure 2.5: Various defect arrangements compatible with nematic order on a sphere: a) two aster defects, b) two vortex defects, c) four $+1/2$ defects in tetrahedral arrangement, d) one $+1$ defect and two $+1/2$ defects arranged in an isosceles triangle. Defects are marked with red dots and position vectors. The tetrahedron is the global free energy minimiser, but the other configurations are found experimentally with a similar frequency in passive nematic shells due to the small energetic differences [Koning et al., 2016].

$+1/2$ defects arranged in an isosceles triangle. The occurrence and long-time stability of all three configurations could stem from the free energy differences being small, but the energy barriers between the states being high [Koning et al., 2016]. In shells with varying thickness defects migrate to thinner regions, which reduces the energy due to their three-dimensional nature.

Splay-dominated textures with either two antipodal asters or two pairs of $+1/2$ defects are found to be energy-minimising in simulations of hard arcs [Zhang et al., 2012] or rods [Bates, 2008; Shin et al., 2008] on a sphere, respectively. Such simulations reflect a nematic with strong elastic anisotropy, where splay is much softer than bend. In the limit of infinite anisotropy, for instance $K_3 \to \infty$, one can even expect a continuous family of degenerate ground states, which are constructed by starting with antipodal $+1$ defects and rotating one hemisphere along a great circle passing through the defects [Shin et al., 2008].

Four half-defects in a nematic shell can arrange in a variety of configurations, if other effects are included, that compete with the repulsion between defects. For instance a bipolar configuration, where defects pair up at opposite sides of the shell, is induced if the shell is deformed into a prolate ellipsoid [Bates et al., 2010; Kralj et al., 2011], if a homogeneous electric field is applied [Skačej and Zannoni, 2008], in the case of strong elastic anisotropy [Bates, 2008; Shin et al., 2008], or if the nematic is chiral [Wand and Bates, 2015]. The relative orientation of the two pairs can range from perpendicular [Bates et al., 2010; Kralj et al., 2011] to parallel [Skačej and Zannoni, 2008; Bates et al., 2010; Shin et al., 2008], where all defects are aligned on one great circle. In Chapter 5 we explore a new, dynamic way in which the tetrahedron of four half-defects can be distorted due to the active self-propulsion of the defects.

Toroidal, or even higher genus, nematic shells have not been experimentally realised to date. However, three dimensional nematics confined to tori and other handle-

bodies with degenerate tangential anchoring have been produced using a yield-stress material as outer fluid [Pairam et al., 2013]. In tori a doubly-twisted texture without defects is adopted [Koning et al., 2014], but with each additional handle two -1 boojums appear in saddle regions of the surface. These and other experiments [Campbell et al., 2014; Tasinkevych et al., 2014] could soon lead the way to testing theoretical predictions of defect unbinding and stabilisation in toroidal shells [Jesenek et al., 2015; Selinger et al., 2011]. The active counterparts of such systems could then display interesting defect dynamics.

Active nematic shells

In the recent experiments conducted by Keber et al. [2014] a MT-based active nematic [Sanchez et al., 2013], described in Section 2.4.4, adheres to the inner surface of a lipid vesicle. In sufficiently large spherical vesicles four half-integer defects are found to be in steady motion accompanied by streaming flows. As shown in Figure 2.6, the defects oscillate between tetrahedral and planar configurations. This behaviour is the result of the competition between elastic relaxation to a tetrahedron, which is one of the expected configurations for a thin nematic shell [Lubensky and Prost, 1992; Koning et al., 2016], and the self-propulsion of active half-defects. It is reproduced by a particle-based model [Keber et al., 2014] described below. For a vesicle radius of ~ 20 μm the frequency of oscillations is given as 12 mHz, but no data is shown for other sizes. When vesicles are smaller than 18 μm in radius, a different configuration is sometimes observed, in which the active nematic forms a ring around the equator of the vesicle, which is equivalent to two $+1$ vortex defects. Although the material is nematic, the rings are rotating. Buckling instabilities of the ring form transient four-defect-states, which occur more often with increasing radius. Still more novel states are found if vesicles are allowed to deform, either due to excess membrane or due to stiffer MTs. In the oscillatory regime, when vesicles are deflated due to applied hypertonic stress, the shape of the vesicle starts to elongate and shrink periodically and it also develops four long, filopodia-like protrusions at the locations of the half-defects. Such deformed vesicles are reported to be motile, but no details of the type of motion are given. Finally, stiffer MTs self-assemble into a dynamic spindle-like structure with two $+1$ aster defects at the poles and deform the vesicle accordingly. The two asters periodically collapse into one and reform again as a result of cycles of MT extension and buckling. In summary, active nematic vesicles display a variety of dynamical defect states and shape deformations as a result of activity [Keber et al., 2014].

In an older experiment, microtubules and motors confined into a vesicle were found to self-organise into protrusions, single asters, and rings, but there all structures were

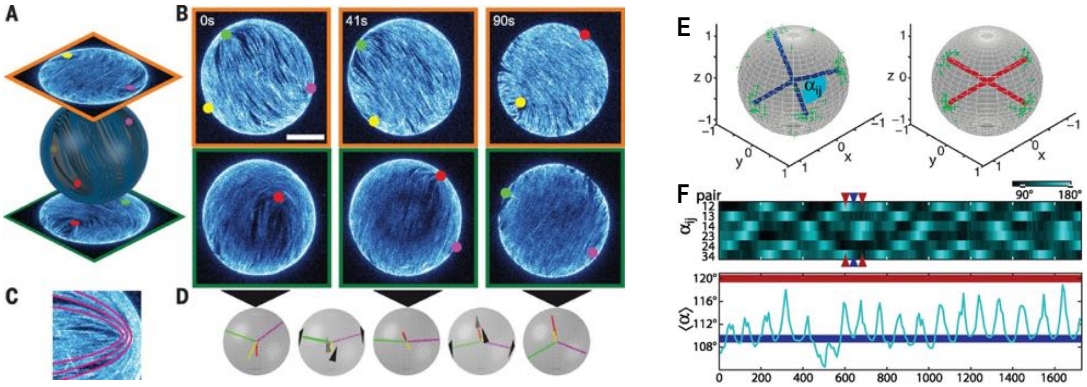

Figure 2.6: A spherical vesicle coated with a MT-based active nematic displays four half-integer defects that oscillate between tetrahedral and planar configurations, which are shown in panel E. Panels A, B, and D show the defect positions at consecutive points in time. Panel C illustrates the director around a $+1/2$ defect. The oscillations are clearly visible in the plot of the angular distances α_{ij} between the defects and the their mean angular distance $\langle\alpha\rangle$ in panel F. Taken from Reference [Keber et al., 2014].

static [Pinot et al., 2009]. Although artificial actin-myosin cortices may also be regarded as active spherical shells, topological considerations and defects have played a minor role so far [Loiseau et al., 2016]. This is possibly because orientational order emerges only locally in actin-myosin shells, for instance in the form of contractile rings [Salbreux et al., 2009]. Finally, recent experiments with a swarm of *Escherichia coli* confined to an emulsion droplet revealed accumulation of bacteria at the spherical surface at high densities and for large enough droplets, but a quantitative analysis of the flow patterns and orientational order of bacteria was not presented yet [Vladescu et al., 2014].

Models of active matter on curved surfaces

The defect oscillations found in the active nematic vesicle were captured by a model of four self-propelled defects [Keber et al., 2014]. Here, we give account of the main parts and results of this model, because it served as a starting point for our approach in Chapter 5. In [Keber et al., 2014], the interaction energy (2.22) and the overdamped dynamics (2.24) were formulated on the surface of a sphere. The four $+1/2$ defects, whose comet-head directions were represented by arrows $\hat{\boldsymbol{d}}_i$, self-propelled with velocities $\boldsymbol{u} = v_0\hat{\boldsymbol{d}}_i$. The imposed speed v_0 was taken from a two-dimensional calculation [Giomi et al., 2014], see equation (2.34) with the vesicle radius R chosen as the relevant length scale. The translational dynamics were complemented by rotational dynamics of the directions $\hat{\boldsymbol{d}}_i$, which were also derived from the interaction energy (2.22). The dynamics were solved numerically, with defects initially placed on the equator with random orientations. It was found that up to $v_0 \approx 0.25$ the defects relaxed into a static, increasingly skewed tetrahedron, in which the orientations formed two co-planar pairs.

Above this value the defects would oscillate between two different tetrahedral configurations, passing through square-like planar configurations in between. The defects are described to group into pairs and revolve at constant angular velocity around the pair centre. The oscillations were found when the rotational dynamics of the $\hat{\boldsymbol{d}}_i$ was much faster compared to the translation of the defect core. In the experiment the defect cores are depleted of MT-bundles, so moving them involves transport of mass, but reorienting the director around the defect does not. Therefore, it was argued that fast rotational dynamics are a good representation of the experimental system. Further, the frequency of oscillations is predicted to scale as $f \sim v_0/R$, which from (2.34) results in linear dependence on activity, but no dependence on vesicle size. While this model [Keber et al., 2014] reproduces the oscillations found in experiments, it does not resolve the fluid flow in the active nematic layer and is restricted to the case of four half-defects. The structure of active flows in this new type of confinement is one of the important insights provided by our model of a thin active shell, described in Chapter 5.

Another paper has considered the swarming of soft SPPs on a sphere in a Vicsek-like model [Sknepnek and Henkes, 2015]. Spherical confinement leads to the formation of a polar vortex state, in which all particles move around the sphere in one surface-spanning flock, or a dense, circulating band at higher self-propulsion velocities. Interestingly, the respective +1 defects in the velocity and the alignment fields are spatially separated in the low activity regime. Although this model elucidated the interplay of activity with a curved surface, it left any questions about hydrodynamic interactions and active flows unanswered.

CHAPTER 3

Flow singularities in thin active films

The thin film approximation is an established framework to study the flow of passive fluids in geometries with one very small length scale [Oron et al., 1997], which has already been successfully adapted to describe flow instabilities and spreading of active fluid films [Voituriez et al., 2005; Sankararaman and Ramaswamy, 2009; Joanny and Ramaswamy, 2012]. We aim to extend this approach to active films in different thin geometries, with a focus on defects and the active flows they produce. In this chapter we introduce the thin film approximation for a three-dimensional film of active liquid crystal placed on a flat, rigid substrate and bounded by a free, deformable interface from the other side. First, the closed form solution for the active flow driven by a given director with only small vertical variations is derived. The in-plane component of the director is parametrised as a minimiser of the Frank free energy with an arbitrary collection of defects. This parametrisation allows to analyse the local flow structure in the vicinity of a defect and it is found that within the thin film approach defects generate active flow singularities at their location, whose winding number relates to the topological strength of the defect. For the self-propelling half-integer defect the active flow inside the defect core is solved for in a two-dimensional model and matched with the thin film flow to obtain a finite propulsion speed.

3.1. Model assumptions

In this thesis we consider minimal models that allow us to capture the effect of activity on defects in thin films, droplets and spherical shells of active liquid crystal and to extract new phenomenology and qualitative predictions, which can then be compared against existing and future numerical work and experiments. The full coupled dynamics of flow, orientation and concentration as described in Section 2.2.2 is uncompliable to theoretical analysis and a number of simplifications has to be made. Therefore, in order to keep calculations tractable and obtain closed form solutions we base our modelling on the following common assumptions:

- We work in the one-elastic-constant approximation and focus on director configurations with defects, which minimise two-dimensional Frank free energy in the plane of the film, and have only small variations in the third dimension. Such directors can be parametrised entirely by the defect locations and topological strengths. Therefore, the director dynamics, given by equation (2.8) in its general form, is to first approximation governed by the motion of defects in the active flow and for given defect locations the director approaches its minimum instantaneously. In other words, we assume that the elastic relaxation time of the director is much smaller than the time scale of active flows, which has been argued to well represent MT-based active nematics at intermediate activity [Keber et al., 2014]. This reflects a situation in which a passive LC is allowed to equilibrate and then activity is "switched on", but restricted to small or intermediate values way below the onset of active turbulence. A natural consequence of using a director with defects is that no activity threshold exists for active flows to occur, since the large distortions present around defects can drive a flow at arbitrarily small values of activity [Ravnik and Yeomans, 2013].

- We are interested in the main effect of activity on the dynamics of the flow, given by the force balance (2.11). Therefore, we ignore the coupling of elastic distortions to velocity gradients, setting $\nu_1 = 0$. This simplification is common to theoretical and numerical investigations of active fluids [Joanny and Ramaswamy, 2012; Neef and Kruse, 2014]. Furthermore, some numerical work reports that no significant differences are found if $\nu_1 \neq 0$ [Neef and Kruse, 2014; Whitfield et al., 2014]. As described above, $\boldsymbol{h} \approx \mathbf{0}$ for the directors we consider, so elastic stresses are negligible compared to active. In the context of flow-aligning active rods, this assumption would reflect a material with very small Leslie angles in shear-flow. However, experimentally measured values for ν_1 in active liquid crystals are not available to date.

- Finally, already in Section 2.2.2 we have assumed a constant concentration of active constituents in the suspension. From simulations it is known that this approximation works well if there is no self-advection of active particles [Giomi et al., 2008; Elgeti et al., 2011], which is the case in the nematic ALCs we consider. Although at the defect core this approximation breaks down, unless the effect of the concentration drop at the defect core significantly exceeds the active flows due to the strong director distortions our approach will still lead to the correct geometrical structure of the flow at defects.

We take these assumptions as a valid starting point to discern the effect of active stresses in the systems we consider – thin films of active liquid crystals with defects in

different geometries – and proceed with their mathematical description within these assumptions. Comparison of our predictions with existing experimental work further supports this approach.

3.2. Thin films of active liquid crystals

3.2.1. Description of thin films with one free boundary

We will focus on active liquid crystals in different thin geometries, which are liable to a theoretical description in the thin film approximation [Oron et al., 1997]. In this description a separation of length scales yields a simplified version of the Stokes equation for the fluid. In the current and the next chapter, we consider a layer of active fluid spread on a flat substrate with a soft fluid-fluid or fluid-air interface at the top, which can deform due to active flows generated in the film [Sankararaman and Ramaswamy, 2009; Joanny and Ramaswamy, 2012]. The lower interface is non-permeable, but allows for finite slip of fluid through viscous friction.

A thin film approximation in a film with two rigid boundaries, i.e. a Hele-Shaw geometry, reduces to a two-dimensional model, which is equivalent to starting in a two-dimensional setting and including strong enough friction with the substrate [Doostmohammadi et al., 2016a]. In contrast, when at least one boundary is free to deform, the model is not strictly two-dimensional, because flows in the third dimension are allowed and necessary to drive deformations of the boundary. Retaining the full, three-dimensional description of the thin film will turn out to be crucial for several features of the systems that we study, for instance for the shape of active droplets on a surface and for the defect dynamics in a thin active shell.

First, we introduce the height representation, or Monge gauge [Chaikin and Lubensky, 2000], for surfaces that are almost flat to describe the upper interface of the film. The local coordinates in the surface are identified with the coordinates in the plane, for instance Cartesian coordinates $s_1 = x$ and $s_2 = y$, and the surface is given by $\boldsymbol{X}(x, y) = (x, y, h(x, y))$. Alternatively, it can be defined as the zeros of the surface function $F(x, y, z) = z - h(x, y) \equiv 0$. From the two tangent vectors

$$\boldsymbol{e}_1 = (1, 0, \partial_x h)^\top \quad \text{and} \quad \boldsymbol{e}_2 = (0, 1, \partial_y h)^\top \tag{3.1}$$

the outward unit normal to the surface is obtained

$$\hat{\boldsymbol{n}}_h = \frac{(-\nabla_\perp h, 1)^\top}{\sqrt{1 + (\nabla_\perp h)^2}} \approx (-\nabla_\perp h, 1)^\top, \tag{3.2}$$

where the approximation holds for small gradients in the height of the film. We adopt

the notation $\boldsymbol{x}_\perp = (x, y)^\top$ and $\nabla_\perp = \hat{\boldsymbol{e}}_x \partial_x + \hat{\boldsymbol{e}}_y \partial_y$ for vectors and gradients in the plane of the substrate.

Let the flow field in the film be denoted by $\boldsymbol{u}(\boldsymbol{x}_\perp, z, t) = (u_x, u_y, u_z) = (\boldsymbol{u}_\perp, u_z)$. The kinematic boundary condition relates the speed of the interface with the normal component of the fluid velocity at the interface

$$\partial_t h = \boldsymbol{u}|_{z=h} \cdot \hat{\boldsymbol{n}}_h = -\boldsymbol{u}_\perp|_{z=h} \cdot \boldsymbol{\nabla}_\perp h + u_z|_{z=h}. \tag{3.3}$$

Three-dimensional incompressibility, $\boldsymbol{\nabla} \cdot \boldsymbol{u} = 0$, allows to express this condition entirely through the height-integrated in-plane flow

$$\bar{\boldsymbol{u}}_\perp(\boldsymbol{x}_\perp) = \int_0^h \boldsymbol{u}_\perp(x, y, z)\, \mathrm{d}z\,. \tag{3.4}$$

Employing Leibniz' rule [Riley et al., 2006] for differentiating integrals yields

$$\boldsymbol{\nabla}_\perp \cdot \int_0^{h(x,y)} \boldsymbol{u}_\perp(\boldsymbol{x})\, \mathrm{d}z = \boldsymbol{u}_\perp(x, y, h) \cdot \boldsymbol{\nabla}_\perp h + \int_0^{h(x,y)} \boldsymbol{\nabla}_\perp \cdot \boldsymbol{u}_\perp\, \mathrm{d}z\,. \tag{3.5}$$

On the other hand, with $u_z(z = 0) = 0$, from incompressibility it follows that

$$u_z|_{z=h} = -\int_0^h \boldsymbol{\nabla}_\perp \cdot \boldsymbol{u}_\perp\, \mathrm{d}z\,, \tag{3.6}$$

so equation (3.3) becomes a local conservation law

$$\partial_t h = -\boldsymbol{\nabla}_\perp \cdot \bar{\boldsymbol{u}}_\perp, \tag{3.7}$$

from which a self-consistent evolution equation for $h(x, y)$ is obtained if the right hand side can be expressed in terms of the height function and its gradients only. In this chapter we consider a film that is unbounded in the lateral directions, so no further conditions are required to describe the surface of the film.

3.2.2. Orientation field in a thin film

Let the three-dimensional orientation field of active filaments in the film be given by $\boldsymbol{S}(\boldsymbol{x})$. We restrict the analysis to directors which are tangentially anchored to both bounding surfaces. At the flat substrate the orientation is given by $\boldsymbol{S}(x, y, 0) = (n_x, n_y, 0)$ in terms of the two-dimensional director $\boldsymbol{n} = (n_x, n_y)$, with $|\boldsymbol{n}| = 1$, which at this stage is completely generic but will be specified in Section 3.3. This can be mapped to a tangential director at the upper surface, $\boldsymbol{S}(x, y, h) \propto (n_x, n_y, n_z)$ up to

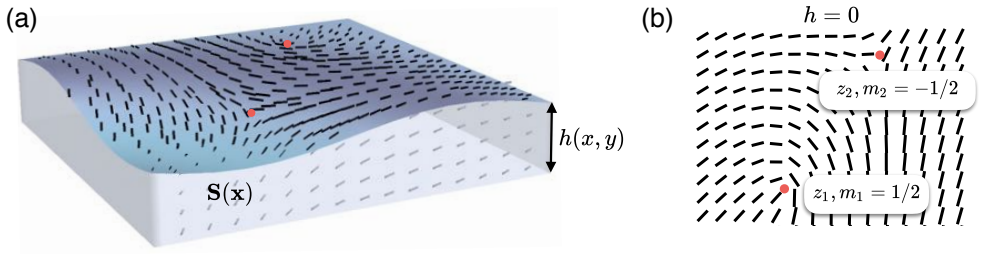

Figure 3.1: (a) Schematic representation of a section of the thin film of active nematic, with the height function $h(x,y)$ and the three-dimensional director $\boldsymbol{S}(\boldsymbol{x})$. (b) Two-dimensional director $\boldsymbol{n}(x,y)$ in the plane of the substrate. Two defects are shown, with their complex positions $z_j = x_j + iy_j$ and topological strengths m_j.

normalisation, by defining

$$n_z = (n_x \boldsymbol{e}_1 + n_y \boldsymbol{e}_2) \cdot \hat{\boldsymbol{e}}_z \approx \boldsymbol{n} \cdot \boldsymbol{\nabla}_\perp h, \tag{3.8}$$

to linear order in $\boldsymbol{\nabla}_\perp h$. This corresponds to a projection of the director at the lower to the upper surface with no rotation about the z-axis, so that the final, three-dimensional director has no twist. Finally, the three-dimensional unit length orientation field is constructed by a smooth interpolation between the two surfaces, using the prefactor z/h in the z-component,

$$\boldsymbol{S}(\boldsymbol{x}) = \frac{1}{s(\boldsymbol{x})} \begin{pmatrix} n_x \\ n_y \\ \frac{z}{h} n_z \end{pmatrix}, \tag{3.9}$$

where the normalisation prefactor is $s(\boldsymbol{x}) = \sqrt{1 + (z/h)^2 n_z^2}$. Equation (3.9) is the most general form of a polarisation field that satisfies the tangential anchoring condition and is consistent with the assumption of a thin film, where the variations of the polarisation in the z-direction are small.

3.2.3. Thin film approximation for active fluids

The fluid flow in the active film is determined by the Stokes and continuity equations

$$-\nabla p + \mu \Delta \boldsymbol{u} + \nabla \cdot (\boldsymbol{\sigma}^a + \boldsymbol{\sigma}^e) = 0, \tag{3.10}$$

$$\nabla \cdot \boldsymbol{u} = 0, \tag{3.11}$$

as explained in Section 2.2.2. The geometry of the film can be exploited to simplify equation (3.10). We assume that its horizontal extension, characterised by the length scale L, is much larger than its average height h_0. Therefore, as we are interested in long-wavelength phenomena, the variations of the flow in the x and y directions are

much more gradual than in the z direction. We define the small parameter

$$\varepsilon = \frac{h_0}{L} \ll 1 \tag{3.12}$$

and perform an expansion of the governing equations, as commonly done for thin films of passive [Oron et al., 1997] or active fluids [Sankararaman and Ramaswamy, 2009; Joanny and Ramaswamy, 2012].

We define dimensionless coordinates, rescaling with L in the lateral direction and with h_0 in the vertical direction,

$$\tilde{x} = \frac{\varepsilon x}{h_0} \ , \ \tilde{y} = \frac{\varepsilon y}{h_0} \ , \ \tilde{z} = \frac{z}{h_0} \ , \text{ and likewise } \tilde{h} = \frac{h}{h_0}. \tag{3.13}$$

We assume that compared to the height the extension of the film is similar in both horizontal directions, therefore we treat the x and the y directions analogously. With a characteristic active flow velocity U_0 we define dimensionless flow components

$$\tilde{u}_x = \frac{u_x}{U_0} \quad \text{and} \quad \tilde{u}_y = \frac{u_y}{U_0}. \tag{3.14}$$

With (3.14) the incompressibility condition (3.11) becomes

$$\frac{U_0 \varepsilon}{h_0} \left(\frac{\partial \tilde{u}_x}{\partial \tilde{x}} + \frac{\partial \tilde{u}_y}{\partial \tilde{y}} \right) + \frac{1}{h_0} \frac{\partial u_z}{\partial \tilde{z}} = 0, \tag{3.15}$$

which for the last term to be of the same order as the first two requires

$$\tilde{u}_z = \frac{u_z}{\varepsilon U_0}. \tag{3.16}$$

Alternatively, it is possible to set $u_z = 0$ and reduce (3.11) to two-dimensional incompressibility, which would restrict the model to two flat, unchanging surfaces. Finally, for completeness, the time scale active flows in the plane of the film is set by $T = L/U_0$, and therefore $\tilde{t} = \frac{\varepsilon U_0 t}{h_0}$.

The active stress in equation (3.10) is

$$\sigma^a_{ij} = -\sigma_0 (S_i S_j - \delta_{ij}/3), \tag{3.17}$$

as defined in (2.14) but with the director $\boldsymbol{S}(\boldsymbol{x})$, given by (3.9). The prefactor in (3.9) is $s(\boldsymbol{x}) = 1 + \mathcal{O}(\varepsilon^2)$, hence we omit it from $\boldsymbol{S}(\boldsymbol{x})$. We treat the two-dimensional director $\boldsymbol{n}$ as given. Further, $\boldsymbol{n}$ is normalised, so its components are $n_x, n_y \sim O(1)$. The components of the active stress divergence are calculated in Appendix A and have

the following form and scaling with ε

$$\boldsymbol{\nabla}\cdot\boldsymbol{\sigma}^a = -\sigma_0\begin{pmatrix} \frac{1}{h}\boldsymbol{\nabla}_\perp\cdot(hn_x\boldsymbol{n}) \\ \frac{1}{h}\boldsymbol{\nabla}_\perp\cdot(hn_y\boldsymbol{n}) \\ \boldsymbol{\nabla}_\perp\cdot(\boldsymbol{n}\frac{z}{h}(\boldsymbol{n}\cdot\boldsymbol{\nabla}_\perp h)) + \frac{2z}{h^2}(\boldsymbol{n}\cdot\boldsymbol{\nabla}_\perp h)^2 \end{pmatrix} \approx -\frac{\varepsilon}{h_0}\frac{\sigma_0}{\tilde{h}}\begin{pmatrix} \tilde{\boldsymbol{\nabla}}_\perp\cdot(\tilde{h}n_x\boldsymbol{n}) \\ \tilde{\boldsymbol{\nabla}}_\perp\cdot(\tilde{h}n_y\boldsymbol{n}) \\ 0 \end{pmatrix}, \tag{3.18}$$

where we have neglected the z-component, which is $\mathcal{O}(\varepsilon^2)$, in the second line.

The tensor $\boldsymbol{\sigma}^e$ in (3.10) accounts for stresses due to nematic elasticity and was given in equation (2.13). We will consider director profiles which minimise elastic energy in the xy-plane, see Section 3.3, and have only a small out-of-plane tilt, suggesting that flows due to elasticity should be small compared to active flows. Specifically, assuming one elastic constant, the leading order term in the Frank free energy (2.2) is the one associated with splay in z-direction, $\frac{K}{2}(\nabla\cdot\boldsymbol{S})^2 \sim O(\varepsilon^2)$. Thus, in relation to the active stresses $\boldsymbol{\sigma}^e$ is small and we will omit it from now on.

Having made the main terms dimensionless and using also (3.18), the components of the Stokes equation (3.10) become

$$-\frac{\varepsilon h_0}{\mu U_0}\partial_{\tilde{x}}p + \varepsilon^2\tilde{\nabla}_\perp^2\tilde{u}_x + \partial_{\tilde{z}}^2\tilde{u}_x - \frac{\varepsilon h_0}{\mu U_0}\sigma_0\frac{1}{\tilde{h}}\tilde{\boldsymbol{\nabla}}_\perp\cdot\left(\tilde{h}n_x\boldsymbol{n}\right) = 0, \tag{3.19}$$

$$-\frac{\varepsilon h_0}{\mu U_0}\partial_{\tilde{y}}p + \varepsilon^2\tilde{\nabla}_\perp^2\tilde{u}_y + \partial_{\tilde{z}}^2\tilde{u}_y - \frac{\varepsilon h_0}{\mu U_0}\sigma_0\frac{1}{\tilde{h}}\tilde{\boldsymbol{\nabla}}_\perp\cdot\left(\tilde{h}n_y\boldsymbol{n}\right) = 0, \tag{3.20}$$

$$-\frac{1}{\mu U_0}\partial_{\tilde{z}}p + \varepsilon^3\tilde{\nabla}_\perp^2\tilde{u}_z + \varepsilon\partial_{\tilde{z}}^2\tilde{u}_z + \mathcal{O}(\varepsilon^2) = 0. \tag{3.21}$$

Note, that p and σ_0 still carry dimensions and that in (3.19) and (3.20) the leading order terms are $\partial_{\tilde{z}}^2\tilde{u}_x$ and $\partial_{\tilde{z}}^2\tilde{u}_y$, respectively. Because we want to study flows that are driven by active stresses, we require that the active stress term be of the same order and therefore define the dimensionless active parameter as

$$\tilde{\sigma}_0 = \frac{\varepsilon h_0}{\mu U_0}\sigma_0, \tag{3.22}$$

which also fixes the velocity scale to

$$U_0 = \frac{\sigma_0 h_0^2}{\mu L}. \tag{3.23}$$

Similarly, in conformance with passive thin films [Oron et al., 1997],

$$\tilde{p} = \frac{\varepsilon h_0}{\mu U_0}p. \tag{3.24}$$

This completes the expansion of the Stokes equations in ε, leaving them in a simplified form

$$-\partial_{\tilde{x}}\tilde{p} + \partial_{\tilde{z}}^2\tilde{u}_x - \frac{\sigma_0}{\tilde{h}}\tilde{\boldsymbol{\nabla}}_\perp \cdot \left(\tilde{h} n_x \boldsymbol{n}\right) = 0, \tag{3.25}$$

$$-\partial_{\tilde{y}}\tilde{p} + \partial_{\tilde{z}}^2\tilde{u}_y - \frac{\sigma_0}{\tilde{h}}\tilde{\boldsymbol{\nabla}}_\perp \cdot \left(\tilde{h} n_y \boldsymbol{n}\right) = 0, \tag{3.26}$$

$$\partial_{\tilde{z}}\tilde{p} = 0, \tag{3.27}$$

which can be solved once the boundary conditions are specified.

3.2.4. Effective active force

From the in-plane components of (3.18) we define a two-component vector $\boldsymbol{f}^a$ representing the effective active force

$$\boldsymbol{f}^a(\boldsymbol{x}_\perp) = -\frac{\sigma_0}{h}\begin{pmatrix} \boldsymbol{\nabla}_\perp \cdot (h n_x \boldsymbol{n}) \\ \boldsymbol{\nabla}_\perp \cdot (h n_y \boldsymbol{n}) \end{pmatrix}. \tag{3.28}$$

A short calculation shows that it can be written in a coordinate-independent form

$$\boldsymbol{f}^a(\boldsymbol{x}_\perp) = -\sigma_0 \left(\boldsymbol{n}\left(\boldsymbol{\nabla}_\perp \cdot \boldsymbol{n} + \frac{1}{h}\boldsymbol{n} \cdot \boldsymbol{\nabla}_\perp h\right) + (\boldsymbol{n} \cdot \boldsymbol{\nabla}_\perp)\,\boldsymbol{n}\right), \tag{3.29}$$

which allows a geometric interpretation of the individual contributions. From left to right we identify[1] in (3.29) the splay of $\boldsymbol{n}$, a coupling to gradients in the film thickness, and bend of $\boldsymbol{n}$. These contributions will be discussed in detail in the context of a thin drop of active fluid on a surface in Chapter 4.

Equations (3.25) and (3.26) may now be combined into

$$\partial_{\tilde{z}}^2\tilde{\boldsymbol{u}}_\perp = \tilde{\boldsymbol{\nabla}}_\perp\tilde{p} - \tilde{\boldsymbol{f}}^a. \tag{3.30}$$

3.2.5. Boundary conditions

In this section we first state the boundary conditions for the velocities and stresses in terms of unscaled variables, before transforming to dimensionless variables and expanding in the small parameter ε. At the base we allow for partial slip with viscous friction, as given in equation (2.18). The shear stress acting on the fluid at the substrate is proportional to the fluid velocity evaluated at the boundary,

$$(\hat{\boldsymbol{e}}_z \cdot \boldsymbol{\sigma}) \cdot \hat{\boldsymbol{e}}_i = \sigma_{iz} = -\frac{1}{\xi}u_i \quad \text{for } i = x, y, \tag{3.31}$$

[1] Compare with the contributions in the Frank free energy (2.2).

where $\boldsymbol{\sigma}$ is the total stress tensor of the fluid as given by (2.12), but with $\boldsymbol{\sigma}^e$ omitted, as justified above. Therefore,

$$\sigma_{ij} = -p\delta_{ij} + \mu(\partial_i u_j + \partial_j u_i) + \sigma^a_{ij}. \tag{3.32}$$

Here ξ is the inverse friction coefficient, so that $\xi = 0$ corresponds to a no-slip condition, and its dimensionless form is $\tilde{\xi} = \frac{\xi\mu}{h_0}$. For small ε condition (3.31) becomes

$$\boldsymbol{u}_\perp\big|_{z=0} = -\xi\partial_z \boldsymbol{u}_\perp\big|_{z=0} \tag{3.33}$$

in dimensionless variables with tildes omitted. The substrate is non-permeable and therefore the z-component of the flow vanishes there

$$u_z|_{z=0} = 0. \tag{3.34}$$

At the free boundary the stress component tangent to the surface should vanish,

$$\hat{\boldsymbol{n}}_h \cdot \boldsymbol{\sigma} - ((\hat{\boldsymbol{n}}_h \cdot \boldsymbol{\sigma}) \cdot \hat{\boldsymbol{n}}_h)\, \hat{\boldsymbol{n}}_h = \mathbf{0}, \tag{3.35}$$

which for small ε and in dimensionless variables, with tildes omitted, simplifies to

$$\partial_z \boldsymbol{u}_\perp\big|_{z=h} = \mathbf{0}. \tag{3.36}$$

The normal stress at the upper boundary is given in terms of the mean curvature H of the surface, the surface tension γ and the pressure p_0 in the surrounding medium [Joanny and Ramaswamy, 2012],

$$(\hat{\boldsymbol{n}}_h \cdot \boldsymbol{\sigma}) \cdot \hat{\boldsymbol{n}}_h = -p_0 + \gamma H. \tag{3.37}$$

The mean curvature is the surface divergence of the normal $\hat{\boldsymbol{n}}_h$, see equation (3.2), which in a thin film amounts to

$$H = -\boldsymbol{\nabla}_s \cdot \hat{\boldsymbol{n}}_h = -\left(\boldsymbol{e}_1\partial_x + \boldsymbol{e}_2\partial_y\right) \cdot \hat{\boldsymbol{n}}_h = \partial_x^2 h + \partial_y^2 h = \nabla_\perp^2 h \tag{3.38}$$

and condition (3.37) then becomes

$$p|_{z=h} = p_0 + \frac{\sigma_0}{3} - \gamma\nabla_\perp^2 h, \tag{3.39}$$

which, in the absence of activity, reduces to the Young-Laplace law [Oron et al., 1997].

Making all quantities but γ dimensionless we get

$$\tilde{p}|_{\tilde{z}=\tilde{h}} = \tilde{p}_0 + \frac{\tilde{\sigma}_0}{3} - \frac{\varepsilon^3}{\mu U_0}\gamma\tilde{\nabla}_\perp^2\tilde{h}. \tag{3.40}$$

The surface tension term is currently three powers of ε smaller than the leading terms and there are two ways to approach this discrepancy [Oron et al., 1997]. If we wanted to retain surface tension effects, the coefficient has to be rescaled as $\tilde{\gamma} = \gamma\varepsilon^3/\mu U_0$, which would reflect very large surface tensions $\gamma \sim \varepsilon^{-3}$. This results in

$$\tilde{p}|_{\tilde{z}=\tilde{h}} = \tilde{p}_0 + \frac{\tilde{\sigma}_0}{3} - \tilde{\gamma}\tilde{\nabla}_\perp^2\tilde{h}. \tag{3.41}$$

Earlier we identified that the active stress coefficient should scale as $\sigma_0 \sim \varepsilon^{-1}$, see equation (3.22). In view of the main focus of this work, namely the effect of activity, a different approach would be to neglect surface tension in equation (3.40), that is to assume $\gamma \sim \mathcal{O}(1) \ll \sigma_0$.

3.2.6. General solution for the flow field

We will omit the tildes in all dimensionless equations derived so far for clarity and solve equations (3.27) and (3.30) subject to boundary conditions (3.33), (3.36), and (3.41). First, equation (3.27) with condition (3.41) results in a height-independent pressure

$$p(x,y) = p(x,y,h) = p_0 + \frac{\sigma_0}{3} - \gamma\nabla_\perp^2 h, \tag{3.42}$$

which makes the right-hand-side of equation (3.30) z-independent and yields $\boldsymbol{\nabla}_\perp p = -\gamma\boldsymbol{\nabla}_\perp\nabla_\perp^2 h$. We integrate equation (3.30) twice, using first the no shear boundary condition (3.36) in

$$-\partial_z\boldsymbol{u}_\perp = \int_z^h \partial_z^2\boldsymbol{u}_\perp \,\mathrm{d}z = (z-h)(\gamma\boldsymbol{\nabla}_\perp\nabla_\perp^2 h + \boldsymbol{f}^a) \tag{3.43}$$

and then the viscous friction condition (3.33) in

$$-\boldsymbol{u}_\perp - \xi\partial_z\boldsymbol{u}_\perp|_{z=0} = -\int_0^z \partial_z\boldsymbol{u}_\perp \,\mathrm{d}z = \left(\frac{z^2}{2} - hz\right)(\gamma\boldsymbol{\nabla}_\perp\nabla_\perp^2 h + \boldsymbol{f}^a). \tag{3.44}$$

But from (3.43) we have $\partial_z\boldsymbol{u}_\perp|_{z=0} = h(\gamma\boldsymbol{\nabla}_\perp\nabla_\perp^2 h + \boldsymbol{f}^a)$, which yields the instantaneous horizontal flow component

$$\boldsymbol{u}_\perp = \left(h\,(z-\xi) - \frac{z^2}{2}\right)\left(\gamma\boldsymbol{\nabla}_\perp\nabla_\perp^2 h + \boldsymbol{f}^a\right). \tag{3.45}$$

The height-integrated horizontal flow is

$$\bar{\boldsymbol{u}}_\perp = h^2 \left(\frac{h}{3} - \xi\right) \left(\gamma \boldsymbol{\nabla}_\perp \nabla_\perp^2 h + \boldsymbol{f}^a\right). \tag{3.46}$$

The instantaneous vertical flow component can be obtained by integrating the three-dimensional incompressibility equation (3.11) with condition (3.34)

$$\begin{aligned} u_z &= \int_0^z (-\boldsymbol{\nabla}_\perp \cdot \boldsymbol{u}_\perp)\, \mathrm{d}z \\ &= -\left(\frac{z^2}{2} - \xi z\right) \boldsymbol{\nabla}_\perp h \cdot (\gamma \boldsymbol{\nabla}_\perp \nabla_\perp^2 h + \boldsymbol{f}^a) - \left(h\left(\frac{z^2}{2} - \xi z\right) - \frac{z^3}{6}\right) \left(\gamma \nabla_\perp^4 h + \boldsymbol{\nabla}_\perp \cdot \boldsymbol{f}^a\right). \end{aligned} \tag{3.47}$$

Finally, using (3.46) in equation (3.7), the time evolution equation for the shape of the free boundary is obtained

$$\partial_t h = h^2 \left(\xi - \frac{h}{3}\right) \left(\gamma \nabla_\perp^4 h + \boldsymbol{\nabla}_\perp \cdot \boldsymbol{f}^a\right) + h(2\xi - h) \boldsymbol{\nabla}_\perp h \cdot \left(\gamma \boldsymbol{\nabla}_\perp \nabla_\perp^2 h + \boldsymbol{f}^a\right). \tag{3.48}$$

These results generalise those in Reference [Joanny and Ramaswamy, 2012] to a large class of orientation fields, which are energy-minimisers, which can contain an arbitrary collection of defects restricted only by the topology of the film. How such orientation fields are parametrised is described below.

3.3. Nematic director with defects

A two-dimensional nematic director can be written as $\boldsymbol{n} = \cos(\alpha)\hat{\boldsymbol{e}}_x + \sin(\alpha)\hat{\boldsymbol{e}}_y$ with $\alpha = \alpha(x, y)$. An example of a director with one defect of strength m at the origin was given in Section (2.4) as $\alpha = m\phi + \alpha_0$, where ϕ is the polar angle. Here, we will construct a director with an arbitrary collection of defects that is a minimiser of the Frank free energy in the one-elastic-constant approximation, see equation (2.6).

Two-dimensional problems can be conveniently represented in the complex plane, with the complex coordinate $z = x + iy$ and its complex conjugate $\bar{z} = x - iy$ [Riley et al., 2006; Needham, 1998]. It is well-known that planar solutions of the Laplace equation (2.7) with defects can be given in terms of holomorphic functions [Chaikin and Lubensky, 2000; Ovrut and Thomas, 1991; Lubensky and Prost, 1992]. For instance, the function $(z - z_0)^m$ has a pole of order $|m|$, if $m < 0$, or a zero of order m, if $m > 0$. Thus the phase winds around z_0 by $2\pi m$ and we can use this function to construct a director with one defect at z_0. The unit vector field $\boldsymbol{n}$ can be "complexified" to

$$n(z, \bar{z}) = e^{i\alpha(z,\bar{z})} \tag{3.49}$$

and the angle is expressed through the argument of the holomorphic function as

$$\alpha(z,\bar{z}) = \arg((z-z_0)^m) = \mathrm{Im}\big\{\ln\big((z-z_0)^m\big)\big\} \tag{3.50}$$

Differential operators transform as $\frac{\partial}{\partial z} = \frac{1}{2}(\frac{\partial}{\partial x} - i\frac{\partial}{\partial y})$ and $\frac{\partial}{\partial \bar{z}} = \frac{1}{2}(\frac{\partial}{\partial x} + i\frac{\partial}{\partial y})$. Writing $\alpha(z,\bar{z}) = \frac{m}{2i}\ln\Big(\frac{z-z_0}{\bar{z}-\bar{z}_0}\Big)$, it is easy to see that it is a solution of the complex Laplace equation

$$\frac{\partial}{\partial \bar{z}}\frac{\partial}{\partial z}\alpha(z,\bar{z}) = 0\,. \tag{3.51}$$

Consequently, a director with n_{def} defects, with the j-th defect located at z_j and having strength m_j, is constructed from a holomorphic function with an appropriate arrangement of poles and zeros

$$f(z) = \prod_{j=1}^{n_{\mathrm{def}}}(z-z_j)^{m_j}\,. \tag{3.52}$$

The director for this collection of defects is then given by the angle

$$\alpha(z,\bar{z}) = \alpha_0 + \mathrm{Im}\{\ln f(z)\} = \alpha_0 + \sum_{j=1}^{n_{\mathrm{def}}} m_j\,\mathrm{Im}\{\ln(z-z_j)\}\,, \tag{3.53}$$

where, as before in Section 2.4.1, we have added a constant phase α_0 allowed in the one-constant-approximation. By linearity this superposition also satisfies equation (3.51).

This parametrisation of the director is the starting point for our analysis of the active flow. In a laterally unbounded thin film with a quasi-two dimensional director, that is a director with only small vertical variations due to a coupling to the bounding surface, the choice of defects has to confirm with the topological constraint

$$\sum_{j=1}^{n_{\mathrm{def}}} m_j = 0\,, \tag{3.54}$$

but otherwise the configuration of defects is arbitrary.

3.4. Active flow singularities

Consider a thin film, where the two-dimensional polarisation is $\boldsymbol{n} = \cos(\alpha)\hat{\boldsymbol{e}}_x + \sin(\alpha)\hat{\boldsymbol{e}}_y$, with the angle given by (3.53). The active force (3.29) may be written

in a complexified form as

$$f^a(z,\bar{z}) = f^a_x + i f^a_y \tag{3.55}$$

$$= -\sigma_0 \left(\partial_z \left(n^2\right) + n^2 \frac{\partial_z h}{h} + \frac{\partial_{\bar{z}} h}{h} \right) \tag{3.56}$$

$$= -\sigma_0 \left(e^{i2\alpha} \left(\sum_{j=1}^{n_{\mathrm{def}}} m_j \frac{1}{z - z_j} + \frac{\partial_z h}{h} \right) + \frac{\partial_{\bar{z}} h}{h} \right) \tag{3.57}$$

where $h = h(z,\bar{z})$ and we have used $n\bar{n} = 1$ to obtain (3.56). Consider the active force in the vicinity of the k-th defect, specifically on a circle of radius ρ given by $z(s) = z_k + \rho e^{is}$, with $s \in [0, 2\pi)$. First, on this circle the director angle becomes

$$\alpha(s) = \alpha_0 + \sum_{j \neq k} m_j \operatorname{Im}\{\ln(z_k - z_j + \rho e^{is})\} + m_k \operatorname{Im}\{\ln(\rho e^{is})\} \tag{3.58}$$

$$= w(z_k) + m_k s + \mathcal{O}(1), \tag{3.59}$$

where we have defined the constant

$$w(z_k) := \alpha_0 + \sum_{j \neq k} m_j \operatorname{Im}\{\ln(z_k - z_j)\}. \tag{3.60}$$

In the following we assume that the variation of the film height across the small circle is much smaller than the variation of the director. Indeed, for the spherical cap shape used in Chapter 4, see equation (4.4), we have $\partial_{\bar{z}} h, \partial_z h \sim const. + \mathcal{O}(\rho)$. However, this is not always the case, since the active film may become unstable [Sankararaman and Ramaswamy, 2009] or the defects may lead to strong deformations of the film. In the latter case, flows driven by the defect and flows due to shape gradients are of comparable magnitude and a stationary shape of the film is characterised by a balance of the two contributions, as discussed in Chapter 4.4.

If $\partial_z h, \partial_{\bar{z}} h \sim \mathcal{O}(1)$ on the circle we have

$$f^a(s) = -\sigma_0 \left(e^{i2\alpha(s)} \left(\frac{m_k}{\rho} e^{-is} + \sum_{j \neq k}^{n_{\mathrm{def}}} m_j \frac{1}{z_k - z_j + \rho e^{is}} + \frac{\partial_z h}{h} \right) + \frac{\partial_{\bar{z}} h}{h} \right) \tag{3.61}$$

$$= -\sigma_0 \frac{m_k}{\rho} e^{i2w(z_k)} e^{i(2m_k - 1)s} + \mathcal{O}(1). \tag{3.62}$$

This reveals the following about the instantaneous horizontal flow $\boldsymbol{u}_\perp$, evaluated at a fixed height. Firstly, in the vicinity of a defect the flow diverges as $\sim 1/\rho$ as a result of the thin film approach. Therefore, a cut-off at some finite ρ_0 is required. The circle radius ρ is a dimensionless scale and ρ_0 may be associated with the length at which

the thin film approximation breaks down in the vicinity of the defects, which is either the film thickness h_0 or the core size r_c of the defect,

$$\rho_0 = \frac{1}{L}\max\{h_0, r_c\}. \tag{3.63}$$

Secondly, the dominant contribution to the active flow $\boldsymbol{u}_\perp$ at a defect of strength m_k is a flow singularity with winding number

$$\mathcal{I} = 2m_k - 1 \tag{3.64}$$

at the location of the defect, where $m_k \neq 0$. The flow singularities for different defect types are illustrated in Figure 3.2. Unit strength defects produce a flow vortex[2] ($\mathcal{I} = 1$). These flow vortices may acquire a sink- or source-like character according to whether the defect resembles an aster or a vortex, respectively. Since this instantaneous flow is coupled to the film shape, such flows are allowed and, for instance, lead to novel stationary shapes of a drop of active fluid on a surface, see Section 4.4. For most types of defects the flow singularity will be a higher order stagnation point, as for instance for $m_k = -1/2$ or $m_k = -1$ in Figure 3.2. Interestingly, simple stagnation points ($\mathcal{I} = -1$) cannot be created at defect locations.

On the other hand, from equation (3.64) it is evident that the active flow is not winding at a $+1/2$ defect. Instead, it is directed along the defect's symmetry axis. The direction of the axis is found from $\phi/2 + \alpha_0 = \phi \pm n\pi$, $n \in \mathbb{N}$, so it is given by the vector $(\cos(2\alpha_0 \pm 2n\pi), \sin(2\alpha_0 \pm 2n\pi))$, which points away from the defect's comet-head. Consider for simplicity a single $+1/2$ defect in the film, such that $w(z_k) = \alpha_0$, and $\xi = 0$. The active flow at the defect, here evaluated for instance at the upper surface, $z = h(x, y)$, is then given by

$$\boldsymbol{u}_\perp^{+1/2} = -\frac{\sigma_0}{4}\frac{h^2}{\rho_0}\begin{pmatrix} \cos(2\alpha_0) \\ \sin(2\alpha_0) \end{pmatrix} \tag{3.65}$$

in dimensionless quantities. For an extensile defect the flow is towards the comet-head, and it is oppositely directed for a contractile defect.

3.5. Regularisation of the defect core

Since the thin approach yields flow at the defects that diverges in magnitude a different model is required for the defect core to regularise this flow. We perform an exemplary calculation for a $+1/2$ defect. Consider a slice through the cylindrical defect core

[2]Here, we denote a flow singularity a "vortex" only if it has winding $\mathcal{I} = 1$, in contrast to some of the literature.

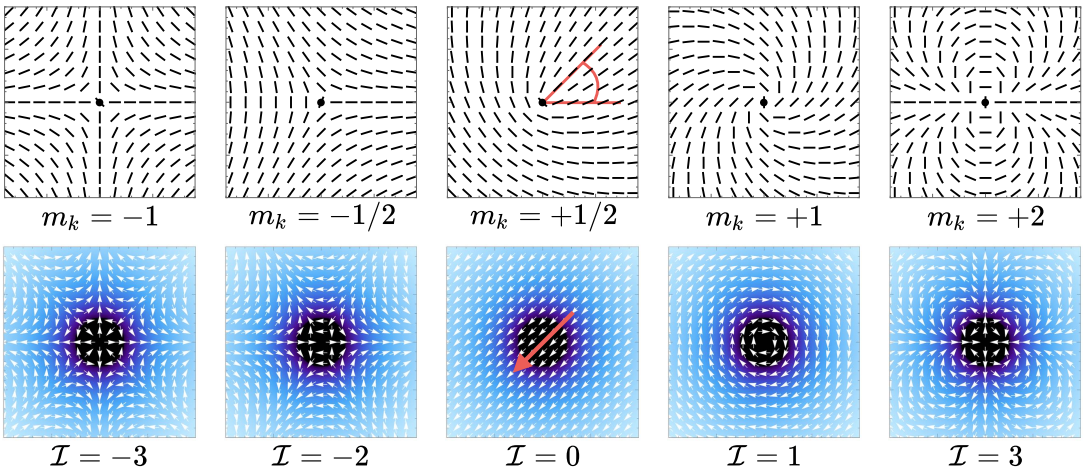

Figure 3.2: Defects (top) and associated active flow singularities (bottom) in a thin film, with winding numbers $\mathcal{I} = 2m_k - 1$, as given by formula (3.62). Phase constants are $\alpha_0 = \pi/8$ for $m_k = 1/2$, $\alpha_0 = \pi/4$ for $m_k = 1$ and $\alpha_0 = 0$ otherwise. For $m_k = 1/2$ the flow is not winding and its direction is given by the red arrow (bottom). It coincides with the direction of the comet-head of the defect. The angle $2\alpha_0$ is indicated in the director. The flow directions are evaluated for an extensile material with $\sigma_0 = 1$. Only the dominant contribution to the flow is shown, which is $\sim 1/\rho$ with the distance from the defect and is cut off at a finite ρ_0.

region of radius $r_0 = \max\{r_c, h_0\}$ at a given height. Inside the core in-plane gradients of the flow are dominant, therefore a two-dimensional description is appropriate,

$$-\nabla_\perp p + \mu\nabla_\perp^2 \boldsymbol{u} - \sigma_0 \left(\boldsymbol{n}\left(\boldsymbol{\nabla}_\perp \cdot \boldsymbol{n}\right) + \left(\boldsymbol{\nabla}_\perp \cdot \boldsymbol{n}\right)\boldsymbol{n}\right) = 0, \tag{3.66}$$

$$\nabla_\perp \cdot \boldsymbol{u} = 0\,, \tag{3.67}$$

with $p = p(x, y)$, $\boldsymbol{u} = (u_x, u_y)$ and the director $\boldsymbol{n} = \cos(\phi/2 + \alpha_0)\hat{\boldsymbol{e}}_x + \sin(\phi/2 + \alpha_0)\hat{\boldsymbol{e}}_y$. With

$$\boldsymbol{n}\left(\boldsymbol{\nabla}_\perp \cdot \boldsymbol{n}\right) = \frac{1}{4}\left(\frac{x}{r^2} + \frac{\cos(2\alpha_0)}{r}\right)\hat{\boldsymbol{e}}_x + \frac{1}{4}\left(\frac{y}{r^2} + \frac{\sin(2\alpha_0)}{r}\right)\hat{\boldsymbol{e}}_y \quad \text{and} \tag{3.68}$$

$$\left(\boldsymbol{\nabla}_\perp \cdot \boldsymbol{n}\right)\boldsymbol{n} = \frac{1}{4}\left(-\frac{x}{r^2} + \frac{\cos(2\alpha_0)}{r}\right)\hat{\boldsymbol{e}}_x + \frac{1}{4}\left(-\frac{y}{r^2} + \frac{\sin(2\alpha_0)}{r}\right)\hat{\boldsymbol{e}}_y \tag{3.69}$$

the active force becomes

$$\boldsymbol{f}^a = -\frac{\sigma_0}{2}\frac{\cos(2\alpha_0)}{r}\hat{\boldsymbol{e}}_x - \frac{\sigma_0}{2}\frac{\sin(2\alpha_0)}{r}\hat{\boldsymbol{e}}_y. \tag{3.70}$$

Taking the in-plane divergence of equation (3.66) and using (3.67) yields a Poisson-type equation for the pressure

$$\nabla_\perp^2 p = \frac{\sigma_0}{2r^2}\cos(\phi - 2\alpha_0). \tag{3.71}$$

Making the ansatz $p \propto r^k \cos(\phi - 2\alpha_0)$ provides a particular integral for $k = 0$ and complementary functions of the homogeneous equation for $k = \pm 1$. A general solution can thus be written as

$$p = \cos(\phi - 2\alpha_0)\left(-\frac{\sigma_0}{2} + Ar + \frac{B}{r}\right) \tag{3.72}$$

$$= \cos(2\alpha_0)\left(-\frac{\sigma_0}{2}\frac{x}{r} + Ax + B\frac{x}{r^2}\right) + \sin(2\alpha_0)\left(-\frac{\sigma_0}{2}\frac{y}{r} + Ay + B\frac{y}{r^2}\right), \tag{3.73}$$

with two constants A and B. Plugging this pressure back into the Stokes equation (3.66) cancels the active force, such that

$$\mu\nabla_\perp^2 \boldsymbol{u} = \left(\frac{\sigma_0}{4r} - \frac{B}{r^2}\right)\begin{pmatrix} \cos(2(\phi - \alpha_0)) \\ \sin(2(\phi - \alpha_0)) \end{pmatrix} + \left(\frac{\sigma_0}{4r} + A\right)\begin{pmatrix} \cos(2\alpha_0) \\ \sin(2\alpha_0) \end{pmatrix}. \tag{3.74}$$

We set $B = 0$, as otherwise a divergent term $\propto \ln(r)^2$ would arise. For the first σ_0-term in (3.74) we make the ansatz $\boldsymbol{u} \propto r^k(\cos(m(\phi - \alpha_0)), \sin(m(\phi - \alpha_0)))$, which produces

$$\begin{aligned}\nabla_\perp^2(r^k(\cos(m(\phi - \alpha_0))) &= \cos(m(\phi - \alpha_0))\frac{1}{r}\partial_r(r\partial_r r^k) + \frac{1}{r^2}r^k\partial_{\phi\phi}\cos(m(\phi - \alpha_0)) \\ &= r^{k-2}(k^2 - m^2)\cos(m(\phi - \alpha_0)),\end{aligned} \tag{3.75}$$

and a similar expression in the y-component. This yields a particular integral for the first σ_0-term for $k = 1$ and $m = 2$, and complementary functions for $k = m$. Likewise, the ansatz $\propto r^k$ produces the last two terms in (3.74) for $k = 1$ and $k = 2$, respectively. The flow around the defect is thus given by

$$\boldsymbol{u} = \frac{1}{4\mu}(\sigma_0 r + Ar^2 + D)\begin{pmatrix} \cos(2\alpha_0) \\ \sin(2\alpha_0) \end{pmatrix} + \frac{\sigma_0}{4\mu}(Cr^2 - \frac{r}{3})\begin{pmatrix} \cos(2(\phi - \alpha_0)) \\ \sin(2(\phi - \alpha_0)) \end{pmatrix}. \tag{3.76}$$

We have added a complementary, harmonic function with $k = m = 2$ and additional constants C and D in order to match the boundary conditions at $r = r_0$ and ensure self-propulsion of the defect. Along the circular boundary the solution of the core and the thin film calculation have to match, so

$$\boldsymbol{u}(r = r_0) = v_0\begin{pmatrix} \cos(2\alpha_0) \\ \sin(2\alpha_0) \end{pmatrix}, \tag{3.77}$$

where we have combined the prefactor in (3.65) into $v_0 \propto 1/r_0$. The boundary condition (3.77) is satisfied by choosing

$$A = -\frac{\sigma_0}{r_0}, \quad C = \frac{1}{3r_0}, \text{ and } \quad D = 4\mu v_0. \tag{3.78}$$

The regularised self-propulsion speed of the $+1/2$ defect in physical quantities is then

$$|\boldsymbol{u}(r=0)| = v_0 = -\frac{\sigma_0 h_0}{4\mu} \tag{3.79}$$

as required by the thin film solution, where we chose $r_0 = h_0$. This result justifies a simple cut-off at a finite distance away from the defect as an approximation to the flow at the defect centre.

3.6. Discussion

We have extended the active thin film model of Sankararaman and Ramaswamy [2009] and Joanny and Ramaswamy [2012] to a more general director, specified by its in-plane component $\boldsymbol{n}$ and the height gradients of the film. Writing the active force in the form of (3.29) reveals the role of its three components – splay, bend, and coupling to the shape – and allows for instance to study how they compete in an active droplet of finite size, see Chapter 4.

We find a general relationship between a defect and the type of flow singularity it produces at its location. The result coincides with those known for half-integer defects [Giomi et al., 2014] and $+1$ defects [Kruse et al., 2004], but also extends to other types of defects for which the active flow was not yet analysed. However, the thin film approximation ceases to be valid close to a defect, at a distance comparable to the film thickness or the core size. This results in divergent flow magnitudes at defects, instead of a finite flow strength for a $+1/2$ defect [Giomi et al., 2014] and vanishing velocity for a $+1$ defect [Kruse et al., 2004] and, similarly, for all other types of defects. We resolve this problem for a $+1/2$ defect by solving for the active flow in the core region separately and matching the two models at the cut-off distance, which results in a finite defect speed and regularised flow in the core region. Such a matching procedure could be done for other types of defects, too. For instance, the core region of a $+1$ defect could be described as a cylinder with only azimuthal active flows in the interior, like in Reference [Kruse et al., 2004], but radial in- or outflux from the thin film solution across the core boundary.

The general solution for the flow (3.76) in the core region of a $+1/2$ defect is equivalent to the result obtained by Giomi et al. [2014]. However, the boundary

conditions used here are different, leading to a different flow structure. Giomi et al. [2014] consider a circular patch with a no-slip boundary, which together with the directed flow at the defect results in two flow vortices occurring either side of the defect. This boundary condition also leads to a linear dependence of the defect speed on the domain size, see equation (2.34). Instead, here we impose the unidirectional flow from the thin film calculation at the cross-over boundary, which results in a defect speed inversely proportional to the cut-off length. If this length is the film thickness, then the defect speed (3.79) has a form analogous to equation (2.34), but with the crucial difference that the relevant length scale is the film thickness h_0 rather than a lateral length scale R.

We have not yet considered the deformations of the free boundary that would result from the instantaneous flow (3.45) through the kinematic boundary condition (3.48). Such deformations are studied in Chapter 4 in the context of a thin active drop with one defect.

Apart from deforming the boundary, the active flows generated by the defective director will advect the defects themselves. Positive half-integer defects drive their own self-advection, but defects with $m_k \neq 1/2$ may also move due to flows generated by the other defects in their surrounding. This advection is of subleading order in the active force expansion (3.62). We postpone the study of defect motion to Chapter 5, where the excess topological charge enforced by spherical topology stabilises states with defects. In a planar film with no specific anchoring at the rim one should expect all defects to annihilate for intermediate activity. However, recent numerical work has shown the existence of intriguing defect and flow vortex patterns arising in different slab-like geometries just before the cross-over to the active turbulent state [Theillard et al., 2016; Doostmohammadi et al., 2016b]. Such geometries and the corresponding defect patterns might also be studied within a thin film approach.

CHAPTER 4

Thin drop of active fluid on a surface

In contrast to their well-studied passive counterparts [Oron et al., 1997; De Gennes et al., 2003], droplets of active liquid crystals attached to a surface have received little attention so far [Joanny and Ramaswamy, 2012; Tjhung et al., 2015]. The geometry of a drop is important in the context of biofilms [Kasyap et al., 2014; Drescher et al., 2016], motile cell fragments or spreading cells on substrates [Keren et al., 2009; Étienne and Duperray, 2011; Gabella et al., 2014], and active emulsion droplets [Sanchez et al., 2013], which might be turned into artificial crawlers. A first theoretical analysis has revealed new spreading laws and stationary shapes originating from activity for several highly symmetric director fields with defects [Joanny and Ramaswamy, 2012], accounting for a no-slip boundary only. Questions related to the motility of such drops along the surface remained unexplored.

Here, we study the onset of motility of such drops and how it is controlled by spatial variations and defects in the director, the shape of the drop, and the surface friction at the substrate. Numerical work on two-dimensional active polar drops [Tjhung et al., 2012] has revealed the existence of steady moving states with a splayed or bent director, in which the amount of distortion is proportional to the activity. The increase in splay or bend can culminate in the creation of a defect in the drop, which then continues to move, as long as the defect is located off-centre [Tjhung et al., 2012]. Motivated by these findings, we impose asymmetric directors with defects or distortions in an active drop shaped like a flat spherical cap. First, utilising the results of the previous chapter the structure of the instantaneous active flows generated in the drop by such directors is analysed for several examples. We then calculate analytically the centre-of-mass velocity of the drop in dependence of the position of an aster or vortex defect and give an estimate for the amount of slip at the substrate, for which the drop would stop moving. Solutions for the stationary shape of an axisymmetric drop with either a vortex or a spiral defect are derived.

4.1. Description of drops on surfaces

We consider a three-dimensional drop of active fluid, illustrated schematically in Figure 4.1, with mixed boundary conditions: a flat, rigid substrate providing frictional dissipation underneath and air or a fluid of much lower viscosity with zero tangential stress above the drop, allowing the shape to deform. In this way, the drop is equivalent to a film that is bounded laterally. The dynamics of the drop for a given static director is thus described by the active force (3.29), the instantaneous active flow (3.45) and the shape evolution (3.48), derived for a thin film of ALC in Chapter 3, but supplemented by additional boundary conditions which we formulate for a radially symmetric drop for simplicity [Oron et al., 1997]. An idealised drop touches the surface along a time-dependent contact line of radius $R(t)$, defined through the condition

$$h(R(t), t) = 0. \tag{4.1}$$

The drop has a finite volume

$$V_0 = 2\pi \int_0^{R(t)} h(r) r \mathrm{d}r. \tag{4.2}$$

The shape of the drop along the contact line is characterised by a contact angle θ_c, which is defined by

$$\partial_r h|_{r=R(t)} = -\tan\theta_c. \tag{4.3}$$

In the regime of partial wetting a drop on a surface in equilibrium takes the shape of a spherical cap [De Gennes et al., 2003]. The height function for a drop with a radius of curvature R_c and maximum height $h(r=0) = h_0$ is given by

$$h(r) = \sqrt{R_c^2 - r^2} - R_c + h_0 \tag{4.4}$$

and its radius is

$$R = \sqrt{h_0(2R_c - h_0)}, \tag{4.5}$$

so the radius of curvature can be expressed as $R_c = (R^2 + h_0^2)/2h_0$. We restrict to shapes for which $h_0/R \ll 1$, so that the thin film approximation of Section 3.2 applies. In this case $R \approx \sqrt{2h_0R_c} \ll R_c$, so the drop is a flat spherical cap with a small contact angle. Further, expanding $h(r)$ as given in (4.4) for $r/R_c \ll 1$ yields a parabolic profile

$$h(r) \approx \frac{h_0}{R^2}\left(R^2 - r^2\right), \tag{4.6}$$

which is a stationary solution of the shape evolution equation (3.48) in the passive

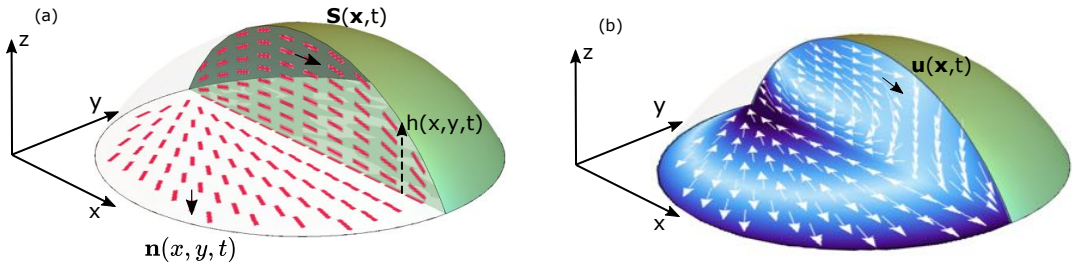

Figure 4.1: (a): Schematic view of a droplet of active fluid with filaments oriented according to the three-dimensional director $\boldsymbol{S}$, which has the two-dimensional projection $\boldsymbol{n}$. The filaments are anchored parallel to the bounding surface, which is given by its height function h. (b): The active stresses induced by the filaments generate a flow $\boldsymbol{u}$, which is separated into direction (white arrows) and magnitude (increasing from white to dark blue).

limit, $\sigma_0 = 0$, where it reads

$$\partial_t h = \boldsymbol{\nabla}_\perp \cdot \left(h \left(\frac{h}{3} - \xi \right) \gamma \boldsymbol{\nabla}_\perp \nabla_\perp^2 h \right). \tag{4.7}$$

For the director we impose tangential anchoring at both the base of the drop and the free surface, as in Section 3.2.2, and work with directors of the form (3.9). We are interested in the effect of a single defect inside the drop, or of strong director distortions equivalent to a virtual defect located outside the drop. Therefore, the in-plane director is taken to be

$$\boldsymbol{n} = \cos\left(m\psi(x_0) + \alpha_0\right) \hat{\boldsymbol{e}}_x + \sin\left(m\psi(x_0) + \alpha_0\right) \hat{\boldsymbol{e}}_y, \tag{4.8}$$

where, as before, m is the strength of the defect and α_0 controls the geometry of the director around it, for example whether it is an aster ($\alpha_0 = 0$) or a vortex ($\alpha_0 = \pi/2$) for strength $m = +1$, as shown in Figure 4.2 (d) and Figure 4.3 (d), respectively. Since the defect can be located anywhere along the x-axis, the angle $\psi(x_0) = \arctan\left(\frac{y}{x - x_0}\right)$ depends on the defect's position x_0. If $|x_0| > R$, there is no defect in the interior of the drop, but the virtual defect generates a distorted director in the drop, see for instance the splayed configuration in Figure 4.2 (a).

We have not yet specified the anchoring along the contact line. In order to obtain a static alignment, which minimises elastic energy up to small vertical distortions, we first specify the type of defect and its location and then choose the anchoring such that it matches the director generated by this particular defect. By imposing directors in this way, we mimic the moving steady states of active droplets found in simulations [Tjhung et al., 2012], which are characterised by stable splayed or bent directors and, at stronger activity, by stable defects located off-centre.

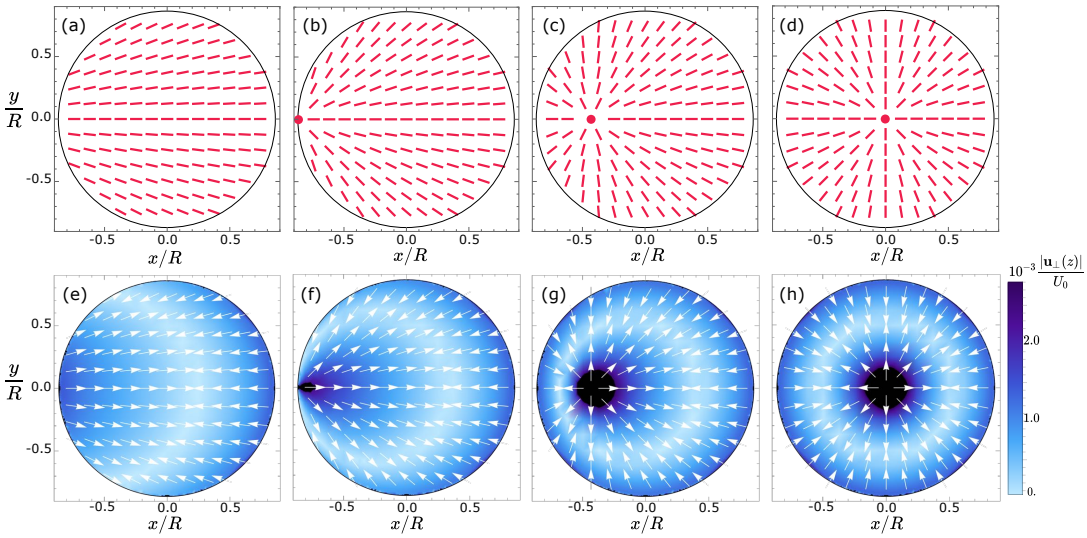

Figure 4.2: (a)-(d): Top view of drops with a splayed polarisation field ($m = 1, \alpha_0 = 0$) due to an aster defect at $x_0 = -2R, -R, -\frac{1}{2}R, 0$. (e)-(h): Plot of the resulting flow field (4.9) at $z = 0.01h_0$, for a contractile drop with no slip ($\sigma_0 = -1, \xi = 0$). The flow is aligned with the polarisation, but changes sign along a line where the splay of $\boldsymbol{n}$ balances the coupling term (4.11). Here and in the following plots red lines represent the polarisation field, and the flow field is decomposed into direction (white arrows) and magnitude (colour coded). At a defect the flow typically diverges and is cut off in the display (black region).

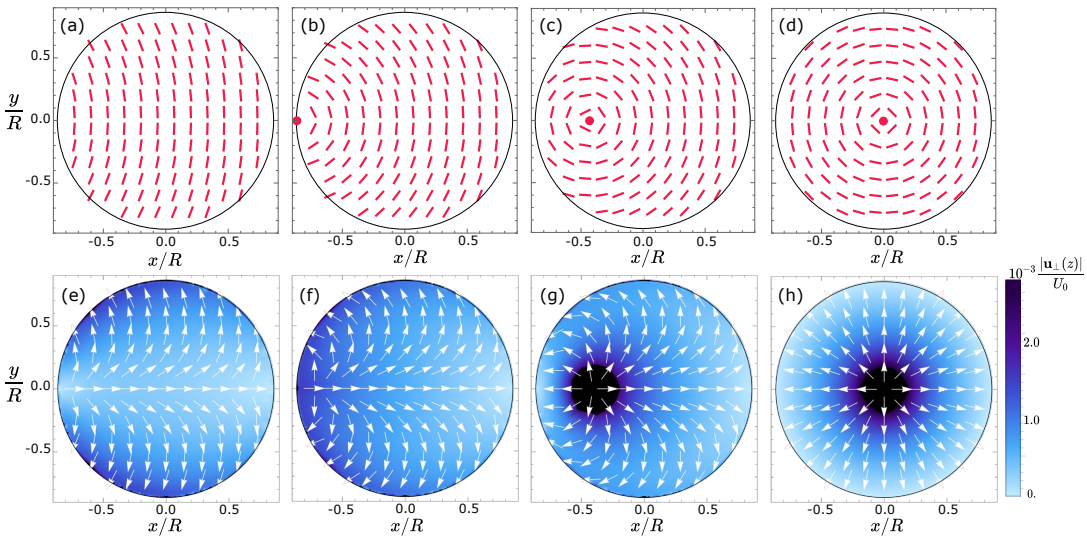

Figure 4.3: (a)-(d): Top view of drops with a bent polarisation field ($m = 1, \alpha_0 = \frac{\pi}{2}$) due to a vortex defect at $x_0 = -2R, -R, -\frac{1}{2}R, 0$. (e)-(h): Plot of the resulting flow field (4.9) at $z = 0.01h_0$, for an extensile drop with no slip ($\sigma_0 = 1, \xi = 0$). The flow is perpendicular to the polarisation in the bulk, but in (e)-(g) it aligns with the polarisation close to the boundary due to the coupling term (4.11). In the axisymmetric case, (d) and (h), the coupling term vanishes and the flow points radially outwards.

4.2. Instantaneous active flows

We consider the situation in which the drop of ALC on a surface contains a defect that generates an asymmetric director and study the instantaneous active flows in the drop for a given initial shape, which might then deform due to the flows. For this purpose the drop is chosen to be initially in the shape of a flat spherical cap with radius $R = 1$ and height $h_0 = 0.1$ given by the profile (4.6), or equivalently the profile (4.4) with $R_c = 5.05$.

In Chapter 3 we have used a thin film approximation to find the solution for the instantaneous flow $\boldsymbol{u}_\perp$ resulting from a particular orientation field $\boldsymbol{S}$ and shape h of a film, which also holds for a droplet of finite size. Since the flat spherical cap considered here is an equilibrium shape, equation (3.45) reduces to the active flow contribution

$$\begin{aligned}\boldsymbol{u}_\perp &= -\left(\frac{z^2}{2} + h\,(\xi - z)\right)\boldsymbol{f}^a \\ &= \sigma_0\left(\frac{z^2}{2} + h\,(\xi - z)\right)\left(\boldsymbol{n}\left(\nabla_\perp\cdot\,\boldsymbol{n} + \frac{1}{h}\boldsymbol{n}\cdot\nabla_\perp h\right) + (\boldsymbol{n}\cdot\nabla_\perp)\boldsymbol{n}\right)\,.\end{aligned} \tag{4.9}$$

The $\boldsymbol{x}_\perp$-dependence of $\boldsymbol{u}_\perp$ is primarily determined by the effective active force $\boldsymbol{f}^a$ and can be decomposed into three parts, each with a clear interpretation in terms of spatial variations in $\boldsymbol{n}$ and h. The vertical flow component (3.47), with active terms only, reads

$$u_z = \frac{z^3}{6}\nabla_\perp\cdot\,\boldsymbol{f}^a_\perp - \left(\frac{z^2}{2} - \xi z\right)\nabla_\perp\cdot\,(h\boldsymbol{f}^a_\perp)\,, \tag{4.10}$$

from which it is obvious that the three-dimensional nature of the flow will be most prominent in regions of strongly varying $\boldsymbol{f}^a_\perp$, in particular at topological defects in $\boldsymbol{n}$. Figure 4.1(b) provides an insight into one example of the full three-dimensional flow field $(\boldsymbol{u}_\perp, u_z)$ in the interior of a drop, however in the following we restrict the visual presentation to two-dimensional cross-sections.

4.2.1. Pure splay and pure bend directors

We illustrate the properties of the flow in the drop on examples of polarisation fields that are generated by defects of different topological strength. In simulations of active polar droplets stable splayed directors are found in the moving steady state in the contractile case and stable bent directors in the extensile [Tjhung et al., 2015]. Here, we impose similar directors with an aster defect in the contractile and a vortex defect in the extensile case.

The first $\boldsymbol{n}$-dependent term in (4.9) produces flow in direction of the polarisation

field and is proportional to the sum of its splay, $\nabla_\perp \cdot \boldsymbol{n}$, and the term

$$u_h = \frac{1}{h}\boldsymbol{n} \cdot \nabla_\perp h \ , \tag{4.11}$$

which couples the polarisation of the filaments to the shape of the drop and accounts for splay into the third dimension. Since term (4.11) is large in the vicinity of the contact line, where $h \to 0$, it dominates the flow at the boundary and aligns it there with the director. The second contribution, $(\boldsymbol{n} \cdot \nabla_\perp)\boldsymbol{n}$, creates flow that is perpendicular to the director and equal to its bend. This is a manifestation of the instabilities towards splay or bend in contractile or extensile active fluids, respectively, which are described in Section 2.2.3. For a drop on a surface this mechanism means that both pure splay or pure bend, in an asymmetric configuration, should generate a directed flow in the bulk of the drop and thus enable it to propel itself along the substrate, similar to a moving active droplet in two dimensions [Tjhung et al., 2015; Whitfield et al., 2014]. The direction of propulsion will depend on the sign of the activity σ_0 and on the friction parameter ξ, see Section 4.3. Figures 4.2 and 4.3 show examples for orientation fields with pure splay or pure bend and the resulting active flows in a plane close to the substrate.

A director with pure splay can be produced by varying the position of an aster defect, as illustrated in Figure 4.2. The resulting flow will be aligned with the polarisation and have a large component in direction of the splay. However, the flow changes its direction along a line where the splay of $\boldsymbol{n}$ is balanced by the coupling term (4.11), $u_h + \nabla_\perp \cdot \boldsymbol{n} = 0$. At the right boundary the flow is driven by the vertical splay due to the tangential anchoring to the bounding surface and directed inwards in this example. Note, that in the limit of uniform $\boldsymbol{n}$, that is $x_0 \to \pm\infty$, the flow is completely symmetric with respect to the mid-plane. The coupling to the surface, that is term (4.11), is then solely responsible for generating a flow in the drop and leads to symmetric spreading. This type of droplet was studied in detail by Joanny and Ramaswamy [2012]. Here, however, the flow at the boundary counteracts the bulk flow that is driven by strong variations in $\boldsymbol{n}$, and therefore also the propulsion of the drop.

A director with pure bend, as in Figure 4.3, can be generated by a variably positioned vortex defect. The flow is perpendicular to the director in the bulk, but aligns with the director close to the boundary due to the coupling term (4.11). However, in the axisymmetric case in Figure 4.3 (h) u_h vanishes, because h is now constant along closed circles in $\boldsymbol{n}$, leading to purely radial flow.

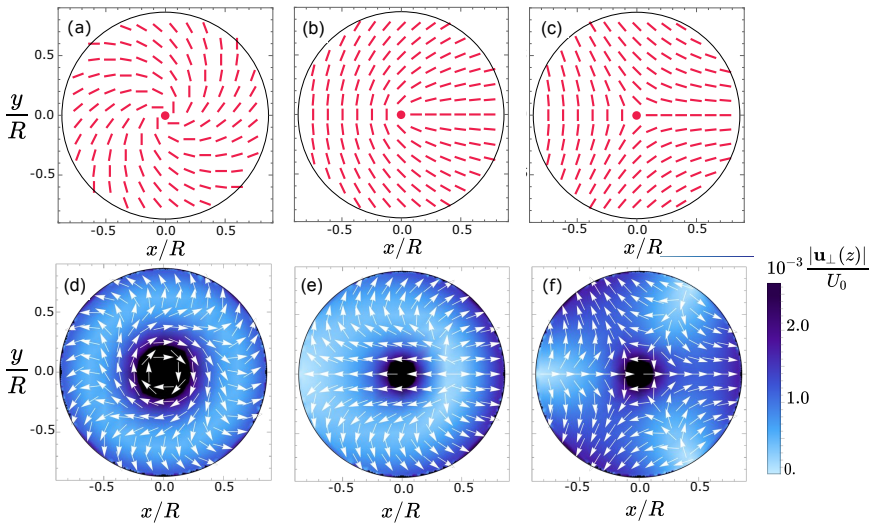

Figure 4.4: (a)-(c): Top view of directors with (a) spiral ($m = 1, \alpha_0 = \pi/4$), (c) $+1/2$ defect ($\alpha_0 = 0$), and (e) $-1/2$ defect ($\alpha_0 = 0$) in the centre of the drop ($x_0 = 0$). (d)-(e): Plot of the corresponding active flow fields (4.9) for $z = 0.01h_0$. Parameters are $\sigma_0 = 1$ (extensile) and $\xi = 0$ (no slip).

4.2.2. More complex directors

For more complex polarisation fields, in particular with $m \neq 1$, all contributions to (4.9) are present, as shown in Figure 4.4 for three different types of defects placed in the centre of the drop. The spiral defect in Figure 4.4 (a) generates rotational flow around the centre, as expected from the results of Section 3.4. However, close to the boundary the direction of rotation reverses, which is here again can be attributed to the coupling to $\nabla_\perp h$. Interestingly, a similar flow pattern, including the change of rotational direction, was observed in thin drops of bacteria suspensions where the swimming bacteria self-organised into a spiral vortex [Wioland et al., 2013].

In addition to profiles with integer strength defects, which can be found in systems with polar or nematic order, we also consider half-strength defects that only exist in nematic systems and are intrinsically asymmetric. In the setup of a droplet such defects may be stabilised by anchoring conditions that vary along the contact line, for instance mainly tangential on one side and mainly homeotropic on the other side in the case of a $+1/2$ defect. A $+1/2$ defect in the centre of the drop, shown in Figure 4.4 (c), creates unidirectional flow in the bulk, as expected from its self-propelling nature, see Section 3.4. A $-1/2$ defect, on the other hand leads to no net direction of the flow in the bulk due to its three-fold symmetry, as shown in Figure 4.4 (e), but might lead to interesting, triangular spreading along the directions of the three splay-dominated regions.

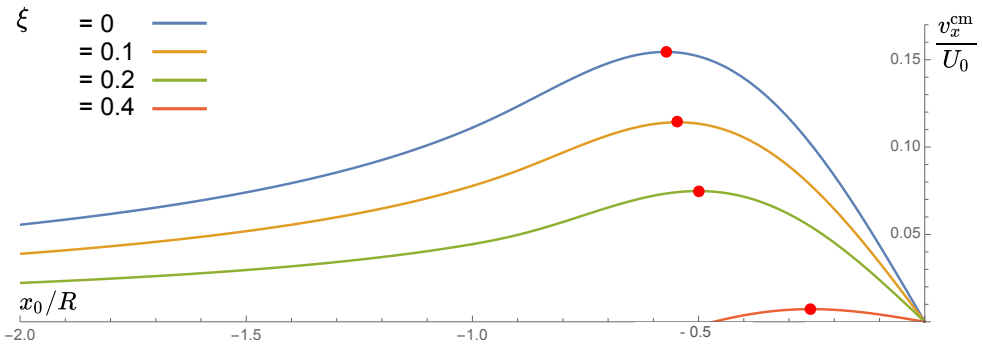

Figure 4.5: Centre-of-mass velocity as given by (4.15) for different values of friction and different positions of an aster defect in, or outside of, a contractile drop, like in Figure 4.3. The velocity only has an x-component in this case ($\alpha_0 = 0$), whose maxima (red dots) are indicated. A vortex defect in an extensile drop would produce the same plot. A no-slip boundary yields the highest maximum velocity in the direction away from the defect and for large enough slip, $\xi \gtrsim 0.4$, the drop comes to a halt. Maximal propulsion speeds are achieved with the defect being placed asymmetrically in the interior of the drop, $|x_0| < R$. Parameters are $R = 0$, $h_0 = 0.1$, $\sigma_0 = -1$.

4.3. Velocity of a moving drop

To determine whether strongly directed in-plane flows in the bulk of the drop, like those in Figure 4.2 (f) or 4.3 (f), will displace the drop as a whole we introduce the centre-of-mass velocity

$$\boldsymbol{v}^{\mathrm{cm}} = \frac{1}{V_0}\int_{\mathrm{drop}} \boldsymbol{u}_\perp \,\mathrm{d}V = \frac{1}{V_0}\int_{\mathrm{base}} \bar{\boldsymbol{u}}_\perp \,\mathrm{d}x\,\mathrm{d}y\,, \tag{4.12}$$

where $V_0 = \pi h_0 R^2/2$ is the volume of the drop in the partial wetting regime. The integral only contains the tangential flow, as the vertical flow component cannot lead to propulsion, only to deformations of the upper interface.

We consider a $+1$ defect located at $(x_0, 0)$, where the exact position of the defect might originate from an active symmetry breaking mechanism [Tjhung et al., 2012] or be induced by some given anchoring conditions along the contact line. Using expression (3.46), write the complexified version of (4.12) as

$$v^{\mathrm{cm}} = \frac{1}{V_0}\int_0^R \mathrm{d}r\, r h^2(r)\left(\frac{h(r)}{3} - \xi\right)\int_0^{2\pi} \mathrm{d}\phi\, f^a(r,\phi) \tag{4.13}$$

with the complexified active force f^a introduced in (3.57) taking the form

$$f^a = -\sigma_0\left(\frac{e^{i2\alpha_0}}{\bar{z}-x_0} - \frac{e^{i2\alpha_0}}{R^2-r^2}\frac{\bar{z}(z-x_0)}{\bar{z}-x_0} - \frac{z}{R^2-r^2}\right). \tag{4.14}$$

The ϕ-integral in (4.13) can be solved by transforming it into a complex contour

integral over the unit circle γ, with $w = e^{i\phi}$,

$$\int_0^{2\pi} \mathrm{d}\phi\, f^a(r,\phi) = -\frac{\sigma_0}{i}\int_\gamma \mathrm{d}w \left(-\frac{e^{i2\alpha_0}}{x_0(w - r/x_0)} + \frac{r^2 e^{i2\alpha_0}}{x_0(R^2 - r^2)}\frac{w - x_0/r}{w(w - r/x_0)} - \frac{r}{R^2 - r^2}\right),$$

which after calculating the residues yields the final result

$$\boldsymbol{v}^{\mathrm{cm}} = |\boldsymbol{v}^{\mathrm{cm}}|\left(\cos(2\alpha_0)\hat{\boldsymbol{e}}_x + \sin(2\alpha_0)\hat{\boldsymbol{e}}_y\right), \tag{4.15}$$

$$|\boldsymbol{v}^{\mathrm{cm}}| = \begin{cases} -\frac{\sigma_0}{9}\frac{h_0}{R}\frac{x_0}{R}\left((9\xi - 4h_0) + (6h_0 - 9\xi)\left(\frac{x_0}{R}\right)^2 + (3\xi - 4h_0)\left(\frac{x_0}{R}\right)^4 + h_0\left(\frac{x_0}{R}\right)^6\right) & \text{if } |x_0| < R, \\ \frac{\sigma_0}{9}\frac{h_0}{x_0}\left(h_0 - 3\xi\right) & \text{if } |x_0| > R. \end{cases}$$

For an aster or vortex the velocity only has an x-component, which we plot for different values of friction and defect positions for the exemplary spherical cap in Figure 4.5. The drop propels in the direction opposite to the location of the defect, as expected. The highest speeds are achieved for a no-slip boundary, whereas the drop slows down and can come to a halt when the amount of slip is sufficient, here at $\xi/h_0 \approx 0.4$. Furthermore, the dependence on the friction coefficient is linear in (4.15). Interestingly, there is an optimal defect position that maximises the magnitude of the propulsion speed. In units of R, this optimal position depends only on h_0 and ξ, but it is not instructive to show the expression here. Speed maxima marked in Figure 4.5 indicate that, for large friction, it moves toward the drop centre as the friction decreases. In the no-slip case maximal speed is achieved if the defect is approximately half-way between the boundary and the centre of the drop. Exactly the same plot as in Figure 4.5 holds for a vortex defect in an extensile drop. For any spiral defect, $\alpha_0 \neq 0, \pi/2$, the centre-of-mass velocity acquires a non-zero y-component, which is maximised for a perfect spiral.

If the director distortions in the drop are non-singular, $|x_0| > R$, the much simpler form of the speed (4.15) reveals that h_0 is the only relevant geometric length scale for the drop propulsion in this case. Moreover, the speed now has a simple linear dependence on $1/x_0$, which can be seen as a measure of the splay or bend of the director in the drop.

The effect of friction on the speed can be explained as follows. The amount of slip at the rigid surface, which is represented here by the effective friction parameter ξ, controls how strong the rotational component of the bulk flow is. We illustrate this on the example of the splayed orientation field from Figure 4.2 (b), where an aster defect is located on the contact line. For a no-slip boundary ($\xi = 0$) the flow vanishes at the base and, at finite height, is directed away from the defect in a mostly laminar way in the bulk of the drop. For small slip (Figure 4.6(a)) a thin treadmilling layer emerges close to the base, on top of which the flow is still laminar. Friction with the substrate

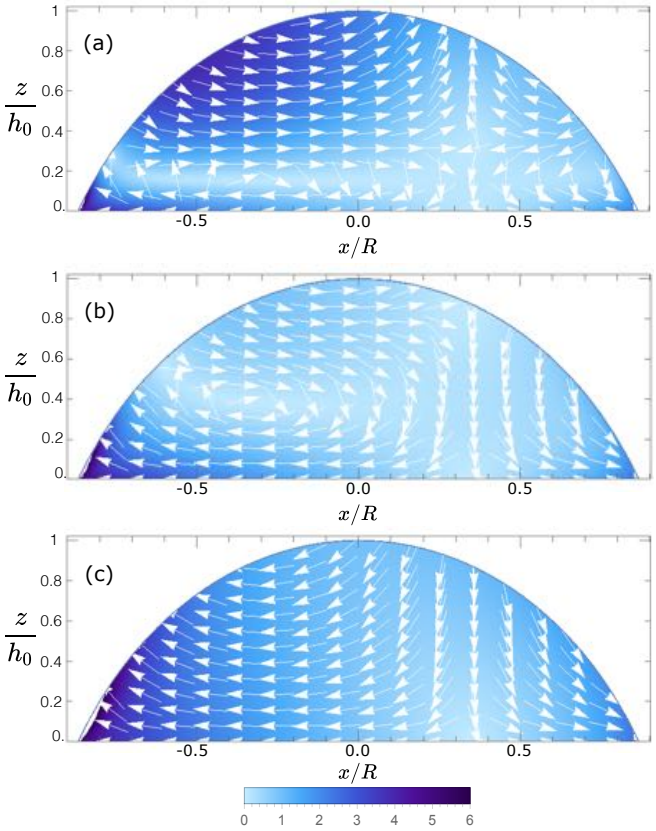

Figure 4.6: Plot of the flow components (u_x, u_z) for $y = 0$, given by (4.9) and (4.10), for the splayed polarisation field in Figure 4.2 (b) in a contractile drop ($\sigma_0 = -1$). In this side view the defect is located in the left corner. The slip increases from (a) to (c), $\xi = 0.07, 0.15, 1.5$. The colour-coded magnitude of the flow corresponds to (c) and scales in the same way as ξ for (a) and (b).

induces a shear flow that opposes the flow generated by active stresses. For finite slip this creates a vortex in the fluid that moves upwards and spans a larger region of the drop with increasing slip (Figure 4.6(b)).

This behaviour is apparent from the role of the friction parameter in the z-dependent prefactor of the flow (4.9), which is bounded from below and above by

$$h\left(\xi - \frac{h}{2}\right) \leq \frac{z^2}{2} + h\,(\xi - z) \leq h\xi\ . \tag{4.16}$$

While the upper bound is $h\xi \geq 0$, the lower bound becomes negative in those regions of the drop where

$$\xi < \frac{h}{2}\ . \tag{4.17}$$

Both horizontal flow components u_x and u_y then change sign at a height $z_0(x, y) = h - \sqrt{h(h - 2\xi)}$. For high enough friction condition (4.17) is satisfied in the bulk of

the drop and the flow is rotational. Since in dimensionless variables $h \approx 1$, friction $\xi \approx 0.4$ at which the speed of the drop vanishes in Figure 4.5 roughly coincides with the threshold in (4.17).

4.4. Steady state shapes

So far we have only considered instantaneous active flows and drop speeds that will arise from these flows in a drop having the shape of a flat spherical cap. The condition of free tangential stress at the upper bounding surface means that it is free to deform in response to the active flows pushing against it. First, we look for steady state solutions of the height evolution equation (3.48) for specific defect configurations. In the steady state the shape adjusts in a way that the imposed $\boldsymbol{n}$ does not induce any further deformations.

4.4.1. Axisymmetric drops

Consider an axisymmetric drop with one defect of strength +1 and variable phase α_0. This situation is most conveniently described in cylindrical coordinates (r, ϕ, z). While a director with one defect of strength m is given by the angle (2.20) in Cartesian coordinates, its polar representation is

$$\boldsymbol{n} = \cos\left((m-1)\,\phi + \alpha_0\right)\hat{\boldsymbol{e}}_r + \sin\left((m-1)\,\phi + \alpha_0\right)\hat{\boldsymbol{e}}_\phi, \tag{4.18}$$

which for $m = 1$ becomes $\boldsymbol{n} = \cos(\alpha_0)\hat{\boldsymbol{e}}_r + \sin(\alpha_0)\hat{\boldsymbol{e}}_\phi$. Due to axial symmetry $h = h(r)$ and the active force (3.29) becomes

$$\boldsymbol{f}^a = -\sigma_0 \left\{ \hat{\boldsymbol{e}}_r \left(\frac{\cos(2\alpha_0)}{r} + \cos^2(\alpha_0)\frac{\partial_r h}{h} \right) + \hat{\boldsymbol{e}}_\phi \left(\frac{\sin(2\alpha_0)}{r} + \frac{\sin(2\alpha_0)}{r}\frac{\partial_r h}{h} \right) \right\}. \tag{4.19}$$

We focus on the radial component, because the azimuthal component does not affect an axially symmetric shape. The $\sim 1/r$ contribution comes from the defect and changes sign at $\alpha_0 = \pi/4$, since a perfect spiral produces purely azimuthal flow. Thus, the presence of the +1 defect should result in thickening or thinning of the drop at its location depending on the director geometry and the sign of the activity. On the other hand, the contribution from splay in the z-direction, $\sim \partial_r h$, vanishes for a vortex defect ($\alpha_0 = \pi/2$). For instance, for the special cases of aster, perfect spiral,

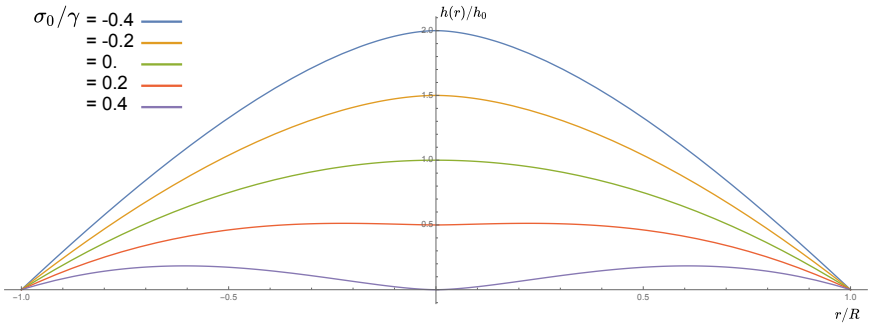

Figure 4.7: Stationary shapes of an active droplet with a vortex defect at the centre, given by (4.24). Extensile activity ($\sigma_0/\gamma > 0$) reduces the height at the defect location, leading to a non-monotonic shape. Contractile activity ($\sigma_0/\gamma < 0$) has the opposite effect and the shape stays monotonic. For $\sigma_0/\gamma = 0$ the equilibrium spherical cap is recovered. Parameters are $R = 1$, $h_0 = 0.1$. Only the cross section of the three-dimensional, axially symmetric shape is shown.

and vortex defect we have

$$f_r^a = \begin{cases} -\sigma_0 \left(\frac{1}{r} + \frac{\partial_r h}{h}\right) & \text{if} \quad \alpha_0 = 0\,(\text{aster}), \\ -\frac{\sigma_0}{2}\frac{\partial_r h}{h} & \text{if} \quad \alpha_0 = \pi/4\,(\text{spiral}), \\ \frac{\sigma_0}{r} & \text{if} \quad \alpha_0 = \pi/2\,(\text{vortex}). \end{cases} \tag{4.20}$$

In summary, the time evolution equation of the shape for this axisymmetric case becomes

$$\partial_t h = \frac{1}{r}\partial_r \left(r h^2 \left(\frac{h}{3} - \xi\right) \left(\gamma \left(\partial_r^3 h + \frac{\partial_r^2 h}{r} - \frac{\partial_r h}{r^2} \right) - \sigma_0 \left(\frac{\cos(2\alpha_0)}{r} + \cos^2(\alpha_0) \frac{\partial_r h}{h} \right) \right) \right). \tag{4.21}$$

Due to the non-linearity of the shape-coupling term an analytical form for a stationary solution to this equation can be found only in specific cases. Note, that in the case of an unbounded film and finite slip a trivial solution to $\partial_t h = 0$ is a film of constant thickness $h \equiv 3\xi$ for any form of director. Considering the results of Section 4.3, in this solution the cross-sectional flow presumably consists of convection cells that take up any vertical flow component that the director might produce, analogously to the rotational flow in Figure 4.6 (b). Another unbounded solution is $h \equiv 0$, which corresponds to the wetting limit where the film spreads over the substrate to infinity and its thickness approaches zero.

4.4.2. Vortex defect

First, we revisit a drop with a vortex defect ($\alpha_0 = \pi/2$), which was discussed in Reference [Joanny and Ramaswamy, 2012]. This configuration corresponds to Figure 4.3

(d) and (h). With a no-slip boundary, the equation for the steady state reads

$$0 = \partial_r \left(r \frac{h^3}{3} \left(\gamma \left(\partial_r^3 h + \frac{\partial_r^2 h}{r} - \frac{\partial_r h}{r^2} \right) + \frac{\sigma_0}{r} \right) \right). \tag{4.22}$$

This can be reduced to

$$\frac{\gamma}{\sigma_0} \left(\partial_r^3 h + \frac{\partial_r^2 h}{r} - \frac{\partial_r h}{r^2} \right) = -\frac{1}{r}, \tag{4.23}$$

for which a solution of the form

$$h(r) = \left(R^2 - r^2\right) \left(\frac{h_0}{R^2} - \frac{\sigma_0}{4\gamma} \right) - \frac{\sigma_0}{4\gamma} r^2 \ln(r/R) \tag{4.24}$$

can be obtained using the replacement $u = \partial_r h$ and the ansatz $u \sim r^k$. The constants are chosen such that for $\sigma_0 = 0$ the equilibrium shape (4.6) is recovered and terms $\sim \ln(r)$ vanish. The ratio σ_0/γ is the defining parameter and (4.24) is evaluated for different values of it in Figure 4.7. For extensile activity ($\sigma_0/\gamma > 0$) the shape becomes non-monotonic, as shown in Reference [Joanny and Ramaswamy, 2012], since the defect acts as a flow source that pushes fluid away from its location. The height of the droplet at the origin is

$$h(0) = h_0 - \frac{R^2 \sigma_0}{4\gamma}, \tag{4.25}$$

which shows that it can vanish and one such example is shown in Figure 4.7 for $\sigma_0/\gamma = 0.4$. This case was not mentioned in Reference [Joanny and Ramaswamy, 2012]. In principle, the height $h(0)$ can even become negative, for instance if $\sigma_0 > 4h_0\gamma/R^2$. This might indicate that active droplets with defects could rupture at the centre. The rupture might be similar to a dewetting transition [De Gennes et al., 2003]. Moreover, $\partial_r h(0) = 0$, so the contact angle is vanishing when the upper interface touches the substrate in Figure 4.7. On the contrary, contractile activity ($\sigma_0/\gamma < 0$) drives fluid in towards the defect, so the thickness of the drop increases at the centre.

4.4.3. Spiral defect

For a range of spiral defects a stationary shape can be obtained in the limit of negligible surface tension, $\gamma/\sigma_0 \approx 0$. In this limit the stationary version of equation (4.21) can be written as

$$0 = -\frac{\sigma_0}{r} \partial_r \left(r h^2 \left(\frac{h}{3} - \xi \right) \left(\frac{\cos(2\alpha_0)}{r} + \cos(\alpha_0)^2 \frac{\partial_r h}{h} \right) \right) \tag{4.26}$$

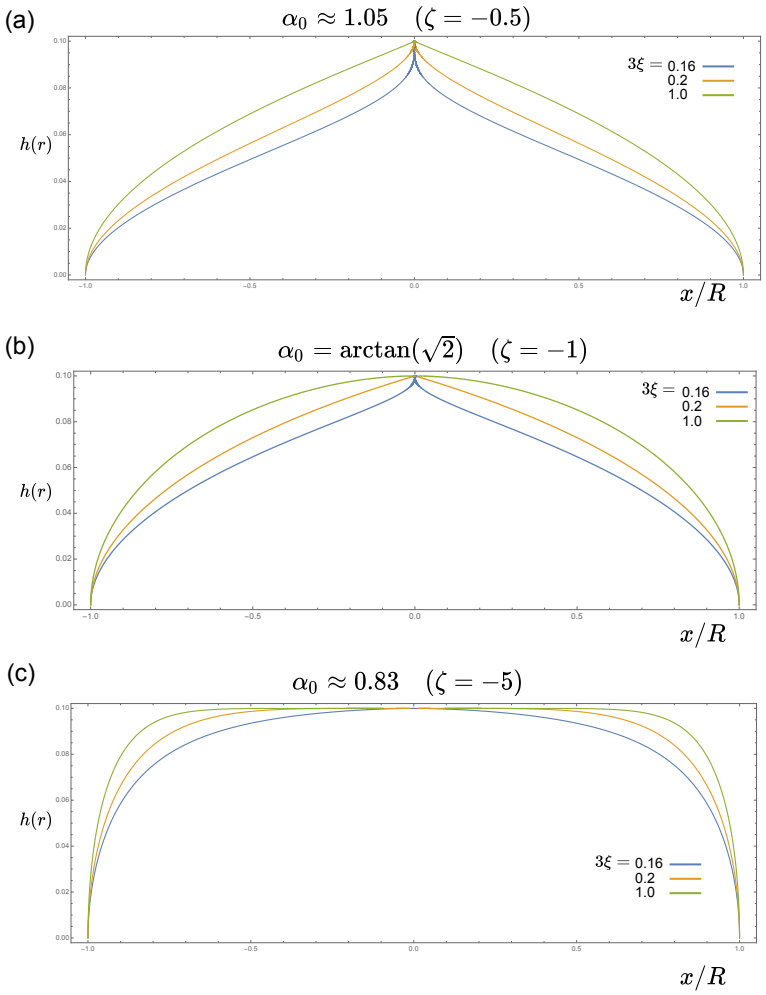

Figure 4.8: Stationary shapes for an active droplet with a spiral defect at the centre, for different phases in the range $\alpha_0 \in (\pi/4, \pi 2)$. Plotted are numerical solutions to the implicit equation (4.36) for the phase values (a) $\alpha_0 \approx 1.05$, (b) $\alpha_0 = \arctan(\sqrt{2}) \approx 0.95$, (c) $\alpha_0 \approx 0.83$. Further, the parameters $R = 1$, $h_0 = 0.1$ and different friction coefficients satisfying $3\xi > 3h_0/2$ are used.

or equivalently

$$0 = \partial_r \left(h \left(h - 3\xi \right) \left(h + \zeta r \partial_r h \right) \right), \tag{4.27}$$

where we have defined $\zeta = \cos(\alpha_0)^2 / \cos(2\alpha_0)$. Here, finite slip, $\xi > 0$, is required to regularise the shape at the origin. A first integration of equation (4.27) yields

$$h(h - 3\xi)(h + \zeta r \partial_r h) = c_0, \tag{4.28}$$

where the constant is the left-hand-side evaluated at $r = 0$,

$$c_0 = h_0^2 (h_0 - 3\xi) \tag{4.29}$$

and we have imposed a finite height at the origin, $h(0) = h_0$. A separation of variables in equation (4.28) and a second integration yield

$$-\frac{1}{\zeta}\ln(R/r) = \int_r^R \frac{\mathrm{d}r}{r} = \int_{h(r)}^0 \frac{h(h-3\xi)}{h^2(h-3\xi) - h_0^2(h_0-3\xi)}\,\mathrm{d}h \tag{4.30}$$

To integrate the right-hand-side of (4.30) we want to decompose the integrand into partial fractions,

$$\frac{h(h-3\xi)}{h^2(h-3\xi) - h_0^2(h_0-3\xi)} = \frac{A}{h-h0} + \frac{B}{h-h_1} + \frac{C}{h-h_2} \tag{4.31}$$

with $h_{1/2}$ being solutions to $(h-h_1)(h-h_2) = h^2 + (h+h_0)(h_0-3\xi)$. Using the shorthand $a = 3\xi$, the solutions are

$$h_{1/2} = \frac{1}{2}\left(a - h_0 \pm \sqrt{(a-h_0)(a+3h_0)}\right). \tag{4.32}$$

By comparing the coefficients in equation (4.31) one obtains

$$A = -\frac{h_0(h_0-a)}{(h_1-h_0)(h_0-h_2)}, \tag{4.33}$$

$$B = \frac{h_1(h_1-a)}{(h_1-h_2)(h_1-h_0)}, \tag{4.34}$$

$$C = \frac{h_2(h_2-a)}{(h_2-h_1)(h_2-h_0)}. \tag{4.35}$$

Equation (4.30) can be integrated exactly to give an implicit equation for the solution $h(r)$ for the stationary shape of a drop of radius R and height h_0, which is given through

$$A\ln\left(\frac{h_0}{h_0-h(r)}\right) + B\ln\left(\frac{h_1}{h_1-h(r)}\right) + C\ln\left(\frac{h_2}{h_2-h(r)}\right) = \frac{1}{\zeta}\ln\left(\frac{r}{R}\right). \tag{4.36}$$

In order for all terms on the left-hand-side to be real the friction is required to satisfy $a = 3\xi > 3h_0/2$, which ensures both $h_{1/2} \in \mathbb{R}$ and $h_{1/2} > h_0 > h(r)$. This indicates a lower limit for the amount of slip required at the substrate to obtain a stationary shape in the case of a spiral defect.

Solutions to equation (4.36) with finite h_0 exist for $\zeta < 0$, corresponding to the range of phases $\alpha_0 \in (\pi/4, \pi/2)$. Cross sections of stationary drop shapes are plotted in Figure 4.8 for different values of α_0 and of the friction coefficient. The shapes are different from those obtained for a vortex defect in Section 4.4.2 regarding two main features. Firstly, activity generates a right angle at the contact line, $\theta_c = \pi$, which is

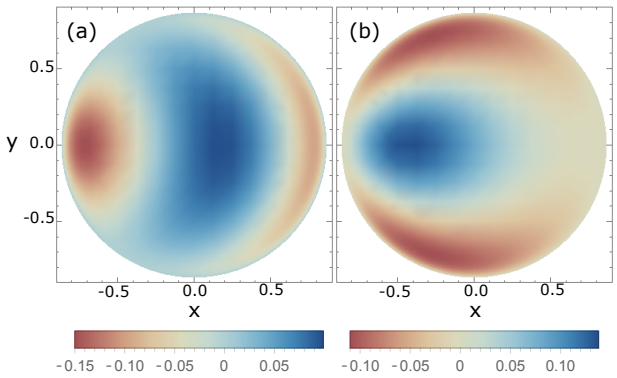

Figure 4.9: Shape deformation away from the spherical cap after a small time step Δt for a contractile drop with (a) splayed and (b) bent orientation field (see Figure 4.2 (a) and Figure 4.3 (a)) and a no-slip boundary.

also seen from

$$\partial_r h|_{r=R} = \lim_{r\to R}\left(-\frac{1}{\zeta r}\frac{h^2(h-a)-c_0}{h(h-a)}\right) = -\infty. \tag{4.37}$$

Further, in Figure 4.8 (a) and (b) the drop develops a cusp at the centre – a point at which $\partial_r h$ is discontinuous. It was not possible to obtain a closed form for $\partial_r h|_{r=0}$, but the discontinuity can be seen clearly for the bigger values of friction. The formation of a cusp is a new prediction for an active fluid, but is known from passive liquid crystal drops [de Gennes and Prost, 1995].

On the other hand, the choice of α_0 that is closest to a perfect spiral leads to shapes which are flat across the main part of the drop. This is reminiscent of the "flat pancake" shape that was obtained numerically by Joanny and Ramaswamy [2012] for small surface tension. Although this flat shape was associated to an axisymmetric drop with an aster defect, the defect itself was ignored in the calculation [Joanny and Ramaswamy, 2012]. Ignoring the defect, however, effectively describes the situation with a perfect spiral, for which the drop deforms only due to the active coupling to shape gradients, see equation (4.20). Therefore, the "flat pancake" represents the limiting case of our solution for $\alpha_0 \to \pi/4$, as Figure 4.8 (c) correctly suggests.

4.4.4. Asymmetric drops

For the asymmetric polarisation fields considered in Section 4.2.1 it is not possible to obtain an analytical result for the steady state. We can however qualitatively describe the deviation Δh from the initial spherical cap shape at time t_0 after a small time interval Δt if we plot $\Delta h \approx \partial_t h(t_0)\Delta t$ for a particular orientation field, see Figure 4.9. We consider a contractile drop a with no-slip boundary for this purpose. For a splayed orientation field as in Figure 4.2 (a) the instantaneous flow results in an increase in

height along a crescent-like area and a decrease to the front and back of it, as shown in Figure 4.9 (a). For a bent orientation field as in Figure 4.3 (a) the height grows in the rear of the drop and decreases along the sides, so we can expect the drop to become more slender. However, the changes in shape will alter the orientation field and thus the flow. To investigate the dynamics of the shape over longer time periods it would be necessary to perform numerical simulations with moving boundaries.

4.5. Discussion

We have derived exact expressions for the active flow field in and the resulting sliding velocity of a drop of a given shape and with a prescribed director profile. The flow structure turns out to be guided by both the familiar instabilities towards bend and splay in active systems [Simha and Ramaswamy, 2002a] and the coupling of the orientation to gradients in the height profile, which has previously been studied in the context of spreading of drops [Joanny and Ramaswamy, 2012]. The exact formula for the centre-of-mass velocity allows us to address a variety of aspects of drop motility in an analytical way. Our model reveals that asymmetric spatial variations in the orientation are key to enable drop propulsion and explains why friction at the substrate is essential. We also find that topological defects can both drive drop motility and also induce singular vertical flows that can lead to dramatic deformations of the free interface.

The high motility of the drop for an asymmetrically positioned aster defect is in qualitative agreement with three-dimensional active polar droplets observed in simulations [Tjhung et al., 2012], where an aster defect emerges spontaneously at high levels of activity. In simulations both the speed and the splay of the director increased with activity, but no data was shown for how this changes when the director becomes singular. It was reported that at a critical activity the defect reaches the centre of the drop and the drop comes to a halt, indicating that there also might be an optimal defect position and this would be interesting to compare with our results.

Whitfield et al. [2014] have calculated an analytical expression for the speed of a two-dimensional active droplet with imposed splay and we can compare it with our result for the case of a virtual aster defect, that is with expression (4.15) for $|x_0| > R$. We also get a linear dependence of the speed on the splay parameter and the activity. One difference is the way in which friction enters the model, due to the different propulsion mechanisms. In Reference [Whitfield et al., 2014] the droplet swims through a viscous medium, so the velocity vanishes in the no-slip limit. Here, the drop slides on a rigid substrate, which requires friction. Interestingly, equation (4.15) for $|x_0| > R$ does not include the lateral extension R of the drop, only its thickness h_0.

A recent numerical paper has studied the motility of polar active fluid droplets on

a substrate, but with a stronger focus on crawling cells, obtaining various biologically relevant shapes and motile steady states [Tjhung et al., 2015]. The computation included both actin treadmilling and a variable effective friction representing the focal adhesions as mechanisms that are crucial for cell motility on a substrate. The motile state with the morphology of a lamellipodium has striking similarity to the examples of splayed directors in Figure 4.2 regarding the active flow field, which also follows the splay of the director in Reference [Tjhung et al., 2015]. Another interesting parallel is the decrease of the sliding velocity of the drop with slip, which can be seen in Figure 1 of Reference [Tjhung et al., 2015], but is not commented upon. We think that this observation could be captured by the same mechanism that we describe in Section 4.3, in particular because the cross section of the flow shown in Supplementary Figure 3 of Reference [Tjhung et al., 2015] reveals a similar, rotational flow structure like we get for small values of slip, see Figure 4.6 (a). It is important to note that treadmilling was not necessary for the motion of the drop in the numerical model, but it was crucial for generating cell-specific shapes.

The backward flow at the leading edge in Figure 4.6(a) (see Figure 4.2(f) for top view) is a result of the strong tangential anchoring of filaments to both bounding surfaces, which splays the filaments vertically. This flow enhances spreading of fore-aft symmetric active droplets [Joanny and Ramaswamy, 2012], but in the case of a strong directed bulk flow driven by horizontal variations in the orientation, as in Figure 4.6, it can turn into a backflow on one side and counteract drop propulsion. There are two ways in which our model could be modified to eliminate this backflow at the leading edge. Firstly, one could locally remove the tangential anchoring condition in a region opposite the defect and with it the source of the backflow. Secondly, we expect that including self-propulsion of the filaments along their direction of orientation, which is the simplest way to model actin treadmilling [Tjhung et al., 2012, 2015], would enhance the bulk flow and compensate the backflow flow at the frontal boundary.

Our choice of tangential anchoring at the bounding surfaces of the drop is motivated by experiments where active filaments tend to adhere to the interface of an emulsion droplet [Sanchez et al., 2013; Keber et al., 2014]. In the lamellipodia of crawling cells actin filaments also lie tangential to the substrate, but push perpendicularly against the leading edge [Yam et al., 2007]. Homeotropic alignment at the upper part of the interface, which is typical for passive nematic films [Poulard et al., 2006], is unlikely for long cytoskeletal filaments in the thin geometry of a droplet on a surface, but is observed in situations with shorter active particles like bacteria [Drescher et al., 2016]. Alternatively, the orientation may be free to point in any direction at the contact line. This would allow the defect to change its position and would add another degree of freedom, which we have chosen to ignore here.

The cusped shapes we obtain for drops with a spiral defect are reminiscent of the free interface of thin passive nematic films, which can also acquire cusps or dips associated with unit strength point defects [de Gennes and Prost, 1995; De Gennes and de Gennes, 1970; Meyer, 1972]. In these thin films or droplets the anchoring is tangential at the free surface, but normal at the other surface. Applying a magnetic field then generates point defects and cusps on the interface. In the passive case the cusps arise from a balance of surface tension and nematic elasticity in the magnetic field [De Gennes and de Gennes, 1970]. On the contrary, in our model the cusped shapes are generated by activity and slip at the substrate, in the limit of negligible surface tension and nematic elasticity. Further, the anchoring conditions used here also differ from those of the passive nematics.

CHAPTER 5

Spherical shell of active fluid

In their recent experiments Keber et al. [2014] have realised an ALC in a new type of geometry – a closed, curved surface. Specifically, in the spherical geometry of the experiment a prominent observation was the oscillatory dynamics of four $+1/2$ defects, which was captured by a minimal model with four self-propelled particles. A variety of other states was observed, like vesicle deformations, two vortex defects in smaller spherical vesicles and two aster defects in spindle-like vesicles. Most aspects of this geometry are not yet understood, for instance the structure of the active flows underlying the defect motion, which we study in this Chapter. We also make predictions for other types and configurations of defects in spherical shells of ALC.

In analogy to the planar model of Chapter 3, we formulate a spherical version of a thin film of ALC with one free boundary. It is shown that an equilibrium nematic director on a sphere can be parametrised in the same way as in the plane, whereby on the sphere defects are unavoidable. This is done by using stereographic projection from the sphere to the complex plane. Locally, the hydrodynamic model is like a planar thin film, but topology imposes constraints on the global structure of the active flow, which then typically acquires two counterrotating flow vortices. An expansion of the active flow at defects in powers of the distance from the defect reveals that to leading order the flow singularities coincide with those of Chapter 3. The subleading order term allows to quantify the advection of $+1$ defects. The global structure of the instantaneous active flow in the shell is discussed for examples of different defect configurations.

The director dynamics is assumed to be dominated by the motion of defects, which corresponds to a fast reorientation of the director into its equilibrium for given defect positions and was argued to represent well the dynamics of the MT-based active nematic [Keber et al., 2014]. A system of overdamped dynamical equations for a collection of defects on the sphere, which move due to active advection and elastic interactions, are formulated and solved numerically. The dynamics of four $+1/2$ defects, two $+1$ defects, and four $+1/2$ defects with additional $\pm 1/2$ pairs are

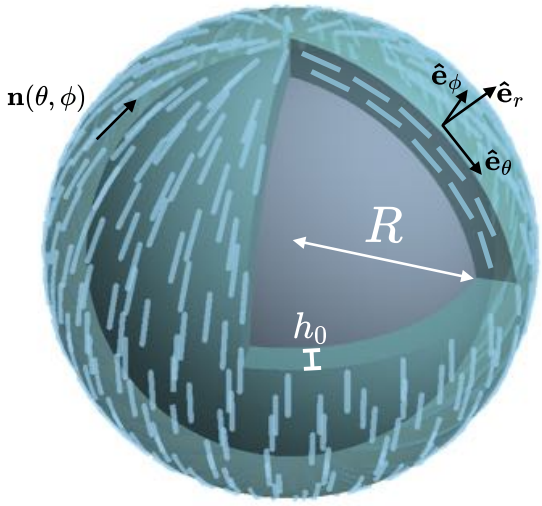

Figure 5.1: Schematic view of the spherical shell of active liquid crystal with inner radius R and thickness h_0. The inner shell is no-slip and the outer interface is free to deform, analogously to the planar setup of Chapter 3. The director $\boldsymbol{n}(\theta,\phi)$ is taken to be tangential to the inner sphere everywhere throughout the shell. The spherical orthonormal basis is indicated.

simulated in this way. For four half-defects we also perform a linear stability analysis to characterise the transition from the static to the dynamic regime. Finally, we estimate the speed of the shape changes of the initially spherical shell that may accompany the defect dynamics.

5.1. Thin film approximation on the sphere

We consider a thin layer of ALC coating a no-slip, rigid sphere and having a shear-free, deformable outer interface. The setup is illustrated in Figure 5.1. We work in standard spherical coordinates (r,θ,ϕ), $\theta\in[0,\pi]$, $\phi\in[0,2\pi)$, and the corresponding orthonormal basis $\{\hat{\boldsymbol{e}}_r,\hat{\boldsymbol{e}}_\theta,\hat{\boldsymbol{e}}_\phi\}$. When convenient, we will use the non-unit orthogonal basis vectors $\boldsymbol{e}_\theta = R\hat{\boldsymbol{e}}_\theta$ and $\boldsymbol{e}_\phi = R\sin\theta\hat{\boldsymbol{e}}_\phi$, specifically in Section 5.2.

Initially, both confining surfaces of the shell are taken to be spherical. The director is tangential to the spherical surfaces everywhere throughout the thickness of the shell,

$$\boldsymbol{P}(\boldsymbol{r}) = \cos\psi(\theta,\phi)\hat{\boldsymbol{e}}_\theta + \sin\psi(\theta,\phi)\hat{\boldsymbol{e}}_\phi\,. \tag{5.1}$$

As a simplification we assume that in the presence of small deviations of the free surface away from a spherical shape the director is still given by expression (5.1). As explained in Section 2.4.2 such a director has to have defects. The parametrisation of equilibrium nematic directors on a sphere is postponed to Section 5.2.

The instantaneous flow in the active nematic shell with a given configuration of

defects is found as the solution of the Stokes equation driven by the active stress tensor $\boldsymbol{\sigma}^a = -\sigma_0 \left(\boldsymbol{PP} - \frac{1}{3}\mathbf{I}\right)$. With the flow field $\boldsymbol{u} = (u_r, u_\theta, u_\phi)$ and the pressure $p(r, \theta, \phi)$ this takes the form [Batchelor, 1967]

$$0 = \partial_r p - \left(\nabla \cdot \boldsymbol{\sigma}^a\right)_r - \mu \left(\Delta u_r - \frac{2}{r^2 \sin\theta} \left(\partial_\theta \left(\sin\theta u_\theta\right) + \partial_\phi u_\phi\right) - \frac{2u_r}{r^2}\right) \tag{5.2}$$

$$0 = \frac{\partial_\theta p}{r} - \left(\nabla \cdot \boldsymbol{\sigma}^a\right)_\theta - \mu \left(\Delta u_\theta - \frac{1}{r^2 \sin^2\theta} \left(2\cos\theta \partial_\phi u_\phi + u_\theta\right) + \frac{2\partial_\theta u_r}{r^2}\right) \tag{5.3}$$

$$0 = \frac{\partial_\phi p}{r \sin\theta} - \left(\nabla \cdot \boldsymbol{\sigma}^a\right)_\phi - \mu \left(\Delta u_\phi + \frac{1}{r^2 \sin\theta} \left(2\partial_\phi u_r + \frac{2\cos\theta}{\sin\theta} \partial_\phi u_\theta - \frac{u_\phi}{\sin\theta}\right)\right) \tag{5.4}$$

with the spherical Laplacian operator having the form

$$\Delta f = \frac{1}{r^2} \partial_r \left(r^2 \partial_r f\right) + \frac{1}{r^2 \sin\theta} \partial_\theta \left(\sin\theta \partial_\theta f\right) + \frac{1}{r^2 \sin^2\theta} \partial_\phi^2 f \,.$$

The three-dimensional continuity equation reads

$$0 = \boldsymbol{\nabla \cdot u} = \frac{1}{r^2} \partial_r \left(r^2 u_r\right) + \frac{1}{r \sin\theta} \partial_\theta \left(\sin\theta u_\theta\right) + \frac{1}{r \sin\theta} \partial_\phi u_\phi \,. \tag{5.5}$$

We consider a spherical shell with a thickness h_0 that is much smaller than its inner radius R, as shown in Figure 5.1, and define the small parameter $\varepsilon = h_0/R \ll 1$. In the long-wavelength limit, flows in the polar and azimuthal directions are $\mathcal{O}(U_0)$, where $U_0 = R/T$ is the typical magnitude and T is the time scale of active flows. We define $\tilde{u}_\theta = u_\theta/U_0$ and $\tilde{u}_\phi = u_\theta/U_0$. Partial derivatives in these directions are independent of ε,

$$\frac{\partial}{\partial\theta}, \frac{\partial}{\partial\phi} \sim \mathcal{O}(1),$$

as opposed to the in-plane derivatives in a planar thin film described in Chapter 2. A point within the shell has the radial position $r = R + r_s$, where $r_s \sim \mathcal{O}(h_0)$. Then

$$\frac{r}{R} = 1 + \frac{r_s}{R} = 1 + \frac{h_0}{R}\frac{r_s}{h_0} = 1 + \varepsilon \tilde{r}_s \,, \tag{5.6}$$

where we have introduced the dimensionless variable $\tilde{r}_s \sim \mathcal{O}(1)$ that measures the radial position within the shell in units of h_0, $\tilde{r}_s \in [0, 1]$. We have

$$\tilde{r}_s = \frac{1}{\varepsilon}\left(\frac{r}{R} - 1\right) , \tag{5.7}$$

so that $\partial\tilde{r}_s/\partial r = 1/\varepsilon R = 1/h_0$ and for some function $f(r)$ the partial derivative in the radial direction transforms as

$$\frac{\partial f}{\partial r} = \frac{1}{h_0}\frac{\partial f}{\partial \tilde{r}_s} \tag{5.8}$$

The scale of the radial flow component can be inferred from ensuring that all terms in the continuity equation are of the same magnitude, or by realising that the length scale of this flow is h_0, so that the dimensionless flow component is $\tilde{u}_r = u_r/\varepsilon U_0$. Any radial component to the flow in the shell is thus a factor of ε smaller compared to tangential flows. These radial flows, though small, are important, in particular for the motion of defects and for the ability of the shell to propel itself through a passive fluid, which will be considered in Chapter 6.

Separation of length scales

Writing the equations (5.2)-(5.4) in a dimensionless form, using the above scalings, allows to identify the leading order terms in ε, like we have done for a planar film in Section 3.2.3. In view of this approximation, we replace factors of r and $1/r$ with R and $1/R$, respectively. First, the Laplacian term in the radial component (5.2) becomes

$$\frac{R^2}{\varepsilon U_0}\Delta u_r = \frac{1}{\varepsilon^2}\partial_{\tilde{r}_s}^2 \tilde{u}_r + \frac{1}{\sin\theta}\partial_\theta\left(\sin\theta\partial_\theta\tilde{u}_r\right) + \frac{1}{\sin^2\theta}\partial_\phi\tilde{u}_r\,. \tag{5.9}$$

In the tangential flow components we have

$$\frac{R^2}{U_0}\Delta u_\theta = \frac{1}{\varepsilon^2}\partial_{\tilde{r}_s}^2 \tilde{u}_\theta + \frac{1}{\sin\theta}\partial_\theta\left(\sin\theta\partial_\theta\tilde{u}_\theta\right) + \frac{1}{\sin^2\theta}\partial_\phi\tilde{u}_\theta\,, \tag{5.10}$$

$$\frac{R^2}{U_0}\Delta u_\phi = \frac{1}{\varepsilon^2}\partial_{\tilde{r}_s}^2 \tilde{u}_\phi + \frac{1}{\sin\theta}\partial_\theta\left(\sin\theta\partial_\theta\tilde{u}_\phi\right) + \frac{1}{\sin^2\theta}\partial_\phi\tilde{u}_\phi\,. \tag{5.11}$$

With the above, components (5.3) and (5.4) of the Stokes equation become

$$0 = -\frac{\varepsilon^2 R}{\mu U_0}\partial_\theta p + \frac{\varepsilon^2 R^2}{\mu U_0}\left(\nabla\cdot\boldsymbol{\sigma}^a\right)_\theta + \partial_{\tilde{r}_s}^2\tilde{u}_\theta + \mathcal{O}(\varepsilon^2) \tag{5.12}$$

$$0 = -\frac{\varepsilon^2 R}{\mu U_0}\frac{1}{\sin\theta}\partial_\phi p + \frac{\varepsilon^2 R^2}{\mu U_0}\left(\nabla\cdot\boldsymbol{\sigma}^a\right)_\phi + \partial_{\tilde{r}_s}^2\tilde{u}_\phi + \mathcal{O}(\varepsilon^2) \tag{5.13}$$

As before in Chapter 3, we require the components of the active stress divergence to be $\sim \mathcal{O}(1)$ to retain in the equations and be strong enough to drive a flow. For a polarisation field given by (5.1) we find that this divergence is of the form

$$\boldsymbol{\nabla}\cdot\boldsymbol{\sigma}^a = -\frac{\sigma_0}{R}\begin{pmatrix} 1 \\ -\sin(2\psi)\,\partial_\theta\psi + \frac{\cos(2\psi)}{\sin\theta}\left(\cos\theta + \partial_\phi\psi\right) \\ \cos(2\psi)\,\partial_\theta\psi + \frac{\sin(2\psi)}{\sin\theta}\left(\cos\theta + \partial_\phi\psi\right) \end{pmatrix}. \tag{5.14}$$

This results from the tensor divergence in spherical coordinates, which including only non-zero terms reads

$$\boldsymbol{\nabla}\cdot\boldsymbol{\sigma}^a = \left\{2\sigma^a_{rr} - (\sigma^a_{\theta\theta}+\sigma^a_{\phi\phi})\right\}\frac{\hat{\boldsymbol{e}}_r}{r} + \left\{\frac{\partial\sigma^a_{\theta\theta}}{\partial\theta} + \cot\theta\sigma^a_{\theta\theta} + \frac{1}{\sin\theta}\frac{\partial\sigma^a_{\phi\theta}}{\partial\phi} - \cot\theta\sigma^a_{\phi\phi}\right\}\frac{\hat{\boldsymbol{e}}_\theta}{r}$$
$$\left\{\frac{\partial\sigma^a_{\theta\phi}}{\partial\theta} + \frac{1}{\sin\theta}\frac{\partial\sigma^a_{\phi\phi}}{\partial\phi} + 2\cot\theta\sigma^a_{\theta\phi}\right\}\frac{\hat{\boldsymbol{e}}_\phi}{r}$$

and is given in full in Appendix B.1. To achieve the correct scaling in (5.12) and (5.13), the dimensionless pressure and activity constant are

$$\tilde{p} = \frac{\varepsilon^2 R}{\mu U_0}p \quad \text{and} \quad \tilde{\sigma}_0 = \frac{\varepsilon^2 R}{\mu U_0}\sigma_0\,, \tag{5.15}$$

which is equivalent to the planar thin film scalings (3.22) and (3.24), with L replaced by R. Then (5.12) and (5.13) become

$$0 = -\partial_\theta\tilde{p} - \tilde{\sigma}_0\left(-\sin(2\psi)\partial_\theta\psi + \frac{\cos(2\psi)}{\sin\theta}\left(\cos\theta + \partial_\phi\psi\right)\right) + \partial^2_{\tilde{r}_s}\tilde{u}_\theta, \tag{5.16}$$

$$0 = -\frac{1}{\sin\theta}\partial_\phi\tilde{p} - \tilde{\sigma}_0\left(\cos(2\psi)\partial_\theta\psi + \frac{\sin(2\psi)}{\sin\theta}\left(\cos\theta + \partial_\phi\psi\right)\right) + \partial^2_{\tilde{r}_s}\tilde{u}_\phi\,. \tag{5.17}$$

The r-component (5.2) reduces to $\partial_{\tilde{r}_s}\tilde{p} = 0$. The boundary condition equivalent to (3.37) for the normal stress at the outer interface is

$$-p|_{\tilde{r}_s=1} + \frac{\sigma_0}{3} + \mathcal{O}(\varepsilon^2) = \sigma_{rr} = -p_0 + \gamma H \tag{5.18}$$

given in dimensionless quantities. The mean curvature of the spherical boundary is

$$H = -\boldsymbol{\nabla}_s\cdot\hat{\boldsymbol{e}}_r = -\left(\hat{\boldsymbol{e}}_\theta\frac{\partial_\theta}{R} + \hat{\boldsymbol{e}}_\phi\frac{\partial_\phi}{R\sin\theta}\right)\cdot\hat{\boldsymbol{e}}_r = -\frac{2}{R}, \tag{5.19}$$

which yields a pressure that is to first approximation in ε constant throughout the shell,

$$p = p_0 + \frac{\sigma_0}{3} + \gamma\frac{2}{R}. \tag{5.20}$$

It therefore disappears from (5.16) and (5.17) and we obtain equations for $\tilde{u}_\theta$ and $\tilde{u}_\phi$, which are analogous to equation (3.30) for a planar thin film. This analogy means that for a thin enough spherical film the curvature is negligible locally, so it does not directly enter the expression for the flow. However, it globally determines the topology of the tangential flow through the underlying formulation of the equations in the spherical basis, in particular enforcing the presence of flow singularities.

We solve equations (5.16) and (5.17), with the constant pressure (5.20), for a

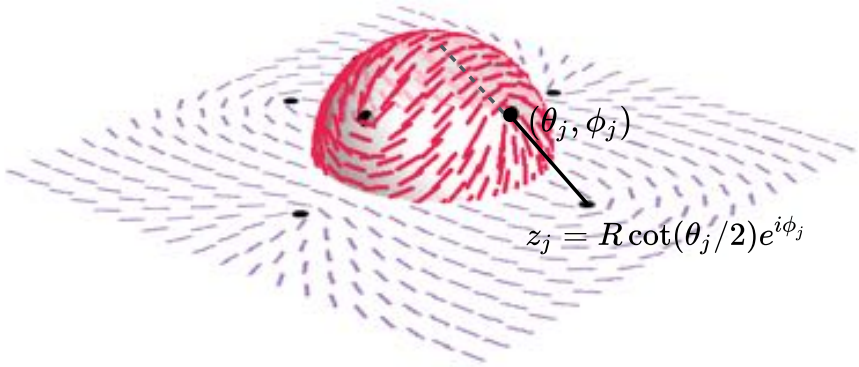

Figure 5.2: Illustration of the stereographic projection between the sphere and the complex plane on the example of a nematic director with four half-defects arranged equidistantly on a circle in the upper hemisphere. A defect on the sphere at position (θ_j, ϕ_j) corresponds to a defect in the plane at $z_j = R\cot(\theta_j/2)e^{i\phi_j}$. Here, the north pole of the sphere is chosen as the projection point and only the upper hemisphere is shown for clarity. The lower hemisphere is projected onto points inside the circle of radius R.

no-slip inner boundary and a shear-free outer boundary, that is

$$\partial_{\tilde{r}_s}\tilde{u}_\phi|_{\tilde{r}_s=1} = 0 \quad \text{and} \quad \tilde{u}_\phi|_{\tilde{r}_s=0} = 0\,, \tag{5.21}$$

and similar expressions for $\tilde{u}_\theta$. With these boundary conditions the tangential flow $\tilde{\boldsymbol{u}}_\perp = (\tilde{u}_\theta, \tilde{u}_\phi)$ becomes

$$\tilde{\boldsymbol{u}}_\perp(\tilde{r}_s, \theta, \phi) = \tilde{r}_s\left(\frac{\tilde{r}_s}{2} - 1\right)\tilde{\sigma}_0 \begin{pmatrix} -\sin(2\psi)\,\partial_\theta\psi + \frac{\cos(2\psi)}{\sin\theta}\,(\cos\theta + \partial_\phi\psi) \\ \cos(2\psi)\,\partial_\theta\psi + \frac{\sin(2\psi)}{\sin\theta}\,(\cos\theta + \partial_\phi\psi) \end{pmatrix}, \tag{5.22}$$

which is analogous to the planar result (3.45) with $\xi = 0$ and $h = 1$. The radial flow component can be obtained from the continuity equation (5.5),

$$\tilde{u}_r = -\int_0^{\tilde{r}_s}\left(\frac{1}{\sin\theta}\partial_\theta\left(\sin\theta\tilde{u}_\theta\right) + \frac{1}{\sin\theta}\partial_\phi\tilde{u}_\phi\right)\mathrm{d}\tilde{r}_s\,, \tag{5.23}$$

where we used $\tilde{u}_r(\tilde{r}_s = 0) = 0$.

5.2. Nematic director on a sphere

5.2.1. Nematic elasticity on a sphere

We follow the approach in [Ovrut and Thomas, 1991; Lubensky and Prost, 1992; Vitelli and Nelson, 2006] of finding expressions for the equilibrium nematic director on a sphere via stereographic projection to the complex plane. We work in the one-elastic-constant

approximation and begin by formulating equation (2.6) for the elastic energy in the local spherical basis. Consider a nematic director in the tangent plane of the sphere, expressed in the orthonormal basis as

$$\boldsymbol{n}(\boldsymbol{x}) = \cos(\alpha(\boldsymbol{x}))\hat{\boldsymbol{e}}_\theta + \sin(\alpha(\boldsymbol{x}))\hat{\boldsymbol{e}}_\phi\,, \tag{5.24}$$

where we have combined the two angular coordinates into the vector $\boldsymbol{x} = (x^1, x^2) = (\theta, \phi)$. The sphere is parametrised as $\boldsymbol{R}(\boldsymbol{x}) = R(\sin\theta\cos\phi, \sin\theta\sin\phi, \cos\theta)$. As explained in Section 2.4.2, we use the covariant derivative of α to write the elastic energy of such a director

$$E = \frac{K}{2}\int_0^{2\pi}\int_0^{\pi} \mathrm{d}\theta\,\mathrm{d}\phi\, R^2 \sin\theta(\boldsymbol{\nabla}\alpha - \boldsymbol{A})^2\,. \tag{5.25}$$

In the orthonormal basis the spin connection is $\boldsymbol{A} = \hat{\boldsymbol{e}}_\theta \cdot \boldsymbol{\nabla}\hat{\boldsymbol{e}}_\phi$, see Section 2.4.2. There is a natural correspondence between the surface of a sphere and the complex plane, which we will use to rewrite expression (5.25) in way that allows to find energy-minimising $\alpha(\theta, \phi)$ explicitly.

Stereographic projection

The stereographic projection [Needham, 1998] from a sphere of radius R to the complex plane, extended to include the point at infinity, is a conformal map

$$\varphi : \mathbb{S}^2 \to \mathbb{C}, \quad \begin{pmatrix} \theta \\ \phi \end{pmatrix} \mapsto \begin{pmatrix} z \\ \bar{z} \end{pmatrix} \quad \text{with} \quad z = z(\theta, \phi) = R\cot\left(\frac{\theta}{2}\right)e^{i\phi}\,. \tag{5.26}$$

Here, the projection is chosen such that the sphere's equator coincides with a circle of radius R centred at the origin in the complex plane and the north pole is the projection point, see Figure 5.2. Interpreted as a coordinate transformation, the map (5.26) provides a new set of coordinates to parametrise the spherical surface, $\boldsymbol{y} = (y^1, y^2) = (z, \bar{z})$. Some useful identities for working in stereographic coordinates are given in Appendix B.2. The inverse map φ^{-1} yields

$$\theta(z, \bar{z}) = 2\arctan(R/|z|) \quad \text{and} \quad \phi(z, \bar{z}) = \frac{1}{2i}\ln(z/\bar{z})\,. \tag{5.27}$$

The basis vectors in the new coordinates, given by $\boldsymbol{e}_k = \partial\boldsymbol{R}(\theta(\boldsymbol{y}), \phi(\boldsymbol{y}))/\partial y^k$, take the form

$$\boldsymbol{e}_z = \boldsymbol{e}_\theta\frac{\partial\theta}{\partial z} + \boldsymbol{e}_\phi\frac{\partial\phi}{\partial z} = \boldsymbol{e}_\theta\left(-\frac{R|z|}{|z|^2 + R^2}\frac{1}{z}\right) + \boldsymbol{e}_\phi\frac{1}{2iz} \tag{5.28}$$

and

$$\boldsymbol{e}_{\bar{z}} = \boldsymbol{e}_\theta \overline{\frac{\partial\theta}{\partial z}} + \boldsymbol{e}_\phi \overline{\frac{\partial\phi}{\partial z}} = \overline{\boldsymbol{e}_z}\,.$$

Note, that for any complex function $f(z,\bar{z})$ we have $\overline{\partial f/\partial z} = \partial\bar{f}/\partial\bar{z}$, which becomes $\partial f/\partial\bar{z}$ if f is real-valued. Using $\sin\theta = 2R|z|/(|z|^2+R^2)$, the corresponding metric tensor reads

$$\boldsymbol{g} = \frac{2}{\left(1+|z|^2/R^2\right)^2}\begin{pmatrix} 0 & 1 \\ 1 & 0 \end{pmatrix} \tag{5.29}$$

and $\sqrt{|\det \boldsymbol{g}|} = 2(1+|z|^2/R^2)^{-2}$. Under this metric the surface element in the complex plane is expressed as

$$\mathrm{d}S = \sqrt{|\det \boldsymbol{g}|}\mathrm{d}z\mathrm{d}\bar{z} = \frac{4R^2 r}{1+r^2/R^2}\mathrm{d}r\mathrm{d}\phi, \tag{5.30}$$

where (r,ϕ) are the standard polar coordinates in the plane. When projected onto the plane, infinitesimal distances on the sphere are stretched by the factor

$$\Lambda = \frac{1}{2}\left(1+\frac{|z|^2}{R^2}\right) = \frac{1}{1-\cos\theta}\,. \tag{5.31}$$

Elasticity in stereographic gauge

First, we express the covariant derivative of α in the stereographic coordinates $\boldsymbol{y}$, using the inverse metric tensor $g^{kl} = (\boldsymbol{g}^{-1})_{kl}$,

$$\begin{aligned}(\boldsymbol{\nabla}\alpha - \boldsymbol{A})^2 &= \left(\frac{\partial\alpha}{\partial y^k} - A_k\right)\left(\frac{\partial\alpha}{\partial y^l} - A_l\right)g^{kl} \\ &= 2g^{z\bar{z}}(\partial_z\alpha - A_z)(\partial_{\bar{z}}\alpha - A_{\bar{z}}) \\ &= (1+|z|^2/R^2)^2|\partial_z\alpha - A_z|^2\,,\end{aligned} \tag{5.32}$$

where Einstein summation is implied in the first line. Using $\cos\theta = (1-R^2/|z|^2)/(1+R^2/|z|^2)$, the components of the spin connection read

$$A_z = \hat{\boldsymbol{e}}_\theta \cdot \partial_z \hat{\boldsymbol{e}}_\phi = -\frac{1}{2iz}\frac{1-R^2/|z|^2}{1+R^2/|z|^2} = \overline{A_{\bar{z}}}\,. \tag{5.33}$$

In this stereographic gauge the total elastic energy (5.25) takes the form [Lubensky and Prost, 1992; Vitelli and Nelson, 2006]

$$E = K\int_{\mathbb{C}} \mathrm{d}z\,\mathrm{d}\bar{z}\,|\partial_z\alpha - A_z|^2\,. \tag{5.34}$$

The variation of this energy with respect to α is

$$\begin{aligned}\delta E &= K\int \mathrm{d}z\,\mathrm{d}\bar{z}\left\{(\partial_{\bar{z}}\alpha - A_{\bar{z}})\partial_z(\delta\alpha) + (\partial_z\alpha - A_z)\partial_{\bar{z}}(\delta\alpha)\right\}\\ &= -K\int \mathrm{d}z\,\mathrm{d}\bar{z}\left\{2\partial_{\bar{z}}\partial_z\alpha - \partial_z A_{\bar{z}} - \partial_{\bar{z}}A_z\right\}\delta\alpha\,,\end{aligned} \tag{5.35}$$

where

$$\partial_{\bar{z}}A_z = \partial_{\bar{z}}\left(-\frac{1}{2iz}\cos\theta\right) = \frac{1}{2iz}\sin\theta\left(-\frac{R|z|}{|z|^2+R^2}\frac{1}{\bar{z}}\right) = -\partial_z A_{\bar{z}}\,, \tag{5.36}$$

which removes the spin connection from (5.35). This leads to Laplace's equation in complex coordinates

$$\partial_{\bar{z}}\partial_z\alpha = 0\,, \tag{5.37}$$

for which we already know the form of the solutions with defects from Chapter 3, see equation (3.53),

$$\alpha(z,\bar{z}) = \sum_{j=1}^{n_{\mathrm{def}}} m_j\,\mathrm{Im}\{\ln(z-z_j)\}\,. \tag{5.38}$$

Finally, we have to ensure that the Poincaré-Hopf index theorem is satisfied, which yields a constraint on the number of defects, n_{def}, and their strengths, m_j. To get the counting right, first note that under our choice of stereographic projection a defect of strength m_j in $\alpha(z,\bar{z})$ contributes a winding number of $-m_j$ to the director on the sphere. Second, as discussed in [Lubensky and Prost, 1992], the limit $|z|\to\infty$ is projected onto the north pole, but in this limit $\alpha \approx \sum_{j=1}^{n_{\mathrm{def}}} m_j\,\mathrm{Im}\{\ln z\} = \phi\sum_{j=1}^{n_{\mathrm{def}}} m_j = 2\phi$. This contributes a winding of $+2$ at the north pole. The basis vectors $\hat{\boldsymbol{e}}_\theta$ and $\hat{\boldsymbol{e}}_\phi$ also add winding of $+1$ to both poles. In total, in addition to the defects whose locations are defined explicitly via (5.38), there is a defect of strength $+3$ at the north pole and a defect of strength $+1$ at the south pole.

5.2.2. Projection of planar director

To accommodate these additional windings we alter the angle in the following way. If $\alpha(z,\bar{z})$ is a solution of equation (5.37), then so is $\phi - \alpha(z,\bar{z})$, because

$$\partial_{\bar{z}}\partial_z(\phi-\alpha) = \partial_{\bar{z}}\partial_z\phi = \partial_{\bar{z}}\left(\frac{1}{2iz}\right) = 0\,. \tag{5.39}$$

With this angle, defects defined explicitly in (5.38) produce the correct strengths on the sphere, but now there is additional winding of -2 at the north pole. Adding ϕ contributes winding of -1 at the south pole and $+1$ at the north pole, such that after

taking into account the basis vectors the director becomes smooth at the poles.

Alternatively, this director angle can also be obtained simply by lifting a planar director onto a sphere, whose angle is a harmonic function in the complex plane and which has a total winding of +2. Here, it is more convenient to use the standard Cartesian coordinates of the complex plane $x = (z+\bar{z})/2$ and $y = (z-\bar{z})/2i$, such that the inverse map becomes $\theta(x,y) = 2\arctan\Big(R/\sqrt{x^2+y^2}\Big)$ and $\phi(x,y) = \arctan(y/x)$. Consider a vector field in the plane, $\boldsymbol{f}(\boldsymbol{x}) = f_x(\boldsymbol{x})\hat{\boldsymbol{e}}_x + f_y(\boldsymbol{x})\hat{\boldsymbol{e}}_y$, written in the complex representation as $f(x,y) = f_x(x,y) + if_y(x,y)$. Its projection onto the sphere is

$$\begin{aligned}
\boldsymbol{f}^s &= f_\theta \boldsymbol{e}_\theta + f_\phi \boldsymbol{e}_\phi && (5.40)\\
&= J_{\varphi^{-1}} \cdot (f_x, f_y) && (5.41)\\
&= -\frac{1-\cos\theta}{R}\left(f_x\cos\phi + f_y\sin\phi, \frac{1}{\sin\theta}\left(f_x\sin\phi - f_y\cos\phi\right)\right), && (5.42)
\end{aligned}$$

where we have used the Jacobian matrix of the inverse map,

$$J_{\varphi^{-1}} = \frac{1-\cos\theta}{R}\begin{pmatrix} -\cos\phi & -\sin\phi \\ -\frac{\sin\phi}{\sin\theta} & \frac{\cos\phi}{\sin\theta} \end{pmatrix}. \tag{5.43}$$

If we start with a unit vector field $\boldsymbol{f} = (\cos\alpha, \sin\alpha)$ in the plane, and also normalise its projection, we obtain

$$\hat{\boldsymbol{f}}^s = -\Big(\cos\big(\phi - \alpha(\theta,\phi)\big)\hat{\boldsymbol{e}}_\theta + \sin\big(\phi - \alpha(\theta,\phi)\big)\hat{\boldsymbol{e}}_\phi \Big), \tag{5.44}$$

now expressed in the orthonormal basis. When constructing a nematic director the sign of $\hat{\boldsymbol{f}}^s$ can be omitted, since $\boldsymbol{n} \sim -\boldsymbol{n}$.

5.2.3. Equilibrium director on the sphere

In summary, an equilibrium nematic director on the sphere with defects of strength m_j at locations (θ_j, ϕ_j) is given by

$$\boldsymbol{n}(\theta,\phi) = \cos\big(\phi - \alpha(\theta,\phi)\big)\hat{\boldsymbol{e}}_\theta + \sin\big(\phi - \alpha(\theta,\phi)\big)\hat{\boldsymbol{e}}_\phi \tag{5.45}$$

with

$$\alpha(\theta,\phi) = \alpha_0 + \sum_{j=1}^{n_{\mathrm{def}}} m_j \,\mathrm{Im}\big\{\ln\big(z(\theta,\phi) - z_j(\theta_j,\phi_j)\big)\big\}, \tag{5.46}$$

satisfying the topological requirement

$$\sum_{j=1}^{n_{\mathrm{def}}} m_j = 2\,. \tag{5.47}$$

This constraint means that on the sphere it is not possible to have defect-free nematic textures. We will use this fact to formulate the active hydrodynamic problem entirely in terms of the positions and topological strengths of the defects. One example of a director with four half-integer defects, all positioned on a circle in the upper hemisphere, and its projection in the complex plane are shown in Figure 5.2.

5.3. Active flow generated by defects

We use a director that is everywhere tangential to the spherical surfaces, such that

$$\boldsymbol{P}(\boldsymbol{r}) = \boldsymbol{P}(\theta,\phi) = \boldsymbol{n}(\theta,\phi) \tag{5.48}$$

for all $r \in [R, R+h_0]$, with the director $\boldsymbol{n}(\theta,\phi)$ given by (5.45)-(5.47). With

$$\psi(\theta,\phi) = \phi - \alpha(\theta,\phi), \tag{5.49}$$

the tangential active flow (5.22) becomes

$$\tilde{\boldsymbol{u}}_\perp = \tilde{\sigma}_0 f(\tilde{r}_s) \begin{pmatrix} \sin\left(2(\phi-\alpha)\right)\partial_\theta\alpha + \frac{\cos(2(\phi-\alpha))}{\sin\theta}\left(\cos\theta + 1 - \partial_\phi\alpha\right) \\ -\cos\left(2(\phi-\alpha)\right)\partial_\theta\alpha + \frac{\sin(2(\phi-\alpha))}{\sin\theta}\left(\cos\theta + 1 - \partial_\phi\alpha\right) \end{pmatrix}, \tag{5.50}$$

where we have abbreviated the $\tilde{r}_s$-dependent part by $f(\tilde{r}_s) = \tilde{r}_s(\tilde{r}_s/2 - 1)$.

5.3.1. Complex representation of the flow

For a constant $\tilde{r}_s$, the form of (5.50) suggests to write the flow in a complex representation. We formally define a local "complexified" flow on the sphere

$$u := \tilde{u}_\theta + i\tilde{u}_\phi\,, \tag{5.51}$$

which we want to express in terms of the variables z and $\bar{z}$, using stereographic projection (see Section 5.2.1). The function u is well-defined, because we can relate it to the projection of the spherical flow field onto the complex plane. The projected field, expressed in the complex form as $u_x + iu_y$, is related to the spherical one through

equation (5.42). In the orthonormal basis we have

$$(\tilde{u}_\theta, \tilde{u}_\phi) = -(1-\cos\theta)\Big(u_x\cos\phi + u_y\sin\phi, u_x\sin\phi - u_y\cos\phi\Big)\,. \tag{5.52}$$

Formally writing the complex representation of this field yields

$$\begin{aligned}\tilde{u}_\theta + i\tilde{u}_\phi &= -(1-\cos\theta)\left\{u_x(\cos\phi + i\sin\phi) + u_y(\sin\phi - i\cos\phi)\right\}\\ &= -(1-\cos\theta)e^{i\phi}(u_x - iu_y)\,,\end{aligned}$$

and through this relation u is indeed a well-defined function in z and $\bar{z}$. In complex representation, the projection of the flow onto the plane is accordingly $u_x + iu_y = -\bar{u}e^{i\phi}/(1-\cos\theta)$. To find the winding of the flow at certain points, we can work with u directly and use stereographic projections of loops on the sphere onto the plane for evaluation, provided they do not encircle the poles, that is the factor $e^{i\phi}$ does not contribute to the winding. However, to interpret the direction of the flow at certain points, we have to use $u_x + iu_y$.

As a first step, from equation (5.50) we find

$$\tilde{u}_\theta + i\tilde{u}_\phi = \tilde{\sigma}_0 f(\tilde{r}_s)e^{i2(\phi-\alpha)}\left\{-i\partial_\theta\alpha + \frac{1}{\sin\theta}(\cos\theta + 1 - \partial_\phi\alpha)\right\}. \tag{5.53}$$

In spherical coordinates, we use $A_j = \cot(\theta/2)\cos\phi - \cot(\theta_j/2)\cos\phi_j$ and $B_j = \cot(\theta/2)\sin\phi - \cot(\theta_j/2)\sin\phi_j$ to express the derivatives

$$\partial_\theta\alpha = -\frac{\cot(\theta/2)}{\sin\theta}\sum_{j=1}^{n_{\mathrm{def}}} m_j\frac{A_j\sin\phi - B_j\cos\phi}{A_j^2 + B_j^2}\,, \tag{5.54}$$

$$\partial_\phi\alpha = \cot(\theta/2)\sum_{j=1}^{n_{\mathrm{def}}} m_j\frac{A_j\cos\phi + B_j\sin\phi}{A_j^2 + B_j^2}\,. \tag{5.55}$$

After some algebraic manipulations we can rewrite (5.53) in terms of z and $\bar{z}$ as

$$u(z,\bar{z}) = \tilde{\sigma}_0 f(\tilde{r}_s)e^{-i2\alpha(z,\bar{z})}\left\{\frac{z^2}{R|z|} - \frac{z}{2}\left(\frac{R}{|z|} + \frac{|z|}{R}\right)\sum_{j=1}^{n_{\mathrm{def}}} m_j\frac{z - z_j}{|z - z_j|^2}\right\}, \tag{5.56}$$

where $\alpha(z,\bar{z})$ is given by (5.38) and we made use of the following relations

$$\begin{aligned} R^2(A_j^2+B_j^2) &= |z-z_j|^2\,, \\ R(A_j+iB_j) &= z-z_j\,, \\ \frac{1+\cos\theta}{\sin\theta} &= \cot\left(\theta/2\right) = \frac{|z|}{R}\,, \\ \text{and}\quad \frac{1}{\sin\theta} &= \frac{1}{2}\left(\frac{R}{|z|}+\frac{|z|}{R}\right). \end{aligned}$$

5.3.2. Flow singularities on the sphere

There have to be singularities in the tangential active flow and some of them are generated by the defects in the director in a way that we describe in this section. The relation between active flow singularities and defects in a thin spherical film turns out to be the same as for a planar film, see Section 3.4, but we derive this result here for completeness.

The active flow diverges in magnitude at the defect locations, which can be seen from the following. Consider a small circle with opening angle ρ on the sphere, centred at the k-th defect, and projected onto the complex plane

$$z(s) = z_k - \frac{\rho R}{1-\cos\theta_k} e^{i(\phi_k - s)}\,, \tag{5.57}$$

where $s\in[0,2\pi]$, see Appendix B.3 for a derivation of this expression. We evaluate the magnitude of $u(z,\bar{z})$ on this circle, keeping only terms of lowest order in ρ,

$$\begin{aligned} |u(s)|^2 &\approx \big(\tilde{\sigma}_0 f(\tilde{r}_s)\big)^2 \left| -\frac{z_k R}{2|z_k|}\left(1+\frac{|z_k|^2}{R^2}\right) m_k \frac{z(s)-z_k}{|z(s)-z_k|^2}\right|^2 \\ &= \big(\tilde{\sigma}_0 f(\tilde{r}_s)\big)^2 \frac{1}{4}\left(1+\frac{|z_k|^2}{R^2}\right)^2 m_k^2 \frac{(1-\cos\theta_k)^2}{\rho^2} \\ &= \big(\tilde{\sigma}_0 f(\tilde{r}_s)\big)^2 m_k^2 \frac{1}{\rho^2}\,. \end{aligned} \tag{5.58}$$

The dimensionless tangential flow diverges as $1/\rho$ in the vicinity of a defect. The winding of the flow around these singularities is found in a similar way. First, on the small circle (5.57) we write

$$\begin{aligned} \alpha(s) &= \alpha_0 + \sum_j m_j \,\mathrm{Im}\left\{\ln(z(s)-z_j)\right\} \\ &= \alpha_0 + \sum_{j\neq k} m_j \,\mathrm{Im}\{\ln(z_k-z_j)\} + m_k(\phi_k - s) + m_k\pi + \mathcal{O}(\rho)\,. \end{aligned} \tag{5.59}$$

The last term results from writing $\ln(-x) = \ln(x) + i\pi$ if $x > 0$. We will use the abbreviation

$$w(z_k) := \alpha_0 + m_k\pi + \sum_{j\neq k} m_j \operatorname{Im}\{\ln(z_k - z_j)\}\,. \tag{5.60}$$

Next, we consider the expansion of all terms contributing to $u(z,\bar{z})$ in powers of ρ. Using (5.59) and (5.60) we find

$$\begin{aligned} e^{-i2\alpha(s)} =& e^{-i2w(z_k)} e^{-i2m_k(\phi_k - s)} \times \\ & \left\{ 1 + \frac{\rho}{2}\left(\frac{R}{|z|} + \frac{|z|}{R}\right) \sum_{j\neq k} m_j \left(\frac{z_k - z_j}{|z_k - z_j|^2}\bar{z}_k e^{is} - \frac{\bar{z}_k - \bar{z}_j}{|z_k - z_j|^2} z_k e^{-is} \right) \right\} + \mathcal{O}(\rho^2)\,. \end{aligned} \tag{5.61}$$

In the sum in (5.56) the k-th term gives

$$\begin{aligned} -\frac{z}{2}\left(\frac{R}{|z|} + \frac{|z|}{R}\right) m_k \frac{z - z_k}{|z - z_k|^2} = & \frac{m_k}{\rho} e^{-is} e^{i2\phi_k} + \frac{m_k}{4} e^{i2\phi_k} \left(\frac{R}{|z_k|} - \frac{|z_k|}{R} \right) \\ & - \frac{m_k}{4} e^{-i2s} e^{i2\phi_k} \left(\frac{R}{|z_k|} + 3\frac{|z_k|}{R} \right) + \mathcal{O}(\rho) \end{aligned} \tag{5.62}$$

and all other summands can be written as

$$-\frac{z}{2}\left(\frac{R}{|z|} + \frac{|z|}{R}\right) \sum_{j\neq k} m_j \frac{z - z_j}{|z - z_j|^2} = -\frac{z_k}{2}\left(\frac{R}{|z_k|} + \frac{|z_k|}{R}\right) \sum_{j\neq k} m_j \frac{z_k - z_j}{|z_k - z_j|^2} + \mathcal{O}(\rho)\,. \tag{5.63}$$

Further, we have

$$\frac{z^2}{R|z|} = \frac{z_k^2}{R|z_k|} + \mathcal{O}(\rho)\,. \tag{5.64}$$

From (5.61)-(5.64), we find that to lowest order in ρ, which is $\sim \mathcal{O}(1/\rho)$, the flow in the vicinity of the defect is

$$u(s) \propto e^{i(2m_k - 1)s} e^{i2(1-m_k)\phi_k} e^{-i2w(z_k)} \frac{m_k}{\rho}\,. \tag{5.65}$$

From the first exponential in (5.65) it follows that this dominant contribution to the flow at the k-th defect has the winding number $\mathcal{I} = 2m_k - 1$. Expression (5.65) is very similar to expression (3.62) for a planar film, but with an additional ϕ_k-dependent term and a slightly different definition of $w(z_k)$. See Figure 3.2 in Section 3.4 for plots of the local flow structure around different types of defects in the plane, which also hold locally for defects on the sphere.

Like in the planar case this relationship is only one-directional, as flow singularities can occur at places in between defects. In the spherical case, this can be seen as a

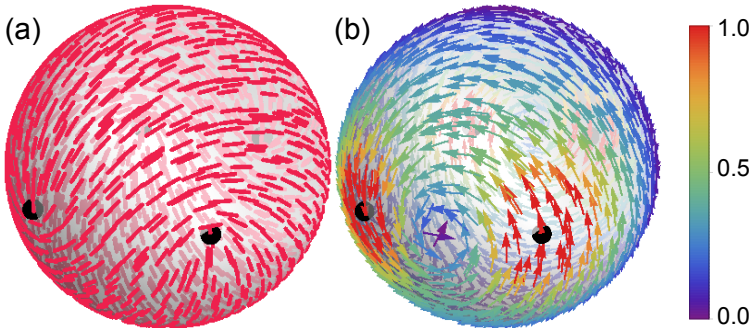

Figure 5.3: (a) Orientation field $\boldsymbol{P}$, given by equation (5.48), with four $+1/2$ defects in a paired planar configuration. (b) Resulting tangential flow $\tilde{\boldsymbol{u}}_\perp$ from equation (5.50), showing the typical two-vortex structure. The flow magnitude is colour-coded and cut off in the vicinity of the defects. Displayed is the outer surface of the shell, $\tilde{r}_s = 1$.

consequence of the Poincaré-Hopf theorem, see Section 2.4.2. If the flow singularities that arise due to defects are to be the only ones present, then their total topological strength has to be

$$2 = \sum_{j=1}^{n_{\text{def}}} (2m_j - 1) = 4 - n_{\text{def}}\,, \tag{5.66}$$

which can only be achieved if there are $n_{\text{def}} = 2$ defects. Thus, a single $+2$ defect and any configuration with more than two defects will inevitably lead to flow vortices which are not at the defects' locations. Moreover, with four $+1/2$ defects there have to be at least two vortices in the flow, even though the flow is not singular at the defects. Figure 5.3 gives an example of the director for four $+1/2$ defects in a planar configuration and the corresponding active flow, given by equation (5.50) and evaluated at the outer surface, which is seen to consist of two counterrotating vortices. This emergence of stable vortices is the germane feature of the active flows on spherical shells.

Another consequence of the unidirectionality of the relation above, is that simple stagnation points ($\mathcal{I} = -1$) cannot be created at defect locations. This is important for flows that have additional ± 1 flow singularity pairs on top of the two minimal vortices. However, higher order stagnation points, with $\mathcal{I} < -1$, can be created by defects, for example in the many-defect configurations considered at the end of this Chapter, in Section 5.7.

We illustrate the relationship between defect configuration and active flow with several examples, shown in Figure 5.4. The only situation in which all flow singularities are located at the defects is when there are two antipodal defects, for instance $\{+1, +1\}$. Higher topological strength defect pairs, like $\{-1, +3\}$ and $\{-2, +4\}$, also fall under this case, but we will not consider them since they are not likely to be of physical relevance. As illustrated in Figure 5.4 (a,d), two antipodal spiral defects

create a pair of counterrotating vortices centred at the defects. Such perfect spirals, with equal amount of splay and bend, are obtained with the phase $\alpha_0 = \pi/4$. For a more splay(bend)-like structure, that is if $0 < \alpha_0 < \pi/4$ ($\pi/4 < \alpha_0 < \pi/2$), the vortices acquire a sink(source)-like component and there will be radial flow, leading to changes in shell thickness.

If two unit strength defects are not antipodal, then additional flow singularities occur, due to the fact that the two minimal defect-centred vortices are counter-rotating. When the axial symmetry is broken there is one additional pair of ± 1 singularities on the great circle passing through the defects, with the stagnation point being on the defect-free hemisphere. One example of this is shown in Figure 5.4 (b,e) for two asters, which generate active flow sinks at their locations. In this example a flow source forms in between them, but in general this singularity will be a vortex possibly with an inward or outward directed component, depending on the splay- or bend-like nature of the director. This flow vortex will advect the defects, even though their local flow is winding, and we study this motion of $+1$ defects in Section 5.6.

For two defects which are not located at the poles of the sphere the amount of splay and bend is controlled through the phase $\alpha_0 = -\arg(z_1 - z_2) + \tilde{\alpha}_0$, as will be shown in Section 5.6. The additional constant, constructed from the projected defect positions, ensures that the geometric type of the two defects does not change as they move. With this phase, $\tilde{\alpha}_0 = 0$ corresponds to two asters and $\tilde{\alpha}_0 > 0$ adds bend to the director, up to two pure vortex defects at $\tilde{\alpha}_0 = \pi/2$.

For a number of defects other than two, additional flow singularities are always required in order to satisfy the Poincaré-Hopf condition. The simplest example is a $+2$ defect, shown in Figure 5.4 (c,f), whose active flow singularity of strength $+3$ requires an additional simple stagnation point, which forms opposite the defect.

5.4. Defect dynamics

In general, the director in the shell will change in time due to the active flows it produces. The assumption of an equilibrium director, together with the necessary presence of defects on the sphere, allows to reduce the director dynamics to the motion of defects. How the defects move, in turn, is captured by an effective point-particle description as explained in Section 2.4.1 for passive defects and extended in Section 2.4.3 to active defects. The motion of active defects is driven by elastic forces, like in a passive system, and by advection due to the active flow they create. We describe these two components and derive dynamical equations for the defect positions in an overdamped Newtonian dynamics approach, generalising equation (2.24) to a collection of active defects on a sphere.

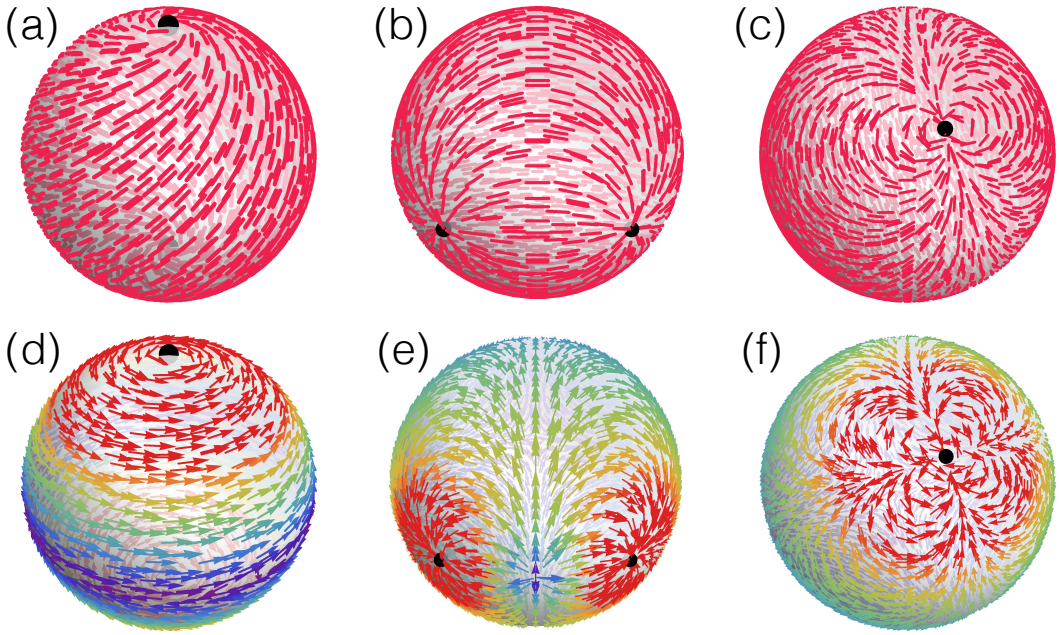

Figure 5.4: Orientational fields (top) with one or two defects and corresponding active flow (bottom) from equation (5.50). (a,d) Two antipodal spiral defects create a pair of counterrotating vortices, whose cores coincide with the defects. Additional flow singularities which are not at the locations of defects do occur, when defects are not antipodal (b,e) or when defect-driven singularities do not satisfy the Poincaré-Hopf condition, which is the case for a $+2$ defect (c,f). Colour-coding of the flow is on the scale (d) $[0, 1]$, (e) $[0, 3]$, and (f) $[0, 4]$.

5.4.1. Elastic forces

Similar to the energy (2.22) of a defective nematic in the plane, the free energy (5.34) of a nematic on a sphere can be rephrased in terms of the defects' pairwise interaction energies, which depend of their geodesic distances, and their self-energies [Lubensky and Prost, 1992; Nelson, 2002; Vitelli and Nelson, 2006],

$$E = -\frac{\pi K}{2} \sum_{\substack{i,j=1 \\ i\neq j}}^{n_{\mathrm{def}}} m_i m_j \ln(1-\cos\beta_{ij}) + \sum_{j=1}^{n_{\mathrm{def}}} \left(E_{def}(R,m_j) + E_c\right). \tag{5.67}$$

Here, $R\beta_{ij}$ is the geodesic distance between defect i and j and

$$\cos\beta_{ij} = \cos\theta_i\cos\theta_j + \sin\theta_i\sin\theta_j\cos(\phi_i-\phi_j)\,, \tag{5.68}$$

which is obtained from the scalar product of the three-dimensional position vectors of the defects. As we will not consider the energetics of defect unbinding or merging, the second sum in equation (5.67) is a constant and hence irrelevant in our model.

The force acting on defect k due to all other defects is [Chaikin and Lubensky, 2000; Keber et al., 2014]

$$\boldsymbol{F}^{(k)} = -\boldsymbol{\nabla}_k E = -\left(\hat{\boldsymbol{e}}_{\theta,k}\frac{1}{R}\partial_{\theta_k}E + \hat{\boldsymbol{e}}_{\phi,k}\frac{1}{R\sin\theta_k}\partial_{\phi_k}E\right), \tag{5.69}$$

which is the spherical version of equation (2.23). We use the notation $\hat{\boldsymbol{e}}_{\theta,k} = \hat{\boldsymbol{e}}_\theta(\theta_k,\phi_k)$ and $\hat{\boldsymbol{e}}_{\phi,k} = \hat{\boldsymbol{e}}_\phi(\theta_k,\phi_k)$. Because $\cos\beta_{kj} = \cos\beta_{jk}$, we have

$$\partial_{\theta_k}E = K\pi m_k \sum_{j=1,\, j\neq k}^{n_{\mathrm{def}}} m_j \frac{\partial_{\theta_k}\cos\beta_{kj}}{1-\cos\beta_{kj}} \tag{5.70}$$

and a similar expression for $\partial_{\phi_k}E$, where

$$\partial_{\theta_k}\cos\beta_{kj} = -\sin\theta_k\cos\theta_j + \cos\theta_k\sin\theta_j\cos(\phi_k-\phi_j)\,, \tag{5.71}$$

$$\partial_{\phi_k}\cos\beta_{kj} = -\sin\theta_k\sin\theta_j\sin(\phi_k-\phi_j)\,. \tag{5.72}$$

Energy-minimising defect configurations

For a given collection of defects on a sphere, the elastic forces (5.69) work to minimise the energy in (5.67) by adjusting the positions of the defect. The global energy minimum for a nematic in the one-constant-approximation is achieved if four half-defects are arranged at the vertices of a tetrahedron [Lubensky and Prost, 1992]. The

angular distances in a perfect tetrahedron are

$$\beta_{ij} = \beta = 2\arctan\left(\sqrt{2}\right) \approx 109.47^\circ, \tag{5.73}$$

so $\cos\beta_{ij} = -1/3$ for all pairs of defects. With the self-energy of a defect given by equation (2.21) the total energy of this configuration becomes

$$E^{\text{tetra}} \approx \pi K\left(-0.431 + \ln\left(R/r_c\right)\right) + 4E_c. \tag{5.74}$$

On the other hand, the energetic ground state of an orientation field with polar order on a sphere is an antipodal configuration of two +1 defects, for which the energy is

$$E^{\text{polar}} \approx \pi K\left(-0.693 + 2\ln\left(R/r_c\right)\right) + 2E_c. \tag{5.75}$$

Another configuration, which is found to be metastable for a nematic on a sphere [Koning et al., 2016], is an isosceles triangle with $m_1 = 1$ and $m_2 = m_3 = 1/2$. If the defect strengths are given, the optimal triangle has the angles $\beta_{12} = \beta_{13} = \pi - \arccos(2/3)$ and $\beta_{23} = 2\arccos(2/3)$, so $\cos\beta_{12} = -2/3$ and $\cos\beta_{23} = -1/9$. The total energy of this configuration is

$$E^{\text{tri}} \approx \pi K\left(-0.537 + \frac{3}{2}\ln\left(R/r_c\right)\right) + 3E_c. \tag{5.76}$$

5.4.2. Active advection

Self-propelling +1/2 defects

To find the active advection of +1/2 defects, we can directly evaluate the flow, since it is non-winding ($\mathcal{I} = 0$). For simplicity, we use only the dominant term $\propto 1/\rho$. From equation (5.65) with $m_k = 1/2$, the self-propelling velocity of the k-th +1/2 defect is

$$\tilde{\boldsymbol{u}}^{\text{def}} = \tilde{\sigma}_0 f(\tilde{r}_s)\frac{1}{2\rho}\begin{pmatrix} \cos\left(\phi_k - 2w(z_k)\right) \\ \sin\left(\phi_k - 2w(z_k)\right) \end{pmatrix}, \tag{5.77}$$

with $w(z_k)$ given in (5.60). The divergent flow magnitude is cut off at an angular distance ρ, which is the opening angle of the small circle considered earlier. It can be associated with the core size of the defect or with the thickness of the film, whichever is bigger,

$$\rho = \frac{1}{R}\max\{r_c, h_0\}. \tag{5.78}$$

The core size r_c is a constant, which can be measured for a particular experimental system and defect type. It can be assumed to be independent of the shell size. The

justification to use a simple cut-off was given for the planar case in Section 3.5, where the divergent thin film solution was matched with a regularised defect core. The same argument holds for defects in a spherical shell, since the same local regularisation procedure could be performed here.

Through the relation (5.44) for vectors under stereographic projection, the direction of the velocity vector (5.77) corresponds to the direction of $e^{i2w(z_k)}$ in the complex plane, where the nematic director is given by $e^{i\alpha}$. Consider a small circle given by $z(s) = z_k + \rho e^{is}$, $s \in [0, 2\pi]$. Then, in analogy to (5.59), we have $\alpha(s) = w(z_k) + s/2$. Along the direction of the symmetry axis of the defect, given by the angle $\tilde{s}$, the director orientation coincides with this angle[1]

$$\tilde{s} = \alpha(\tilde{s}) = w(z_k) + \tilde{s}/2\,. \tag{5.79}$$

So, $2w(z_k) = \tilde{s}$, from which it follows that the velocity of the defect on the sphere points along its symmetry axis. For extensile activity the defect moves in direction of its comet-head and for contractile activity it moves in the reverse direction. This is an alternative derivation of this well-known behaviour as the dominant part of the active flow in a thin film. Notably, in this approach the direction of the comet-head is fixed by the locations of the other defects through $w(z_k)$.

For the simulations we evaluate the tangential flow at the outer surface, $\tilde{r}_s = 1$, where the flow magnitude is maximal and $f(1) = -1/2$. The prefactor in (5.77) then becomes $-\tilde{\sigma}_0/4\rho$.

Averaged active flow

For defects with $m_k \neq 1/2$ the dominant part of the flow is winding, so it is not possible to extract a well-defined direction of motion from evaluating this flow at the defect. Instead, we can average the flow over a small circle centred at the defect, which will pick up higher order contributions that may be non-winding. Thus, one advantage of having a solution for the whole flow field in the active nematic shell is the possibility to study the motion of defects which are not self-propelling, but which are instead advected in the flow created by other defects.

Consider a small circle on the sphere centred at the k-th defect and given by $\theta(s) = \theta_k + \rho\cos(s)$ and $\phi(s) = \phi_k + \rho\sin(s)/\sin(\theta_k)$, with $s \in [0, 2\pi]$ (see Appendix B.3). We approximate the flow at the k-th defect with $m_k \neq 1/2$ by the average flow on the circle

$$\tilde{\boldsymbol{u}}^{\mathrm{def}} = \frac{1}{2\pi}\int_0^{2\pi} \tilde{\boldsymbol{u}}_\perp(s)\,\mathrm{d}s\ . \tag{5.80}$$

[1] More precisely, $\tilde{s} + n\pi = \alpha(\tilde{s})$ with $n \in \mathbb{Z}$, which leads to the same result.

Clearly, the velocity (5.77) can also be cast in terms of the integral (5.80), but here we focus on the cases when the singular term $\sim 1/\rho$ is winding and hence does not contribute to the integral. To study the structure of this type of active advection we collect all $\mathcal{O}(1)$-terms from (5.61)-(5.64), the expansion of $u(s)$ in powers of ρ. This first non-singular contribution to the flow $u(s)$ is proportional to

$$
\begin{aligned}
&e^{-i2w(z_k)}e^{-i2m_k\phi_k}\times\\
&\left\{\frac{m_k}{2}e^{i2(m_k-1)s}e^{i2\phi_k}\left\{\left(\frac{|z_k|}{R}+\frac{R}{|z_k|}\right)\left(-\frac{1}{2}+z_k\sum_{j\neq k}m_j\frac{\bar{z}_k-\bar{z}_j}{|z_k-z_j|^2}\right)-\frac{|z_k|}{R}\right\}\right.\\
&+e^{i2m_ks}\left\{\frac{z_k^2}{R|z_k|}+\frac{m_k}{4}e^{i2\phi_k}\left(\frac{R}{|z_k|}-\frac{|z_k|}{R}\right)\right.\\
&\left.\left.-\left(\frac{z_k}{2}+\frac{m_k\bar{z}_k}{2}e^{i2\phi_k}\right)\left(\frac{|z_k|}{R}+\frac{R}{|z_k|}\right)\sum_{j\neq k}m_j\frac{z_k-z_j}{|z_k-z_j|^2}\right\}\right\}. \qquad (5.81)
\end{aligned}
$$

From the s-dependent exponentials it follows that at this order there is no net advection, unless $m_k = 1$, in which case the first summand gives a non-zero contribution to the integral in (5.80). Advection of +1 defects is thus one order of magnitude in ρ smaller than the velocity of +1/2 defects.

On the other hand, advection of -1/2 defects is at least two orders of magnitude in ρ smaller than the velocity of +1/2 defects, since it can only arise from contributions $\sim \mathcal{O}(\rho)$ or higher. Thus, in collections of $\pm 1/2$ defects, the active motion of negative defects can be neglected.

5.4.3. Dynamical Equations

We denote by $\boldsymbol{r}_k = R\hat{\boldsymbol{e}}_r(\theta_k, \phi_k)$ the three-dimensional position vector of the k-th defect. Since $\partial_\theta \hat{\boldsymbol{e}}_r = \hat{\boldsymbol{e}}_\theta$ and $\partial_\phi \hat{\boldsymbol{e}}_r = \sin\theta \hat{\boldsymbol{e}}_\phi$, its total time derivative is

$$
\begin{aligned}
\frac{\mathrm{d}\boldsymbol{r}_k}{\mathrm{d}t} &= R\frac{\mathrm{d}}{\mathrm{d}t}\hat{\boldsymbol{e}}_r(\theta_k,\phi_k)\\
&= R\left(\frac{\partial}{\partial\theta_k}\hat{\boldsymbol{e}}_r(\theta_k,\phi_k)\frac{\partial}{\partial t}\theta_k+\frac{\partial}{\partial\phi_k}\hat{\boldsymbol{e}}_r(\theta_k,\phi_k)\frac{\partial}{\partial t}\phi_k\right)\\
&= R\big(\hat{\boldsymbol{e}}_{\theta,k}\dot{\theta}_k+\hat{\boldsymbol{e}}_{\phi,k}\sin\theta_k\dot{\phi}_k\big)\,. \qquad (5.82)
\end{aligned}
$$

With $\tilde{\boldsymbol{r}}_k = \boldsymbol{r}_k/R$ and $\tilde{t} = t/\tau$ we arrive at a dimensionless equation

$$
\frac{\mathrm{d}\tilde{\boldsymbol{r}}_k}{\mathrm{d}\tilde{t}} = \big(\hat{\boldsymbol{e}}_{\theta,k}\partial_{\tilde{t}}\theta_k+\hat{\boldsymbol{e}}_{\phi,k}\sin\theta_k\partial_{\tilde{t}}\phi_k\big)\,. \qquad (5.83)
$$

On the other hand, since inertia is negligible, the equations of motion for the

defects are overdamped,

$$\xi\left(\frac{\mathrm{d}\boldsymbol{r}_k}{\mathrm{d}t} - \boldsymbol{u}^{\mathrm{def}}\right) = \boldsymbol{F}^{(k)}, \tag{5.84}$$

as discussed in Section 2.4.1. Making this equation dimensionless and using equation (5.83), we obtain dynamical equations for the spherical coordinates of the k-th defect

$$\frac{\partial\theta_k}{\partial\tilde{t}} = \frac{\tau}{\xi R}F_\theta^{(k)} + \frac{\tau}{R}u_\theta^{\mathrm{def}} \tag{5.85}$$

$$\frac{\partial\phi_k}{\partial\tilde{t}} = \frac{1}{\sin\theta_k}\left(\frac{\tau}{\xi R}F_\phi^{(k)} + \frac{\tau}{R}u_\phi^{\mathrm{def}}\right). \tag{5.86}$$

Dimensional analysis of active and elastic effects

We consider the scaling of the active advection for the cases of $+1/2$ and $+1$ defects, although the analysis is generalisable to any type of defect. The flow is always evaluated at the outer surface, where $f(\tilde{r}_s = 1) = -1/2$. From (5.77), for defects with $m_k = 1/2$ the flow magnitude is expressed in terms of the system parameters as

$$\left|\boldsymbol{u}^{\mathrm{def}}\right| = U_0\frac{1}{4\rho} = \frac{h_0^2\sigma_0}{R\mu}\frac{1}{4\rho}, \tag{5.87}$$

where we have used the scaling

$$U_0 = \frac{h_0^2\sigma_0}{\mu R} \tag{5.88}$$

that follows from equation (5.15). Choosing $\rho = r_c/R$ from (5.78) we get

$$v_0 = \left|\boldsymbol{u}^{\mathrm{def}}\right| = \frac{h_0^2\sigma_0}{4r_c\mu}, \tag{5.89}$$

so the velocity of $+1/2$ defects does not depend on the radius of the shell, but only on its thickness h_0. This agrees with the intuition that a $+1/2$ defect generates its own advection locally and the system size should not affect this. In addition, the flow at the outer surface is higher when the active nematic film is thicker, since the distance to the no-slip boundary increases.

On the other hand, for $m_k = 1$ we have

$$\left|\boldsymbol{u}^{\mathrm{def}}\right| \sim U_0 = \frac{h_0^2\sigma_0}{\mu R}. \tag{5.90}$$

The flow decreases with radius, because the $+1$ defect is advected in the flow generated by other vortices which move further apart, as the radius is increased. The velocity of defects with other topological strengths decreases with shell size at least as $\sim 1/R^2$, since the dimensionless flow is at least $\sim \mathcal{O}(r_c/R)$.

The scaling of the elastic effects does not depend on the defect type. For example for the θ-component, the elastic term in equation (5.85) can be written as

$$\frac{\tau}{\xi R} F_\theta^{(k)} = -\frac{\tau K}{\xi R^2} \pi m_k \sum_{j=1,\, j\neq k}^{n_{\mathrm{def}}} m_j \frac{\partial_{\theta_k} \cos\beta_{kj}}{1-\cos\beta_{kj}} \,. \tag{5.91}$$

Because the material parameters have the units $[\xi] = \mathrm{Ns/m}$ and $[K] = \mathrm{Nm}$, the dimensionless elasticity prefactor

$$\tilde{K} = \frac{\tau K}{\xi R^2} \tag{5.92}$$

defines a time scale

$$\tau = \frac{\xi R^2}{K} \,, \tag{5.93}$$

which can be identified with the time scale of elastic relaxation of defects into their equilibrium positions in the absence of activity. This choice of time scale sets $\tilde{K} = 1$.

On the other hand, the scaling of the dimensionless activity parameter in equation (5.15),

$$\tilde{\sigma}_0 = \frac{h_0^2 \sigma_0}{R\mu U_0} = \frac{h_0^2 \sigma_0 T}{R^2 \mu} \tag{5.94}$$

determines the active time scale in terms of the other system parameters,

$$T = \frac{R^2 \mu}{h_0^2 \sigma_0} = \frac{\mu}{\sigma_0 \varepsilon^2} \,, \tag{5.95}$$

with $[\mu] = \mathrm{Ns/m^2}$ and $[\sigma_0] = \mathrm{N/m^2}$, which we already used to make equations dimensionless in Section 5.1. Hence, if the time of the dynamics is in units of τ, there will be a factor

$$\frac{\tau}{T} = \frac{\xi h_0^2 \sigma_0}{K\mu} \tag{5.96}$$

in front of the dimensionless active advection velocity. For a general defect configuration, equations (5.85) and (5.86) become

$$\partial_{\tilde{t}} \theta_k = -\pi m_k \sum_{j=1,\, j\neq k}^{4} m_j \frac{\partial_{\theta_k} \cos\beta_{kj}}{1-\cos\beta_{kj}} + \frac{\tau}{T} \tilde{u}_\theta^{\mathrm{def}} \tag{5.97}$$

$$\partial_{\tilde{t}} \phi_k = \frac{1}{\sin\theta_k} \left(-\frac{\pi m_k}{\sin\theta_k} \sum_{j=1,\, j\neq k}^{4} m_j \frac{\partial_{\phi_k} \cos\beta_{kj}}{1-\cos\beta_{kj}} + \frac{\tau}{T} \tilde{u}_\phi^{\mathrm{def}} \right) \,. \tag{5.98}$$

However, due to the flow singularities in $\tilde{\boldsymbol{u}}^{\mathrm{def}}$ there is an additional prefactor $(1/\rho)^2 = (R/r_c)^q$, associated to the core size r_c of a defect as discussed above, where the power q depends on the strength of the defect. Therefore, we should consider

the dynamical equations for each defect type separately. Note, that this prefactor is an important consequence of the flow singularities in the thin film model for active defects and could not be guessed from dimensional arguments alone. Moreover, it introduces a dependence of the dynamics on the shell radius R, which is otherwise absent in (5.96).

For a $+1/2$ defect the prefactor of the active terms in equations (5.85) and (5.86) then becomes

$$\frac{\tau}{R}\left|\boldsymbol{u}^{\mathrm{def}}\right| \propto \frac{\xi R h_0^2 \sigma_0}{K \mu r_c} =: \nu\,, \tag{5.99}$$

which we define as the dimensionless ratio of active to elastic effects. This ratio determines the type of dynamics of four $+1/2$ defects in the spherical shell, which is analysed in Section 5.5. At $\nu \approx 1$ one can expect a cross over from an elasticity-dominated regime, in which the defects relax into close-to-equilibrium configurations as we will discuss in Section 5.5.1, and an activity-dominated regime of steady motion described in Section 5.5.2.

For a $+1$ defect the corresponding prefactor is

$$\frac{\tau}{R}\left|\boldsymbol{u}^{\mathrm{def}}\right| \propto \frac{\xi R}{K}\frac{h_0^2 \sigma_0}{\mu R} = \frac{\xi h_0^2 \sigma_0}{K \mu} =: \nu^{(1)}\,, \tag{5.100}$$

which reflects that for these defects both active and elastic effects scale with shell radius in the same way, as $\sim 1/R$.

In summary, if there is only one type of defects in the system, like four $+1/2$ or two $+1$ defects, then there is only one parameter that determines the dynamics. This parameter represents the relative importance of active to elastic effects. However, if there is a combination of defects of different strengths, then the ratio $R/r_c = 1/\rho$ is necessary to estimate their relative velocity magnitudes.

Dynamical equations for four $+1/2$ defects

With the above scalings we now write explicitly the dynamical equations for four $+1/2$ defects in the shell

$$\partial_{\tilde{t}}\theta_k = -\frac{\pi}{4}\sum_{j=1,\, j\neq k}^{4}\frac{\partial_{\theta_k}\cos\beta_{kj}}{1-\cos\beta_{kj}} - \frac{\nu}{4}\cos\left(\phi_k - 2w(z_k)\right) \tag{5.101}$$

$$\partial_{\tilde{t}}\phi_k = \frac{1}{\sin\theta_k}\left(-\frac{\pi}{4\sin\theta_k}\sum_{j=1,\, j\neq k}^{4}\frac{\partial_{\phi_k}\cos\beta_{kj}}{1-\cos\beta_{kj}} - \frac{\nu}{4}\sin\left(\phi_k - 2w(z_k)\right)\right) \tag{5.102}$$

for $k = 1,\ldots,4$, where $w(z_k) = \alpha_0 + \frac{\pi}{2} + \frac{1}{2}\sum_{j\neq k}\mathrm{Im}\{\ln(z_k - z_j)\}$. In this dimensionless formulation the ratio ν, defined in (5.99), and the phase α_0 are the only two

parameters.

5.4.4. Numerical method

Numerical simulations are performed using the software *MATLAB 2016a*. Equations (5.97)-(5.98), or (5.101)-(5.102) in the case of four $+1/2$ defects, are solved using the *MATLAB* ordinary differential equation solver `ode23s`, with absolute and relative accuracy set to $10^{-6}\tau$. The function `ode23s` employs a standard lower-order Runge-Kutta method [Reichelt and Shampine, 1997], which is well suited for stiff differential equations. The equations considered here have the potential for being stiff, because the two time scales – the elastic and the active – drift apart when their ratio is increased. Indeed, for this particular dynamical system we find numerically stable results for all considered parameter values with the `ode23s` solver, whereas other solvers seem not reliable for larger activities and long measuring times.

The average flow at a $+1$ defect is obtained with the *MATLAB* function `integral`, with absolute and relative accuracy set to $10^{-4}\tau$ and $10^{-2}\tau$, respectively. The calculations are performed in Cartesian coordinates with the `integral`-option `'ArrayValued'`.

For simulations with four $+1/2$ defects, the defects are initialised at the vertices of a tetrahedron, which has no vertices at either of the spherical poles but for which one of the tetrahedron's 2-fold symmetry axis coincides with the z-axis. For this tetrahedron the defect positions are given by

$$\theta_i^{(0)} = (\beta/2, \pi - \beta/2, \beta/2, \pi - \beta/2) \quad \text{and} \quad \phi_i^{(0)} = (0, \pi/2, \pi, 3\pi/2)\,, \tag{5.103}$$

where $\beta = 2\arctan\big(\sqrt{2}\big)$ is the angular distance between defects in a tetrahedron. Angular distances between defects are measured according to equation (5.68) in the steady state. The mean angular distance $\bar{\beta}(t)$, the mean angular distance $\bar{\beta}$ averaged over a trajectory, and the minimal angular distance $\beta_{\min}$ along a trajectory are calculated as follows

$$\bar{\beta}(t) = \frac{1}{6} \sum_{<i,j>} \beta_{ij}(t), \tag{5.104}$$

$$\bar{\beta} = \big\langle \bar{\beta}(t) \big\rangle_t\,, \tag{5.105}$$

$$\beta_{\min} = \min_{t,<i,j>} \beta_{ij}(t)\,, \tag{5.106}$$

where $< i, j >$ denotes summation over all six defect pairs.

All plots are produced with the software *Mathematica 11*. Director fields and flow fields on the sphere, as in Figure 5.3, are plotted on a randomised grid (θ_i, ϕ_{ij}) for a smoother visual effect. For instance, for $m - 1$ points in the θ-direction, omitting

the poles, we choose $\theta_i = \frac{i}{m}\pi + \xi_i$, for $i = 1, \ldots, m-1$, with a Gaussian noise $\xi_i \sim \mathcal{N}(0, 0.03)$. For each θ_i a grid of ϕ-values is constructed: $\phi_{ij} = \frac{j}{n_i}2\pi$, with $j = 1, \ldots, n_i$ and $n_i = \lceil \zeta_i m \sin\theta_i \rceil$ with a Gaussian noise $\zeta_i \sim \mathcal{N}(1, 0.2)$.

5.5. Motion of four +1/2 defects

The dynamics of four +1/2 defects, given by equations (5.101) and (5.102), is determined primarily by the value of ν, which can be interpreted as the ratio of active to elastic effects. Although ν is a combination of various system parameters, given by (5.99), we imagine a system in which varying ν is facilitated by varying the activity σ_0, with all other parameters kept constant, and investigate the change in dynamics as activity is increased. In particular, we fix the shell radius to $R = R_0$, which also fixes the elastic time scale $\tau = \tau_0$, if K and ξ are fixed. We discuss the complementary case of fixed activity and varying shell radius in Section 5.7, where collections of larger numbers of defects are considered. The main results are presented for extensile active stresses, $\sigma_0 > 0$, in order to relate with microtubule-based active nematics [Sanchez et al., 2013; Keber et al., 2014], but we comment on the contractile case in the Discussion, Section 5.9.

At zero activity the four defects relax into a tetrahedral configuration, when starting at random initial positions, as expected for the passive case (see Section 5.4.1). For non-zero activity a tetrahedron is chosen as the initial configuration. As activity is increased from zero, defects undergo a small transient movement, relaxing into a configuration where they have moved closer in pairs. We call this configuration a "skewed tetrahedron", which is increasingly distorted with activity.

At a critical activity ν^* there is a transition to a dynamical regime, where the defects start moving on periodic orbits. As illustrated in Figure 5.5, the shape of those orbits depends on the strength of the activity. Importantly, the motion of defects is characterised by the formation of flow vortices that separate the defects into two pairs and drive them on their orbits.

From simulations we estimate the critical activity by measuring the mean and minimal angular distances between the four defects along a trajectory, shown in Figure 5.5 (a). Both change rapidly at $\nu^* \approx 0.7$. The mean distance increases, indicating that defects are no longer in a tetrahedral or near-tetrahedral arrangement. The drop in the minimal distance is associated with the formation of rotating pairs in the dynamical regime.

The second parameter that determines the dynamics is the phase α_0, which controls the amount of bend and splay in the nematic texture. We find that $\alpha_0 \in (0, \pi/4)$ and $\alpha_0 \in (\pi/4, \pi/2)$ leads to similar ν-dependence of the dynamics. We first focus on

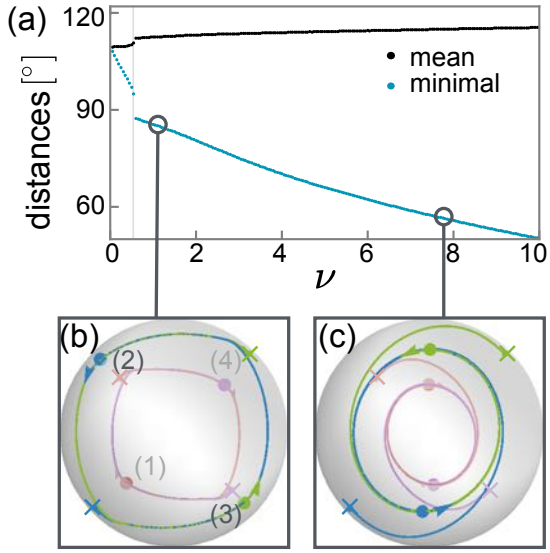

Figure 5.5: (a) Mean and minimal angular distances between four $+1/2$ defects plotted against ν, the ratio of active to elastic effects. The rapid change in both at $\nu^* \approx 0.7$ marks the transition to the dynamical regime, in which defects move on periodic orbits. The shape of these orbits changes smoothly with ν: (b) square-like trajectories for intermediate activity, corresponding to the tetrahedral-planar oscillations found experimentally [Keber et al., 2014], (c) ellipsoid orbits at higher activity, where defects in each pair have moved closer. In (b) and (c), crosses represent the initial tetrahedral configuration, big dots represent the defect positions at a time corresponding to plots in Figure 5.7 and arrows indicate the direction in which defects traverse the orbits.

this range, specifically fixing

$$\alpha_0 = \pi/2 - 0.2 \tag{5.107}$$

for the examples shown in all subsequent figures. The special cases of $\alpha_0 = 0$, which produces a bend-dominated texture, $\alpha_0 = \pi/2$, which produces a splay-dominated texture, and $\alpha_0 = \pi/4$, in which case the texture has comparable amounts of splay and bend, are discussed at the end of this section.

5.5.1. Regime of transient motion

We describe the "skewed tetrahedron" and the transition to the dynamical regime by a linear stability analysis of the dynamical equations (5.101) and (5.102), which for this purpose are rewritten as

$$\frac{\mathrm{d}\boldsymbol{x}(t)}{\mathrm{d}t} = \boldsymbol{g}(\boldsymbol{x}(t))\,, \tag{5.108}$$

where $\boldsymbol{x}(t) = (\theta_1(t), \ldots, \theta_4(t), \phi_1(t), \ldots, \phi_4(t)) \in \mathbb{R}^8$ is the vector of spherical defect positions and $\boldsymbol{g}(\boldsymbol{x}(t))$ are the concatenated right hand sides of equations (5.101) and (5.102).

Since in the low activity regime the defects relax into a steady state in the

simulations, we assume that there is a stable fixed point $\boldsymbol{x}^*(\nu, \alpha_0)$ corresponding to the "skewed tetrahedron". In simulations, we find that the deviations of defect positions relative to the perfect tetrahedron are small. Moreover, the defects move in a symmetric fashion that corresponds to a combination of twisting and stretching of the initial tetrahedron, as illustrated in the inset of Figure 5.6 (a). Consequently, the defect positions in the "skewed tetrahedron" can be described by

$$\theta_1^* = \theta_3^* = \theta_1^{(0)} - \delta\theta, \tag{5.109}$$

$$\theta_2^* = \theta_4^* = \theta_2^{(0)} + \delta\theta, \tag{5.110}$$

$$\phi_1^* = \phi_1^{(0)} - \delta\phi,\ \phi_2^* = \phi_2^{(0)} + \delta\phi, \tag{5.111}$$

$$\phi_3^* = \phi_3^{(0)} - \delta\phi,\ \phi_4^* = \phi_4^{(0)} + \delta\phi, \tag{5.112}$$

with two small deviations $\delta\theta = \delta\theta(\nu, \alpha_0)$ and $\delta\phi = \delta\phi(\nu, \alpha_0)$ for $\nu < \nu^*$, and $\delta\theta, \delta\phi > 0$. Here, $\theta_i^{(0)}$ and $\phi_i^{(0)}$ denote the positions in the initial tetrahedron given by (5.103). To study the linear stability of this fixed point $\boldsymbol{x}^*$ as a function of ν, we look at a small perturbation $\delta\boldsymbol{x}$ away from $\boldsymbol{x}^*$, which evolves according to

$$\frac{\mathrm{d}\delta\boldsymbol{x}}{\mathrm{d}t} = \boldsymbol{\nabla}\boldsymbol{g}\big|_{\boldsymbol{x}^*} \cdot \delta\boldsymbol{x}. \tag{5.113}$$

In Figure 5.6 (b) we plot the eigenvalues of

$$\boldsymbol{\nabla}\boldsymbol{g}\big|_{\boldsymbol{x}^*=(\theta_1^*,\ldots,\phi_4^*)}, \tag{5.114}$$

using the $\theta_1^*, \ldots, \phi_4^*$ from simulation data. Firstly, there are three vanishing eigenvalues, λ_1, λ_2 and λ_3, which correspond to the rigid body rotations of the defect configuration in three dimensional space. All other eigenvalues are negative, therefore as expected the "skewed tetrahedron" is linearly stable for $\nu < 0.7$. However, the data suggests that at $\nu = 0.7$ the eigenvalue λ_7 changes its sign from negative to positive, which would render the "skewed tetrahedron" linearly unstable and explain the transition to the dynamical regime. The data points from simulations can only be plotted for $\nu < 0.7$, since above this value the defects are in periodic motion and the – supposedly unstable – fixed point cannot be extracted.

To corroborate this supposition we make use of approximate analytical solutions for the deviations $\delta\theta(\nu)$ and $\delta\phi(\nu)$, which are derived as follows. We want to find deviations for which the resulting positions are a fixed point $\boldsymbol{x}^*$ of the dynamical system (5.108). Plugging the ansatz from equations (5.109)-(5.112) into the condition

$$\boldsymbol{g}(\boldsymbol{x}(\delta\theta, \delta\phi)) = \boldsymbol{0} \tag{5.115}$$

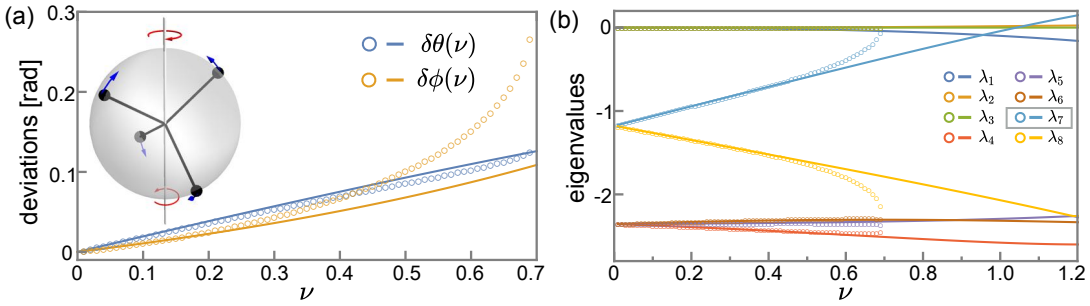

Figure 5.6: (a) Deviations of defect positions from the tetrahedron in the small activity regime. Shown are deviations $\delta\theta$ and $\delta\phi$ measured in simulations (circles) and obtained from linear order calculation of the fixed point (lines). The inset shows the corresponding twist (red arrows) and stretching (blue arrows) modes of deformation of the initial tetrahedron. (b) Spectrum of $\boldsymbol{\nabla g}$ evaluated at the "skewed tetrahedron", using defect positions from the simulation (circles) and positions obtained from analytical expressions for $\delta\theta(\nu)$ and $\delta\phi(\nu)$ given in (5.116) and (5.117) (lines). The data suggests that at $\nu^* = 0.7$ the eigenvalue λ_7 (boxed) becomes positive, which renders the "skewed tetrahedron" linearly unstable. This is qualitatively confirmed by the theoretical prediction, albeit with an overestimated transition point.

and solving its linearised version for small deviations, $\delta\theta \ll 1$ and $\delta\phi \ll 1$, we find

$$\delta\theta(\nu,\alpha_0) = -\frac{2\nu\left(\pi\cos(2\alpha_0)+\sqrt{2}\nu\right)}{2\nu^2\sin^2(2\alpha_0)+3\pi\sqrt{2}\nu\cos(2\alpha_0)+3\pi^2}\,, \tag{5.116}$$

$$\delta\phi(\nu,\alpha_0) = \frac{2\sqrt{3}\nu\left(3\sqrt{2}\pi-2\nu\cos(2\alpha_0)\right)}{12\nu^2\sin(2\alpha_0)+9\pi\csc(\alpha_0)\sec(\alpha_0)\left(\sqrt{2}\nu\cos(2\alpha_0)+\pi\right)}\,. \tag{5.117}$$

Figure 5.6 (a) shows that while $\delta\theta(\nu)$ recovers the simulation data very well, the deviations in ϕ-direction are strongly underestimated with this linear approach for $\nu \geq 0.3$, so the twist in the "skewed tetrahedron" is not accurately described near the transition to the dynamical regime.

Nonetheless, the eigenvalues of (5.114) evaluated at the fixed point $\boldsymbol{x}^*(\delta\theta(\nu),\delta\phi(\nu))$ that is constructed from the deviations (5.116) and (5.117) correlate well with the ones from simulation data up to $\nu \approx 0.5$, as shown in Figure 5.6 (b). There is qualitative agreement in the behaviour of eigenvalue λ_7 for larger ν. Again, while all eigenvalues are non-positive for small ν, λ_7 is continuously growing and becomes positive at $\nu \approx 1.05$. When $\lambda_7 > 0$, the corresponding eigenvector has the structure $(a,-a,a,-a,-b,b,-b,b)$ with $b \gg a > 0$. It represents a deformation which slightly reverses the stretching and, to a much stronger extent, amplifies the twist of the "skewed tetrahedron" (see inset of Figure 5.6 (a) for an illustration of these deformation modes). This is exactly the dynamics found in simulations at early times, see for instance the trajectory between crosses and big dots in Figure 5.5 (b). Although the activity at which the transition happens is overestimated, this theoretical argument shows that the the dynamical regime is indeed initiated by the "skewed tetrahedron"

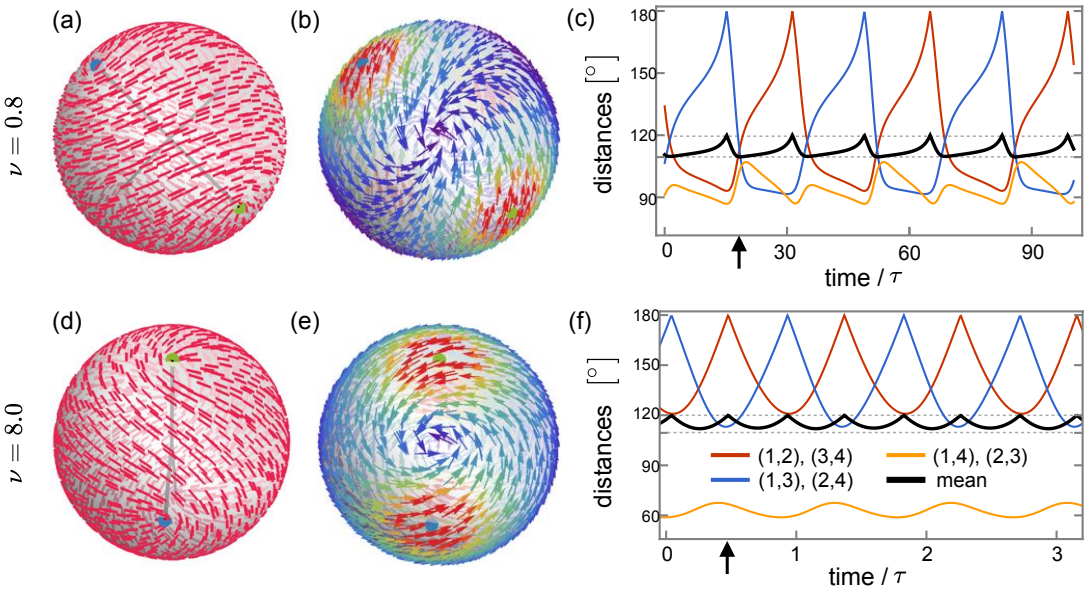

Figure 5.7: The dynamics of four $+1/2$ defects is characterised by the formation of counterrotating flow vortices and defect pairs. (a)-(c): Tetrahedral-planar oscillations in intermediate activity regime ($\nu = 0.8$); Director (a) and flow (b) in tetrahedral configuration at time marked with arrow in (c) ; (c) shows pairwise and mean geodesic distances between defects; tetrahedral and planar configurations correspond to $109.5°$ and $120°$, respectively. (d)-(f): At higher activity ($\nu = 8.0$) the two vortices become more pronounced and the defect pairs are tighter (see yellow line); Director (d) and flow (e) in planar configuration at time marked with arrow in (f); The tetrahedron is no longer approached as seen from pairwise distances in (f). In (c) and (f) (i, j) denotes the distance between defects marked as (i) and (j) in Figure 5.5 (b).

becoming linearly unstable to a specific deformation that is the start of the periodic orbits.

5.5.2. Oscillatory regime

In the dynamical regime the defects settle into periodic orbits, whose shape varies smoothly with increasing activity from square-like to more ellipsoid as seen in Figures 5.5 (b) and (c). To characterise the different dynamics we plot the oscillation of angular distances between the defects and exemplary director and flow fields in Figure 5.7. For intermediate activity ($\nu = 0.8$) the defects periodically pass through tetrahedral and planar configurations, as shown in Figure 5.7 (c), which is the dynamics found in experiments [Keber et al., 2014], see Figure 2.5. Peaks in the mean angular distance at $\bar{\beta} \approx 120°$ correspond to planar arrangements of defects, which are also equidistant at this activity, since the minimal distances are $\approx 90°$. Minima in the mean angular distances are at $\bar{\beta} \approx 110°$ and correspond to tetrahedral configurations, in which all other angles also approach this value.

Figures 5.7 (a) and (b) show the director and the corresponding active flow at

one such tetrahedral arrangement. The flow reveals that the motion is characterised by the formation of two counterrotating flow vortices. The vortices are responsible for the separation of defects into two pairs, in which they rotate around each other. This effect becomes more pronounced as the activity is increased (see Figure 5.7 (e)). The separation of defects within each pair decreases significantly with increasing activity, as seen in Figure 5.5 (a), such that the tetrahedral configurations are no longer approached. The difference in the dynamics is also illustrated in Figure 5.7 (f), where the angular distances now oscillate between two different planar arrangements, but the paired defects always stay close. If activity is further increased the dynamics approaches the situation for two antipodal spirals in the director, which in the limit generate a perfectly symmetric flow vortex pair.

The total defect velocities, comprising motion due to both active advection and elastic repulsion, are found to oscillate in time as shown in Figure 5.8. The speeds are synchronised for all defects, therefore only one line is seen in the plot. For intermediate activity ($\nu = 0.8$) lowest speeds occur around the tetrahedral configurations, and the defects are fastest when they are in planar arrangements. On the other hand, for higher activity ($\nu = 8.0$) the defect speed plateaus over prolonged time intervals, but drops in between those. Notably, there are two types of planar configurations that differ in the separation of paired defects and speed minima correlate with those, in which defects are closer to each other. The different role of planar configurations in these two examples is not surprising, as the total speed depends on the relative orientation of the active velocity and the elastic force acting on the defect, and is not simply determined by the defect distances.

Frequency of defect oscillations

Although the defect speed oscillates, we can estimate from Figure 5.8 that its average scales linearly with ν. Therefore, we can conclude that the total defect speed is dominated by the active contribution and from that estimate how the frequency of defect oscillations will change with system parameters. The active speed of a $+1/2$ defect is $v_0 \sim h_0^2\sigma_0/\mu r_c$, see equation (5.89). If ν is constant, the length of the defect orbits scales as $\sim 2\pi R$, therefore the period of oscillation is $\tau^a \sim R/v_0 \sim \mu r_c R/h_0^2\sigma_0$ or, in units of the elastic relaxation time, $\tilde{\tau}^a = \tau^a/\tau \sim 1/\nu$. Consequently, the frequency is

$$f^a = 1/\tau^a \sim \frac{h_0^2\sigma_0}{\mu r_c R}\,, \tag{5.118}$$

or $\tilde{f}^a = f^a\tau \sim \nu$. This relationship is in agreement with the frequencies measured in simulations for different ν, see Figure 5.8 (b). If the radius of the shell is increased in a way that keeps ν constant, for instance due to an appropriate decrease in activity

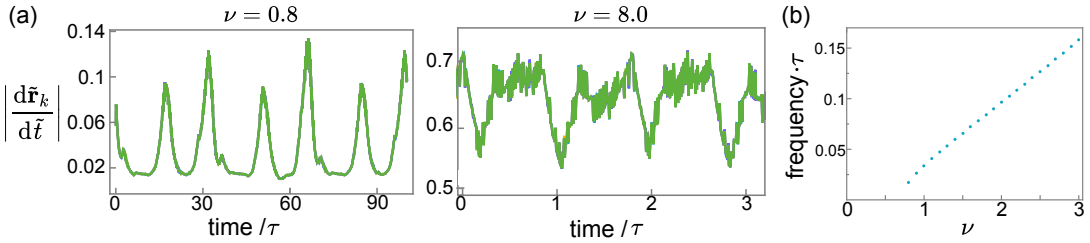

Figure 5.8: (a) Total defect speed, corresponding to the magnitude of (5.83), for intermediate and high activity regimes. The speeds are synchronised for all defects (all lines overlap), but change periodically in accordance with the defect positions. (b) The frequency of defect oscillations grows linearly with ν, if the time scale $\tau = \xi R^2/K$ stays constant, for instance when ν changes due to an increase in activity σ_0.

σ_0, then oscillations would slow down as $f^a \sim 1/R$. On the other hand, if all other system parameters remain the same, ν grows with radius, which affects the shape and with it the length of the orbit. However, comparing the lengths of the trajectories in Figure 5.5 this effect should be small and should not change the frequency scaling dramatically.

Defect pair formation

Both the rotation of defects along their trajectories and the reduction of defect separation with increasing activity is the result of the active flow vortices in the shell. The effective attraction of defects into pairs is mediated by the active flow vortices that form in between them, which in turn are controlled by the underlying director. In the tetrahedral configuration the nematic has a characteristic tennis ball texture [Nelson, 2002; Vitelli and Nelson, 2006], but for generic values of α_0 this texture is skewed, such that each two defects form a separated spiral. The flow vortices accordingly acquire a sink- or source-like component, depending on the tilt in the spiral. As can be seen for instance in Figure 5.7 (b), the paired defects have a sink-like vortex in between them which keeps them together. This active attraction mechanism requires the possibility of radial flows to accommodate this influx, which is guaranteed in the thin film approach and is an advantage compared to a strictly two-dimensional model, in which such flows would be prohibited by in-plane continuity.

Special choices of α_0

We now comment on the special choices of α_0 left out in the previous discussion. Bend-dominated ($\alpha_0 = 0$) and splay-dominated ($\alpha_0 = \pi/2$) textures have a similar dynamics. Starting from the initial tetrahedron, the defects move away in the θ-direction for small activity, which is also captured by $\delta\phi = 0$ in (5.117). The dynamical regime starts at a higher activity, $\nu^* \approx 2.0$ and $\nu^* \approx 1.6$, respectively.

The main difference to the previous dynamics is that the defects keep passing through a tetrahedral or near-tetrahedral configuration for increasing ν, even though the orbits become thinner in one direction. The minimal defect separation decreases at first, but approaches the limit of $\approx 50°$ for high activity. The case of comparable splay and bend ($\alpha_0 = \pi/4$) is quite different, because there is no dynamical regime. The initial motion is mainly in the ϕ-direction, $\delta\theta \ll \delta\phi$ from equations (5.116) and (5.117). The defects always relax into a paired configuration, with defect distance decreasing with ν, but there is no steady motion.

5.6. Motion of two +1 defects

Our model can also be used to study the active motion of +1 defects in an active shell, of which there are two in the ground state of a shell with polar symmetry. Such defects can differ in their geometric type, that is they can be more bend-like or more splay-like. In the one-constant approximation any choice of α_0, that is any combination of splay and bend, results in an energy-minimising texture. This degeneracy is lifted if the elastic constants become unequal. For polar order on a sphere the smallest anisotropy in elastic constants renders pure bend or pure splay textures energetically favoured and spirals become unstable [Vitelli and Nelson, 2006]. In active polar gels, however, this is not the case. Sufficiently large activity is theoretically predicted to favour spiral defects even at unequal elastic constants [Kruse et al., 2004; Elgeti et al., 2011]. Such defects, with different degrees of tilt, were also observed experimentally in active suspensions of biological filaments [Nedelec et al., 1997; Keber et al., 2014]. Moreover, spiral-like structures in two dimensions are rotating due to their strong circulatory active flows and should thus lead to more interesting defect dynamics than pure bend or pure splay textures. We therefore consider all textures allowed in the one-elastic constant approximation, as they might be relevant for active nematics and active polar gels.

First, we note that in the definition of the director (5.46) the choice of α_0 that fixes the defect geometry, that is whether the two defects are more aster-like or more vortex-like, depends on the locations of the defects. In other words, the same choice of α_0 may produce a splay-dominated or a bend-dominated texture around the defects, depending on where they are. We would like to study the motion of two defects of a fixed type so we can single out the effect of the phase, that is that two defects for instance stay asters when they move. We remove this ambiguity with a constant shift c_1,

$$\alpha_0 = c_1 + \tilde{\alpha}_0 \,, \tag{5.119}$$

and vary $\tilde{\alpha}_0 \in [0, \pi/2]$ instead. We find c_1 by imposing an aster-geometry for $\tilde{\alpha}_0 = 0$ for all defect positions. Consider a director with two +1 defects in the plane. If points

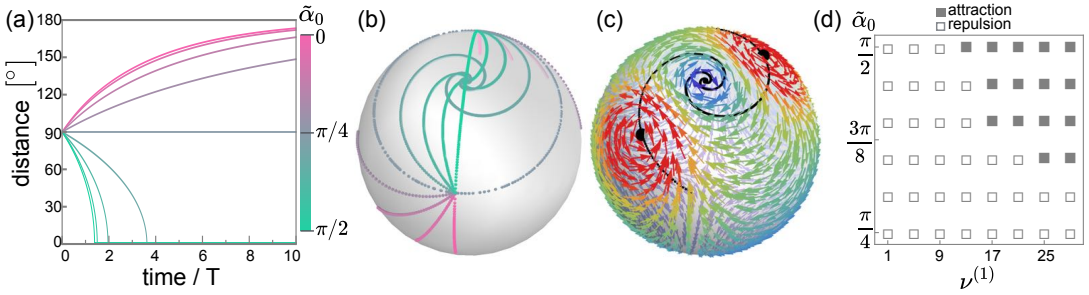

Figure 5.9: Active advection leads to repulsion of two aster-like defects and attraction of two vortex-like defects. (a) Distance of the two +1 defects over time for different local director geometry, controlled by $\tilde{\alpha}_0$, which varies in steps of $\pi/16$. Here, the motion of defects is due to active advection only, with $\tilde{K} = 0$. (b) Perfect asters ($\tilde{\alpha}_0 = 0$) or vortex defects ($\tilde{\alpha}_0 = \pi/2$) move along geodesics, but in general the defects move on outward or inward spiralling trajectories. Two perfect spirals ($\tilde{\alpha}_0 = \pi/4$) move along a circular path, without changing their distance. (c) Two spiral-like defects ($\tilde{\alpha}_0 = 5\pi/16$) are attracted to each other by the sink-like flow vortex that forms in between them. (d) When elasticity is included, attraction of +1 defects is found only above a threshold $\nu^{(1)}$ and for large enough tilt $\tilde{\alpha}_0$.

in the vicinity of the defect at z_1 are described with $z(s) = z_1 + \rho e^{is}$, then the condition for an aster geometry around this defect reads

$$s = \alpha(s) = c_1 + \arg(\rho e^{is}) + \arg(z_1 - z_2)\,, \tag{5.120}$$

which leads to

$$c_1 = -\arg(z_1 - z_2)\,. \tag{5.121}$$

A similar condition formulated in the vicinity of the second defect leads to $c_1 = -\arg(z_2 - z_1)$, which is equivalent to (5.121) since $\arg(z_2 - z_1) = \arg(z_1 - z_2) + \pi$.

We first consider the limit of very strong active advection, setting $\tilde{K} = 0$ and scaling the time with T instead of τ. Figure 5.9 (a) shows the time evolution of the distance between two +1 defects, which move due to their self-generated active flows. We find that the defects are either attracted to or repelled from each other, depending on the local director geometry controlled by $\tilde{\alpha}_0$. Two defects that are aster-like ($0 \leq \tilde{\alpha}_0 < \pi/4$) experience repulsion and relax into an antipodal configuration. On the other hand, two defects which are vortex-like ($\pi/4 < \tilde{\alpha}_0 \leq \pi/2$) are drawn towards each other. In this idealised setting without elasticity, they merge into a +2 boojum.

For symmetry reasons, two perfect asters ($\tilde{\alpha}_0 = 0$) and two perfect vortex defects ($\tilde{\alpha}_0 = \pi/2$) can only move along their connecting geodesics, which is seen from the trajectories in Figure 5.9 (b). In general, however, the trajectories spiral outward or inward until the defects reach maximal separation or merge, respectively. Two perfect spiral defects ($\tilde{\alpha}_0 = \pi/4$) keep a constant distance, rotating around each other on a

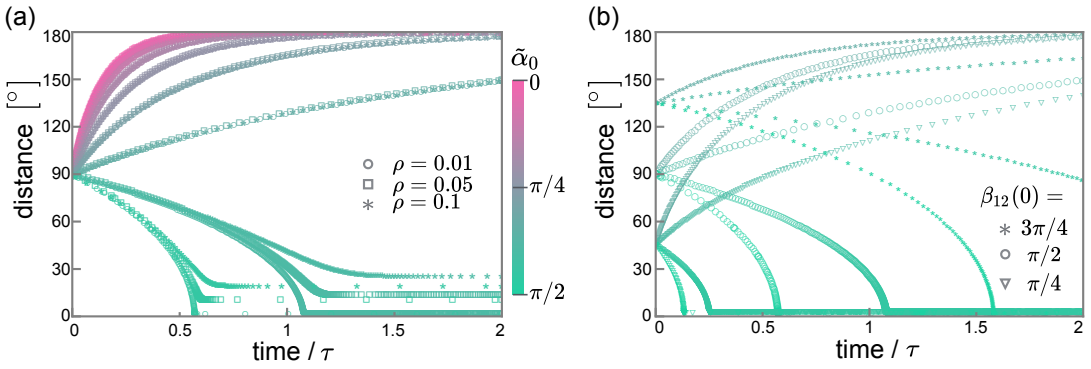

Figure 5.10: When elastic effects are included ($\tilde{K} = 1$) high activity is required to observe attraction between vortex-like defects. (a) Here, $\nu = 15$ and strongly vortex-like defects ($\tilde{\alpha}_0 = 7\pi/16, \pi/2$) are drawn together. The opening angle ρ of the circle, which is used to calculate the advection of a $+1$ defect, only affects the dynamics at short distances, as seen from the splitting of the lines with different symbols. (b) Whether the defects attract or repel each other depends on the activity ν and the phase $\tilde{\alpha}_0$, here $\tilde{\alpha}_0 = 5\pi/16, 3\pi/8, 7\pi/16, \pi/2$ from top to bottom for each symbol, but not on the initial distance $\beta_{12}(0)$ between the defects.

circular path. The initial distance of the defects does not affect the type of dynamics.

The mechanism of this active attraction or repulsion is, like for half-defects, related to the nature of the flow in between the two $+1$ defects. As discussed in Section 5.3.2, if two $+1$ defects are not antipodal then there is an additional ± 1 flow singularity pair on the great circle which goes through the defects. The $+1$ singularity forms in the middle of the connecting geodesic and the -1 stagnation point forms on the opposite side (see Figure 5.4 (e)). The $+1$ singularity is source-like for $0 \leq \tilde{\alpha}_0 < \pi/4$ and sink-like for $\pi/4 < \tilde{\alpha}_0 \leq \pi/2$, causing the repulsive or attractive flows, respectively. Figure 5.9 (c) shows the active flow with the additional sink-like vortex in between the defects ($\tilde{\alpha}_0 = 5\pi/16$), that draws the defects in on a spiralling trajectory. The defects' trajectory rotates in a direction opposite to the rotation of their local flow vortices.

When elastic effects are included, with $\tilde{K} = 1$, a sufficient activity is necessary for active attraction of $+1$ defects to occur, since there is additional elastic repulsion between the defects that acts along their connecting line. We find that for $\nu^{(1)} < 12$ the two defects move into the antipodal position for all $\tilde{\alpha}_0$. For stronger activity, we recover active attraction if defects are sufficiently vortex-like, however the limiting case is not at $\tilde{\alpha}_0 = \pi/4$. Figure 5.9 (d) shows a parameter scan over $\nu^{(1)}$ and $\tilde{\alpha}_0$, giving a rough idea of the boundary between the parameter regions of repulsion and attraction. For this plot, the defects have an initial separation of $7\pi/8$ and a parameter combination of $\nu^{(1)}$ and $\tilde{\alpha}_0$ corresponds to attraction of defects, if the distance measured at a time $t = 2\tau$ is smaller than the initial distance. As an example, in Figure 5.10 (a) the time evolution of the defect distance is shown for $\nu^{(1)} = 15$ and

different $\tilde{\alpha}_0$. Attraction is found for the two highest values, $\tilde{\alpha}_0 = 7\pi/16$ and $\tilde{\alpha}_0 = \pi/2$.

The advection of $+1$ defects is obtained as the average flow over a circle of opening angle ρ centred at the defect. In Section 5.4.3 we argued that the dominant contribution to this average that is directed and not winding is $\sim \mathcal{O}(1)$ in a ρ-expansion. Hence, the motion of two $+1$ defect should not depend on ρ, which is related to the core size of the defect as $\rho = r_c/R$. Indeed, Figure 5.10 (a) shows that the dynamics does not depend on ρ for most part of the data, in agreement with our theoretical analysis. However, when the defects come closer, a larger ρ smoothens the attraction, slowing the defects down and increasing their stationary distance. The effect becomes visible at distances of $\approx 60°$. Finally, Figure 5.10 (b) shows that the initial distance $\beta_{12}(t = 0)$ does not seem to affect whether defects attract or repel each other for the same $\tilde{\alpha}_0$.

In summary, there are thresholds for the activity and for the tilt of the director, above which the antipodal configuration of two $+1$ defects is always unstable. Interestingly, in such cases the defects again collapse into a very close pair, that resembles a $+2$ defect. In an experimental system, fluctuations in the tilt of a spiral around the limiting value of $\tilde{\alpha}_0$ might lead to oscillations between the antipodal and the collapsed configurations.

5.7. Additional $\pm 1/2$ defect pairs

When activity $|\sigma_0|$ or radius R are increased such that $\sqrt{K/|\sigma_0|} = l_a < R$ the nematic shell will transition into the state of active turbulence, where defect pairs are created and annihilated continually and defects move on chaotic trajectories, see Section 2.2.3. Here, we are interested in a regime which is not yet in the realm of active turbulence, such that a small number of additional $\pm 1/2$ defect pairs may be created on top of the four $+1/2$ defects. These would typically occur at random positions, as fluctuations, and distort the oscillatory dynamics. However, the defects could also be specifically guided into configurations which are metastable as a result of a balance between elastic forces and active flows and which produce more complex active flow vortices.

To study such situations we imagine an active nematic shell of larger radius, but with other physical parameters comparable to the previous two sections, where we fixed the radius to R_0. We call the time scale used in Sections 5.5 and 5.6 $\tau_0 = \xi R_0^2/K$. For reference, we use the ratio $\nu_0 = \xi R_0 h_0^2 \sigma_0/K\mu r_c = 1$, that corresponds to the regime of tetrahedral to planar oscillations in Figure 5.5. If relative to this choice of parameters the radius is increased as $R = \gamma R_0$, with $\gamma > 1$, then in order to keep the

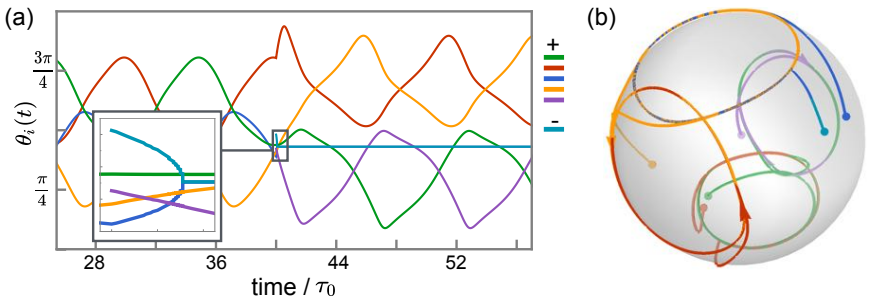

Figure 5.11: (a) Four $+1/2$ defects show regular oscillations before and shortly after the insertion of an additional $\pm 1/2$ defect pair, as seen from $\theta_i(t)$ for $i = 1, \ldots, 6$ with $\gamma = 2$. *Inset:* Close-up on the rapid annihilation of the additional pair. (b) Defects resume similar trajectories after the fluctuation, but with different pairing.

dimensionless elasticity parameter

$$\tilde{K} = \frac{\tau K}{\xi R_0^2 \gamma^2} = 1 \tag{5.122}$$

the time scale has to change to

$$\tau = \frac{\gamma^2 \xi R_0^2}{K} = \gamma^2 \tau_0 \,. \tag{5.123}$$

Alternatively, the value of $\tilde{K}$ could be decreased accordingly, but having a small parameter in the dynamical equations might lead to numerical instabilities. It is therefore favourable to adapt the time scale of simulations instead, also for comparison with previous results. The new activity to elasticity ratio is then $\nu = \gamma \nu_0$, that is with increasing shell size active effects dominate over elastic with the factor γ. Based on the analysis of the flow at the defects in Section 5.4.2, the $+1/2$ defects are advected by the dominant flow in the direction of their symmetry axis and $-1/2$ defects only move due to elastic effects. This should capture their main dynamics very well, as we found that both the next-lowest order directed flow contribution at a $+1/2$ defect as well as the lowest order directed flow at a $-1/2$ defect are at most $\sim \mathcal{O}(\rho)$. They are therefore negligible with respect to the main flow at $+1/2$ defects, which is $\sim \mathcal{O}(1/\rho)$, because here we are interested in the collective dynamics of the defects, rather than the small-distance behaviour of an annihilating $\pm 1/2$ pair.

Simulations with n_{pair} additional $\pm 1/2$ defect pairs were performed with different initial conditions and an additional mechanism for defect annihilation, since defects of opposite strengths attract each other elastically with a force that diverges when they come close, see equations (5.69) and (5.70). On a shell of radius R_0, when two opposite half-defects are closer than $\rho_0 = 0.1$, they coalesce and are removed from the director. The value of ρ_0 is estimated from Figure 1 B in Reference [Keber et al., 2014],

where the radius of the vesicle is $R \approx 25\mu$m and the size of the defective region, which is devoid of microtubules, can be approximated as $r_c \approx 2.5\mu$m. For increasing size this cut-off is adapted as $\rho = 0.1/\gamma$. In the simulation the annihilation is realised by setting $m_k = 0$ for both. As shown below, starting with n_{pair} additional pairs after a time scale characteristic for a particular γ all pairs will have coalesced and only the four $+1/2$ defects remain. This mode represents a system with a fluctuation, which produces transient defect pairs. The defect creation is mimicked by inserting them at positions chosen randomly from a uniform distribution on the sphere. Configurations in which at least one pair is closer than 10ρ are discarded.

First, the situation with $n_{\text{pair}} = 1$ is studied. We consider a system in which four defects undergo tetrahedral-planar oscillations and inject one $\pm 1/2$ pair at a random position. The positions of the two new defects are produced independently from a uniform distribution. Figure 5.11 (a) shows a representative example for how the dynamics reacts to this perturbation for $\gamma = 2$. One of the $+1/2$ defects annihilates with the $-1/2$ on a time scale which is very short compared to the period of oscillation. After the annihilation event the remaining defects resume the oscillation, but in a different pairing. Figure 5.11 (b) illustrates this, since the defect trajectories before and after the transient defect pair are of a similar shape. Similarly, when all defects are placed at random positions the annihilation events happen rapidly, leaving the minimal four-defect state in the oscillating regime. The same is found for more than one additional pair of half-defects in the system, for which data is shown in Appendix C. This indicates that the oscillatory state is stable, as long as additional defect pairs occur as fluctuations and are not produced constantly.

A different approach is to design metastable dynamic defect arrangements by inducing defects at specific positions, in which the elastic forces are almost balanced along a trajectory on which defects move due to active advection. Of course, as the defect distances are changing during this motion, elastic effects will distort the motion and eventually lead to coalescence. The time scale for this to happen should however increase with γ. Configurations with metastable vortices could be achieved if n_{pair} is even, because then all $+1/2$ defects could form pairs and, consequently, active flow vortices. Their arrangement will depend on their number, but we hypothesize a symmetric arrangement in which the negative defects cluster at the poles in equal numbers and the positive defects form a band of vortices along the equator. If n_{pair} is odd, there is inevitably a $+1/2$ defect that is not in a pair and, moreover, a symmetric arrangement of $-1/2$ defects at the poles is not possible.

The simplest many-defect configuration that is metastable is shown in Figure 5.12 (a) and (b), in which there are two additional $\pm 1/2$ defect pairs. The six $+1/2$ defects are allocated to three flow vortices arranged equidistantly around the equator, with

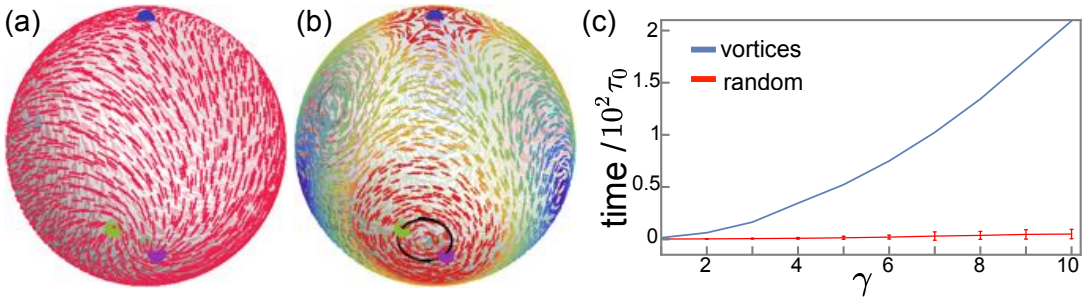

Figure 5.12: (a) Orientation field with eight defects, six $+1/2$ and two $-1/2$, producing a symmetric flow vortex arrangement. (b) Corresponding flow structure with six equidistant vortices on the equator, $+1/2$ defect trajectories marked in black. (c) Time to first coalescence event for the eight defect configuration with vortices as shown in (b) and of a random configuration of eight defects (averaged over 100 initial conditions) over γ.

another three vortices rotating in the opposite direction in between them. The three-fold symmetry of this flow field is guided by the flow singularities at the $-1/2$ defects, which have $\mathcal{I} = -2$ and are located at the poles. This configuration is transient and reduces to the four-defect-state due to coalescence of oppositely charged defects. The corresponding defect trajectories are shown in Figure C.2 in Appendix C. In Figure 5.12 (c) the time to the first annihilation event for this metastable configuration is compared to the average time to first annihilation for $n_{\text{pair}} = 2$ with random initial configurations. The annihilation time for the metastable configuration is orders of magnitude higher than the one for random configurations and increases considerably with γ.

The metastability of such configurations could be aided by an advantageous manipulation of the shell shape, for instance by trapping positive defects in regions of higher curvature [Selinger et al., 2011]. The shape of the shell may change due to the presence of the defects themselves, and the radial flows at the active vortices they generate. This opens an interesting direction of tuning specific many-defect states before the onset of active turbulence by exploiting the topologically required singularities in both flow and director. For instance, in a polar shell a metastable configuration could be composed of four +1 defects distributed around the equator and two -1 defects, one at each pole.

5.8. Shell deformations

In analogy with equation (3.7) for a planar film, we can write a kinematic boundary condition for the outer surface of the shell and incorporate the continuity equation (5.5) to obtain an equation for the time evolution of a deviation $\delta R(t)$ from the

spherical shape of the shell

$$\partial_t(R + h_0 + \delta R(t)) = -\boldsymbol{\nabla}_s \cdot \bar{\boldsymbol{u}}_\perp, \tag{5.124}$$

where $\boldsymbol{\nabla}_s$ is the in-plane divergence and $\bar{\boldsymbol{u}}_\perp$ the thickness-averaged in-plane flow

$$\bar{\boldsymbol{u}}_\perp(\theta, \phi) = \int_R^{R+h_0} \mathrm{d}r\, \boldsymbol{u}_\perp(r, \theta, \phi) \sim h_0 U_0. \tag{5.125}$$

From this the scaling for shape deformation follows

$$\partial_t(\delta R(t)) \sim \frac{h_0 U_0}{R}. \tag{5.126}$$

Thus speed of deformations is a factor $\varepsilon\rho$ smaller than the speed of a $+1/2$ defect, see (5.89), and a factor ε smaller than the speed of a $+1$ defect, see (5.90). Thus, the shell deforms much more slowly than the defects move and can be neglected to first approximation, which is what we have done in the preceding Sections on defect dynamics. In analogy to the scalings derived in Reference [Joanny and Ramaswamy, 2012], we can fix the volume of the spherical shell, $V_0 = 4\pi R^2 h_0$, which leads to

$$\partial_t(\delta R(t)) \sim \frac{V_0 h_0^2 \sigma_0}{\mu R^4} = \frac{\varepsilon V_0 \sigma_0}{R^2 \mu}. \tag{5.127}$$

In the case of four half-defects the flow at the defects is tangential, so now deformations are expected around the defects in this case. Deformations should occur at the centres of the two vortices, which form in between the defects, due to the sink- or source-like nature of the flow. These will be small, according to (5.126). On the other hand, in the case of $+1$ defects the strongest deformations can be expected to be at the locations of the defects themselves, which would lead locally to a different scaling

$$\partial_t(\delta R(t)) \sim \frac{\varepsilon}{\rho} U_0. \tag{5.128}$$

These deformations could significantly alter the motion of $+1$ defects, as we expect that $\varepsilon/\rho \sim \mathcal{O}(1)$. However, numerical simulations would be better suited to explore this coupling and an interesting direction for further work.

5.9. Discussion

5.9.1. Active flow in a spherical shell

In a shell of active liquid crystal the flow has to have in general a total winding of +2. Since the, likewise necessary, defects in the director generate flow singularities that are determined entirely by their topological strength, these are generally not sufficient to satisfy the topological constraint. Only in the case of two +1 defects in an antipodal configuration are the defect-centred flow vortices the only ones present. During the dynamics of four half-defects two counterrotating flow vortices typically dominate the flow and drive the motion of defects on their circular orbits. It appears that two +1/2 defects can generate one stable active flow vortex, if the underlying director has an appropriate spiral-like structure, and this can be utilised to design metastable states with larger numbers of half-integer defects and a more complex flow structure, see Figure 5.12.

Simple stagnation points with $\mathcal{I} = -1$, although they cannot be generated by defects, seem to occur in the shell in regions with nearly uniform directors, see examples in Figure 5.4 (e) and (f). For the extensile material considered in the Figure the stagnation point is oriented with its extensional flow locally along the director. This interesting correspondence of almost uniform, non-singular director regions with extensional flows might explain why simple stagnation points do not occur at defects.

In the case of two +1 defects we have only considered the tangential flow component so far. However, like in a flat drop on a surface, the sink- or source-like nature of the active flow at these defects should lead to local deformations of the shell interface of the types found in Section 4.4. Specifically, in the extensile case the shell should become thicker at asters and thinner at vortices. In the case of two vortices there could be a dewetting of the spherical active film at both defects, similar to what we described in Section 4.4.2, leaving behind a ring of active liquid crystal. The ring of MT-bundles that forms in small vesicles instead of four half-defects [Keber et al., 2014] could be an experimental realisation of such a dewetting active nematic layer. We also expect the formation of cusps in the case of spirals, as obtained in Section 4.4.3 for the droplet on a surface.

5.9.2. Active attraction of +1/2 defects

Our model predicts numerically that +1/2 defects form rotating pairs and that the defect separation in each pair decreases with the parameter ν, roughly linearly as can be seen in Figure 5.5 (a). This active attraction has not been described in the experimental work on active nematic vesicles [Keber et al., 2014], perhaps because the

parameter range realised so far has not allowed to observe it. Since changing the activity severely is difficult in these experiments, we propose to vary the size of the vesicle in order to probe higher values of ν and test the predicted dynamics, such as in Figure 5.7. Vesicles in the range 20 - 100 μm in diameter should show regular, non-turbulent dynamics, but so far only vesicles of up to 60 μm in diameter were reported and, moreover, no size-dependence of the dynamics was given [Keber et al., 2014].

As opposed to Reference [Keber et al., 2014], in our model the speed of $+1/2$ defects does not depend on the radius, see equation (5.89). It is plausible that since the self-propulsion is generated locally, the film thickness should influence it, whereas the system size should be irrelevant. This speed also changes the prediction for the radius-dependence of the frequency of defect oscillations, see equation (5.118), which could also be tested experimentally by changing the size of active vesicles.

The dynamical regime starts at a critical parameter $\nu^* \sim \mathcal{O}(1)$, below which the defects settle into distorted tetrahedra. From (5.99) we have $\nu = \tau/(\rho T)$, where ρT is the time scale of the self-propulsion of the $+1/2$ defect. We can conclude that at the transition this active time scale becomes comparable to the time scale of elastic relaxation, which is a plausible criterion for the switch from an elasticity-dominated to an active, dynamical regime. Another new result from the thin film approach is that this transition can be induced by increasing the film thickness or the shell radius, see equation (5.95), not just by increasing the activity.

In two-dimensional active nematics in the active turbulent phase, with a large number of pairs of $\pm 1/2$ defects, the defect separation is known to be related to the intrinsic length scale l_a [Giomi, 2015], see equation (2.17). It might be possible to establish an analytical relationship between the positive half-defect separation in our model and l_a, since $\nu \propto 1/l_a^2$. For instance, one could try to rewrite the system of equations (5.101)- (5.102) in terms of the six defect distances, rather than the eight coordinates. This could be further simplified by assuming some symmetries in the defect trajectories, so that perhaps the system could be solved for the steady state in this low-parameter subspace.

5.9.3. Interaction of +1 defects

We compare our findings regarding the rotation and translation of two $+1$ defects in the spherical shell with the only other work that considers the interaction of two unit strength active defects. Elgeti et al. [2011] find in simulations that contractile asters settle at a finite distance from each other, which increases as the activity is reduced. Further, extensile spirals are found to rotate around each other at a fixed distance [Elgeti et al., 2011], which is equivalent to our result, see Figure 5.9. In our

model, extensile vortices attract each other, and extensile asters repel. Considering the duality between extensile and contractile activity, the phenomenology is thus the same as in the numerical work of Elgeti et al. [2011], although in their model it is not clear what causes the defects to overcome elastic repulsion, since it is strictly two-dimensional and no sinks or sources are allowed. In a different, but related theoretical work it is found that two co-rotating active rotors are spiralling towards each other if they are pullers, that is if each of them produces radially inward flow locally, and spiralling outwards if they are pushers [Fily et al., 2012]. Although the problem setting is different, in particular there is three-dimensional passive fluid everywhere in between the rotors, the similarity is nonetheless encouraging. Note, that our description of two vortices as counter-rotating refers to the situation when they are positioned on opposite sides of the sphere. When the same vortices were located close to each other on the same side of the sphere they would be called co-rotating.

5.9.4. Contractile activity

Our results can be extended to contractile active fluids by changing the sign of the activity σ_0. The reversed sign of the flow exchanges the role of splay-like and bend-like distortions in the orientation. As the sign of ν is also reversed, the direction of motion of positive half-integer defects is reversed, but the tetrahedral-planar oscillations and the formation of vortices – with opposite rotation sense – is unchanged. Likewise, the attraction or repulsion between integer strength defects is reversed, that is in a contractile system two aster defects in a spherical shell are attracted to each other due to active flows.

5.9.5. Difference between polar and nematic shells

We predict a different scaling of the defect dynamics in thin polar shells compared to nematic shells. This follows from the different parameter combinations in the defining parameters (5.99) and (5.100) for half-integer and unit strength defects, respectively. In polar shells only integer strength defects are present and, notably, the radius of the shell becomes irrelevant for the type of dynamics that the defects undergo.

The simplest many-defect state for polar shells could be constructed from two additional ± 1 defect pairs on top of two $+1$ defects. The -1 defects should be situated at the two poles, guiding the flow into a four-fold symmetric vortex configuration with eight vortices along the equator, of which four should be centred at $+1$ defects. However, because elasticity and activity for unit strength defects have the same scaling with radius, metastability cannot be achieved by increasing the radius, but for instance by a large increase in activity.

5.9.6. Simulations of many-defect states

Initialising the additional defects on top of four $+1/2$ defects at independent positions is an approximation we make, because it is difficult to generate a director in which the two opposite defects are close, but are oriented in a way that the positive will move away from the negative [Giomi et al., 2013]. In the realm of our model, it is possible to control this precisely in the plane for a single $\pm 1/2$ defect pair by manipulating α_0 in a way similar to the procedure for two $+1$ defects (see Section 5.6), where we are adding a constant that depends on the defect positions. How to adapt this strategy for a situation with multiple defects on the sphere has to be figured out in the future.

In an attempt to mimic the active turbulent state of a nematic on a sphere the simulations were modified, such that an annihilated pair was replaced by a new pair of $\pm 1/2$ defects immediately. They were placed at a random position $(\theta_{new}, \phi_{new} \pm 10\rho/\sin(\theta_{new}))$. The initial separation was necessary for them to not coalesce immediately. In this mode a constant number of additional defect pairs was sustained. However, even for very large γ the annihilation and creation events happen very quickly with positive defects moving toward nearby negative defects on almost straight, rather than chaotic, trajectories. We may conclude that the basic underlying assumption of a rapidly reorienting director prevents our model from reproducing the correct dynamics in the active turbulent regime.

CHAPTER 6

Active nematic shell as a squirmer

One of the central questions that drives research on active fluid droplets is whether and how they swim through a passive medium [Hawkins et al., 2011; Tjhung et al., 2012; Whitfield et al., 2014; Giomi and DeSimone, 2014; Whitfield and Hawkins, 2016]. The active nematic shell studied in Chapter 5 may also be regarded as a type of active droplet that generates a slip velocity on its surface, with which it could both propel itself as a whole and produce specific three-dimensional flows in its surrounding. The new feature is that such propulsion would be driven by static or dynamic arrangements of topological defects in the director and thus would present a different route for generating and controlling an artificial swimmer.

In this chapter we present a first analysis of an active nematic shell as a swimmer, using specific defect configurations. The swimming and rotation of a spherical shell can be obtained from integrals of the active flow on its surface. The integrals are solved analytically for the situation of one +2 defect and of two +1 defects with arbitrary positions by reducing them to complex contour integrals using the stereographic projection. For four +1/2 defects they are evaluated numerically for the positions they move through during their periodic dynamics. Finally, we consider a different, triangular defect arrangement, for which the steady state defect positions are obtained in simulations akin to those of Chapter 5. The swimming and rotational velocities of such a shell are calculated numerically.

6.1. Squirmer model for a microscopic swimmer

The swimming of organisms at the microscale is dominated by viscous forces, hence the hydrodynamics of the flow field $\boldsymbol{u}$ and the pressure p of the fluid surrounding the swimmer is governed by the Stokes equation, $-\boldsymbol{\nabla} p + \mu \nabla^2 \boldsymbol{u} = 0$, with appropriate boundary conditions, in particular on the surface of the swimmer [Lauga and Powers, 2009]. The linearity and time-independence of this equation poses constraints on the mechanisms of swimming that exist at these length scales [Lauga, 2011]. Biological

swimmers often move by periodic body deformations, which have to be non-reciprocal in time [Purcell, 1977]. Another strategy that is exploited by microorganisms with a fixed spherical or ellipsoidal shape, such as *Volvox* or *Paramecium*, is to generate a fluid flow on the surface by thousands of cilia or flagella that coat the microorganisms and move synchronously [Pak and Lauga, 2014]. A similar mechanism is employed by artificial chemical swimmers, such as emulsion droplets that swim due to Marangoni flows on their surface [Schmitt and Stark, 2016]. This type of propulsion is well captured by the squirmer model, which was first developed by Lighthill and Blake [Lighthill, 1952; Blake, 1971] and describes a model swimmer with a given slip velocity on the surface, from which its swimming speed and the three-dimensional flow it generates in the external fluid is calculated. Here, we use this model to characterise the swimming of an active nematic shell.

A direct relationship between the surface flow and the swimming speed is available for a sphere [Stone and Samuel, 1996]. The translational and rotational velocities of the spherical swimmer, $\boldsymbol{U}(t)$ and $\boldsymbol{\Omega}(t)$, are obtained as surface integrals of the slip velocity [Stone and Samuel, 1996]

$$\boldsymbol{U}(t) = -\frac{1}{4\pi R^2} \oiint_M \boldsymbol{u}_\perp \,\mathrm{d}S \tag{6.1}$$

$$\boldsymbol{\Omega}(t) = -\frac{3}{8\pi R^3} \oiint_M \hat{\boldsymbol{e}}_r \times \boldsymbol{u}_\perp \,\mathrm{d}S\,, \tag{6.2}$$

where M is the surface of the sphere of radius R. We will use the active flow fields from Chapter 5 as the surface velocity $\boldsymbol{u}_\perp$, see equation (5.50). Writing out the Cartesian components of (6.1) and (6.2) we get

$$\begin{aligned}\boldsymbol{U}(t) = -\frac{1}{4\pi}\int_0^{2\pi}\int_0^{\pi} \sin\theta \big\{&(\cos\theta\cos\phi\, u_\theta - \sin\phi\, u_\phi)\hat{\boldsymbol{x}} \\ &+(\cos\theta\sin\phi\, u_\theta + \cos\phi\, u_\phi)\hat{\boldsymbol{y}} - \sin\theta\, u_\theta\hat{\boldsymbol{z}}\big\}\,\mathrm{d}\theta\,\mathrm{d}\phi\end{aligned} \tag{6.3}$$

and

$$\begin{aligned}\boldsymbol{\Omega}(t) = -\frac{3}{8\pi R}\int_0^{2\pi}\int_0^{\pi} \sin\theta \big\{&-(\sin\phi\, u_\theta + \cos\theta\cos\phi\, u_\phi)\hat{\boldsymbol{x}} \\ &+(\cos\phi\, u_\theta - \cos\theta\sin\phi\, u_\phi)\hat{\boldsymbol{y}} + \sin\theta\, u_\phi\hat{\boldsymbol{z}}\big\}\,\mathrm{d}\theta\,\mathrm{d}\phi\,.\end{aligned} \tag{6.4}$$

In order to make use of the complexified form of the active flow (5.51), we combine

the translational and rotational velocities into a vector with complex components

$$\begin{aligned}\boldsymbol{I}(t) &:= -4\pi\boldsymbol{U}(t) + i\frac{8\pi R}{3}\boldsymbol{\Omega}(t) \\ &= U_0 \int_0^{2\pi}\int_0^{\pi} \sin\theta(\tilde{u}_\theta + i\tilde{u}_\phi)\left\{(\cos\theta\cos\phi + i\sin\phi)\hat{\boldsymbol{x}}\right. \\ &\qquad \left. + (\cos\theta\sin\phi - i\cos\phi)\hat{\boldsymbol{y}} - \sin\theta\,\hat{\boldsymbol{z}}\right\}\mathrm{d}\theta\,\mathrm{d}\phi\,, \end{aligned} \tag{6.5}$$

from which one recovers the two velocities as

$$\boldsymbol{U}(t) = -\frac{1}{4\pi}\,\mathrm{Re}\{\boldsymbol{I}(t)\} \tag{6.6}$$

$$\boldsymbol{\Omega}(t) = \frac{3}{8\pi R}\,\mathrm{Im}\{\boldsymbol{I}(t)\}\,. \tag{6.7}$$

To simplify the calculation further we introduce

$$I_1 := I_x + iI_y = U_0 \int_0^{2\pi}\mathrm{d}\phi \int_0^{2\pi}\mathrm{d}\theta\,\sin\theta(\cos\theta + 1)e^{i\phi}(\tilde{u}_\theta + i\tilde{u}_\phi) \tag{6.8}$$

$$I_2 := I_x - iI_y = U_0 \int_0^{2\pi}\mathrm{d}\phi \int_0^{2\pi}\mathrm{d}\theta\,\sin\theta(\cos\theta - 1)e^{-i\phi}(\tilde{u}_\theta + i\tilde{u}_\phi)\,, \tag{6.9}$$

which can be written entirely in terms of (r, ϕ) using the relations summarised in Appendix B.2. Taking all expressions together, we want to calculate

$$I_1 = U_0 \int_0^{\infty}\mathrm{d}r\,\frac{8R^2r^3}{(r^2+R^2)^3}\int_0^{2\pi}\mathrm{d}\phi\,e^{i\phi}u(r,\phi) \tag{6.10}$$

$$I_2 = -U_0 \int_0^{\infty}\mathrm{d}r\,\frac{8R^4r}{(r^2+R^2)^3}\int_0^{2\pi}\mathrm{d}\phi\,e^{-i\phi}u(r,\phi) \tag{6.11}$$

$$I_z = -U_0 \int_0^{\infty}\mathrm{d}r\,\frac{8R^3r^2}{(r^2+R^2)^3}\int_0^{2\pi}\mathrm{d}\phi\,u(r,\phi) \tag{6.12}$$

for the different defect configurations considered in Chapter 5. Through $I_x = (I_1 + I_2)/2$ and $I_y = (I_1 - I_2)/2i$ the translational and rotational velocities of the shell can be recovered.

Having non-zero in-plane divergence is a requirement for swimming [Stone and Samuel, 1996; Schmitt and Stark, 2016]. Suppose the surface flow is divergence-free, $\boldsymbol{\nabla}_\perp \cdot \boldsymbol{u}_\perp = 0$. There is then a vector potential which only has a radial component, $\boldsymbol{A} = A\hat{\boldsymbol{e}}_r$, such that the slip velocity can be written as $\boldsymbol{u}_\perp = \boldsymbol{\nabla} \times \boldsymbol{A}$. Using Stokes' theorem, it can be shown that the integral (6.1) vanishes for such a flow, see Appendix D.1. In our model the surface flow is in general not in-plane divergence-free, since we impose three-dimensional incompressibility. We therefore expect to find defect configurations with non-zero self-propulsion and rotation of active nematic shells.

6.2. One, two and four defect configurations

6.2.1. One +2 defect

Although this type of defect is usually unfavoured energetically, a shell with one +2 defect is an obvious candidate for a swimming object due to the broken symmetry of this configuration. We therefore first consider a director with one +2 defect at $z_1 = r_1 e^{i\phi_1}$. From equation (5.56) the active flow for this configuration is

$$u = -\frac{\tilde{\sigma}_0}{2} e^{-i2\alpha_0} \left(\frac{re^{-i\phi} - r_1 e^{-i\phi_1}}{re^{i\phi} - r_1 e^{i\phi_1}} \right)^2 \left\{ \frac{r}{R} e^{i2\phi} - \frac{r^2 + R^2}{R} \frac{e^{i\phi}}{re^{-i\phi} - r_1 e^{-i\phi_1}} \right\} \tag{6.13}$$

To rewrite the term $e^{-i2\alpha(z,\bar{z})}$, we made use of the identity

$$e^{i2\arg(z)} = \frac{z}{\bar{z}}. \tag{6.14}$$

Without loss of generality we can move the position of the defect to the origin of the complex plane, $z_1 = 0$. Then the complexified flow on the surface of the shell takes the simple form

$$u(r,\phi) = \frac{\tilde{\sigma}_0}{2} \frac{R}{r} e^{-i2\alpha_0} e^{-i2\phi}, \tag{6.15}$$

so the integrals (6.10)-(6.12) vanish, because in all three of them the integrand is winding in ϕ. Thus, one +2 defect does not generate propulsion or rotation of a spherical nematic shell. Note, that (6.15) has the projection to the plane $u_x + iu_y \propto e^{i\phi}\bar{u} \propto e^{i3\phi}$, which has the correct winding of $\mathcal{I} = 3$ at the origin.

6.2.2. Two +1 defects

Consider a director with two +1 defects, as in Section 5.6. Again, one defect is placed at the origin, so the defects have the positions $z_1 = 0$ and z_2. In this case, the slip velocity in the complex form (5.56) reads

$$u(z,\bar{z}) = -\frac{\tilde{\sigma}_0}{2} e^{-i2\alpha_0} \frac{\bar{z}(\bar{z} - \bar{z}_2)}{z(z - z_2)} \left\{ \frac{re^{i2\phi}}{R} - \frac{re^{i\phi}}{2} \left(\frac{R}{r} + \frac{r}{R} \right) \left(\frac{1}{\bar{z}} + \frac{1}{\bar{z} - \bar{z}_2} \right) \right\} \tag{6.16}$$

$$= -\frac{\tilde{\sigma}_0}{2} e^{-i2\alpha_0} \left\{ \frac{1}{2} \left(\frac{r}{R} - \frac{R}{r} \right) \frac{re^{-i\phi} - r_2 e^{-i\phi_2}}{re^{i\phi} - r_2 e^{i\phi_2}} + \frac{re^{-i\phi}}{2} \left(\frac{R}{r} + \frac{r}{R} \right) \frac{1}{re^{i\phi} - r_2 e^{i\phi_2}} \right\} \tag{6.17}$$

This function is not holomorphic in z, so to evaluate the ϕ-integral in (6.10)-(6.12) with the help of the residue theorem we use a standard transformation to a new

complex variable [Alexander and Ravnik, 2012]

$$w = e^{i(\phi-\phi_2)}\,, \tag{6.18}$$

for which $\bar{w} = 1/w$. In this new variable the integrand becomes holomorphic

$$u(w) = -\frac{\tilde{\sigma}_0}{2} e^{-i2(\alpha_0+\phi_2)} \frac{1}{w(w-r_2/r)} \left\{ \frac{1}{2}\left(\frac{r}{R} - \frac{R}{r}\right)\left(1 - \frac{r_2}{r}w\right) - \frac{1}{2}\left(\frac{R}{r} + \frac{r}{R}\right)\right\}. \tag{6.19}$$

The integrals then become complex contour integrals over the unit circle γ using the transformation

$$\int_0^{2\pi} \mathrm{d}\phi = \frac{1}{i}\int_\gamma \frac{\mathrm{d}w}{w}\,. \tag{6.20}$$

With $u(w)$ the ϕ-integrals in equations (6.10)-(6.12) become

$$I_\phi = e^{-2i(\alpha_0+\phi_2)} \int_\gamma \frac{\mathrm{d}w}{w - r_2/r}\left(\frac{r^2-R^2}{2Rr}\left(1 - \frac{r_2}{r}w\right) - \frac{r^2+R^2}{2Rr}\right) \times \begin{cases} \frac{e^{i\phi_2}}{w} & \text{for } I_1, \\ \frac{e^{-i\phi_2}}{w^3} & \text{for } I_2, \\ \frac{1}{w^2} & \text{for } I_z. \end{cases} \tag{6.21}$$

The integrand has a simple pole at $w_1 = r_2/r$ if $r_2 < r$ and a first, third, or second order pole at $w_2 = 0$, respectively. The corresponding residues $\mathrm{Res}(w_1)$ and $\mathrm{Res}(w_2)$ are given in Appendix D.2. By the residue theorem,

$$I_\phi = e^{-2i(\alpha_0+\phi_2)} 2\pi i\big(H(r-r_2)\,\mathrm{Res}(w_1) + \mathrm{Res}(w_2)\big), \tag{6.22}$$

where $H(r-r_2)$ is the Heaviside step function (see Appendix D.2). Evaluating the r-integrals in (6.10)-(6.12) with this result yields zero in all three cases. For example, for the first integral I_1 the calculation is shown here:

$$I_1 = U_0 \int_0^\infty \mathrm{d}r\, \frac{8R^2r^3}{(r^2+R^2)^3} I_\phi \tag{6.23}$$

$$\propto \int_0^\infty \mathrm{d}r\, \frac{8R^2r^3}{(r^2+R^2)^3}\frac{R}{r_2} + \int_{r_2}^\infty \mathrm{d}r\, \frac{8R^2r^3}{(r^2+R^2)^3}\frac{\left(R^2r_2^2 - r^2\left(2R^2+r_2^2\right)\right)}{2r^2Rr_2} \tag{6.24}$$

$$\propto \left[-\frac{2R^3\left(2r^2+R^2\right)}{r_2\left(r^2+R^2\right)^2}\right]_0^\infty + \left[\frac{2R\left(r^2\left(2R^2+r_2^2\right)+R^4\right)}{r_2\left(r^2+R^2\right)^2}\right]_{r_2}^\infty \tag{6.25}$$

$$= \frac{2R}{r_2} + \left(-\frac{2R}{r_2}\right) = 0. \tag{6.26}$$

Therefore, two +1 defects in the active nematic shell do not lead to propulsion or rotation either, irrespective of their position. This was to be expected as the flow field for two unit strength defects of the same geometric type has a 2-fold rotation

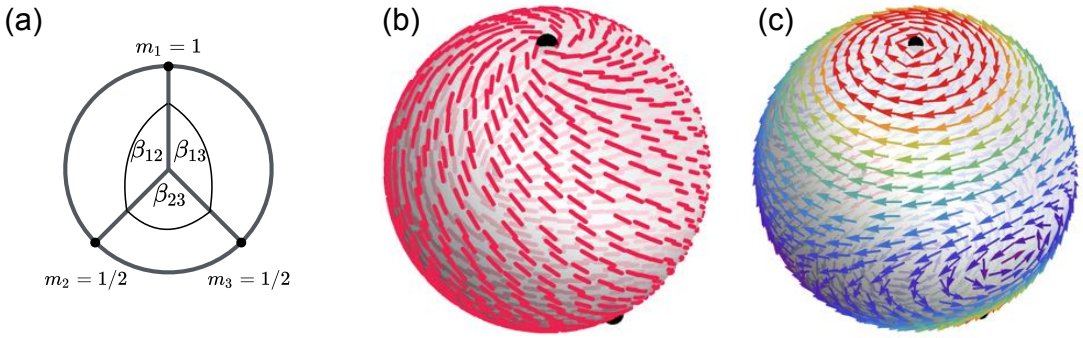

Figure 6.1: (a) Schematic view of the isosceles triangle of one $+1$ defect and two $+1/2$ defects in a trivalent nematic shell. (b) Nematic director in a trivalent shell with $\alpha_0 = \pi/4$, which generates a perfect spiral defect at one pole. (c) Active flow from equation (5.50) corresponding to the director in (b), consisting of four vortices and two simple stagnation points.

symmetry, visible for instance in Figure 5.4 (d,e) and Figure 5.9 (c). The axis of rotation is perpendicular to the great circle passing through the defects at the midpoint between the defects. This symmetry reflects the counterrotating nature of the flow, so the integral over the whole surface vanishes. A promising direction to break this symmetry and render the shell motile would thus be a manipulation of the local defect geometries. This would require the phase α_0 to vary over the shell.

6.2.3. Four $+1/2$ defects

For four half-defects in the shell we find numerically a similar result as for the previous two cases. Calculating the integral $\boldsymbol{I}(t)$ along the trajectories found for different values of ν leads to velocities that are numerical zeros for all points in time. Although not obvious from the defect trajectories themselves, the flows that the defects generate when they move on these trajectories are distorted versions of the symmetric counterrotating vortices found in the limit of two spiral defects, so this result is not surprising. It is to be expected, though, that in an experimental realisation the vortices and trajectories will be distorted by noise, which should result in small erratic motions of the shell. The study of this, possibly biased, diffusion is deferred to further work.

6.3. Trivalent nematic shells

6.3.1. Three defects in isosceles triangle

In passive nematic shells apart from two $+1$ defects and four $+1/2$ defects there is a third configuration of defects that is found in experiments [Koning et al., 2016] and simulations: one $+1$ defect and two $+1/2$ defects, arranged on a great circle in an isosceles triangle as indicated in Figure 6.1 (a). Given these defect strengths, it can

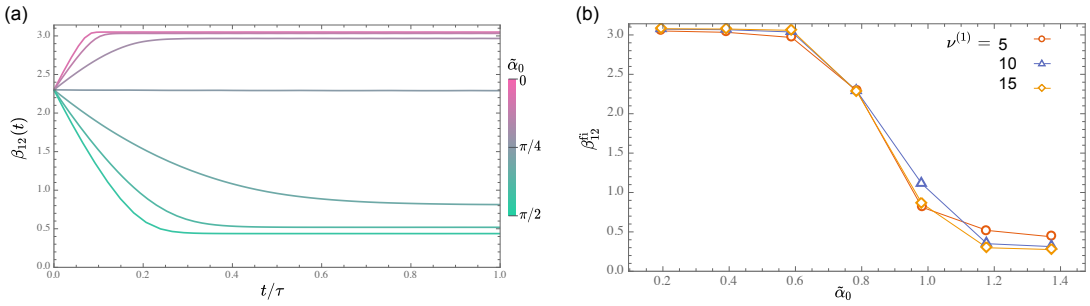

Figure 6.2: (a) Time evolution of the angular distance β_{12}, between the $+1$ and one of the $+1/2$ defects, for different values of the phase $\tilde{\alpha}_0$ for $\nu^{(1)} = 5$. (b) Final angle β_{12}^{fi} of the new isosceles triangle that the active system settles into for three values of activity and different $\tilde{\alpha}_0$. Connecting lines are a guide to the eye.

be shown that the optimal configuration has a sharp angle of $\beta_{23} = 2\arccos\frac{2}{3} \approx 96.4°$ at the $+1$ defect and the angles $\beta_{12} = \beta_{13} = \pi - \arccos\frac{2}{3} \approx 131.8°$ at the $+1/2$ defects [Koning et al., 2016]. In a passive nematic it is metastable due to the high energy barriers to the two and four defect states. The total elastic energy of this configuration is given in equation (5.76).

A trivalent active nematic shell breaks the symmetry along the axis of the triangle, therefore it is a good candidate to generate net motion and rotation along this axis due to the active flows it generates.

6.3.2. Active flows and defect motion

In general, the defect positions change due to the active flows they generate. The equilibrium isosceles triangle is stable under active flows only for $\alpha_0 = \pi/4$. For this choice the $+1$ defect is a perfect spiral and the velocity of the two half-defects is purely azimuthal, as shown in Figures 6.1 (b) and (c). The triangle is thus in constant rotation, but the angles do not change. The two half-defects again create a vortex, which is counterrotating compared to the flow at the $+1$ defect, but the symmetry is broken and there are two additional pairs of ± 1 singularities in between those.

We study the deformation of the equilibrium triangle in an active shell in simulations like in Section 5.4. In the simulations the active advection is obtained from the integral (5.80) for all three defects and both $\nu^{(1)}$ and ρ are required as parameters, since this is a combination of defects with different active velocity scalings. We choose $\rho = 0.1$. The motion of the $+1$ defect, if any, is expected to be slow compared to the $+1/2$ defects, but it is included for completeness.

First, we note that in the absence of activity, $\nu^{(1)} = 0$, the three defects relax into the isosceles triangle from random initial configurations. Therefore, with nonzero activity they are initialised in a specific triangular configuration chosen such that no

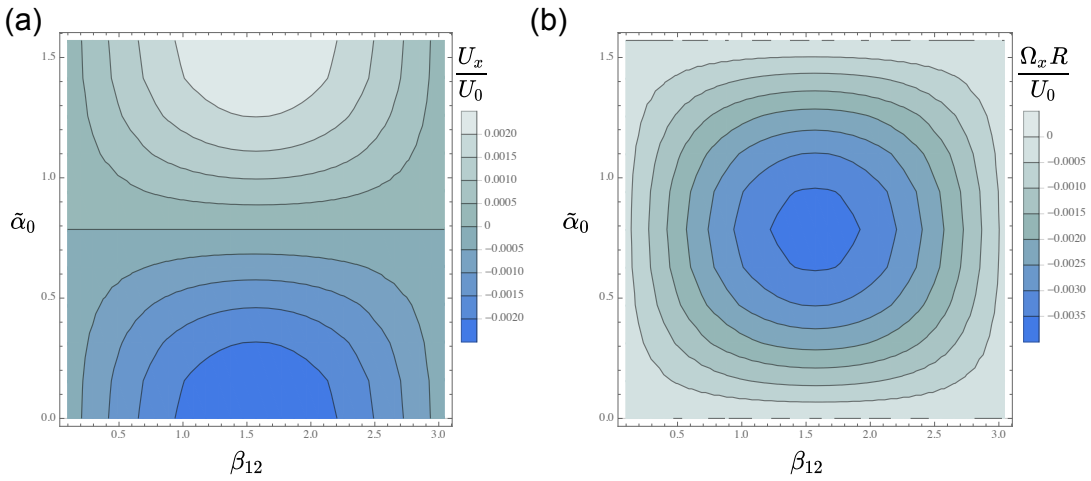

Figure 6.3: The x-component of the (a) translational and (b) angular velocity of a trivalent active nematic shell for different angles β_{12} and phases $\tilde{\alpha}_0$. Plots are obtained by numerically evaluating equations (6.3) and (6.4). The active flow scale U_0 was given in equation (5.88).

defects are at the poles of the coordinate system. We place the defects on the equator, with the positions

$$\theta_1^{(0)} = \theta_2^{(0)} = \theta_3^{(0)} = \pi/2, \quad \phi_1^{(0)} = 0, \quad \phi_2^{(0)} = \beta_{12}, \quad \phi_3^{(0)} = \beta_{12} + \beta_{23}\,. \tag{6.27}$$

Like in the case of two $+1$ defects, we want to gauge α_0 such that the geometric type of the $+1$ defect does not change when the defects move, in order to make the effect of α_0 unambiguous. In the setup of Section 5.6, that is with $\alpha_0 = c_2 + \tilde{\alpha}_0$, this condition can be formulated as

$$s = \alpha(s) = c_2 + s + \frac{1}{2}\arg\left(z_1 - z_2\right) + \frac{1}{2}\arg\left(z_1 - z_3\right). \tag{6.28}$$

So with $c_2 = -(\arg(z_1 - z_2) + \arg(z_1 - z_3))/2$ the geometry of the director around the $+1$ defect is a perfect aster for $\tilde{\alpha}_0 = 0$ and the amount of bend increases with $\tilde{\alpha}_0 \in (0, \pi/2]$.

When activity is turned on, $\nu > 0$, the $+1/2$ defects move out of the initial triangle, if $\tilde{\alpha}_0 \neq \pi/4$, and settle into a new isosceles triangle. No motion of the $+1$ defect occurs. In Figure 6.2 (a) the time evolution of the triangle is shown for different values of $\tilde{\alpha}_0$. For $\tilde{\alpha}_0 < \pi/4$, that is if the $+1$ defect is an aster-like spiral, the two $+1/2$ defects move further apart. In the other case, they move closer together. In Figure 6.2 (b) the final angle β_{12}^{fi}, that characterises the new isosceles triangle, is shown. Interestingly, the value of the active parameter $\nu^{(1)}$ does not seem to have a substantial effect on the final state of the defects, but most important is the phase. With higher activity, however, the final angle is approached more quickly.

6.3.3. Swimming and rotation

The components of (6.3) and (6.4) are evaluated numerically for isosceles triangles with different opening angles. The integrals are taken over the spherical surface with circular cut-outs with radius 0.01 around each defect, but the results were checked to be independent of this radius. As expected, for the particular orientation of the triangle chosen in Section 6.3.2 the x-component of both the translational and the angular velocities is nonzero in general, which are shown in Figure 6.3. The other two components are negligible for this defect configuration, see Appendix D.3. Consistent with the results of Section 6.2, both U_x and Ω_x vanish in the limits $\beta_{12} = 0$ and $\beta_{12} = \pi$. These limits correspond to one $+2$ defect and two antipodal $+1$ defects, respectively.

For any value of the phase, U_x has maximal magnitude if the two half-defects are half-way between the $+1$ defect and the other pole, $\beta_{12} = \pi/2$. For any defect position, the magnitude is maximised when $\tilde{\alpha}_0 = 0$ or $\tilde{\alpha}_0 = \pi/2$, which corresponds to the $+1$ defect being an aster or a vortex, respectively. The magnitude decreases as $\tilde{\alpha}_0$ approaches $\pi/4$, in which case the shell does not move any more. The shell moves in direction of the $+1$ defect if $\pi/4 < \tilde{\alpha}_0 < \pi/2$ and in the opposite direction if $0 < \tilde{\alpha}_0 < \pi/4$.

In general the shell also rotates about the axis given by its direction of translation. The rotation is anticlockwise with respect to the direction of motion for $0 < \tilde{\alpha}_0 < \pi/4$ and clockwise for $\pi/4 < \tilde{\alpha}_0 < \pi/2$. It is maximised when the shell is not moving, $\tilde{\alpha}_0 = \pi/4$, and in addition when the two half-defects are halfway between the poles.

6.4. Discussion

We have investigated analytically and numerically the swimming behaviour of the active nematic shells considered in Chapter 5 and a trivalent shell, assuming a spherical outer surface. The former turn out to be stationary and not rotating. In particular, we find that polar active shells in the ground state cannot swim. The four half-defects also leave the shell stagnant while they move on their periodic orbits, not just over one period but in every instant of time. This was surprising, since four half-defects at random positions generally lead to small, but non-zero propulsion, which was estimated by simply adding the three-dimensional direction vectors of the defects for different positions [Whitfield, 2016].

Inspired by the work on passive nematic shells [Koning et al., 2016], we have found one defect configuration that generates both swimming and rotation of the active shell. The swimming and rotation are along the same axis, therefore leading to straight trajectories. For very high activity and $\tilde{\alpha}_0$ close to $\pi/4$ we observed in

simulations an oscillatory behaviour of the two half-defects, which should be further investigated. Moreover, it would be interesting to check the dynamics that occurs for random initial defect positions at nonzero activity, which might perhaps lead to more complex trajectories. The magnitude of both velocities is rather small compared with the magnitude of active flows on the surface, for instance $\sim 10^{-3}U_0$ in the case of translation, see Figure 6.3 (a). Nonetheless, we look forward to experimental realisations of such trivalent active shells.

A frictional contact of the active fluid in the shell with the external, passive fluid of viscosity μ_{ext} might influence the active dynamics within the shell. To check when this effect becomes relevant we can estimate the frictional stress σ_S on the shell from the Stokes drag $F_S = 6\pi\mu_{ext}RU$ acting on a spherical swimmer [Batchelor, 1967],

$$\sigma_S = F_S/4\pi R^2 = \frac{3}{2}\frac{U}{R}\mu_{ext}. \tag{6.29}$$

For the swimming velocity we can assume $U \sim U_0 \sim h_0^2\sigma_0/\mu R$, see equation (5.88). The back-propagating frictional stress should be negligible if it much smaller than the active stress, $\sigma_S \sim \mu_{ext}h_0^2\sigma_0/\mu R \ll \sigma_0$, which yields a condition on the viscosity ratio

$$\frac{\mu}{\mu_{ext}} \gg \varepsilon^2. \tag{6.30}$$

Only if the external medium has a large enough viscosity will the active hydrodynamics in the shell be distorted.

Another mechanism to swim is through deformations of the shell due to radial flows at the interface [Vlahovska, 2016]. In an alternative calculation one would take the radial component of the active flow and relate the small deformations resulting from it to the swimming velocity [Vlahovska, 2016]. It is reasonable to assume that this approach for the four half-defects would lead to similar, if not identical, results compared with the squirmer approach, where it is also effectively the non-divergence-free part of the flow that contributes to the propulsion velocity. On the other hand, it might lead to propulsion for non-spherical shells with two +1 defects in an asymmetric configuration due to the additional symmetry breaking in the shape. For instance, with two vortex-like spiral defects one might expect the formation of two cusped bumps, locally similar to the shapes of flat droplets in Section 4.4.3. After the equilibration of the shape the residual active flows should lead to a rotation of these bumps around an axis, which might lead to rotary motion of the shell as a whole.

CHAPTER 7

Discussion and conclusion

7.1. Active thin films

In this work we have modelled a film of active liquid crystal, in which the director takes a general form with a collection of topological defects. The local active flow at a defect not only leads to rotation and self-propulsion for specific defects, but also to active advection of the other defects in the system and to deformations of the film. These deformations were studied for a droplet of finite size in Chapter 4, where we found that +1 defects can severely deform the film in their vicinity leading to dips or holes or to cusps, depending on the geometric type of the defect. Similar results should also hold locally in an extended film. Generally, in a polar active film arrays of ± 1 defects may be expected, since active defects occur spontaneously [Nedelec et al., 1997], and our results for a single defect may be generalisable to an active dewetting of such films. An important next step would be a numerical investigation of the shape evolution equations for an active film with defects, since more quantitative results are difficult to achieve with analytical methods due to the strong non-linearities. Another interesting geometry to consider in this context is an active film coating a cylinder, which might have applications for bacterial biofilms in pipes.

7.2. Motile drops on surfaces

We have given an analytic description of dynamic steady state motion of an active drop on a planar substrate. The exact expression for the instantaneous active flow in the drop leads to the identification of two key requirements for self-propulsion. These are an asymmetrically splayed or bent orientation field, for instance induced by a topological defect in the interior of the drop, and sufficient surface friction provided by the substrate for the drop to push itself forward. The active flows in the drop are primarily driven by horizontal variations in the orientation and the coupling to the shape contributes mainly at the contact line, where it can generate flows that work

against drop propulsion. A motile drop will become stagnant, treadmilling on the spot, when the surface friction drops below a certain value.

In the case of a contractile droplet with splay, our model also suggests a possible scenario for the bulk of a polarised and motile cell extract of actomyosin [Verkhovsky et al., 1999], where the effective friction is mediated by focal adhesions that attach the actomyosin gel to the substrate. For instance in Figure 4.6 (a) the bulk of active fluid flows in direction of the splay, away from the defect, therefore such a cell extract would move to the right. The back-slip of the drop at the substrate could be accounted for by a reduced number of focal adhesions. This flow field is also in agreement with the forward flow of cytosol observed experimentally in a moving cell viewed from above [Keren et al., 2009] and with with numerical results for the three-dimensional flow in a crawling cell [Tjhung et al., 2015].

Shape deformations of active droplets could be studied experimentally on vesicles filled with an active suspension, where the surface tension can be reduced by applying hypertonic stress [Keber et al., 2014]. To impose a particular, static orientation of active filaments the drop could be placed on a micro-patterned substrate [Vignaud et al., 2012], specifically to induce axisymmetric defect configurations which would allow to observe the corresponding stationary shapes of the drop. In order to manufacture controllable crawling active droplets one could also manipulate the director in the droplet into asymmetric configurations by an underlying patterned material. For instance, the substrate might be a passive nematic controlled by a magnetic field [Guillamat et al., 2016a].

This model could be extended to allow for different anchoring on the two surfaces of the drop or film. For instance, recent work on active nematic films found that homeotropic anchoring at the substrate and "active" anchoring at the free surface, which prefers tangential anchoring in the extensile case, leads to spontaneous flows as well as irregular undulations and break up of the free surface [Blow et al., 2017]. Such conditions would also more closely resemble the situation studied for passive nematic drops and films, in which cusps occur at the surface [De Gennes and de Gennes, 1970].

7.3. Active fluids in curved geometries

We presented an active thin film model for a spherical shell, which has elucidated for the first time the structure of active flows in this geometry. The relationship between an active defect and its flow singularity derived for a planar film also holds locally in the shell. However, the global flow structure is constrained by the topological requirement of a total winding of +2 in the flow. This typically leads the formation of two counterrotating flow vortices, one in each hemisphere, paralleling the vortex

formation seen in other types of confinement [Woodhouse and Goldstein, 2012; Wioland et al., 2013; Sknepnek and Henkes, 2015]. This flow structure has important implications for the motion of defects and for the swimming properties of the shell.

Tetrahedral to planar oscillations of four $+1/2$ defects are obtained in our model and are attributed to the advection of defects in pairs by the two counterrotating vortices. As the activity is increased the two vortices become more pronounced and the pair of $+1/2$ defects within each are pulled closer together in an effective attraction of like-charge defects. These oscillations appear at a finite threshold of the activity, below which the defects form static configurations of distorted tetrahedra. Linear stability analysis captures the mode of deformation and the threshold for defect motion. The oscillations of four half-defects are found to be stable against additional half-defect pairs created randomly in larger shells. If the defects are instead induced at specific positions, it is possible to generate more complex, metastable flow vortex configurations.

The dynamics of polar configurations with only integer strength defects is similar and we find attraction of pairs of aster-like $+1$ defects in extensile active nematic shells, but repulsion for vortex-like defects. The speed of defects in the polar case is shown to have different scaling than for nematic shells, in particular the type of motion does not depend on the radius in the former case whereas it does in the latter. This fundamental difference in the dynamics of polar shells compared to nematic contributes to the classification of active phenomena according to their symmetry and should hold for other topologies in the same way.

Our work establishes the formation of vortices under confinement, see Section 2.5.2, as a generic feature also for ALCs on spherical surfaces. It would be interesting to extend to other topologies, for instance tori with additional handles. Similarly to the passive case [Jesenek et al., 2015] one can expect metastable states with multiple $\pm 1/2$ defect pairs and a non-trivial dynamics of those defects due to active flows. The toroidal topology is particularly appealing, because it is still relatively simple and therefore might be analytically tractable. Moreover, the MT-based active nematic has very recently been realised in bulk toroidal droplets for the first time [Wu et al., 2017], so more experimental data on this type of confinement should be available soon.

7.4. Active nematic shells as artificial swimmers

It seems that the problem of self-propulsion for active nematic shells is not a straightforward one, at least in the absence of hydrodynamic interactions with boundaries or other shells. In particular, the slip velocity has to be sufficiently asymmetric, which is not in general fulfilled by nematic directors with regular defect arrangements. How-

ever, objects which are immobile on their own can swim collectively by hydrodynamic interactions with each other [Alexander et al., 2009]. For instance, one observation in the experiments done by Sanchez et al. [2013] was a roughly oscillatory motion of two active nematic droplets when in close proximity.

Another promising direction is the calculation of the full, three-dimensional flow field that an active shell generates in the external passive fluid. For the immobile shells, which have two counterrotating vortices, one can expect that the three-dimensional flow has nematic symmetry and is extensile or contractile along the axis of the vortices, depending on the geometric phase of the director. A collection of such shells should then display the same collective hydrodynamic behaviour like a suspension of extensile or contractile shakers, but on considerably larger length scales than the suspension of filaments in the active layer.

Conversely, by reversing the boundary conditions, with a shear-free interface on the inside of the shell, one would be able to find the three-dimensional flows that an active layer would drive in the interior of the drop. This would perhaps shed light on the generation of cytoplasmic flows in cells and could also be extended to the advection of a passive object in this flow. The latter could represent as a simple model for a cell nucleus set in motion by cytoplasmic flows, which is a problem of current interest [Kumar et al., 2014; Fruleux and Hawkins, 2016].

7.5. Elastic anisotropy

We have taken a one elastic constant approximation as a basic assumption, but in systems of elongated filaments like those of the MT-based active nematics one can expect anisotropy. In particular, long flexible nematogens are much more compliant to bend distortions than to splay, which is clearly visible in the dynamics of this system [Sanchez et al., 2013]. In fact, it is known that the splay constant diverges in the limit of infinitely long filaments [De Gennes, 1976].

Available results on passive nematics on a sphere with unequal elastic constants allow to speculate about their effect on the active system. A spherical two-dimensional nematic with infinite elastic anisotropy has a ground state that is very different from the tetrahedral configuration [Shin et al., 2008; Bates, 2008]. Four half-defects are all in the same plane, sitting at the vertices of a rectangle of variable ratio. This rectangle can become infinitely thin, such that each two defects form a $+1$ defect. If $K_1/K_3 \to \infty$, splay is inhibited and the director is pure bend. There is a continuous family of degenerate ground states, which can be achieved by starting with two antipodal vortex defects and rotating the director by an arbitrary angle along a great circle going through the defects. This procedure yields textures with half-defects forming

spiral-like pairs, similar to the pairs we find in the active nematic at high activity, see Section 5.5.2. For strong, but finite anisotropy the situation is similar, but the defects' positions can deviate slightly from the planar one and they never come close enough to form +1 defects [Shin et al., 2008; Bates, 2008]. This suggests that a lower bend constant might favour the formation of tight pairs in the active regime. On the other hand, since flexible filaments bend more easily, the two transitions for four defects – from skewed tetrahedron to regular oscillations and then to active turbulence – would require smaller values of activity, respectively. Situations with unequal constants may be explored in simulations of active nematics. For instance, a good candidate system with softer bend might be a collection of flexible active polymers on a sphere [Prathyusha et al., 2016; Zhang and Chen, 2011], which would complement a hydrodynamic approach.

7.6. Possible applications

Potential microfluidic or biomimetic applications of active droplets might be the following. The first direction is the transport of substances encapsulated in a self-propelled nematic droplet. Because all ingredients of MT-based active nematics are non-toxic[1] this material might be used for directed transport of medical substances to a location in the body where they would be released from the vesicle or emulsion drop. The second direction relates to microfluidics, since active droplets could be prepared in a way that they generate a complex flow field around them over a long period of time, controlled by the ATP concentration inside the droplet. Such flows could be useful to provide mixing of fluid or even size-dependent filtering of micro-particles in the droplet's surrounding. This filtering property was recently discovered in the complex flow fields generated by starfish larvae to collect food, which are composed of six differently sized vortices [Gilpin et al., 2016], and could be recreated with artificial active droplets.

7.7. Conclusion

In summary, we have studied thin films of active liquid crystals in different geometries, where topological defects play an important role. Our results emphasise the importance of defect-driven flows for the large-scale dynamics of these systems, but also show how global topological constraints can feedback on the local defect motion. Further, we found interesting new features like strong shape deformations, or even rupture, of active films and activity-mediated attractive interactions between defects. These rely on a finite film thickness and cannot be grasped with purely two-dimensional models.

[1] Apart from PEG, they are part of every human cell.

The qualitative predictions we make are in good agreement with numerical simulations [Tjhung et al., 2015] and existing experiments [Keber et al., 2014]. This justifies the assumptions described in the beginning of this work and encourages to analyse other geometries with similar minimal models.

APPENDIX A

Calculations for a thin film

A.1. Active stress tensor divergence in a thin film

$$(\boldsymbol{\nabla}\cdot\boldsymbol{\sigma}^a)_x = \partial_x(n_x^2 - 1/3) + \partial_y(n_x n_y) + \partial_z(n_x\frac{z}{h}\boldsymbol{n}\cdot\boldsymbol{\nabla}_\perp h) \tag{A.1}$$

$$= \partial_x(n_x^2) + \partial_y(n_x n_y) + n_x\frac{1}{h}\boldsymbol{n}\cdot\boldsymbol{\nabla}_\perp h \tag{A.2}$$

$$= \boldsymbol{\nabla}_\perp\cdot(n_x\boldsymbol{n}) + n_x\frac{1}{h}\boldsymbol{n}\cdot\boldsymbol{\nabla}_\perp h \tag{A.3}$$

$$= \frac{1}{h}(h\boldsymbol{\nabla}_\perp\cdot(n_x\boldsymbol{n}) + n_x\boldsymbol{n}\cdot\boldsymbol{\nabla}_\perp h) \tag{A.4}$$

$$= \frac{1}{h}\boldsymbol{\nabla}_\perp\cdot(hn_x\boldsymbol{n}) \tag{A.5}$$

$$= \frac{\varepsilon}{h_0}\frac{1}{\tilde{h}}\tilde{\boldsymbol{\nabla}}_\perp(\tilde{h}n_x\boldsymbol{n}) \tag{A.6}$$

$$(\boldsymbol{\nabla}\cdot\boldsymbol{\sigma}^a)_y = \partial_x(n_x n_y) + \partial_y(n_y^2 - 1/3) + \partial_z(n_y\frac{z}{h}\boldsymbol{n}\cdot\boldsymbol{\nabla}_\perp h) \tag{A.7}$$

$$= \boldsymbol{\nabla}_\perp\cdot(n_y\boldsymbol{n}) + n_y\frac{1}{h}\boldsymbol{n}\cdot\boldsymbol{\nabla}_\perp h \tag{A.8}$$

$$= \frac{1}{h}\boldsymbol{\nabla}_\perp\cdot(hn_y\boldsymbol{n}) \tag{A.9}$$

$$= \frac{\varepsilon}{h_0}\frac{1}{\tilde{h}}\tilde{\boldsymbol{\nabla}}_\perp(\tilde{h}n_y\boldsymbol{n}) \tag{A.10}$$

$$(\boldsymbol{\nabla}\cdot\boldsymbol{\sigma}^a)_z = \partial_x(n_x\frac{z}{h}\boldsymbol{n}\cdot\boldsymbol{\nabla}_\perp h) + \partial_y(n_y\frac{z}{h}\boldsymbol{n}\cdot\boldsymbol{\nabla}_\perp h) + \partial_z(\frac{z^2}{h^2}(\boldsymbol{n}\cdot\boldsymbol{\nabla}_\perp h)^2) \tag{A.11}$$

$$\sim \mathcal{O}(\varepsilon^2) \tag{A.12}$$

APPENDIX B

Expressions for spherical geometry

B.1. Spherical coordinates

In the spherical coordinates $r \in [0, \infty)$, $\theta \in (0, \pi)$, and $\phi \in (0, 2\pi)$, the local orthonormal basis vectors are

$$\hat{\boldsymbol{e}}_r = \sin\theta(\cos\phi\hat{\boldsymbol{e}}_x + \sin\phi\hat{\boldsymbol{e}}_y) + \cos\theta\hat{\boldsymbol{e}}_z \tag{B.1}$$

$$\hat{\boldsymbol{e}}_\theta = \cos\theta(\cos\phi\hat{\boldsymbol{e}}_x + \sin\phi\hat{\boldsymbol{e}}_y) - \sin\theta\hat{\boldsymbol{e}}_z \tag{B.2}$$

$$\hat{\boldsymbol{e}}_\phi = -\sin\phi\hat{\boldsymbol{e}}_x + \cos\phi\hat{\boldsymbol{e}}_y \tag{B.3}$$

and their spatial derivatives are

$$\partial_r\hat{\boldsymbol{e}}_r = 0, \quad \partial_\theta\hat{\boldsymbol{e}}_r = \hat{\boldsymbol{e}}_\theta, \quad \partial_\phi\hat{\boldsymbol{e}}_r = \sin\theta\hat{\boldsymbol{e}}_\phi, \tag{B.4}$$

$$\partial_r\hat{\boldsymbol{e}}_\theta = 0, \quad \partial_\theta\hat{\boldsymbol{e}}_\theta = -\hat{\boldsymbol{e}}_r, \quad \partial_\phi\hat{\boldsymbol{e}}_\theta = \cos\theta\hat{\boldsymbol{e}}_\phi, \tag{B.5}$$

$$\partial_r\hat{\boldsymbol{e}}_\phi = 0, \quad \partial_\theta\hat{\boldsymbol{e}}_\phi = 0, \quad \partial_\phi\hat{\boldsymbol{e}}_\phi = -\sin\theta\hat{\boldsymbol{e}}_r - \cos\theta\hat{\boldsymbol{e}}_\theta. \tag{B.6}$$

For a scalar function $f(r, \theta, \phi)$, a vector $\boldsymbol{f}(r, \theta, \phi)$, and a tensor $\boldsymbol{T}(r, \theta, \phi)$:

$$\boldsymbol{\nabla} f = \partial_r f\hat{\boldsymbol{e}}_r + \frac{1}{r}\partial_\theta f\hat{\boldsymbol{e}}_\theta + \frac{1}{r\sin\theta}\partial_\phi f\hat{\boldsymbol{e}}_\phi, \tag{B.7}$$

$$\boldsymbol{\nabla}\cdot\boldsymbol{f} = \frac{1}{r^2}\partial_r\left(r^2 f_r\right) + \frac{1}{r\sin\theta}\partial_\theta\left(\sin\theta f_\theta\right) + \frac{1}{r\sin\theta}\partial_\phi f_\phi, \tag{B.8}$$

$$\begin{aligned}\boldsymbol{\nabla}\cdot\boldsymbol{T} = &\left[\frac{\partial T_{rr}}{\partial r} + 2\frac{T_{rr}}{r} + \frac{1}{r}\frac{\partial T_{\theta r}}{\partial\theta} + \frac{\cot\theta}{r}T_{\theta r} + \frac{1}{r\sin\theta}\frac{\partial T_{\varphi r}}{\partial\varphi} - \frac{1}{r}(T_{\theta\theta} + T_{\varphi\varphi})\right]\hat{\boldsymbol{e}}_r \\ &+ \left[\frac{\partial T_{r\theta}}{\partial r} + 2\frac{T_{r\theta}}{r} + \frac{1}{r}\frac{\partial T_{\theta\theta}}{\partial\theta} + \frac{\cot\theta}{r}T_{\theta\theta} + \frac{1}{r\sin\theta}\frac{\partial T_{\varphi\theta}}{\partial\varphi} + \frac{T_{\theta r}}{r} - \frac{\cot\theta}{r}T_{\varphi\varphi}\right]\hat{\boldsymbol{e}}_\theta \\ &+ \left[\frac{\partial T_{r\varphi}}{\partial r} + 2\frac{T_{r\varphi}}{r} + \frac{1}{r}\frac{\partial T_{\theta\varphi}}{\partial\theta} + \frac{1}{r\sin\theta}\frac{\partial T_{\varphi\varphi}}{\partial\varphi} + \frac{T_{\varphi r}}{r} + \frac{\cot\theta}{r}(T_{\theta\varphi} + T_{\varphi\theta})\right]\hat{\boldsymbol{e}}_\phi.\end{aligned} \tag{B.9}$$

B.2. Useful identities for stereographic projection

With the complex variable $z = R\cot(\theta/2)e^{i\phi} = re^{i\phi}$:

$$\sin\theta = \frac{2Rr}{r^2+R^2}$$

$$\cos\theta = \frac{r^2-R^2}{r^2+R^2}$$

$$\int_0^\pi \mathrm{d}\theta = \int_\infty^0 \mathrm{d}r\left(-\frac{2R}{r^2+R^2}\right) = \int_0^\infty \mathrm{d}r\,\frac{2R}{r^2+R^2}$$

Some useful trigonometric formulae:

$$\cot(x/2) = \frac{1+\cos x}{\sin x} = \frac{\sin x}{1-\cos x} \quad \text{for} \quad x \in (0,\pi]$$

$$\sin(x/2) = \sqrt{\frac{1-\cos x}{2}} \quad \text{for} \quad x \in [0,2\pi]$$

$$\cos(x/2) = \sqrt{\frac{1+\cos x}{2}} \quad \text{for} \quad x \in [-\pi,\pi]$$

$$\sin(2x) = \frac{2\tan x}{1+\tan^2 x}$$

$$\cos(2x) = \cos^2 x - \sin^2 x = \frac{1-\tan^2 x}{1+\tan^2 x}$$

$$\sin(\arctan x) = \frac{x}{\sqrt{1+x^2}}, \quad \cos(\arctan x) = \frac{1}{\sqrt{1+x^2}}$$

B.3. Parametrisation of circles on a sphere

Consider a sphere of radius R centred at the origin. We want to parametrise a circle with opening angle γ. If the circle is centred on the z-axis, it is described by the vector $\boldsymbol{r}(t) = R(\sin\gamma\cos t, \sin\gamma\sin t, \cos\gamma)$, with $t \in [0, 2\pi)$. To have it centred at the point (θ_0, ϕ_0) we apply first a rotation by θ_0 about the y-axis and then a rotation by ϕ_0 about the z-axis,

$$\boldsymbol{r}_\gamma(t) = R\begin{pmatrix} \cos\phi_0\cos\theta_0\sin\gamma\cos t - \sin\phi_0\sin\gamma\sin t + \cos\phi_0\sin\theta_0\cos\gamma \\ \sin\phi_0\cos\theta_0\sin\gamma\cos t + \cos\phi_0\sin\gamma\sin t + \sin\phi_0\sin\theta_0\cos\gamma \\ -\sin\theta_0\sin\gamma\cos t + \cos\theta_0\cos\gamma \end{pmatrix}. \quad \text{(B.10)}$$

For an expression for a small circle with $\gamma \ll 1$ given in terms of $\big(\theta(t), \phi(t)\big)$ we Taylor-expand $\theta(t) = \arccos\big(z_\gamma(t)/R\big)$ and $\phi(t) = \arctan\big(y_\gamma(t)/x_\gamma(t)\big)$ to first order

in γ, and obtain

$$\theta(t) = \theta_0 + \gamma \cos t \tag{B.11}$$

$$\phi(t) = \phi_0 + \frac{\gamma}{\sin\theta_0} \sin t\,. \tag{B.12}$$

Using the stereographic projection described in Section 5.2.1, the image of this circle in the complex plane is

$$\begin{aligned} z(t) &= R\cot(\theta(t)/2)e^{i\phi(t)} \\ &\approx R\cot(\theta_0/2)e^{i\phi_0} + \gamma R e^{i\phi_0}\left(\frac{\cos t}{\cos\theta_0 - 1} + i\frac{\sin t\cot(\theta_0/2)}{\sin\theta_0}\right) \\ &= R\cot(\theta_0/2)e^{i\phi_0} + \gamma R e^{i\phi_0}\frac{\cos t - i\sin t}{\cos\theta_0 - 1} \\ &= z_0 - \frac{\gamma R}{1-\cos\theta_0}e^{i(\phi_0 - t)}\,. \end{aligned} \tag{B.13}$$

Note, that the projected circle is traversed in a direction opposite to that of the original circle on the sphere.

APPENDIX C

Simulations with additional defect pairs

To quantify the annihilation of one additional defect pair we measure the time to coalescence of the $-1/2$ defect with any of the $+1/2$ defects. The measurement time is chosen as $400\tau_0$, to ensure that no coalescence events are missed for large γ. Histograms of these times for 500 initial conditions are shown in Figure C.1. The shape of distribution is similar for different values of γ The mean time to coalescence grows with γ, as can be seen in Figure C.1 (d), although most coalescence events still happen at very small times as the distributions are skewed to the left. Figure C.1 (e) shows the defect trajectories, which correspond to the largest time to coalescence for $\gamma = 10$. This plot elucidates the reason for this long time, since the defects are guided by the active advection into swirly trajectories along which some of the defects encircle each other. This motion is reminiscent of the oscillations found for four defects, but much more erratic and transient. Due to the changing positions of the $+1/2$ defects the direction of motion of the $-1/2$ defect also changes several times, before it finally coalesces with one of the $+1/2$ defects. The positive defects are found to move towards the negative one in a pair, which is an interesting superposition of active advection and elastic attraction. As can be seen from the histograms such dynamics, however, is very rare.

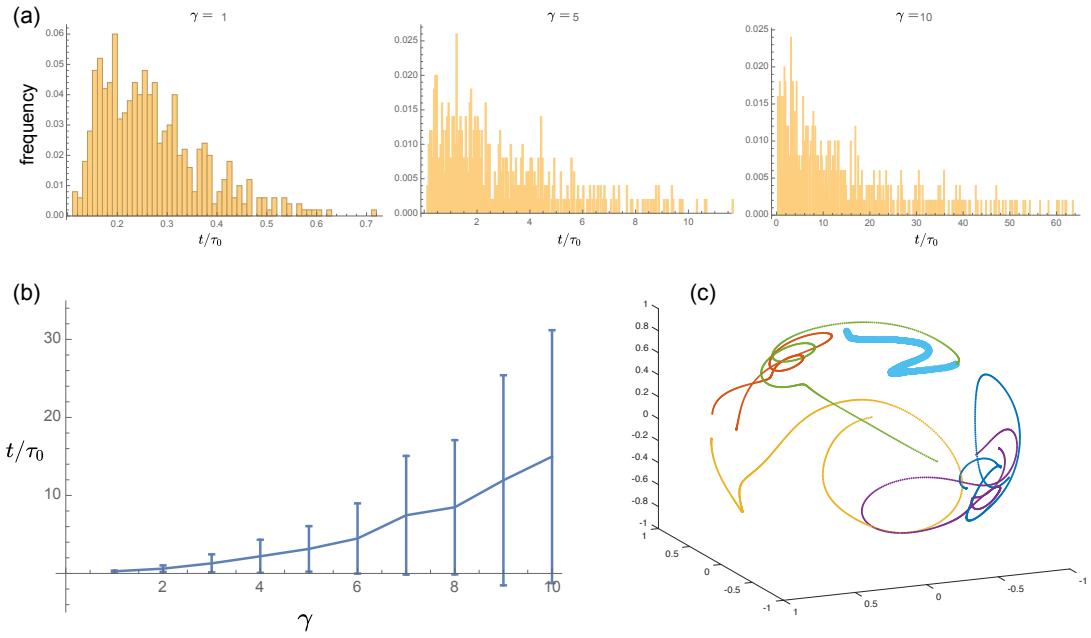

Figure C.1: (a) Histograms of times to coalescence of an additional $\pm 1/2$ defect pair on top of four half-defects, $n_{\text{pair}} = 1$, for $\gamma = 1, 5, 10$. (b) Mean and standard deviation of the time to first coalescence over γ. (c) Defect trajectories for the sample with the longest time for $\gamma = 10$. The $-1/2$ defect is marked with a thick line.

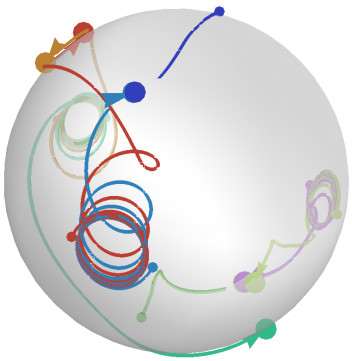

Figure C.2: Trajectories for the coalescence of defect pairs from the metastable configuration shown in Figure 5.12 in the main text.

APPENDIX D

Integrals for squirmer calculations

D.1. Integral of divergence-free slip velocity

With the vector potential $\boldsymbol{A} = A\hat{\boldsymbol{n}}$, where $\hat{\boldsymbol{n}} = n_k\hat{\boldsymbol{e}}_k$ is the unit surface normal of the sphere, the in-plane-divergence-free slip velocity can be written as $\boldsymbol{u}_\perp = \boldsymbol{\nabla} \times \boldsymbol{A}$. The integral (6.1) then becomes

$$\boldsymbol{U}(t) = -\frac{1}{4\pi R^2} \oiint_M \boldsymbol{\nabla} \times \boldsymbol{A} \, \mathrm{d}S \tag{D.1}$$

With Einstein summation implied and ε_{ijk} the Levi-Civita tensor, the i-th component of the integrand is

$$\varepsilon_{ijk}\partial_j A_k = \varepsilon_{ijk}\partial_j(An_k) = \varepsilon_{ijk}(\partial_j A)n_k + \varepsilon_{ijk}A(\partial_j n_k) = \varepsilon_{ijk}(\partial_j A)n_k = -\varepsilon_{kji}\partial_j A n_k, \tag{D.2}$$

where we used $\boldsymbol{\nabla} \times \hat{\boldsymbol{n}} = 0$. We can relate the components of integral (D.1) to a new vector $\boldsymbol{B} = B_k\hat{\boldsymbol{e}}_k$ with $B_k = A \; \forall k$, for which

$$0 = \oiint_M (\boldsymbol{\nabla} \times \boldsymbol{B}) \cdot \mathbf{d}\boldsymbol{S} = \oiint_M \varepsilon_{ijk}\partial_j B_k n_i \, \mathrm{d}S = \oiint_M (\varepsilon_{ij1}\partial_j A n_i + \varepsilon_{ij2}\partial_j A n_i + \varepsilon_{ij3}\partial_j A n_i) \, \mathrm{d}S \,, \tag{D.3}$$

from invoking Stokes' theorem and using the fact that a sphere has no boundary. The sum of all components thus vanishes, but since this result is independent of the basis each of them has to vanish identically.

D.2. Residues for contour integrals in Section 5.1

$$\mathrm{Res}(w_1 = r_2/r) = \begin{cases} \frac{e^{i\phi 2}\left(R^2 \mathrm{r}2^2 - r^2\left(2R^2 + \mathrm{r}2^2\right)\right)}{2r^2 R \mathrm{r}2} & \text{for } I_1, \\ \frac{e^{-i\phi 2}\left(R^2 \mathrm{r}2^2 - r^2\left(2R^2 + \mathrm{r}2^2\right)\right)}{2R\mathrm{r}2^3} & \text{for } I_2, \\ -\frac{rR}{\mathrm{r}2^2} - \frac{r}{2R} + \frac{R}{2r} & \text{for } I_z. \end{cases} \tag{D.4}$$

$$\mathrm{Res}(w_2 = 0) = \begin{cases} \frac{Re^{i\phi 2}}{\mathrm{r}2} & \text{for } I_1, \\ \frac{e^{-i\phi 2}\left(r^2\left(2R^2 + \mathrm{r}2^2\right) - R^2 \mathrm{r}2^2\right)}{2R\mathrm{r}2^3} & \text{for } I_2, \\ \frac{rR}{\mathrm{r}2^2} + \frac{r}{2R} - \frac{R}{2r} & \text{for } I_z. \end{cases} \tag{D.5}$$

The Heaviside step function used in the integrals is defined as

$$H(x) = \begin{cases} 1 & \text{if } x \geq 0 \\ 0 & \text{if } x < 0. \end{cases} \tag{D.6}$$

D.3. Integrals for trivalent shell

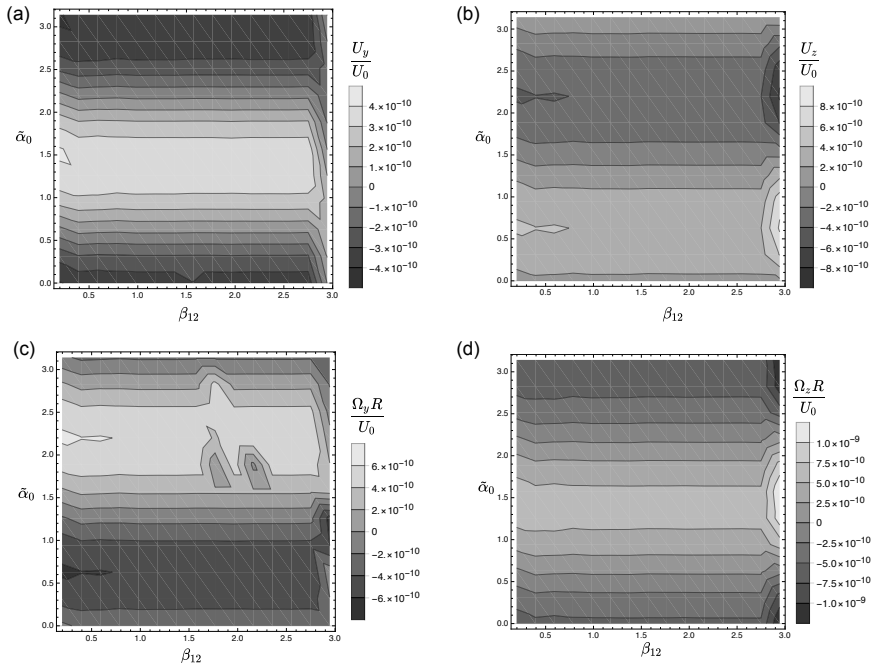

Figure D.1: The y- and z-components of the (a,b) translational and (c,d) angular velocity of a trivalent active nematic shell for different angles β_{12} and phases $\tilde{\alpha}_0$. Plots are obtained by numerically evaluating equations (6.3) and (6.4).

Bibliography

B. Alberts, A. Johnson, J. Lewis, D. Morgan, M. Raff, K. Roberts, and P. Walter. *Molecular Biology of the Cell*. Garland Science, 2014. ISBN 9780815344322. URL https://books.google.co.uk/books?id=_NkpygAACAAJ.

G. P. Alexander and M. Ravnik. Flows induced by defects in active liquid crystals. Unpublished research notes, 2012.

G. P. Alexander, C. M. Pooley, and J. M. Yeomans. Hydrodynamics of linked sphere model swimmers. *Journal of Physics: Condensed Matter*, 21(20):204108–7, Apr. 2009. doi: 10.1088/0953-8984/21/20/204108. URL http://stacks.iop.org/0953-8984/21/i=20/a=204108?key=crossref.4d8e7218a551df8012c3d1542e6b4d94.

G. P. Alexander, B. G. Chen, E. A. Matsumoto, and R. D. Kamien. Colloquium: Disclination loops, point defects, and all that in nematic liquid crystals. *Reviews of Modern Physics*, 84(2):497–514, Apr. 2012. doi: 10.1103/RevModPhys.84.497. URL http://link.aps.org/doi/10.1103/RevModPhys.84.497.

A. Baskaran and M. C. Marchetti. Statistical mechanics and hydrodynamics of bacterial suspensions. In *Proceedings of the National Academy of Sciences*, pages 15567–15572, Aug. 2009. doi: 10.1073/pnas.0906586106. URL http://adsabs.harvard.edu/cgi-bin/nph-data_query?bibcode=2009PNAS..10615567B&link_type=EJOURNAL.

G. K. Batchelor. *An introduction to fluid dynamics*. Cambridge University Press, 1967.

M. A. Bates. Nematic ordering and defects on the surface of a sphere: A Monte Carlo simulation study. *The Journal of Chemical Physics*, 128(10):104707–5, 2008. doi: 10.1063/1.2890724. URL http://scitation.aip.org/content/aip/journal/jcp/128/10/10.1063/1.2890724.

M. A. Bates, G. Skačej, and C. Zannoni. Defects and ordering in nematic coatings on uniaxial and biaxial colloids. *Soft Matter*, 6(3):655–663, 2010. doi: 10.1039/B917180K. URL http://xlink.rsc.org/?DOI=B917180K.

H. Berthoumieux, J.-L. Maître, C.-P. Heisenberg, E. K. Paluch, F. Jülicher, and G. Salbreux. Active elastic thin shell theory for cellular deformations. *New Journal of Physics*, 16(6):1–33, June 2014. doi: 10.1088/1367-2630/16/6/065005. URL http://stacks.iop.org/1367-2630/16/i=6/a=065005?key=crossref.c69a88f82e0487d48891f6f7e9af8eeb.

J. R. Blake. A spherical envelope approach to ciliary propulsion. *Journal of Fluid Mechanics*, 46(01):199–208, 1971. doi: 10.1017/S002211207100048X. URL http://adsabs.harvard.edu/cgi-bin/nph-data_query?bibcode=1971JFM....46..199B&link_type=EJOURNAL.

C. Blanch-Mercader and J. Casademunt. Spontaneous Motility of Actin Lamellar Fragments. *Physical Review Letters*, 110(7):078102, Feb. 2013. doi: 10.1103/PhysRevLett.110.078102. URL http://adsabs.harvard.edu/cgi-bin/nph-data_query?bibcode=2013PhRvL.110g8102B&link_type=EJOURNAL.

M. L. Blow, M. Aqil, B. Liebchen, and D. Marenduzzo. Motility of active nematic films driven by "active anchoring". *arXiv.org*, Feb. 2017. URL http://arxiv.org/abs/1702.04695v1.

A. Bricard, J.-B. Caussin, N. Desreumaux, O. Dauchot, and D. Bartolo. Emergence of macroscopic directed motion in populations of motile colloids. *Nature*, 503(7474):95–98, Nov. 2013. doi: 10.1038/nature12673. URL http://dx.doi.org/10.1038/nature12673.

J. Brugués and D. Needleman. Physical basis of spindle self-organization. *Proceedings of the National Academy of Sciences*, 111(52):18496–18500, Dec. 2014. doi: 10.1073/pnas.1409404111. URL http://www.pnas.org/lookup/doi/10.1073/pnas.1409404111.

A. C. Callan-Jones and F. Jülicher. Hydrodynamics of active permeating gels. *New Journal of Physics*, 2011. doi: 10.1088/1367-2630/9/11/422. URL http://iopscience.iop.org/article/10.1088/1367-2630/13/9/093027/meta.

A. C. Callan-Jones, J.-F. Joanny, and J. Prost. Viscous-Fingering-Like Instability of Cell Fragments. *Physical Review Letters*, 100(25):258106–4, June 2008. doi: 10.1103/PhysRevLett.100.258106. URL http://link.aps.org/doi/10.1103/PhysRevLett.100.258106.

A. C. Callan-Jones, V. Ruprecht, S. Wieser, C. P. Heisenberg, and R. Voituriez. Cortical Flow-Driven Shapes of Nonadherent Cells. *Physical Review Letters*, 116(2):028102–5, Jan. 2016. doi: 10.1103/PhysRevLett.116.028102. URL http://link.aps.org/doi/10.1103/PhysRevLett.116.028102.

M. G. Campbell, M. Tasinkevych, and I. I. Smalyukh. Topological Polymer Dispersed Liquid Crystals with Bulk Nematic Defect Lines Pinned to Handlebody Surfaces. *Physical Review Letters*, 112(19):197801–5, May 2014. doi: 10.1103/PhysRevLett.112.197801. URL http://link.aps.org/doi/10.1103/PhysRevLett.112.197801.

M. E. Cates and J. Tailleur. Motility-Induced Phase Separation. *Annual Review of Condensed Matter Physics*, 6(1):219–244, Mar. 2015. doi: 10.1146/annurev-conmatphys-031214-014710. URL http://www.annualreviews.org/doi/abs/10.1146/annurev-conmatphys-031214-014710.

M. E. Cates, S. M. Fielding, D. Marenduzzo, E. Orlandini, and J. M. Yeomans. Shearing Active Gels Close to the Isotropic-Nematic Transition. *Physical Review Letters*, 101(6):068102–4, Aug. 2008. doi: 10.1103/PhysRevLett.101.068102. URL http://link.aps.org/doi/10.1103/PhysRevLett.101.068102.

P. M. Chaikin and T. C. Lubensky. *Principles of Condensed Matter Physics*. Cambridge Univ Press, 2000. doi: 10.1007/BF02179565.

G. Charras and E. Paluch. Blebs lead the way: how to migrate without lamellipodia. *Nature Reviews Molecular Cell Biology*, 9(9):730–736, Sept. 2008. doi: 10.1038/nrm2453. URL http://www.nature.com/doifinder/10.1038/nrm2453.

P.-G. De Gennes. Polymeric liquid crystals: Frank elasticity and light scattering. *Molecular Crystals and Liquid Crystals*, 34(8):177–182, Aug. 1976. doi: 10.1080/15421407708083702. URL http://www.tandfonline.com/doi/abs/10.1080/15421407708083702.

P.-G. De Gennes and P.-G. de Gennes. Structures en domaines dans un nematique sous champ magnetique. *Solid State Communications*, 8(3):213–216, Feb. 1970. doi: 10.1016/0038-1098(70)90084-0. URL http://linkinghub.elsevier.com/retrieve/pii/0038109870900840.

P.-G. de Gennes and J. Prost. *The Physics of Liquid Crystals*. International Series of Monographs on Physics. Clarendon Press, 1995. ISBN 9780198517856. URL https://books.google.de/books?id=0Nw-dzWz5agC.

P.-G. De Gennes, F. Brochard-Wyart, and D. Quere. *Capillarity and Wetting Phenomena: Drops, Bubbles, Pearls, Waves*. Springer New York, 2003. ISBN 9780387005928. URL https://books.google.co.uk/books?id=MxLQk8vms-kC.

S. R. De Groot and P. Mazur. *Non-Equilibrium Thermodynamics*. Dover Books on Physics. Dover Publications, 1984. URL https://books.google.co.uk/books?id=HFAIv43rlGkC.

S. J. DeCamp, G. S. Redner, A. Baskaran, M. F. Hagan, and Z. Dogic. Orientational order of motile defects in active nematics. *Nature Materials*, pages 1–6, Aug. 2015. doi: 10.1038/nmat4387. URL http://www.nature.com/doifinder/10.1038/nmat4387.

C. Denniston. Disclination dynamics in nematic liquid crystals. *Physical review. B, Condensed matter*, 54(9):6272–6275, Sept. 1996. URL http://eutils.ncbi.nlm.nih.gov/entrez/eutils/elink.fcgi?dbfrom=pubmed&id=9986642&retmode=ref&cmd=prlinks.

I. Dierking, M. Ravnik, E. Lark, J. Healey, G. P. Alexander, and J. M. Yeomans. Anisotropy in the annihilation dynamics of umbilic defects in nematic liquid crystals. *Physical Review E*, 85(2):021703–11, Feb. 2012. doi: 10.1103/PhysRevE.85.021703. URL http://link.aps.org/doi/10.1103/PhysRevE.85.021703.

M. Dogterom and B. Yurke. Measurement of the force-velocity relation for growing microtubules. *Science*, 278(5339):856–860, Oct. 1997. URL http://eutils.ncbi.nlm.nih.gov/entrez/eutils/elink.fcgi?dbfrom=pubmed&id=9346483&retmode=ref&cmd=prlinks.

A. Doostmohammadi, M. F. Adamer, S. P. Thampi, and J. M. Yeomans. Stabilization of active matter by flow-vortex lattices and defect ordering. *Nature Communications*, 7:10557, Feb. 2016a. doi: 10.1038/ncomms10557. URL http://www.nature.com/doifinder/10.1038/ncomms10557.

A. Doostmohammadi, T. N. Shendruk, and K. Thijssen. Onset of meso-scale turbulence in living fluids. *arXiv.org*, 2016b. URL https://arxiv.org/abs/1607.01376.

K. Drescher, R. E. Goldstein, N. Michel, M. Polin, and I. Tuval. Direct Measurement of the Flow Field around Swimming Microorganisms. *Physical Review Letters*, 105(16):168101–4, Oct. 2010. doi: 10.1103/PhysRevLett.105.168101. URL http://link.aps.org/doi/10.1103/PhysRevLett.105.168101.

K. Drescher, J. Dunkel, and L. H. Cisneros. Fluid dynamics and noise in bacterial cell–cell and cell–surface scattering. In *Proceedings of the National Academy of Sciences*, 2011. doi: 10.1073/pnas.1019079108/-/DCSupplemental. URL http://www.pnas.org/content/108/27/10940.short.

K. Drescher, J. Dunkel, C. D. Nadell, S. van Teeffelen, I. Grnja, N. S. Wingreen, H. A. Stone, and B. L. Bassler. Architectural transitions in Vibrio choleraebiofilms at single-cell resolution. *Proceedings of the National Academy of Sciences*, 113(14):E2066–E2072, Apr. 2016. doi: 10.1073/pnas.1601702113. URL http://www.pnas.org/lookup/doi/10.1073/pnas.1601702113.

G. Duclos, S. Garcia, H. G. Yevick, and P. Silberzan. Perfect nematic order in confined monolayers of spindle-shaped cells. *Soft Matter*, 10(14):2346–2353, 2014. doi: 10.1039/C3SM52323C. URL http://xlink.rsc.org/?DOI=C3SM52323C.

G. Duclos, C. Erlenkämper, J.-F. Joanny, and P. Silberzan. Topological defects in confined populations of spindle-shaped cells. *Nature Physics*, pages 1–6, Sept. 2016. doi: 10.1038/nphys3876. URL http://www.nature.com/doifinder/10.1038/nphys3876.

J. Dunkel, S. Heidenreich, K. Drescher, H. H. Wensink, M. Bär, and R. E. Goldstein. Fluid Dynamics of Bacterial Turbulence. *Physical Review Letters*, 110(22):228102–5, May 2013. doi: 10.1103/PhysRevLett.110.228102. URL http://link.aps.org/doi/10.1103/PhysRevLett.110.228102.

J. Elgeti, M. E. Cates, and D. Marenduzzo. Defect hydrodynamics in 2D polar active fluids. *Soft Matter*, 7(7):3177, 2011. doi: 10.1039/c0sm01097a. URL http://xlink.rsc.org/?DOI=c0sm01097a.

J. Étienne and A. Duperray. Initial Dynamics of Cell Spreading Are Governed by Dissipation in the Actin Cortex. *Biophysical Journal*, 101(3):611–621, Aug. 2011. doi: 10.1016/j.bpj.2011.06.030. URL http://dx.doi.org/10.1016/j.bpj.2011.06.030.

S. Even-Ram and K. M. Yamada. Cell migration in 3D matrix. *Current Opinion in Cell Biology*, 17 (5):524–532, Oct. 2005. doi: 10.1016/j.ceb.2005.08.015. URL http://eutils.ncbi.nlm.nih.gov/entrez/eutils/elink.fcgi?dbfrom=pubmed&id=16112853&retmode=ref&cmd=prlinks.

A. Fernandez-Nieves, V. Vitelli, A. S. Utada, D. R. Link, M. Márquez, D. R. Nelson, and D. A. Weitz. Novel Defect Structures in Nematic Liquid Crystal Shells. *Physical Review Letters*, 99(15): 157801–4, Oct. 2007. doi: 10.1103/PhysRevLett.99.157801. URL http://link.aps.org/doi/10.1103/PhysRevLett.99.157801.

Y. Fily, A. Baskaran, and M. C. Marchetti. Cooperative self-propulsion of active and passive rotors. *Soft Matter*, 8(10):3002, 2012. doi: 10.1039/c2sm06952k. URL http://xlink.rsc.org/?DOI=c2sm06952k.

A. Fruleux and R. J. Hawkins. Physical role for the nucleus in cell migration. *Journal of Physics: Condensed Matter*, 28(36):1–11, July 2016. doi: 10.1088/0953-8984/28/36/363002. URL http://dx.doi.org/10.1088/0953-8984/28/36/363002.

S. Fürthauer, M. Neef, S. W. Grill, K. Kruse, and F. Jülicher. The Taylor–Couette motor: spontaneous flows of active polar fluids between two coaxial cylinders. *New Journal of Physics*, 14(2):023001–17, Feb. 2012. doi: 10.1088/1367-2630/14/2/023001. URL http://stacks.iop.org/1367-2630/14/i=2/a=023001?key=crossref.cadda989de94693c657cff852af3e3cb.

C. Gabella, E. Bertseva, C. Bottier, N. Piacentini, A. Bornert, S. Jeney, L. Forró, I. F. Sbalzarini, J.-J. Meister, and A. B. Verkhovsky. Contact angle at the leading edge controls cell protrusion rate. *Current Biology*, 24(10):1126–1132, May 2014. doi: 10.1016/j.cub.2014.03.050. URL http://eutils.ncbi.nlm.nih.gov/entrez/eutils/elink.fcgi?dbfrom=pubmed&id=24794299&retmode=ref&cmd=prlinks.

S. Ganguly, L. S. Williams, and I. M. Palacios. Cytoplasmic streaming in Drosophila oocytes varies with kinesin activity and correlates with the microtubule cytoskeleton architecture. In *Proceedings of the National Academy of Sciences*, 2012. doi: 10.1073/pnas.1203575109/-/DCSupplemental. URL http://www.pnas.org/content/109/38/15109.short.

M. L. Gardel, B. Sabass, L. Ji, G. Danuser, U. S. Schwarz, and C. M. Waterman. Traction stress in focal adhesions correlates biphasically with actin retrograde flow speed. *The Journal of Cell Biology*, 183(6):999–1005, Dec. 2008. doi: 10.1083/jcb.200810060. URL http://www.jcb.org/lookup/doi/10.1083/jcb.200810060.

F. Gerbal, P. Chaikin, Y. Rabin, and J. Prost. An elastic analysis of Listeria monocytogenes propulsion. *Biophysical Journal*, 79(5):2259–2275, 2000. doi: 10.1016/S0006-3495(00)76473-3. URL http://linkinghub.elsevier.com/retrieve/pii/S0006349500764733.

W. Gilpin, V. N. Prakash, and M. Prakash. Vortex arrays and ciliary tangles underlie the feeding–swimming trade-off in starfish larvae. *Nature Physics*, pages 1–7, Dec. 2016. doi: 10.1038/nphys3981. URL http://www.nature.com/doifinder/10.1038/nphys3981.

L. Giomi. Geometry and Topology of Turbulence in Active Nematics. *Physical Review X*, 5 (3):031003, July 2015. doi: 10.1103/PhysRevX.5.031003. URL http://adsabs.harvard.edu/cgi-bin/nph-data_query?bibcode=2015PhRvX...5c1003G&link_type=EJOURNAL.

L. Giomi and A. DeSimone. Spontaneous Division and Motility in Active Nematic Droplets. *Physical Review Letters*, 112(14):147802, Apr. 2014. doi: 10.1103/PhysRevLett.112.147802. URL http://link.aps.org/doi/10.1103/PhysRevLett.112.147802.

L. Giomi and M. C. Marchetti. Polar patterns in active fluids. *Soft Matter*, 8(1):129–139, 2012. doi: 10.1039/C1SM06077E. URL http://xlink.rsc.org/?DOI=C1SM06077E.

L. Giomi, M. C. Marchetti, and T. B. Liverpool. Complex Spontaneous Flows and Concentration Banding in Active Polar Films. *Physical Review Letters*, 101(19):198101–4, Nov. 2008. doi: 10.1103/PhysRevLett.101.198101. URL http://link.aps.org/doi/10.1103/PhysRevLett.101.198101.

L. Giomi, L. Mahadevan, B. Chakraborty, and M. F. Hagan. Excitable Patterns in Active Nematics. *Physical Review Letters*, 106(21):218101–4, May 2011. doi: 10.1103/PhysRevLett.106.218101. URL http://link.aps.org/doi/10.1103/PhysRevLett.106.218101.

L. Giomi, N. Hawley-Weld, and L. Mahadevan. Swarming, swirling and stasis in sequestered bristlebots. *Proceedings of the Royal Society A: Mathematical, Physical and Engineering Sciences*, 469(2151):20120637–20120637, Dec. 2012. doi: 10.1098/rspa.2012.0637. URL http://rspa.royalsocietypublishing.org/cgi/doi/10.1098/rspa.2012.0637.

L. Giomi, M. J. Bowick, X. Ma, and M. C. Marchetti. Defect Annihilation and Proliferation in Active Nematics. *Physical Review Letters*, 110(22):228101, May 2013. doi: 10.1103/PhysRevLett.110.228101. URL http://link.aps.org/doi/10.1103/PhysRevLett.110.228101.

L. Giomi, M. J. Bowick, P. Mishra, R. Sknepnek, and M. Cristina Marchetti. Defect dynamics in active nematics. *Philosophical Transactions of the Royal Society A: Mathematical, Physical and Engineering Sciences*, 372(2029):20130365–20130365, Oct. 2014. doi: 10.1098/rsta.2013.0365. URL http://rsta.royalsocietypublishing.org/cgi/doi/10.1098/rsta.2013.0365.

R. E. Goldstein and I. Tuval. Microfluidics of cytoplasmic streaming and its implications for intracellular transport. In *Proceedings of the National Academy of Sciences*, 2008. URL http://www.pnas.org/content/105/10/3663.short.

P. Guillamat, J. Ignés-Mullol, and F. Sagués. Patterning active materials with addressable soft interfaces. *arXiv.org*, page 3880, Nov. 2015. URL http://arxiv.org/abs/1511.03880v1.

P. Guillamat, J. Ignés-Mullol, and F. Sagués. Control of active liquid crystals with a magnetic field. *Proceedings of the National Academy of Sciences*, 113(20):5498–5502, May 2016a. doi: 10.1073/pnas.1600339113. URL http://www.pnas.org/lookup/doi/10.1073/pnas.1600339113.

P. Guillamat, J. Ignés-Mullol, and F. Sagués. Taming active turbulence with patterned soft interfaces. Nov. 2016b. URL http://arxiv.org/abs/1611.06416v1.

P. Guillamat, J. Ignés-Mullol, S. Shankar, M. C. Marchetti, and F. Sagués. Probing the shear viscosity of an active nematic film. *Physical Review E*, 94(6-1):060602, Dec. 2016c. doi: 10.1103/PhysRevE.94.060602. URL http://eutils.ncbi.nlm.nih.gov/entrez/eutils/elink.fcgi?dbfrom=pubmed&id=28085294&retmode=ref&cmd=prlinks.

M. Harasim, B. Wunderlich, O. Peleg, M. Kröger, and A. R. Bausch. Direct Observation of the Dynamics of Semiflexible Polymers in Shear Flow. *Physical Review Letters*, 110(10):108302–5, Mar. 2013. doi: 10.1103/PhysRevLett.110.108302. URL http://link.aps.org/doi/10.1103/PhysRevLett.110.108302.

Y. Hatwalne, S. Ramaswamy, M. Rao, and R. A. Simha. Rheology of active-particle suspensions. *Physical Review Letters*, 2004. doi: 10.1103/PhysRevLett.92.118101. URL http://journals.aps.org/prl/abstract/10.1103/PhysRevLett.92.118101.

R. J. Hawkins, R. Poincloux, O. Bénichou, M. Piel, P. Chavrier, and R. Voituriez. Spontaneous Contractility-Mediated Cortical Flow Generates Cell Migration in Three-Dimensional Environments. *Biophysical Journal*, 101(5):1041–1045, Sept. 2011. doi: 10.1016/j.bpj.2011.07.038. URL http://dx.doi.org/10.1016/j.bpj.2011.07.038.

G. Henkin, S. J. DeCamp, D. T. N. Chen, T. Sanchez, and Z. Dogic. Tunable dynamics of microtubule-based active isotropic gels. *Philosophical Transactions of the Royal Society A: Mathematical, Physical and Engineering Sciences*, 372(2029):20140142–20140142, Oct. 2014. doi: 10.1098/rsta.2014.0142. URL http://rsta.royalsocietypublishing.org/cgi/doi/10.1098/rsta.2014.0142.

M. Herant and M. Dembo. Form and Function in Cell Motility: From Fibroblasts to Keratocytes. *Biophysical Journal*, 98(8):1408–1417, Apr. 2010. doi: 10.1016/j.bpj.2009.12.4303. URL http://adsabs.harvard.edu/cgi-bin/nph-data_query?bibcode=2010BpJ....98.1408H&link_type=EJOURNAL.

F. Hilitski, A. R. Ward, L. Cajamarca, M. F. Hagan, G. M. Grason, and Z. Dogic. Measuring Cohesion between Macromolecular Filaments One Pair at a Time: Depletion-Induced Microtubule Bundling. *Physical Review Letters*, 114(13):138102, 2015. doi: 10.1103/physrevlett.114.138102. URL http://link.aps.org/doi/10.1103/PhysRevLett.114.138102.

L. S. Hirst, A. Ossowski, and M. Fraser. Morphology transition in lipid vesicles due to in-plane order and topological defects. In *Proceedings of the National Academy of Sciences*, 2013. doi: 10.1073/pnas.1213994110/-/DCSupplemental. URL http://www.pnas.org/content/110/9/3242.short.

H. Hopf. *Differential Geometry in the Large*. Lecture Notes in Mathematics. Springer Berlin Heidelberg, 1989. ISBN 9783540514978. URL https://books.google.co.uk/books?id=zNnw8NduHL0C.

M. Huber and H. Stark. Tetravalent colloids by nematic wetting. *Europhysics Letters*, 2004. doi: 10.1143/JJAP.31.3895. URL http://iopscience.iop.org/article/10.1209/epl/i2004-10316-1/meta.

H. Imura and K. Okano. Interaction between disinclinations in nematic liquid crystals. *Physics Letters A*, 1973. URL http://www.sciencedirect.com/science/article/pii/0375960173907299.

D. Jesenek, S. Kralj, R. Rosso, and E. G. Virga. Defect unbinding on a toroidal nematic shell. *Soft Matter*, 11(12):2434–2444, Mar. 2015. doi: 10.1039/C4SM02540G. URL http://dx.doi.org/10.1039/C4SM02540G.

J.-F. Joanny and S. Ramaswamy. A drop of active matter. *Journal of Fluid Mechanics*, 705:46–57, Apr. 2012. doi: 10.1017/jfm.2012.131. URL http://www.journals.cambridge.org/abstract_S0022112012001310.

J.-F. Joanny, F. Jülicher, K. Kruse, and J. Prost. Hydrodynamic theory for multi-component active polar gels. *New Journal of Physics*, 2007. doi: 10.1088/1367-2630/13/9/093027. URL http://iopscience.iop.org/article/10.1088/1367-2630/9/11/422/meta.

F. Jülicher, K. Kruse, J. Prost, and J.-F. Joanny. Active behavior of the Cytoskeleton. *Physics Reports*, 449(1-3):3–28, Sept. 2007. doi: 10.1016/j.physrep.2007.02.018. URL http://linkinghub.elsevier.com/retrieve/pii/S0370157307001330.

R. D. Kamien. The geometry of soft materials: a primer. *Reviews of Modern Physics*, 74(4):953–971, Sept. 2002. doi: 10.1103/RevModPhys.74.953. URL http://adsabs.harvard.edu/cgi-bin/nph-data_query?bibcode=2002RvMP...74..953K&link_type=EJOURNAL.

T. V. Kasyap, D. L. Koch, and M. Wu. Bacterial collective motion near the contact line of an evaporating sessile drop. *Physics of Fluids*, 26(11):111703–8, Nov. 2014. doi: 10.1063/1.4901958. URL http://aip.scitation.org/doi/10.1063/1.4901958.

F. C. Keber, E. Loiseau, T. Sanchez, S. J. DeCamp, L. Giomi, M. J. Bowick, M. C. Marchetti, Z. Dogic, and A. R. Bausch. Topology and dynamics of active nematic vesicles. *Science*, 345 (6201):1135–1139, Sept. 2014. doi: 10.1126/science.1254784. URL http://www.sciencemag.org/cgi/doi/10.1126/science.1254784.

R. Kemkemer, D. Kling, and D. Kaufmann. Elastic properties of nematoid arrangements formed by amoeboid cells. *The European Physical Journal E*, 1(2):215, 2000. doi: 10.1007/s101890050024. URL http://link.springer.com/10.1007/s101890050024.

K. Keren, Z. Pincus, G. M. Allen, E. L. Barnhart, G. Marriott, A. Mogilner, and J. A. Theriot. Mechanism of shape determination in motile cells. *Nature*, 453(7194):475–480, May 2008. doi: 10.1038/nature06952. URL http://www.nature.com/doifinder/10.1038/nature06952.

K. Keren, P. T. Yam, A. Kinkhabwala, A. Mogilner, and J. A. Theriot. Intracellular fluid flow in rapidly moving cells. *Nature Cell Biology*, 11(10):1219–1224, Sept. 2009. doi: 10.1038/ncb1965. URL http://dx.doi.org/10.1038/ncb1965.

D. Khoromskaia, R. J. Harris, and S. Grosskinsky. Dynamics of non-Markovian exclusion processes. *Journal of Statistical Mechanics: Theory and Experiment*, 12(1):12013, Dec. 2014. doi: 10.1088/1742-5468/2014/12/P12013. URL http://adsabs.harvard.edu/cgi-bin/nph-data_query?bibcode=2014JSMTE..12..013K&link_type=EJOURNAL.

T. Kim, M. T. Kao, E. Meyhöfer, and E. F. Hasselbrink. Biomolecular motor-driven microtubule translocation in the presence of shear flow: analysis of redirection behaviours. *Nanotechnology*,

2006. doi: 10.1088/0957-4484/19/12/125505. URL http://iopscience.iop.org/article/10.1088/0957-4484/18/2/025101/meta.

S. Köhler, V. Schaller, and A. R. Bausch. Structure formation in active networks. *Nature Materials*, 10(6):462–468, June 2011. doi: 10.1038/nmat3009. URL http://adsabs.harvard.edu/cgi-bin/nph-data_query?bibcode=2011NatMa..10..462K&link_type=EJOURNAL.

A. B. Kolomeisky and M. E. Fisher. Molecular Motors: A Theorist's Perspective. *Annual Review of Physical Chemistry*, 58(1):675–695, May 2007. doi: 10.1146/annurev.physchem.58.032806.104532. URL http://www.annualreviews.org/doi/abs/10.1146/annurev.physchem.58.032806.104532.

V. Koning, B. C. van Zuiden, R. D. Kamien, and V. Vitelli. Saddle-splay screening and chiral symmetry breaking in toroidal nematics. *Soft Matter*, 10(23):4192–7, 2014. doi: 10.1039/c4sm00076e. URL http://xlink.rsc.org/?DOI=c4sm00076e.

V. Koning, T. Lopez-Leon, A. Darmon, A. Fernandez-Nieves, and V. Vitelli. Spherical nematic shells with a threefold valence. *Physical Review E*, 94(1):012703–7, July 2016. doi: 10.1103/PhysRevE.94.012703. URL http://link.aps.org/doi/10.1103/PhysRevE.94.012703.

S. Kralj, R. Rosso, and E. G. Virga. Curvature control of valence on nematic shells. *Soft Matter*, 7(2):670–683, 2011. doi: 10.1039/C0SM00378F. URL http://xlink.rsc.org/?DOI=C0SM00378F.

K. Kruse, J.-F. Joanny, F. Jülicher, J. Prost, and K. Sekimoto. Asters, Vortices, and Rotating Spirals in Active Gels of Polar Filaments. *Physical Review Letters*, 92(7):078101–4, Feb. 2004. doi: 10.1103/PhysRevLett.92.078101. URL http://link.aps.org/doi/10.1103/PhysRevLett.92.078101.

K. Kruse, J.-F. Joanny, F. Jülicher, J. Prost, and K. Sekimoto. Generic theory of active polar gels: a paradigm for cytoskeletal dynamics. *The European Physical Journal E*, 16(1):5–16, Jan. 2005. doi: 10.1140/epje/e2005-00002-5. URL http://www.springerlink.com/index/10.1140/epje/e2005-00002-5.

K. Kruse, J.-F. Joanny, F. Jülicher, and J. Prost. Contractility and retrograde flow in lamellipodium motion. *Physical biology*, 3(2):130–137, June 2006. doi: 10.1088/1478-3975/3/2/005. URL http://eutils.ncbi.nlm.nih.gov/entrez/eutils/elink.fcgi?dbfrom=pubmed&id=16829699&retmode=ref&cmd=prlinks.

A. Kumar, A. Maitra, M. Sumit, S. Ramaswamy, and G. V. Shivashankar. Actomyosin contractility rotates the cell nucleus. *Scientific Reports*, 4, Jan. 2014. doi: 10.1038/srep03781. URL http://www.nature.com/doifinder/10.1038/srep03781.

E. Lauga. Life around the scallop theorem. *Soft Matter*, 7(7):3060, 2011. doi: 10.1039/c0sm00953a. URL http://xlink.rsc.org/?DOI=c0sm00953a.

E. Lauga and T. R. Powers. The hydrodynamics of swimming microorganisms. *Reports on Progress in Physics*, 72(9):096601–36, Aug. 2009. doi: 10.1088/0034-4885/72/9/096601. URL http://stacks.iop.org/0034-4885/72/i=9/a=096601?key=crossref.736a5c13368e75b7395f94099aead8e4.

M. Lenz. Geometrical Origins of Contractility in Disordered Actomyosin Networks. *Physical Review X*, 4(4):041002–9, Oct. 2014. doi: 10.1103/PhysRevX.4.041002. URL http://link.aps.org/doi/10.1103/PhysRevX.4.041002.

O. L. Lewis, S. Zhang, R. D. Guy, and J. C. del Alamo. Coordination of contractility, adhesion and flow in migrating Physarum amoebae. *Journal of The Royal Society Interface*, 12(106):20141359–20141359, Mar. 2015. doi: 10.1098/rsif.2014.1359. URL http://rsif.royalsocietypublishing.org/cgi/doi/10.1098/rsif.2014.1359.

B. Li and S. X. Sun. Coherent Motions in Confluent Cell Monolayer Sheets. *Biophysical Journal*, 107 (7):1532–1541, Oct. 2014. doi: 10.1016/j.bpj.2014.08.006. URL http://dx.doi.org/10.1016/j.bpj.2014.08.006.

A. D. Lieber, Y. Schweitzer, M. M. Kozlov, and K. Keren. Front-to-Rear Membrane Tension Gradient in Rapidly Moving Cells. *Biophysical Journal*, 108(7):1599–1603, Apr. 2015. doi: 10.1016/j.bpj.2015.02.007. URL http://dx.doi.org/10.1016/j.bpj.2015.02.007.

M. J. Lighthill. On the squirming motion of nearly spherical deformable bodies through liquids at very small reynolds numbers. *Communications on Pure and Applied Mathematics*, 5(2):109–118, 1952. doi: 10.1002/cpa.3160050201. URL http://doi.wiley.com/10.1002/cpa.3160050201.

A. Lindner and M. Shelley. Elastic fibers in flows. In *Fluid-structure interactions at low Reynolds numbers. ...* in Low-Reynolds-Number Flows, 2015. URL http://books.google.com/books?hl=en&lr=&id=IGjuCgAAQBAJ&oi=fnd&pg=PA168&dq=Elastic+Fibers+in+Flows+(Lindner+Shelley)&ots=2p5bLs8sK6&sig=ry5RcVn9IxJFeL3wCvAOLS-FG5w.

T. B. Liverpool and M. C. Marchetti. Rheology of Active Filament Solutions. *Physical Review Letters*, 97(26):268101–4, Dec. 2006. doi: 10.1103/PhysRevLett.97.268101. URL http://link.aps.org/doi/10.1103/PhysRevLett.97.268101.

H. Lodish, A. Berk, C. Kaiser, M. Krieger, and M. Scott. *Molecular Cell Biology*. Macmillan Higher Education, 2007. ISBN 9781429214834. URL https://books.google.co.uk/books?id=bSTHPAAACAAJ.

E. Loiseau, J. A. M. Schneider, F. C. Keber, C. Pelzl, G. Massiera, G. Salbreux, and A. R. Bausch. Shape remodeling and blebbing of active cytoskeletal vesicles. *Science Advances*, 2(4):e1500465–e1500465, Apr. 2016. doi: 10.1126/sciadv.1500465. URL http://advances.sciencemag.org/cgi/doi/10.1126/sciadv.1500465.

H. M. López, J. Gachelin, C. Douarche, H. Auradou, and E. Clément. Turning Bacteria Suspensions into Superfluids. *Physical Review Letters*, 115(2):028301–5, July 2015. doi: 10.1103/PhysRevLett.115.028301. URL http://link.aps.org/doi/10.1103/PhysRevLett.115.028301.

T. Lopez-Leon and A. Fernandez-Nieves. Drops and shells of liquid crystal. *Colloid and Polymer Science*, 289(4):345–359, Jan. 2011. doi: 10.1007/s00396-010-2367-7. URL http://link.springer.com/10.1007/s00396-010-2367-7.

T. Lopez-Leon, V. Koning, K. B. S. Devaiah, V. Vitelli, and A. Fernandez-Nieves. Frustrated nematic order in spherical geometries. *Nature Physics*, 7(5):391–394, Feb. 2011. doi: 10.1038/nphys1920. URL http://dx.doi.org/10.1038/nphys1920.

T. C. Lubensky and J. Prost. Orientational order and vesicle shape. *Journal de Physique II*, 1992. doi: 10.1051/jp2:1992133⟩. URL http://jp2.journaldephysique.org/articles/jp2/abs/1992/03/jp2v2p371/jp2v2p371.html.

E. Lushi, H. Wioland, and R. E. Goldstein. Fluid flows created by swimming bacteria drive self-organization in confined suspensions. *Proceedings of the National Academy of Sciences*, 111(27): 9733–9738, July 2014. doi: 10.1073/pnas.1405698111. URL http://www.pnas.org/cgi/doi/10.1073/pnas.1405698111.

T. Machon and G. P. Alexander. Knots and nonorientable surfaces in chiral nematics. *Proceedings of the National Academy of Sciences*, 110(35):14174–14179, Aug. 2013. doi: 10.1073/pnas.1308225110. URL http://www.pnas.org/cgi/doi/10.1073/pnas.1308225110.

T. Machon and G. P. Alexander. Knotted Defects in Nematic Liquid Crystals. *Physical Review Letters*, 113(2):027801–5, July 2014. doi: 10.1103/PhysRevLett.113.027801. URL http://link.aps.org/doi/10.1103/PhysRevLett.113.027801.

M. C. Marchetti, J.-F. Joanny, S. Ramaswamy, T. B. Liverpool, J. Prost, M. Rao, and R. A. Simha. Hydrodynamics of soft active matter. *Reviews of Modern Physics*, 85(3):1143–1189, July 2013. doi: 10.1103/RevModPhys.85.1143. URL http://link.aps.org/doi/10.1103/RevModPhys.85.1143.

D. Marenduzzo, E. Orlandini, and J. Yeomans. Hydrodynamics and Rheology of Active Liquid Crystals: A Numerical Investigation. *Physical Review Letters*, 98(11):118102, Mar. 2007. doi: 10.1103/PhysRevLett.98.118102. URL http://link.aps.org/doi/10.1103/PhysRevLett.98.118102.

W. Marth, S. Praetorius, and A. Voigt. A mechanism for cell motility by active polar gels. *Journal of The Royal Society Interface*, 12(107):20150161–20150161, Apr. 2015. doi: 10.1098/rsif.2015.0161. URL http://rsif.royalsocietypublishing.org/cgi/doi/10.1098/rsif.2015.0161.

P. C. Martin, O. Parodi, and P. S. Pershan. Unified Hydrodynamic Theory for Crystals, Liquid Crystals, and Normal Fluids. *Physical Review A*, 6(6):2401–2420, Dec. 1972. doi: 10.1103/PhysRevA.6.2401. URL http://adsabs.harvard.edu/cgi-bin/nph-data_query?bibcode=1972PhRvA...6.2401M&link_type=EJOURNAL.

N. D. Mermin. The topological theory of defects in ordered media. *Reviews of Modern Physics*, 51 (3):591–648, 1979. doi: 10.1103/RevModPhys.51.591. URL http://link.aps.org/doi/10.1103/RevModPhys.51.591.

N. D. Mermin. E Pluribus Boojum: the physicist as neologist. *Physics Today*, 34(4):46–53, Apr. 1981. doi: 10.1063/1.2914510. URL http://physicstoday.scitation.org/doi/10.1063/1.2914510.

R. B. Meyer. Point Disclinations at a Nematic-lsotropic Liquid Interface. *Molecular Crystals and Liquid Crystals*, 16(4):355–369, Apr. 1972. doi: 10.1080/15421407208082796. URL http://www.tandfonline.com/doi/abs/10.1080/15421407208082796.

D. Mizuno, C. Tardin, C. F. Schmidt, and F. C. MacKintosh. Nonequilibrium mechanics of active cytoskeletal networks. *Science*, 315(5810):370–373, 2007. doi: 10.1126/science.1134404. URL http://science.sciencemag.org/content/315/5810/370.short.

A. Mogilner and K. Keren. The Shape of Motile Cells. *Current Biology*, 19(17):R762–R771, Sept. 2009. doi: 10.1016/j.cub.2009.06.053. URL http://dx.doi.org/10.1016/j.cub.2009.06.053.

T. Mohammad Nejad, S. Iannaccone, W. Rutherford, P. M. Iannaccone, and C. D. Foster. Mechanics and spiral formation in the rat cornea. *Biomechanics and Modeling in Mechanobiology*, 14(1): 107–122, June 2014. doi: 10.1007/s10237-014-0592-6. URL http://link.springer.com/10.1007/s10237-014-0592-6.

R. L. Mort, T. Ramaesh, D. A. Kleinjan, S. D. Morley, and J. D. West. Mosaic analysis of stem cell function and wound healing in the mouse corneal epithelium. *BMC Developmental Biology*, 9(1): 4–14, 2009. doi: 10.1186/1471-213X-9-4. URL http://www.biomedcentral.com/1471-213X/9/4.

S. Muhuri, M. Rao, and S. Ramaswamy. Shear-flow–induced isotropic-to-nematic transition in a suspension of active filaments. *Europhysics Letters*, 78(4):48002, 2007. doi: 10.1209/0295-5075/78/48002. URL http://iopscience.iop.org/article/10.1209/0295-5075/78/48002/meta.

M. Murrell, P. W. Oakes, M. Lenz, and M. L. Gardel. Forcing cells into shape: the mechanics of actomyosin contractility. *Nature Publishing Group*, 16(8):486–498, July 2015. doi: 10.1038/nrm4012. URL http://dx.doi.org/10.1038/nrm4012.

V. Narayan, S. Ramaswamy, and N. Menon. Long-Lived Giant Number Fluctuations in a Swarming Granular Nematic. *Science*, 317(5834):105–108, 2007. doi: 10.1126/science.1140414.

F. J. Nedelec, T. Surrey, A. C. Maggs, and S. Leibler. Self-organization of microtubules and motors. *Nature*, 389(6):305–308, Sept. 1997. doi: 10.1038/38532. URL http://www.nature.com/doifinder/10.1038/38532.

T. Needham. *Visual Complex Analysis*. Clarendon Press, 1998. ISBN 9780198534464. URL https://books.google.co.uk/books?id=ogz5FjmiqlQC.

M. Neef and K. Kruse. Generation of stationary and moving vortices in active polar fluids in the planar Taylor-Couette geometry. *Physical Review E*, 90(5):052703–8, Nov. 2014. doi: 10.1103/PhysRevE.90.052703. URL http://link.aps.org/doi/10.1103/PhysRevE.90.052703.

D. R. Nelson. Toward a Tetravalent Chemistry of Colloids. *Nano Letters*, 2(10):1125–1129, Oct. 2002. doi: 10.1021/nl0202096. URL http://pubs.acs.org/doi/abs/10.1021/nl0202096.

T.-S. Nguyen, J. Geng, R. L. B. Selinger, and J. V. Selinger. Nematic order on a deformable vesicle: theory and simulation. *Soft Matter*, 9(34):8314–14, 2013. doi: 10.1039/c3sm50489a. URL http://xlink.rsc.org/?DOI=c3sm50489a.

A. Oron, S. H. Davis, and S. G. Bankoff. Long-scale evolution of thin liquid films. *Reviews of Modern Physics*, 69(3):931–980, July 1997. doi: 10.1103/RevModPhys.69.931. URL http://adsabs.harvard.edu/cgi-bin/nph-data_query?bibcode=1997RvMP...69..931O&link_type=EJOURNAL.

B. A. Ovrut and S. Thomas. Theory of vortices and monopoles on a sphere. *Physical Review D*, 1991. URL http://journals.aps.org/prd/abstract/10.1103/PhysRevD.43.1314.

E. Pairam, J. Vallamkondu, and V. Koning. Stable nematic droplets with handles. In *Proceedings of the National Academy of Sciences*, 2013. doi: 10.1073/pnas.1221380110/-/DCSupplemental. URL http://www.pnas.org/content/110/23/9295.short.

O. S. Pak and E. Lauga. Generalized squirming motion of a sphere. *Journal of Engineering Mathematics*, 88(1):1–28, May 2014. doi: 10.1007/s10665-014-9690-9. URL http://link.springer.com/10.1007/s10665-014-9690-9.

J. Palacci, S. Sacanna, A. P. Steinberg, D. J. Pine, and P. M. Chaikin. Living Crystals of Light-Activated Colloidal Surfers. *Science*, 339(6122):936–940, Feb. 2013. doi: 10.1126/science.1230020. URL http://www.sciencemag.org/cgi/doi/10.1126/science.1230020.

J. Palacci, S. Sacanna, S. H. Kim, G. R. Yi, D. J. Pine, and P. M. Chaikin. Light-activated self-propelled colloids. *Philosophical Transactions of the Royal Society A: Mathematical, Physical and Engineering Sciences*, 372(2029):20130372–20130372, Oct. 2014. doi: 10.1098/rsta.2013.0372. URL http://rsta.royalsocietypublishing.org/cgi/doi/10.1098/rsta.2013.0372.

D. Pearce and M. S. Turner. Density regulation in strictly metric-free swarms. *New Journal of Physics*, 16(8):082002, 2014. doi: 10.1088/1367-2630/16/8/082002. URL http://iopscience.iop.org/article/10.1088/1367-2630/16/8/082002/meta.

D. J. G. Pearce, A. M. Miller, G. Rowlands, and M. S. Turner. Role of projection in the control of bird flocks. *Proceedings of the National Academy of Sciences*, 111(29):10422–10426, July 2014. doi: 10.1073/pnas.1402202111. URL http://www.pnas.org/cgi/doi/10.1073/pnas.1402202111.

R. Penrose. The topology of ridge systems. *Annals of human genetics*, 42(4):435–444, May 1979. URL http://eutils.ncbi.nlm.nih.gov/entrez/eutils/elink.fcgi?dbfrom=pubmed&id=475332&retmode=ref&cmd=prlinks.

R. Phillips, J. Kondev, and J. Theriot. *Physical biology of the cell*. Garland Science, 2009. URL http://www.worldcat.org/isbn/9780815341635.

M. Pinot, F. Chesnel, J. Z. Kubiak, I. Arnal, F. J. Nedelec, and Z. Gueroui. Effects of confinement on the self-organization of microtubules and motors. *Current biology : CB*, 19(11):954–960, June 2009. doi: 10.1016/j.cub.2009.04.027. URL http://linkinghub.elsevier.com/retrieve/pii/S0960982209010252.

M. Pinot, V. Steiner, B. Dehapiot, B. K. Yoo, F. Chesnel, L. Blanchoin, C. Kervrann, and Z. Gueroui. Confinement induces actin flow in a meiotic cytoplasm. *Proceedings of the National Academy of Sciences*, 109(29):11705–11710, July 2012. doi: 10.1073/pnas.1121583109. URL http://adsabs.harvard.edu/cgi-bin/nph-data_query?bibcode=2012PNAS..10911705P&link_type=EJOURNAL.

R. Poincloux, O. Collin, F. Lizarraga, M. Romao, M. Debray, M. Piel, and P. Chavrier. Contractility of the cell rear drives invasion of breast tumor cells in 3D Matrigel. In *Proceedings of the National Academy of Sciences*, pages 1943–1948, Feb. 2011. doi: 10.1073/pnas.1010396108. URL http://adsabs.harvard.edu/cgi-bin/nph-data_query?bibcode=2011PNAS..108.1943P&link_type=EJOURNAL.

C. M. Pooley, G. P. Alexander, and J. M. Yeomans. Hydrodynamic Interaction between Two Swimmers at Low Reynolds Number. *Physical Review Letters*, 99(22):228103–4, Nov. 2007. doi: 10.1103/PhysRevLett.99.228103. URL http://link.aps.org/doi/10.1103/PhysRevLett.99.228103.

A. Pototsky, U. Thiele, and H. Stark. Stability of liquid films covered by a carpet of self-propelled surfactant particles. *Physical Review E*, 90(3):030401–5, Sept. 2014. doi: 10.1103/PhysRevE.90.030401. URL http://link.aps.org/doi/10.1103/PhysRevE.90.030401.

A. Pototsky, U. Thiele, and H. Stark. Mode instabilities and dynamic patterns in a colony of self-propelled surfactant particles covering a thin liquid layer. *The European Physical Journal E*, 39(5):51–19, May 2016. doi: 10.1140/epje/i2016-16051-4. URL http://link.springer.com/10.1140/epje/i2016-16051-4.

N. Pottier. *Nonequilibrium Statistical Physics: Linear Irreversible Processes*. Oxford University Press, 2010.

C. Poulard, M. Voué, J. De Coninck, and A. M. Cazabat. Spreading of nematic liquid crystals on hydrophobic substrates. *Colloids and Surfaces A: Physicochemical and Engineering Aspects*, 282-283:240–246, July 2006. doi: 10.1016/j.colsurfa.2005.10.022. URL http://linkinghub.elsevier.com/retrieve/pii/S0927775705007466.

K. R. Prathyusha, S. Henkes, and R. Sknepnek. Dynamically Generated Patterns in Dense Suspensions of Active Filaments. *arXiv.org*, Aug. 2016. URL http://arxiv.org/abs/1608.03305v1.

J. Prost, F. Jülicher, and J.-F. Joanny. Active gel physics. *Nature Physics*, 11(2):111–117, Feb. 2015. doi: 10.1038/nphys3224. URL http://adsabs.harvard.edu/cgi-bin/nph-data_query?bibcode=2015NatPh..11..111P&link_type=EJOURNAL.

E. M. Purcell. Life at low Reynolds number. *American journal of physics*, 1977. doi: 10.1119/1.10903. URL http://aapt.scitation.org/doi/abs/10.1119/1.10903.

S. Ramaswamy. The Mechanics and Statistics of Active Matter. *Annual Review of Condensed Matter Physics*, 1(1):323–345, Aug. 2010. doi: 10.1146/annurev-conmatphys-070909-104101. URL http://www.annualreviews.org/doi/abs/10.1146/annurev-conmatphys-070909-104101.

S. Ramaswamy and M. Rao. Active-filament hydrodynamics: instabilities, boundary conditions and rheology. *New Journal of Physics*, 9(11):423–423, Nov. 2007. doi: 10.1088/1367-2630/9/11/423. URL http://stacks.iop.org/1367-2630/9/i=11/a=423?key=crossref.27e3a96b5d133cea2119e37671ad9515.

S. Ramaswamy, A. R. Simha, and J. Toner. Active nematics on a substrate: Giant number fluctuations and long-time tails. *Europhysics Letters*, 62(2):196–202, Apr. 2003. doi: 10.1209/epl/i2003-00346-7. URL http://stacks.iop.org/0295-5075/62/i=2/a=196?key=crossref.c3dab8c54e63b296ae54d843c818330d.

W. J. Rappel, A. Nicol, A. Sarkisian, H. Levine, and W. F. Loomis. Self-organized Vortex State in Two-dimensional Dictyostelium Dynamics. *Physical Review Letters*, 83(patt-sol/9811001. 6):1247, 1999. URL http://cds.cern.ch/record/372201.

M. Ravnik and J. Yeomans. Confined Active Nematic Flow in Cylindrical Capillaries. *Physical Review Letters*, 110(2):026001, Jan. 2013. doi: 10.1103/PhysRevLett.110.026001. URL http://link.aps.org/doi/10.1103/PhysRevLett.110.026001.

M. W. Reichelt and L. F. Shampine. *The MATLAB ODE suite*. SIAM Journal on Scientific Computing, 1997. URL http://scholar.google.com/scholar?q=related:nsmv34mcF54J:scholar.google.com/&hl=en&num=20&as_sdt=0,5.

K. F. Riley, M. P. Hobson, and S. J. Bence. *Mathematical Methods for Physics and Engineering: A Comprehensive Guide*. Cambridge University Press, 2006. ISBN 9781139450997. URL https://books.google.co.uk/books?id=Mq1nlEKhNcsC.

M. Rubenstein, A. Cornejo, and R. Nagpal. Robotics. Programmable self-assembly in a thousand-robot swarm. *Science*, 345(6198):795–799, Aug. 2014. doi: 10.1126/science.1254295. URL http://eutils.ncbi.nlm.nih.gov/entrez/eutils/elink.fcgi?dbfrom=pubmed&id=25124435&retmode=ref&cmd=prlinks.

R. Rusconi, M. Garren, and R. Stocker. Microfluidics Expanding the Frontiers of Microbial Ecology. *Annual Review of Biophysics*, 43(1):65–91, May 2014. doi: 10.1146/annurev-biophys-051013-022916. URL http://www.annualreviews.org/doi/abs/10.1146/annurev-biophys-051013-022916.

G. Ryskin and M. Kremenetsky. Drag force on a line defect moving through an otherwise undisturbed field: Disclination line in a nematic liquid crystal. *Physical Review Letters*, 67(12):1574–1577, Sept. 1991. doi: 10.1103/PhysRevLett.67.1574. URL https://link.aps.org/doi/10.1103/PhysRevLett.67.1574.

G. Salbreux, J.-F. Joanny, J. Prost, and P. Pullarkat. Shape oscillations of non-adhering fibroblast cells. *Physical biology*, 4(4):268–284, Nov. 2007. doi: 10.1088/1478-3975/4/4/004. URL http://eutils.ncbi.nlm.nih.gov/entrez/eutils/elink.fcgi?dbfrom=pubmed&id=18185005&retmode=ref&cmd=prlinks.

G. Salbreux, J. Prost, and J.-F. Joanny. Hydrodynamics of Cellular Cortical Flows and the Formation of Contractile Rings. *Physical Review Letters*, 103(5):058102, July 2009. doi: 10.1103/PhysRevLett.103.058102. URL http://link.aps.org/doi/10.1103/PhysRevLett.103.058102.

T. Sanchez, D. T. N. Chen, S. J. DeCamp, M. Heymann, and Z. Dogic. Spontaneous motion in hierarchically assembled active matter. *Nature*, 491(7424):431–434, Apr. 2013. doi: 10.1038/nature11591. URL http://dx.doi.org/10.1038/nature11591.

S. Sankararaman and S. Ramaswamy. Instabilities and Waves in Thin Films of Living Fluids. *Physical Review Letters*, 102(11):118107–4, Mar. 2009. doi: 10.1103/PhysRevLett.102.118107. URL http://link.aps.org/doi/10.1103/PhysRevLett.102.118107.

V. Schaller, C. Weber, C. Semmrich, E. Frey, and A. R. Bausch. Polar patterns of driven filaments. *Nature*, 467(7311):73–77, Feb. 2010. doi: 10.1038/nature09312. URL http://dx.doi.org/10.1038/nature09312.

M. Schmitt and H. Stark. Marangoni flow at droplet interfaces: Three-dimensional solution and applications. *Physics of Fluids*, 28(1):012106–30, Jan. 2016. doi: 10.1063/1.4939212. URL http://scitation.aip.org/content/aip/journal/pof2/28/1/10.1063/1.4939212.

E. Schrödinger. *What is Life?* Cambridge University Press, 1944.

U. S. Schwarz and S. A. Safran. Physics of adherent cells. *Reviews of Modern Physics*, 85(3):1327–1381, Aug. 2013. doi: 10.1103/RevModPhys.85.1327. URL http://link.aps.org/doi/10.1103/RevModPhys.85.1327.

F. J. Segerer, F. Thüroff, A. Piera Alberola, E. Frey, and J. O. Rädler. Emergence and Persistence of Collective Cell Migration on Small Circular Micropatterns. *Physical Review Letters*, 114(22):228102, June 2015. doi: 10.1103/PhysRevLett.114.228102. URL http://link.aps.org/doi/10.1103/PhysRevLett.114.228102.

R. L. B. Selinger, A. Konya, A. Travesset, and J. V. Selinger. Monte Carlo Studies of the XY Model on Two-Dimensional Curved Surfaces. *The Journal of Physical Chemistry B*, 115(48):13989–13993, Dec. 2011. doi: 10.1021/jp205128g. URL http://pubs.acs.org/doi/abs/10.1021/jp205128g.

B. Senyuk, Q. Liu, S. He, R. D. Kamien, R. B. Kusner, T. C. Lubensky, and I. I. Smalyukh. Topological colloids. *Nature*, 493(7431):200–205, Jan. 2013. doi: 10.1038/nature11710. URL http://dx.doi.org/10.1038/nature11710.

L. R. Serbus. Dynein and the actin cytoskeleton control kinesin-driven cytoplasmic streaming in Drosophila oocytes. *Development*, 132(16):3743–3752, July 2005. doi: 10.1242/dev.01956. URL http://dev.biologists.org/cgi/doi/10.1242/dev.01956.

F. Serra. Curvature and defects in nematic liquid crystals. *Liquid Crystals*, pages 1–17, July 2016. doi: 10.1080/02678292.2016.1209698. URL http://www.tandfonline.com/doi/full/10.1080/02678292.2016.1209698.

E. A. Shah and K. Keren. Symmetry breaking in reconstituted actin cortices. *eLife*, 3, 2014. doi: 10.7554/elife.01433.

D. Shao, W.-J. Rappel, and H. Levine. Computational Model for Cell Morphodynamics. *Physical Review Letters*, 105(10):108104–4, Sept. 2010. doi: 10.1103/PhysRevLett.105.108104. URL http://link.aps.org/doi/10.1103/PhysRevLett.105.108104.

H. Shin, M. J. Bowick, and X. Xing. Topological Defects in Spherical Nematics. *Physical Review Letters*, 101(3):037802–4, July 2008. doi: 10.1103/PhysRevLett.101.037802. URL http://link.aps.org/doi/10.1103/PhysRevLett.101.037802.

A. R. Simha and S. Ramaswamy. Hydrodynamic Fluctuations and Instabilities in Ordered Suspensions of Self-Propelled Particles. *Physical Review Letters*, 89(5):058101, July 2002a. doi: 10.1103/PhysRevLett.89.058101. URL http://link.aps.org/doi/10.1103/PhysRevLett.89.058101.

R. A. Simha and S. Ramaswamy. Statistical hydrodynamics of ordered suspensions of self-propelled particles: waves, giant number fluctuations and instabilities. *Physica A: Statistical Mechanics and its Applications*, 306:262–269, 2002b. doi: 10.1016/s0378-4371(02)00503-4. URL http://linkinghub.elsevier.com/retrieve/pii/S0378437102005034.

G. Skačej and C. Zannoni. Controlling Surface Defect Valence in Colloids. *Physical Review Letters*, 100(19):197802–4, May 2008. doi: 10.1103/PhysRevLett.100.197802. URL http://link.aps.org/doi/10.1103/PhysRevLett.100.197802.

R. Sknepnek and S. Henkes. Active swarms on a sphere. *Physical Review E*, 91(2):022306–13, Feb. 2015. doi: 10.1103/PhysRevE.91.022306. URL http://link.aps.org/doi/10.1103/PhysRevE.91.022306.

A. Sokolov and I. S. Aranson. Reduction of Viscosity in Suspension of Swimming Bacteria. *Physical Review Letters*, 103(14):148101–4, Sept. 2009. doi: 10.1103/PhysRevLett.103.148101. URL http://link.aps.org/doi/10.1103/PhysRevLett.103.148101.

A. Sokolov, I. S. Aranson, J. O. Kessler, and R. E. Goldstein. Concentration Dependence of the Collective Dynamics of Swimming Bacteria. *Physical Review Letters*, 98(15):158102–4, Apr. 2007. doi: 10.1103/PhysRevLett.98.158102. URL http://link.aps.org/doi/10.1103/PhysRevLett.98.158102.

H. A. Stone and A. Samuel. Propulsion of microorganisms by surface distortions. *Physical Review Letters*, 77(19):4102–4104, 1996. doi: 10.1103/physrevlett.77.4102. URL http://link.aps.org/doi/10.1103/PhysRevLett.77.4102.

Y. Sumino, K. H. Nagai, Y. Shitaka, D. Tanaka, K. Yoshikawa, H. Chaté, and K. Oiwa. Large-scale vortex lattice emerging from collectively moving microtubules. *Nature*, 483(7390):448–452, Mar. 2012. doi: 10.1038/nature10874. URL http://dx.doi.org/10.1038/nature10874.

T. Surrey, F. Nédélec, S. Leibler, and E. Karsenti. Physical Properties Determining Self-Organization of Motors and Microtubules. *Science*, 292(5):1167–1171, May 2001. doi: 10.1126/science.1059758. URL http://adsabs.harvard.edu/cgi-bin/nph-data_query?bibcode=2001Sci...292.1167S&link_type=EJOURNAL.

D. Takagi and H. E. Huppert. Flow and instability of thin films on a cylinder and sphere. *Journal of Fluid Mechanics*, 647:221–18, Mar. 2010. doi: 10.1017/S0022112009993818. URL http://www.journals.cambridge.org/abstract_S0022112009993818.

M. Tasinkevych, M. G. Campbell, and I. I. Smalyukh. Splitting, linking, knotting, and solitonic escape of topological defects in nematic drops with handles. *Proceedings of the National Academy of Sciences*, 111(46):16268–16273, Nov. 2014. doi: 10.1073/pnas.1405928111. URL http://www.pnas.org/lookup/doi/10.1073/pnas.1405928111.

S. P. Thampi, R. Golestanian, and J. M. Yeomans. Velocity Correlations in an Active Nematic. *Physical Review Letters*, 111(11):118101–5, Sept. 2013. doi: 10.1103/PhysRevLett.111.118101. URL http://link.aps.org/doi/10.1103/PhysRevLett.111.118101.

S. P. Thampi, R. Golestanian, and J. M. Yeomans. Instabilities and topological defects in active nematics. *Europhysics Letters*, 105(1):18001, Jan. 2014a. doi: 10.1209/0295-5075/105/18001. URL http://stacks.iop.org/0295-5075/105/i=1/a=18001?key=crossref.cd21aad1b853e1671cdb9a8439a5c6b0.

S. P. Thampi, R. Golestanian, and J. M. Yeomans. Vorticity, defects and correlations in active turbulence. *Philosophical Transactions of the Royal Society A: Mathematical, Physical and Engineering Sciences*, 372(2029):20130366–20130366, Oct. 2014b. doi: 10.1098/rsta.2013.0366. URL http://rsta.royalsocietypublishing.org/cgi/doi/10.1098/rsta.2013.0366.

S. P. Thampi, A. Doostmohammadi, T. N. Shendruk, R. Golestanian, and J. M. Yeomans. Active micromachines: Microfluidics powered by mesoscale turbulence. *Science Advances*, 2(7):e1501854–e1501854, July 2016. doi: 10.1126/sciadv.1501854. URL http://advances.sciencemag.org/cgi/doi/10.1126/sciadv.1501854.

M. Theillard, R. Alonso-Matilla, and D. Saintillan. Geometric control of active collective motion. *Soft Matter*, 13(2):1–13, Dec. 2016. doi: 10.1039/C6SM01955B. URL http://dx.doi.org/10.1039/C6SM01955B.

E. Tjhung, M. E. Cates, and D. Marenduzzo. Nonequilibrium steady states in polar active fluids. *Soft Matter*, 7(16):7453–12, 2011. doi: 10.1039/c1sm05396e. URL http://xlink.rsc.org/?DOI=c1sm05396e.

E. Tjhung, D. Marenduzzo, and M. E. Cates. Spontaneous symmetry breaking in active droplets provides a generic route to motility. *Proceedings of the National Academy of Sciences*, 109(31):12381–12386, July 2012. doi: 10.1073/pnas.1200843109. URL http://adsabs.harvard.edu/cgi-bin/nph-data_query?bibcode=2012PNAS..10912381T&link_type=EJOURNAL.

E. Tjhung, A. Tiribocchi, D. Marenduzzo, and M. E. Cates. A minimal physical model captures the shapes of crawling cells. *Nature Communications*, 6:5420, Jan. 2015. doi: 10.1038/ncomms6420. URL http://adsabs.harvard.edu/cgi-bin/nph-data_query?bibcode=2015NatCo...6E5420T&link_type=EJOURNAL.

J. Toner and Y. Tu. Flocks, herds, and schools: A quantitative theory of flocking. *Physical Review E*, 58(4):4828–4858, 1998. doi: 10.1103/physreve.58.4828. URL http://link.aps.org/doi/10.1103/PhysRevE.58.4828.

J. Toner, Y. Tu, and S. Ramaswamy. Hydrodynamics and phases of flocks. *Annals of Physics*, 318 (1):170–244, July 2005. doi: 10.1016/j.aop.2005.04.011. URL http://linkinghub.elsevier.com/retrieve/pii/S0003491605000540.

G. Tóth, C. Denniston, and J. M. Yeomans. Hydrodynamics of Topological Defects in Nematic Liquid Crystals. *Physical Review Letters*, 88(10):105504–4, Feb. 2002. doi: 10.1103/PhysRevLett.88.105504. URL http://link.aps.org/doi/10.1103/PhysRevLett.88.105504.

H. Turlier, B. Audoly, J. Prost, and J.-F. Joanny. Furrow Constriction in Animal Cell Cytokinesis. *Biophysical Journal*, 106(1):114–123, Jan. 2014. doi: 10.1016/j.bpj.2013.11.014. URL http://dx.doi.org/10.1016/j.bpj.2013.11.014.

P. Vallotton, G. Danuser, and S. Bohnet. Tracking retrograde flow in keratocytes: news from the front. *Molecular biology of ...*, 16(3):1223–1231, 2005. doi: 10.1091/mbc.e04-07-0615. URL http://www.molbiolcell.org/cgi/doi/10.1091/mbc.E04-07-0615.

J. Verchot-Lubicz and R. E. Goldstein. Cytoplasmic streaming enables the distribution of molecules and vesicles in large plant cells. *Protoplasma*, 240(1-4):99–107, Nov. 2009. doi: 10.1007/s00709-009-0088-x. URL http://link.springer.com/10.1007/s00709-009-0088-x.

A. B. Verkhovsky, T. M. Svitkina, and G. G. Borisy. Self-polarization and directional motility of cytoplasm. *Current Biology*, 9(1):11–S1, 1999. doi: 10.1016/s0960-9822(99)80042-6. URL http://linkinghub.elsevier.com/retrieve/pii/S0960982299800426.

T. Vicsek and A. Zafeiris. Collective motion. *Physics Reports*, 517(3-4):71–140, Aug. 2012. doi: 10.1016/j.physrep.2012.03.004. URL http://dx.doi.org/10.1016/j.physrep.2012.03.004.

T. Vicsek, A. Czirók, E. Ben-Jacob, I. Cohen, and O. Shochet. Novel Type of Phase Transition in a System of Self-Driven Particles. *Physical Review Letters*, 75(6):1226–1229, 1995. doi: 10.1103/physrevlett.75.1226. URL http://link.aps.org/doi/10.1103/PhysRevLett.75.1226.

T. Vignaud, L. Blanchoin, and M. Théry. Directed cytoskeleton self-organization. *Trends in Cell Biology*, 22(12):671–682, Dec. 2012. doi: 10.1016/j.tcb.2012.08.012. URL http://dx.doi.org/10.1016/j.tcb.2012.08.012.

V. Vitelli and D. R. Nelson. Nematic textures in spherical shells. *Physical Review E*, 74(2):021711–18, Aug. 2006. doi: 10.1103/PhysRevE.74.021711. URL http://link.aps.org/doi/10.1103/PhysRevE.74.021711.

I. D. Vladescu, E. J. Marsden, J. Schwarz-Linek, V. A. Martinez, J. Arlt, A. N. Morozov, D. Marenduzzo, M. E. Cates, and W. C. K. Poon. Filling an Emulsion Drop with Motile Bacteria. *Physical Review Letters*, 113(26):268101–5, Dec. 2014. doi: 10.1103/PhysRevLett.113.268101. URL http://link.aps.org/doi/10.1103/PhysRevLett.113.268101.

P. M. Vlahovska. Dynamics of membrane-bound particles: Capsules and vesicles. In *Fluid-Structure Interactions in Low-Reynolds-Number Flows*, pages 313–346. The Royal Society of Chemistry, 2016. ISBN 978-1-84973-813-2. doi: 10.1039/9781782628491-00313. URL http://dx.doi.org/10.1039/9781782628491-00313.

R. Voituriez, J.-F. Joanny, and J. Prost. Spontaneous flow transition in active polar gels. *Europhysics Letters*, 2005. doi: 10.1209/epl/i2004-10501-2. URL http://iopscience.iop.org/article/10.1209/epl/i2004-10501-2/meta.

R. Voituriez, J.-F. Joanny, and J. Prost. Generic Phase Diagram of Active Polar Films. *Physical Review Letters*, 96(2):028102, Jan. 2006. doi: 10.1103/PhysRevLett.96.028102. URL http://link.aps.org/doi/10.1103/PhysRevLett.96.028102.

G. E. Volovik and O. D. Lavrentovich. Topological dynamics of defects: boojums in nematic drops. *Zh Eksp Teor Fiz*, 1983. URL http://www.personal.kent.edu/~olavrent/pdf/33_topologicaldynamicsdefectsboojumsnematicdrops1983.pdf.

A. J. Vromans and L. Giomi. Orientational properties of nematic disclinations. *Soft Matter*, 12(30):6490–6495, July 2016. doi: 10.1039/C6SM01146B. URL http://dx.doi.org/10.1039/C6SM01146B.

C. R. Wand and M. A. Bates. Monte Carlo simulations of nematic and chiral nematic shells. *Physical Review E*, 91(1):012502–4, Jan. 2015. doi: 10.1103/PhysRevE.91.012502. URL http://link.aps.org/doi/10.1103/PhysRevE.91.012502.

X. Wang, D. S. Miller, E. Bukusoglu, J. J. de Pablo, and N. L. Abbott. Topological defects in liquid crystals as templates for molecular self-assembly. *Nature Materials*, 15(1):106–112, Sept. 2015. doi: 10.1038/nmat4421. URL http://www.nature.com/doifinder/10.1038/nmat4421.

A. Ward, F. Hilitski, W. Schwenger, D. Welch, A. W. C. Lau, V. Vitelli, L. Mahadevan, and Z. Dogic. Solid friction between soft filaments. *Nature Materials*, 14(6):583–588, Mar. 2015. doi: 10.1038/nmat4222. URL http://www.nature.com/doifinder/10.1038/nmat4222.

C. A. Whitfield. Private communication, 2016.

C. A. Whitfield and R. J. Hawkins. Instabilities, motion and deformation of active fluid droplets. *New Journal of Physics*, 18(12):123016–12, Dec. 2016. doi: 10.1088/1367-2630/18/12/123016. URL http://stacks.iop.org/1367-2630/18/i=12/a=123016?key=crossref.7817e32f2d8fcd0c0bf5cd171f8377f5.

C. A. Whitfield, D. Marenduzzo, R. Voituriez, and R. J. Hawkins. Active polar fluid flow in finite droplets. *The European Physical Journal E*, 37(2):8, Feb. 2014. doi: 10.1140/epje/i2014-14008-3. URL http://link.springer.com/10.1140/epje/i2014-14008-3.

H. Wioland, F. G. Woodhouse, J. Dunkel, J. O. Kessler, and R. E. Goldstein. Confinement Stabilizes a Bacterial Suspension into a Spiral Vortex. *Physical Review Letters*, 110(26):268102, June 2013. doi: 10.1103/PhysRevLett.110.268102. URL http://link.aps.org/doi/10.1103/PhysRevLett.110.268102.

H. Wioland, E. Lushi, and R. E. Goldstein. Directed collective motion of bacteria under channel confinement. *New Journal of Physics*, 18(7):1–12, June 2016a. doi: 10.1088/1367-2630/18/7/075002. URL http://dx.doi.org/10.1088/1367-2630/18/7/075002.

H. Wioland, F. G. Woodhouse, J. Dunkel, and R. E. Goldstein. Ferromagnetic and antiferromagnetic order in bacterial vortex lattices. *Nature Physics*, pages 1–6, Jan. 2016b. doi: 10.1038/nphys3607. URL http://www.nature.com/doifinder/10.1038/nphys3607.

F. G. Woodhouse and R. E. Goldstein. Spontaneous Circulation of Confined Active Suspensions. *Physical Review Letters*, 109(16):168105, Oct. 2012. doi: 10.1103/PhysRevLett.109.168105. URL http://link.aps.org/doi/10.1103/PhysRevLett.109.168105.

F. G. Woodhouse and R. E. Goldstein. Cytoplasmic streaming in plant cells emerges naturally by microfilament self-organization. In *Proceedings of the National Academy of Sciences*, 2013. doi: 10.1073/pnas.1302736110/-/DCSupplemental. URL http://www.pnas.org/content/110/35/14132.short.

K.-T. Wu, J. B. Hishamunda, D. T. N. Chen, S. J. DeCamp, Y.-W. Chang, A. Fernandez-Nieves, S. Fraden, and Z. Dogic. Transition from turbulent to coherent flows in confined three-dimensional active fluids. *Science*, 355(6331):eaal1979–11, Mar. 2017. doi: 10.1126/science.aal1979. URL http://www.sciencemag.org/lookup/doi/10.1126/science.aal1979.

P. T. Yam, C. A. Wilson, L. Ji, B. Hebert, E. L. Barnhart, N. A. Dye, P. W. Wiseman, G. Danuser, and J. A. Theriot. Actin myosin network reorganization breaks symmetry at the cell rear to spontaneously initiate polarized cell motility. *The Journal of Cell Biology*, 178(7):1207–1221, Sept. 2007. doi: 10.1083/jcb.200706012. URL http://www.jcb.org/cgi/doi/10.1083/jcb.200706012.

J. M. Yeomans. The Hydrodynamics of Active Systems. page arXiv:1603.00194, Mar. 2016. URL http://arxiv.org/abs/1603.00194v1.

K. Yi, J. R. Unruh, M. Deng, B. D. Slaughter, B. Rubinstein, and R. Li. Dynamic maintenance of asymmetric meiotic spindle position through Arp2/3-complex-driven cytoplasmic streaming in mouse oocytes. *Nature Cell Biology*, 13(10):1252–1258, Aug. 2011. doi: 10.1038/ncb2320. URL http://dx.doi.org/10.1038/ncb2320.

W. Y. Zhang and J. Chen. Tennis-ball state of a self-avoiding wormlike polymer on a spherical surface. *Europhysics Letters*, 94(4):43001, 2011. doi: 10.1209/0295-5075/94/43001. URL http://iopscience.iop.org/article/10.1209/0295-5075/94/43001/meta.

W.-Y. Zhang, Y. Jiang, and J. Z. Y. Chen. Onsager Model for the Structure of Rigid Rods Confined on a Spherical Surface. *Physical Review Letters*, 108(5):057801–5, Jan. 2012. doi: 10.1103/PhysRevLett.108.057801. URL http://link.aps.org/doi/10.1103/PhysRevLett.108.057801.

S. Zhou, A. Sokolov, O. D. Lavrentovich, and I. S. Aranson. Living liquid crystals. *Proceedings of the National Academy of Sciences*, 111(4):1265–1270, Jan. 2014. doi: 10.1073/pnas.1321926111. URL http://www.pnas.org/cgi/doi/10.1073/pnas.1321926111.

F. Ziebert, S. Swaminathan, and I. S. Aranson. Model for self-polarization and motility of keratocyte fragments. *Journal of The Royal Society Interface*, 9(70):1084–1092, Mar. 2012. doi: 10.1098/rsif.2011.0433. URL http://rsif.royalsocietypublishing.org/cgi/doi/10.1098/rsif.2011.0433.